Modelling Non-Catalytic Gas-Solid Reactions

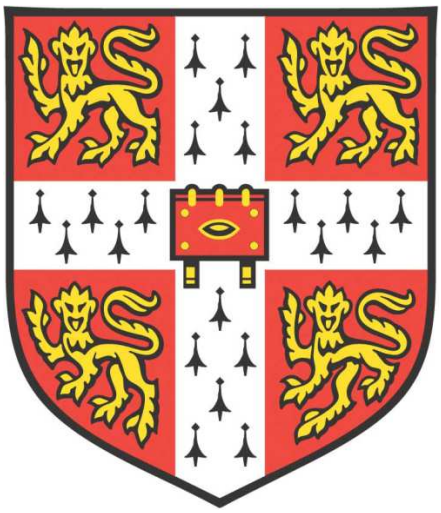

Peng Dai

Emmanuel College

Department of Chemical Engineering and Biotechnology

University of Cambridge

This dissertation is submitted for the degree of Doctor of Philosophy

April 2017

Revisited December 2017

To Heather

And

"When you desperately want something, all the universe conspires in helping you to achieve it."

— Paulo Coelho, The Alchemist

Preface

The work in this Dissertation was carried out in the Department of Chemical Engineering and Biotechnology, University of Cambridge, between January 2014 and March 2017. It is the result of my own original work and includes nothing, which is the outcome of work done in collaboration except where specifically indicated in the text.

It is not substantially the same as any that I have submitted, or, is being concurrently submitted for a degree or diploma or other qualification at the University of Cambridge or any other University or similar institution except as declared in the Preface and specified in the text. I further state that no substantial part of my dissertation has already been submitted, or, is being concurrently submitted for any such degree, diploma or other qualification at the University of Cambridge or any other University or similar institution except as declared in the Preface and specified in the text.

This Dissertation contains approximately 52300 words and 71 figures in total and does not exceed the prescribed word limit for the Degree Committee.

Peng Dai

Department of Chemical Engineering and Biotechnology

University of Cambridge

April 2017

Revisited December 2017

Acknowledgement

First and foremost, I would like to thank my supervisor, Prof. John S. Dennis, for his continued guidance, encouragement and advice during my PhD. I would also like to thank my advisor, Dr Stuart Scott, for his support. My special appreciation goes to Dr Marco Saucedo for his generous help and advice in my initial experimental work, and to Dr Wen Liu and Dr Belén González, for their advices and efficient collaboration in some of the work of my research.

I would also like to thank the staff of the Department of Chemical Engineering and Biotechnology, in particular, Zlatko Saracevic, Amanda Taylor, Wei-Yao Ma, John Gannon and Jonathan Cowper. Many thanks go to my fellow group members of the Combustion Group: Dr Wenting Hu, Dr Felix Donat, Ross Hubble, Matthias Schnellmann, Martin Chan, Paul Hodgson, Zachary Bond, Pieterjan Van Uytvanck, Lei Hu and Dr Christopher Boyce. Special thanks to members of the B9 office on Pembroke Street, where I had so much joy over many of the exciting discussions and Tiddlywink games.

I am extremely grateful to my parents for funding my study and Emmanuel College, Cambridge for the invaluable support during my PhD. Special thanks to my Graduate Tutor at Emmanuel, Revd. Jeremy Caddick, for his advices and help in my third year.

Finally, I am truly thankful to my parents and sisters for their support and to my beloved wife, Heather, for believing in me even at moments when I didn't myself.

Abstract

The overall objective of the work described in this Dissertation was to develop and verify a general reaction and diffusion model for non-catalytic reactions between gases and porous solids, particularly those relevant to the clean use of fossil fuels. Here, the internal pore structure of the solid was characterised by observing the kinetics in a regime limited only by intrinsic chemical reaction. It was hypothesised that a simple arbitrary function, $f(X)$, determined from experimental measurements of rate *vs.* conversion in a kinetically-controlled regime, could be used in place of formal, mathematical pore models, to describe the evolution of pore structure during a reaction influenced by intraparticle mass transfer. The approach was used to study (i) the gasification of chars by CO_2, where the only product was gaseous, (ii) the calcination of $CaCO_3$ cycled between calcined and carbonated states, where the products were a gas and a solid, and (iii) the sulphation of virgin and sintered CaO by SO_2, the only product being solid.

The full model was able to account for chemical kinetics, intraparticle heat and mass transfer, external mass transfer and the evolution of pore structure in a particle of a reacting solid. The Cylindrical Pore Interpolation Model was used to describe intraparticle mass transfer and the Stefan-Maxwell equations were employed to model external mass transfer. The full form of the energy balance equation was used, including an allowance, albeit small, for change in momentum of the gas as gaseous species were abstracted from, or emitted to, the gases diffusing through the porous structure during the reaction. The whole system was solved using the method of Orthogonal Collocation on Finite Elements with adaptable numerical meshes for the spatial dimension and marched forward in time dimension using the method of Finite Difference.

To verify the model, batch experiments involving the three types of reaction identified above were conducted in a fluidised bed reactor. The rates of reaction and conversion as functions of time were measured experimentally and compared with the theoretical predictions. The results from gasification showed that the experimentally-determined $f(X)$ function was capable of describing the evolution of pore structures during the reaction of different sizes of particles, for experiments at the same temperature.

However, there were some disparities between theory and experiment when the $f(X)$, which should be invariant with temperature, was applied to results obtained at higher temperatures. The most probable reason for this was the different contributions from multiple types of active sites within the char particles.

Studies of calcination showed that, at least for limestones subjected to a history of cycling between the calcined and carbonated states, a correctly-determined $f(X)$ could be applied to different sizes of particles at temperatures different to that at which $f(X)$ was determined. Somewhat surprisingly, it was found that the $f(X)$ determined from one, cycled, limestone was successful in predicting the conversion of other cycled limestones of different geological origin. It was concluded that the process of cycling between the calcined and carbonated states at the same process condition had significantly reduced the differences apparent in the pore structures of the different limestones when first calcined from the virgin materials. The experimentally-observed effects of pressure, concentration of CO_2 and temperature described in the literature were explained successfully by the mathematical model.

Finally, the study of sulphation explained satisfactorily (i) the reason for there being a maximum in the ultimate conversion of CaO to $CaSO_4$ at a specific temperature, and (ii) the processes controlling the overall uptake of SO_2 by sintered CaO, such as might be produced from a calcium-looping cycle for capturing CO_2 from flue gases. For both the virgin and the cycled calcines, the ultimate conversion to $CaSO_4$ seemed to be limited by the pore volume below 300 nm diameter. Two mechanisms were identified to explain why CaO cannot be fully sulphated to $CaSO_4$.

In summary, this work has demonstrated the applicability of the general reaction and diffusion model to gasification, calcination and sulphation reactions, and verified the $f(X)$ approach for describing pore evolution during reaction.

Contents

List of Tables

List of Figures

List of Abbreviations and Acronyms

A_A, A_K, A_C	Coefficients in pressure gradient equation	Pa s m $g^{-0.5}$ $mol^{-0.5}$
$A_{s,0}$	Initial pore area per unit mass	m^2 g^{-1}
$C_{p,n}$	Molar heat capacity of species *n*	J mol^{-1} K^{-1}
c_0	Initial number of active sites per unit mass of char	g^{-1}
$D_{A,nm}$	Diffusivity at arbitrary Knudsen number, for species *n* and *m*	m^2 s^{-1}
$D_{B,nm}$	Molecular diffusivity, involving species *n* in *m*	m^2 s^{-1}
$D_{K,n}$	Knudsen diffusivity of species *n*	m^2 s^{-1}
D_{ref}	Referenced molecular diffusivity at bulk condition	m^2 s^{-1}
D_P	Product layer diffusivity	m^2 s^{-1}
d_{pore}	Pore diameter	m
$d_{pore,0}$	Initial pore diameter	m
$\overline{d_b}$	Mean bubble diameter	m
E_a	Activation energy of rate constant	kJ mol^{-1}
F	Energy flux	J m^{-2} s^{-1}
H_n	Partial molar enthalpy of species *n*	J mol^{-1}
H_f	Partial molar enthalpy of formation	J mol^{-1}
h	Bed height	m
h_{mf}	Bed height at minimum fluidisation	m
J_n	Total molar flux of species *n*	mol m^{-2} s^{-1}
k_1, k_{-1}	Rate constant per active site of CO_2 gasification	mol s^{-1} bar^{-1}
k_2	Rate constant per active site of CO_2 gasification	mol s^{-1}
K_P	Equilibrium constant of CO_2 gasification	-
k_c	Rate constants of calcination reaction	mol m^{-2} s^{-1}
k_c'	Modified rate constants of calcination reaction	s^{-1}
k_0	Arrhenius coefficient of rate constant k_c'	s^{-1}
$\bar{k}$	Rate constant of carbonation reaction	m s^{-1}
k_s	Rate constants of sulphation reaction	m s^{-1}
k_{Avg}	Overall rate constants of sulphation reaction	m s^{-1}
N	Total number of species	-

NE	Total number of finite elements	-
NP	The number of collocation points within each finite element	-
NT	Total number of collocation points	-
M_n	Molecular mass of species *n*	kg mol^{-1}
P	Total pressure	bar
$p_{\mathrm{CO_2}}\vert_r$	Local partial pressure of CO_2	bar
$p_{\mathrm{CO_2}}^{\mathrm{bulk}}, p_{\mathrm{CO_2}}^{eq}$	Bulk and equilibrium partial pressure of CO_2	bar
q_{c}	Intrinsic rate of calcination per unit of surface area	mol m^{-2} s^{-1}
Q_n	Net rate of reaction of gas species *n*	mol m^{-3} s^{-1}
Q_{S1}	Net rate of reaction of solid species S1	mol m^{-3} s^{-1}
$\hat{Q}_{\mathrm{S1}}$	Net rate of reaction of solid species S1	mol g^{-1} s^{-1}
r	Radial distance from the particle centre	m
r_p	Radius of a limestone particle	m
r_{pore}	Pore radius	m
$r_{pore,0}$	Initial pore radius	m
R	Universal gas constant	kJ mol^{-1} K^{-1}
R_g'	Rate of production of CO from gasification	mol s^{-1} g^{-1}
t	Time	s
t_d	Dead time	s
T	Absolute temperature	K
U_b	Bubble velocity	m s^{-1}
U_{mf}	Flow velocity at minimum fluidisation	m s^{-1}
u_M	Mass-averaged velocity	m s^{-1}
V_M	Molar volume	m^3 mol^{-1}
X	Solid conversion	-
y_n	Mole fraction of species *n*	-
Greek letters		
α_t	Time step growth factor	-
α_x	Finite element spacing decay factor	-
Λ_{k_c}	Pre-exponential coefficient of the rate constant k_c	mol m^{-2} s^{-1}
λ	Thermal conductivity	W m^{-1} K^{-1}
λ_{eff}	Effective thermal conductivity of the particle	W m^{-1} K^{-1}

ε	Porosity of the particle	-
ε_0	Initial porosity of the particle	-
ε_b	Bubble fraction in the fluidised bed	-
ε_{bed}	Porosity of the fluidised bed around the particle	-
ε_{mf}	Porosity of the fluidised bed at incipient fluidisation	-
ρ_e	Bulk density of a particle	kg m^{-3}
ρ_m	Skeletal density of the particle	kg m^{-3}
ρ_g	Gas density from ideal gas law	kg m^{-3}
τ_M	Mean residence time of CSTR	s
τ^2	Tortuosity factor of the particle	-
τ_{bed}^2	Tortuosity factor of the fluidised bed	-
δ	External diffusion boundary layer thickness	m
Δh	Product layer thickness	m
φ	Thiele modulus	-
η	Dimensionless radius	-
υ	Kinematic viscosity	m^2 s^{-1}
μ	Dynamic viscosity	Pa s
ν	Stoichiometric coefficient	-
Ω_μ	Collision integral for viscosity between two molecules	-
Ω_D	Collision integral for diffusivity between two molecules	-
σ_n	Collision diameter of the molecule of species n	Å
ϵ_n	Maximum energy of attraction between two molecules of species *n*	J
κ	Boltzmann's constant	J K^{-1}
κ_{eff}	Effectiveness factor during gasification	-

Subscripts

0	At time of 0
n	Gas species *n*
m	Gas species *m*
mix	Gas mixture

Superscripts

I	Inside the particle
E	External to the particle
S	Particle surface
B	Bulk

Abbreviation

BET	Brunauer–Emmett–Teller
BJH	Barrett-Joyner-Halenda
CPIM	Cylindrical Pore Interpolation Model
CRM	Continuous Reaction Model
CSTR	Continuous Stirred Tank Reactor
DGM	Dusty Gas Model
MPTM	Mean Pore Transport Model
OCFE	Orthogonal Collocation on Finite Element
PFR	Plug Flow Reactor
RPM	Random Pore Model
SCM	Shrinking Core Model

Chapter 1 Introduction

1.1 Background

1.1.1 World energy demand and supply

The projected total world consumption of energy is likely to expand from 1.6×10^8 GWh in 2012 to 1.8×10^8 GWh in 2020 and reaching 2.4×10^8 GWh in 2040 (EIA, 2016). This constitutes an average increase of 1.4%/y and a total increase of 48% between 2012 and 2040. Much of the increase in energy demand is occurring, and will occur, in developing countries such as China and India, where strong economic growth and expanding populations will lead to a ~71% increase in world energy use between 2012 and 2040. In the more mature, and slower-growing, economies such as the U.S. and the U.K., the total energy use over the same period might rise by ~ 18% (EIA, 2016). Figure 1.1 shows the world's consumption of energy from various sources to 2040, at which time, fossil fuels will still account for ~78% of energy use, even though the consumption of non-fossil fuels is expected to grow faster than the consumption of fossil fuels.

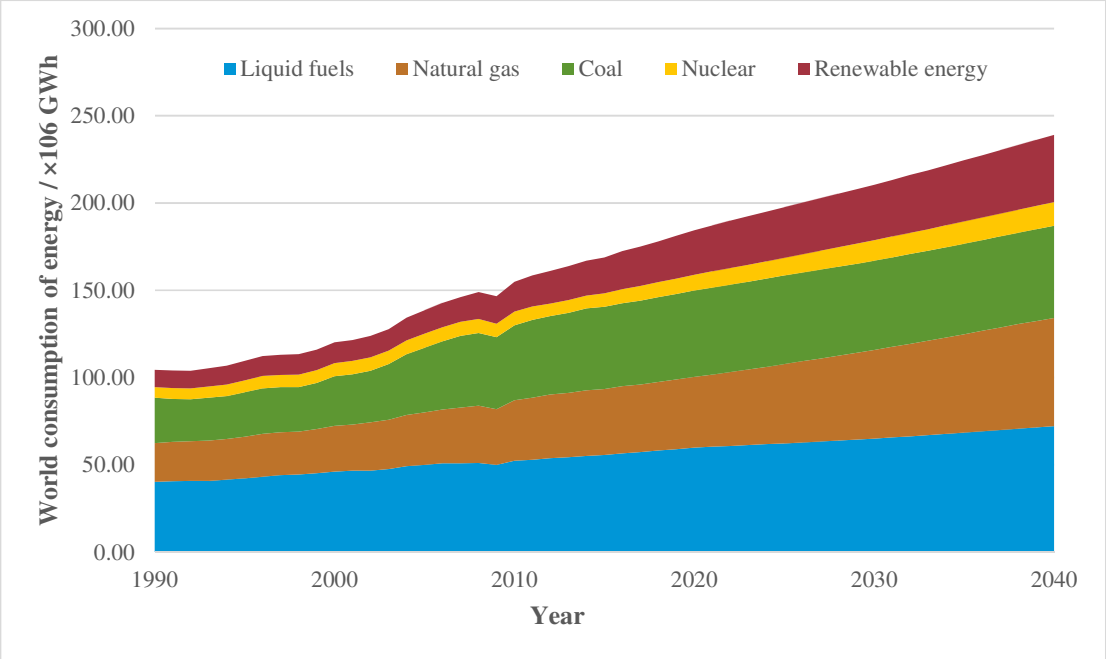

Figure 1.1 World consumption of energy by energy source between 1990 and 2040 (EIA, 2016).

Figure 1.1 shows that coal will probably remain the second-largest energy source worldwide behind petroleum and other liquid fuels until 2030. Moreover, coal is

the world's most abundant fossil fuel with estimated reserves sufficient for 150 – 170 years at the current rate of consumption (BGR, 2011). Many countries with electricity challenges, particularly those in Asia and southern Africa, can access coal resources in an affordable and secure way to ensure the growth in their electricity supply. Coal will therefore play a major role in supporting the development of base-load electricity where it is most needed. Figure 1.2 shows the world's net electricity generation by fuel sources, showing that coal will continue as the largest single fuel used for electricity generation until generation from renewable sources overtakes coal-fired generation by about 2040.

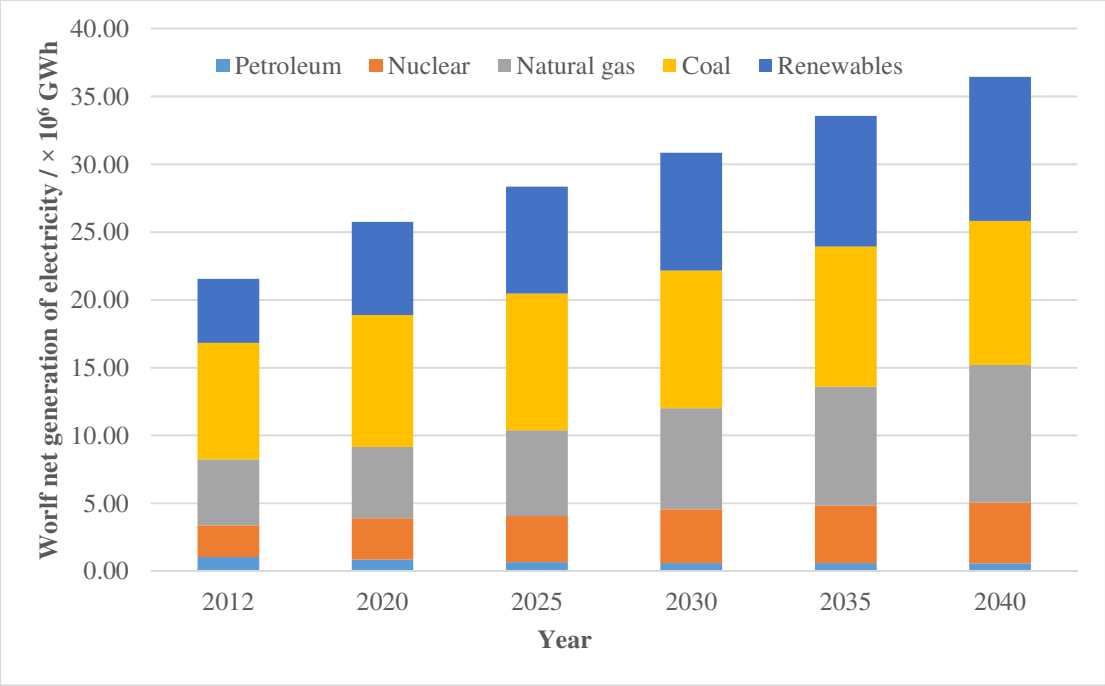

Figure 1.2 Projected world net generation of electricity by energy source from 2012 and 2040 (EIA, 2016).

Therefore, the implementation of modern, highly-efficient and clean technologies for the utilisation of coal is the key to the development of economies if the effects of burning coal on society and environment are to be minimised (WEC, 2013). Depending on the end-use and the environmental constraints, coal might be utilized in four major ways – gasification, combustion, liquefaction and pyrolysis. In each case, the process efficiency depends considerably on the heterogeneous kinetics controlling (a) coal char gasification with steam, carbon dioxide and hydrogen and, or, (b) char combustion with oxygen or air. In many cases, the rate of gasification of solid chars controls the reactor volume required in most conversion processes producing power or synthesis gas (Laurendeau, 1978). Therefore, having a theoretical model to simulate

reactions such as gasification can contribute to better design of the reaction system and higher process efficiency.

1.1.2 Carbon dioxide emissions

Figure 1.3 shows the projected global emissions of CO_2 emissions associated with energy use. It can be seen that coal became the leading source of CO_2 emissions in 2006 and remains so up to at least 2040 (EIA, 2016; IPCC, 2005). Thus, the use of low-emission coal technologies is important if international targets on climate change are to be achieved. The two principal avenues for reducing carbon emissions from coal-fired power generation are (i) the use of high efficiency power plant such as Integrated Gasification Combined Cycles (IGCC), and (ii) the use of carbon capture and storage (CCS). CCS is a process consisting of the separation of CO_2, usually from industrial and energy-related sources, transport to a storage location and long-term isolation from the atmosphere. Such disposal is only feasible if the CO_2 is almost pure, largely free of nitrogen and other gases (IPCC, 2005). There are three main approaches to capturing the CO_2 generated from a primary fossil fuel (*i.e.* coal, natural gas or oil), biomass, or mixtures of these fuels (IPCC, 2005): (i) post-combustion capture, where CO_2 is separated from the flue gases produced by the combustion of the fuel in air, (ii) pre-combustion capture, where CO_2 is separated from a mixture of the CO_2 and H_2 produced from the gasification of the fuels and the subsequent water-gas shift reaction between CO and H_2O, and (iii) oxy-fuel combustion, where pure stream of CO_2 is obtained by removing the steam from the flue gases produced by the combustion of the fuels in pure oxygen. One of the most promising type of technologies for CO_2 capture is separation with liquid absorbent or solid sorbent that is capable of capturing CO_2 (IPCC, 2005). For separation with solid sorbents, the used sorbent is usually regenerated by releasing the captured CO_2 after being heated or after any other change in the conditions around the sorbent. Then the regenerated sorbent is sent back to capture more CO_2 in a cyclic process. In some situations, the solid sorbent may be a solid oxide which reacts in a vessel with fossil fuel or biomass producing heat and mainly CO_2. The spent sorbent is then circulated to a second vessel where it is re-oxidized in air for reuse with some loss and make up of fresh sorbent.

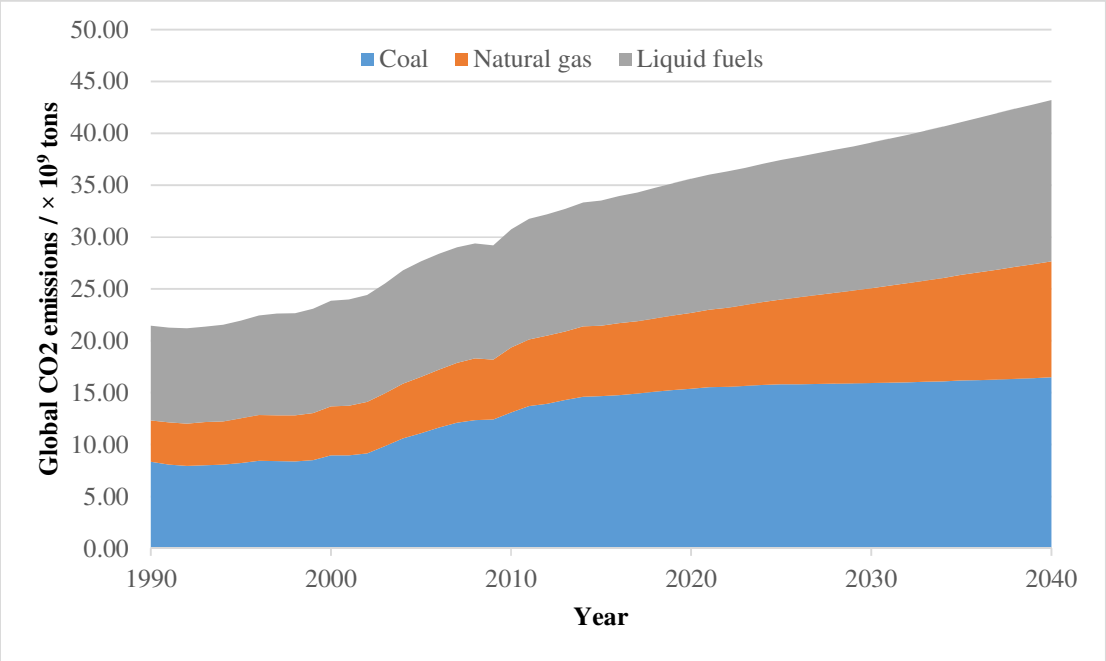

Figure 1.3 Global CO_2 emissions from all energy-related operations by fuel type projected to 2040 (EIA 2016).

Natural limestone, containing mostly $CaCO_3$ in its virgin form or CaO in its calcined form, has the potential as a solid sorbent for post-combustion CO_2 capture (IPCC, 2005). Limestone is abundant, inexpensive and safe, which makes it potentially suitable for large-scale capture of CO_2 (Arias *et al.*, 2013; Boot-Handford *et al.*, 2014; Hanak *et al.*, 2015; Erans *et al.*, 2016). The carbonation – calcination cycling process involves Ca-based sorbents being cycled between their carbonated ($CaCO_3$) and calcined (CaO) states at relatively high temperature (*e.g.* carbonation at $T > 600$ºC and calcination at $T > 900$ºC), giving the potential to reduce efficiency penalties arisen from the loss of heat compared to absorption methods involving wetted sorbents (*e.g.* wet-carbonation of the natural silicate olivine) (IPCC, 2005). One of the challenges is that natural sorbents (*e.g.* limestones and dolomites) deactivate rapidly during repeated cycling between the calcined and carbonated state and a large make-up flow of sorbent (of the order of the mass flow of fuel entering the plant) is required to maintain the activity in the carbonation – calcination cycle (Abanades *et al.*, 2004b). Although the cost of the natural sorbent is low, and the deactivated sorbent might find applications in the cement industry and in processes to remove SO_2 from flue gases (Li *et al.*, 2014; Cordero *et al.*, 2014), it would still be highly beneficial to improve the capacity of the sorbents to capture CO_2. A range of experimental approaches are being pursued to increase the capacity of Ca-based sorbents (Wu *et al.*, 2010; Manovic & Anthony, 2010; Basinas *et al.*, 2014; Kavosh *et al.*, 2015; Erans *et al.*, 2016; González *et al.*, 2016).

However, these approaches often lack a theoretical framework, so that rigorously-constructed reaction models can help identify the key variables to consider for enhancing CO_2 capturing capacity.

1.1.3 Sulphur dioxide emissions

Another aspect of environmental concern with fossil fuels, particularly coal, is the emission of SO_2 during combustion (UNEP, 2012). SO_2 emissions have detrimental effects on human health, by contributing to $PM_{2.5}$ (*i.e.* atmospheric-borne particles < 2.5 μm dia.), on terrestrial and freshwater ecosystems by acidification (Rodhe *et al.*, 1995), on man-made materials and cultural heritage by corrosion (Kucera *et al.*, 2007), and on biodiversity (Bobbink *et al.*, 1998) and forestry (Menz & Seip, 2004). Global efforts are being made to reduce the SO_2 emissions. For example, as part of its five-year plans, China implemented flue-gas desulphurization and the phasing out of small, inefficient units in the power sector in a move to achieve the national goal of a 10% reduction in SO_2 emissions between 2005 and 2010 (Zhang, 2010).

When cycled Ca-based sorbents have lost a significant amount of their capacity to take up CO_2, they can be injected into fluidised bed coal combustors to capture SO_2 (Manovic *et al.*, 2009; Li *et al.*, 2014; Cordero *et al.*, 2014). The absorption of SO_2 in a fluidised bed typically involves the gas-solid reaction between a calcium-based sorbent containing CaO or $Ca(OH)_2$ with the SO_2 and oxygen in the post-combustion flue gases (Anthony & Granatstein, 2001). The product $CaSO_4$ is stable and does not decompose readily at the temperatures used in fluidised bed combustion (Córdoba, 2015; Cordero & Alonso, 2015). However, one of the challenges of this desulphurisation process is, as with carbonation, the low absorption capacity of the sorbents. Extensive studies have been carried out to investigate how the properties of the sorbent (Pacciani *et al.*, 2009; Arias *et al.*, 2012; de las Obras-Loscertales *et al.*, 2015) and the operating conditions (Wu *et al.*, 2006; Stewart *et al.*, 2010; de Diego *et al.*, 2013; Basinas *et al.*, 2014) affect the sorption capacity. Such studies involve understanding the mechanism of reaction and diffusion between CaO and SO_2 as well as how the change of particle structure during reaction affects the reaction process and intraparticle mass transfer, where a rigorously constructed reaction and diffusion model can be valuable.

1.2 Modelling non-catalytic gas-solid reactions

1.2.1 The modelling scale

To design a reactor with defined capabilities, theoretical models are usually constructed using information from a variety of areas: thermodynamics, chemical kinetics, fluid mechanics, heat transfer, mass transfer, and process economics. This is a very demanding task with complex interactions between different factors. It is important to model in sufficient detail the rate-controlling processes affecting the design, which means a model focusing on the rate controlling processes at a single particle scale can be more deterministic in explaining the effect of some key parameters and their limits of control. The result of such a model can then help to decide what factors can be safely ignored in the large-scale reactor model. In this Dissertation, the theoretical models are focused on a single particle scale.

1.2.2 The reaction models

This Dissertation is focused on non-catalytic, heterogeneous reactions between a gas and solid. Broadly-speaking, two classes of model exist to describe such reactions, namely the Shrinking Core Model (SCM) and the Continuous Reaction Model (CRM). The SCM is one of the earliest models used for non-catalytic heterogenous reactions between gas and solid (Ramachandran & Doraiswamy, 1982), for example, the combustion of solid carbon and the calcination of non-porous, virgin particles of limestone (generally close to pure $CaCO_3$). In SCM, as shown in Figure 1.4, the reaction takes place at the outside surface of the particle at first, but as the reaction proceeds, the sharp reaction front will move towards the particle centre leaving behind a layer of inert ashes. During the process, an unreacted core is formed which shrinks with time, but the external radius of the particle remains the same, assuming no deformation of the ash layer that has been formed. For the gaseous reactants to reach the surface of the unreacted core or the gaseous product to leave the particle, it must move through various layers of resistances in series. Hence, the rate of reaction might be limited variously by (i) chemical kinetics, (ii) diffusion through the porous product layer, (iii) transport of heat to or from a reaction interface, or (iv) diffusion through the external gas film. A typical SCM prediction for the relationships between the conversion of the solid with time for a non-shrinking particle with a first order reaction occurring is shown in Figure 1.5, where the above-mentioned case (i), (ii) and (iv) are plotted.

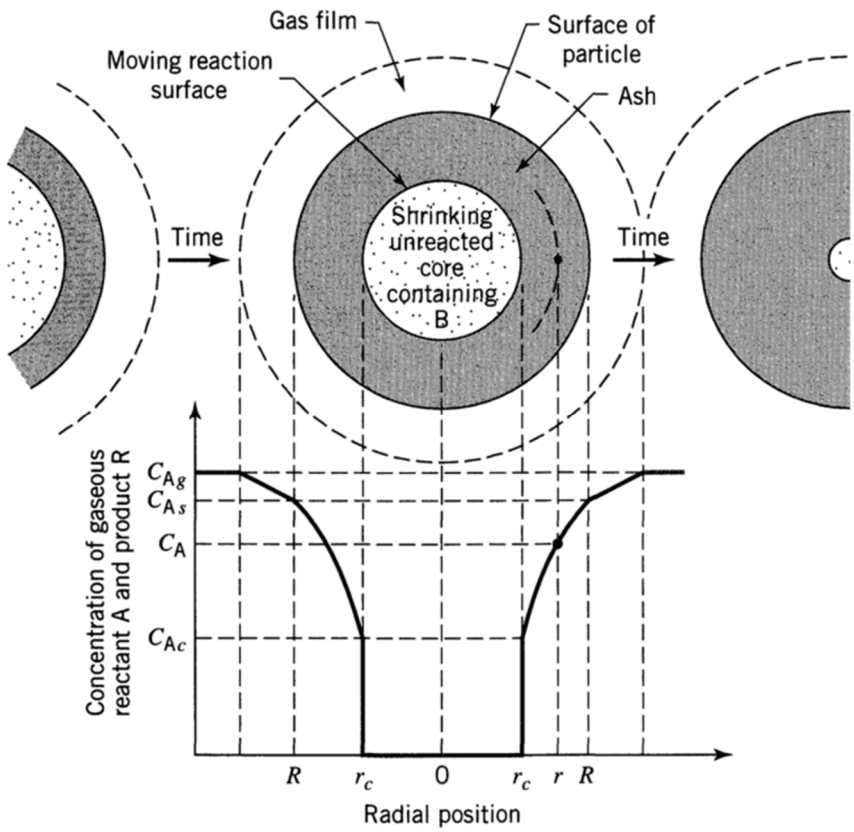

Figure 1.4 The physical representation and the concentration profiles of the reactants and products in a SCM for a non-shrinking particle (Levenspiel, 1999).

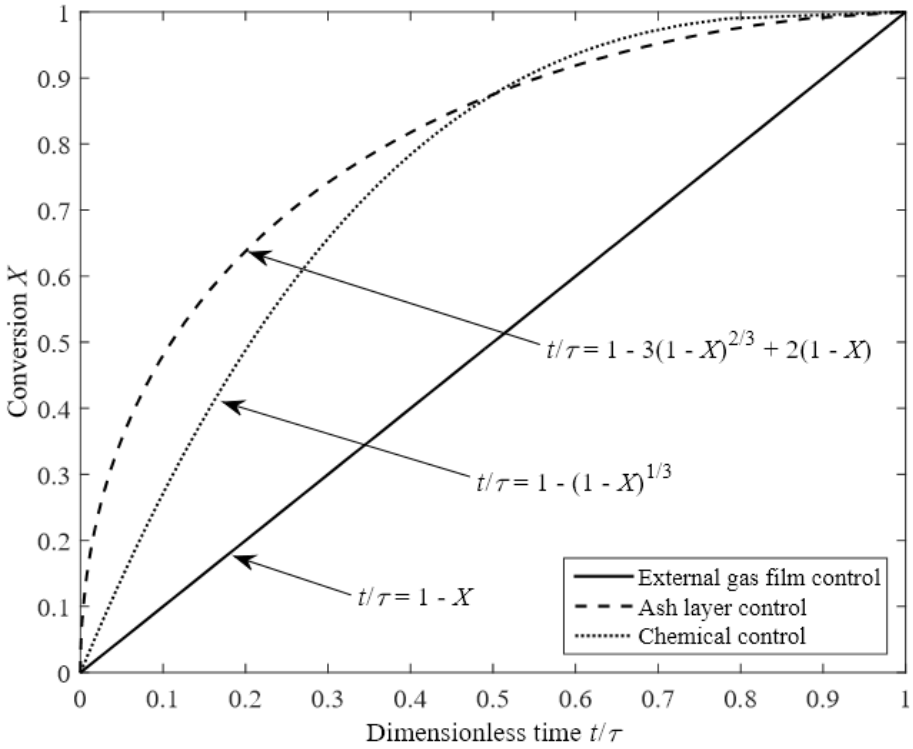

Figure 1.5 The shrinking core models for a non-shrinking particle with first order reaction. The parameter τ is the time for complete reaction.

Normally, the SCM is a reasonable representation of a reacting gas-solid system. However, there are two broad classes of exceptions where the assumptions of the SCM do not match reality precisely (Levenspiel, 1999): (1) slow reaction of a gas with a very porous solid, where reaction occurs throughout the solid, and (2) the solid is converted by the action of heat without needing contact with gas. In these cases, the CRM is a better description of the reaction process where the reaction, and, or, the transfer of heat, occur in a broad front across the entire particle. Reactions such as the gasification of chars, the calcination of cycled, as opposed to virgin, limestone and the sulphation of calcined limestones possess the characteristics of the CRM, where the gaseous reactants can penetrate into the initially-porous particles and react with the solid throughout the entire particle. Generally, the rate of reaction can be limited by: (i) chemical kinetics, (ii) diffusion through the porous particle, (iii) transport of heat across the particle, or (iv) diffusion through the external gas film. Figure 1.6 shows the difference in the local conversion profiles of the SCM and the CRM at fixed average conversions of the solid. Depending on the intraparticle heat and mass transfer resistance relative to the reaction rate, the conversion profile of the CRM could either be steep when resistance is high or flat when resistance is low.

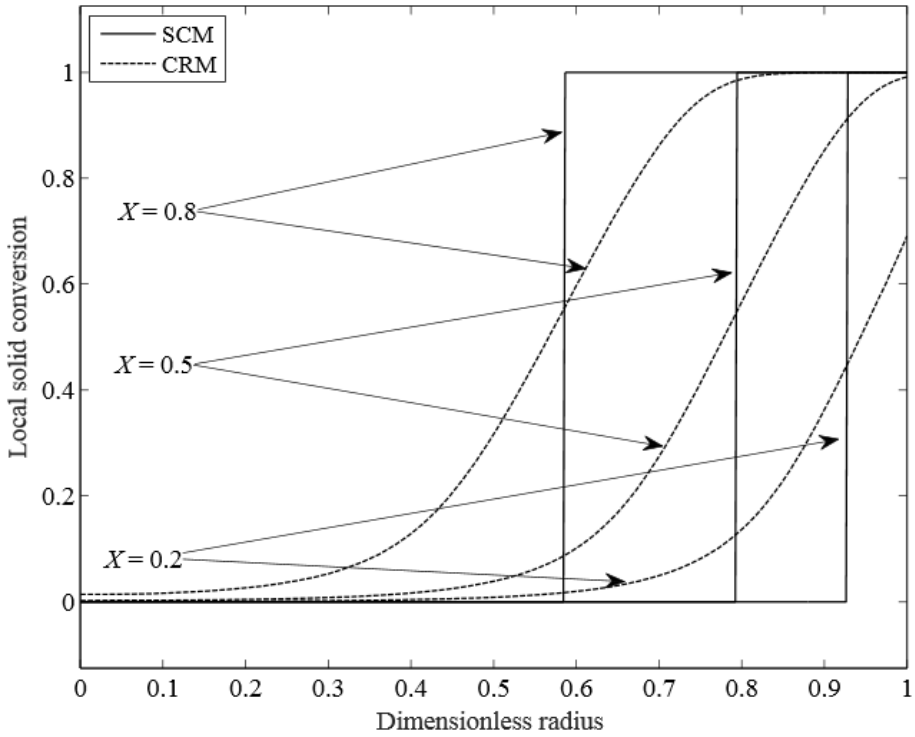

Figure 1.6. Local conversion profiles of shrinking core model (SCM) and continuous reaction model (CRM) for fixed average conversion of particle.

There is a third class of reaction models sitting between the SCM and the CRM – the Grain Model (GM). The GM assumes the solid particle to consist of many smaller non-porous grains and the porosity of the particle is made up from the space between the grains. In GM, the reaction takes place across the entire particle like the CRM, but on the grain-scale the reaction occurs on a sharp reaction according to the SCM. Just like the SCM, the product layer will form during reaction in the outer regions of each grain which will in turn result in some resistance to diffusion. Szekely & Evans (1970) first developed the classic grain model for gas-solid reactions, where the uniformly sized the spherical grains sit at an equal distance apart from each other within the solid particle. During the reaction, the gaseous reactant diffused into the particle through the interstices and reacted with the solid grains which was assumed to have unchanging size. Since GM represents a significant advance compared to SCM and its description of the structure corresponds effectively to that of numerous porous solids, the grain model has been extensively employed and has proved quite successful (Patisson *et al.*, 1998). However, the simplifying assumptions that GM makes (*e.g.* uniform grain size, no variation in grains or porosity during reaction) cannot be overlooked and led various extensions to the original model. The variation of the grains and porosity was first introduced by the development of the Changing Grain Size Model (CGSM) to incorporate the decreasing porosity during reaction between sulphur dioxide and limestone, where the product solid $CaSO_4$ took up more volume than the reacting solid CaO (Hartman & Coughlin, 1976). Later, Dam-Johansen *et al.* (1991) developed a Micro-Grain Model for the sulphation of limestone, where the particle was made up from porous grains composed of non-porous micro-grains. The Grain Size Distribution Model (GSDM) was developed by Heesink *et al.* (1993) to include a distribution of grain sizes.

Figure 1.7 summarised the different types of reaction models discussed above, which also includes the classification based on how the models describe the structural change to the particle during reaction. One of the key difference between the GM and the CRM is that GM assumed the particle structure composed of grains with interstices between them, while CRM commonly considers the particle consisting of continuous solid phase with porous space. While the GM describe the structural change of the particle during reaction via the changes to the solid grains, the CRM describes the structural change via the geometrical variation of the pores due to the reaction. When dealing with a large variation in porosity, with either formation and growth of pores, as

in the case of char gasification, or closure and obstruction of pores, as during the sulphation of lime, researchers have tended to prefer CRM such as RPM (Patisson *et al.*, 1998).

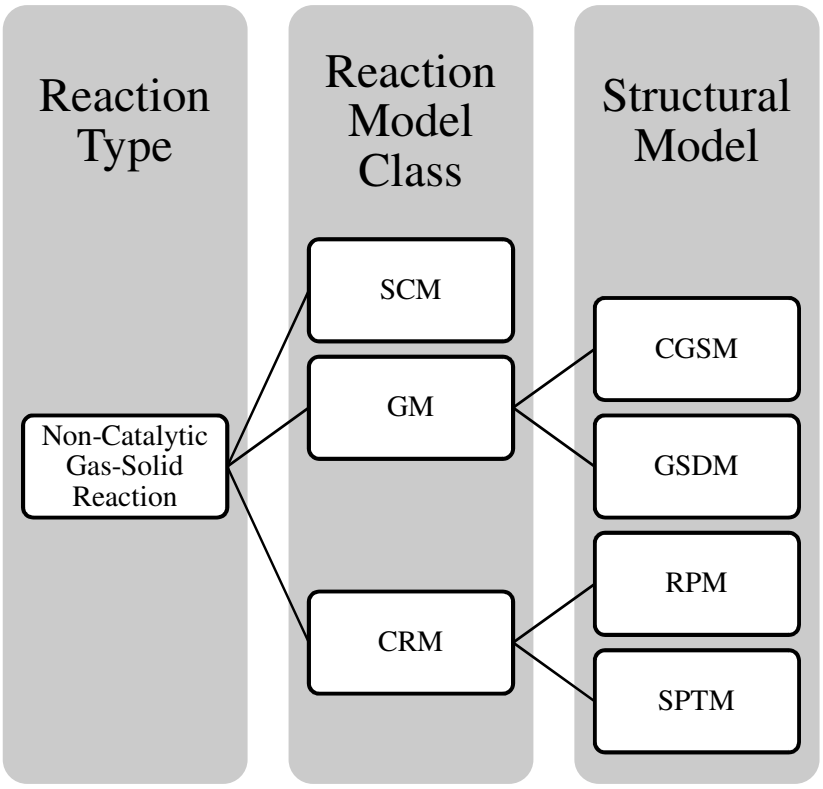

Figure 1.7 Classification of models for non-catalytic gas-solid reactions. Abbreviation: CGSM: Changing Size Grain Model; GSDM: Grain Size Distribution Model; RPM: Random Pore Model; SPTM: Statistical Pore Tree Model.

1.2.3 The evolution of pore structure

During a typical non-catalytic reaction between a gas and solid particles, the structure of the particle's interior changes with conversion of the solid as a result of the solid along the pore surfaces being converted into gaseous or solid products. In turn, this affects the rate of reaction by changing the available contact area within the particle and altering the diffusion rate of gases as pores sizes change. Many researchers have sought to model the development of the internal particle structure with conversion during gas-solid reactions, which can be grouped into the two classes of models shown in Figure 1.7 – GM (Grain) and CRM (Porous). In GM, the structural changes of the particle during reaction is considered by modelling the variation of the internal solid matrix. For example, Szekely & Evans (1970) made the first attempt to incorporate the structural parameters such as grain size, porosity and pore size into their grain model.

They assumed that the pore structure was unaffected by the progress of reaction, although later variants (Hartman & Coughlin, 1976) were able to account for change in grain size with reaction. The GM has considerable flexibility when it uses a grain size distribution which could potentially be related to the pore size distribution measurements. However, according to the model, the interfacial area between reactant solid and product solid decreases with conversion, so that the total reaction rate decreases monotonically with conversion. In certain reactions, *e.g.* the gasification of carbonaceous solids, often the surface area and reaction rate first increase, reaching a maximum, and then decrease as conversion approaches 100%. For this reason, Sotirchos (1987) developed the Overlapping Grain Model (OGM), where each grain was assumed to have a hard core and a soft permeable shell. The hard core did not overlap with the cores of neighbouring grains, and the soft permeable shell could overlap with the shells of other grains. By adjusting the ratio of core radius and grain radius, the development of surface area during conversion could be simulated. More recently, Liu *et al.* (2012) developed a version of the OGM using a fitted size distribution of grains and had accounted for the evolution of the particle structure during the carbonation reaction.

On the other hand, CRM models the structural change to the particle by considering the evolution of the internal pore structure as reaction proceeds, which enables the CRM to describe a variety of rate *vs.* conversion patterns. For example, by considering pore growth and coalescence, the CRM can provide conversion curves with a maximum. The main difficulty in treating the evolution of gas-solid and solid-solid interfaces is the overlap between interfaces belonging to neighbouring elements. It so happens that the overlap between pore elements of arbitrary shape can be described exactly when the location of the pore is completely random, *i.e.* obeying the Poisson distribution (Sahimi *et al.*, 1990). The exact relationship for the overlap volume was first derived by Avrami (1940) in his work of nucleation processes in solids. Bhatia & Perlmutter (1980) further extended the theory to develop the RPM, which modelled the total surface area at any conversion as a function of the initial morphological parameters. The RPM was subsequently applied to char gasification (Bhatia & Perlmutter, 1981b), the sulphation reaction (Bhatia & Perlmutter, 1981a) and the carbonation reaction (Bhatia & Perlmutter, 1983). Using different approaches based on cylindrical pore assumptions, Gavalas (1980) independently arrived at the same RPM and applied it to char combustion, which also provided the expressions for the

frequency of intersections between capillaries and addressed issues concerning the validity of the use of effective diffusion coefficient. One of the key parameter used in the RPM is the arbitrary dimensionless structural parameter indicating the initial pore structure, which is calculated from pore length and porosity per unit volume of the particle solid. The RPM can only simulate the reaction rate peak commonly observed for char gasification, provided the structural parameter is above certain value.

In a somewhat different approach, Simons & Finson (1979) developed a mass transport model using statistical methods to specify the pore structure as a continuously branching tree – Statistical Pore Tree Model (SPTM). According to this model, the pore space consisted of finite cylindrical elements connected in tree-like structures beginning on the particle surface and progressing towards the interior with branches of ever decreasing diameter. The main rational behind the tree-like structure was to describe the limited connectivity within the porous medium. However, the quantification of the effects of connectivity was obscured by a number of simplifications and empirical relationships relating to the evolution of the pore geometry (Sahimi *et al.*, 1990). For example, in their model the small pore trees were found to be kinetically limited while the larger pore trees were diffusion limited. This is the opposite of what one would normally expect, since diffusion should be less limited in large pores. The existing mathematical pore models such as the random pore model, statistical pore tree model and grain model contain parameters that are difficult to measure and thus become fitting parameters, which are complicated and equally arbitrary, *e.g.* the diffusivity of SO_2 through a layer of $CaSO_4$. In many cases, the use of complicated mathematical pore models leads to the need to modify the original models in order to fit experimental measurements.

It would be ideal if the evolution of the pore structure could be determined experimentally for the specific reaction, so that it could be applied locally within a particle to describe how the reaction rate varies with the pore evolution. Together with a rigorous description of the intraparticle heat and mass transfer across the entire particle, the theoretical model might able to help find the causes for some of the unexplained experimental observations.

A feature of most models of non-catalytic reactions between gases and solids generally is that the intrinsic rate of reaction, r, at a local point within a solid particle is of the form $r = g(C_i, T, P) \times f(X)$. Here, g describes the intrinsic reaction kinetics as a

function of the temperature, T, the total pressure, P, and the concentration, C_i, of the reaction gases. The term $f(X)$ is a direct function of the conversion of the particle and is correlated with the internal morphology of the particle, *e.g.* surface area, pore size, pore size distribution *etc*. at a particular conversion. In addition, $f(X)$ is not a function of C_i, T, or P. An experimentally-determined $f(X)$ function from common measurements, such as reaction rate and conversion, offers a straightforward method to describe the change of internal morphology at a local point within the particle being reacted under conditions affected by intraparticle mass transfer. This is exemplified by recent studies of char gasification in a fluidised bed (Saucedo *et al.*, 2014), where it was found that a simple, arbitrary function, $f(X)$, could be determined from the plot of measurements of rate *vs.* conversion of the solid char in the kinetically-controlled regime. It was proposed that the ratio between the rate of reaction at any conversion and the initial rate of reaction reflects, generally, the variation of the rate of reaction due to pore structure changes as the reaction proceeds in the absence of intraparticle mass transfer limitation (*e.g.* at low temperature or using small particles or with particles of low reactivity) (Saucedo, 2014; Saucedo *et al.*, 2014), thus giving $f(X) = r(X)/r(X = 0)$.

However, complex reactions are hard to simulate realistically and might not be useful when modelling the detailed reaction and diffusion process. For example, reactions involving multiple solid phases and many by-products could be challenging to predict the pore evolution and particle changes. Whereas, gas-solid reactions with relatively simple reaction kinetics are useful for getting a clear understanding of the reaction and diffusion processes. Therefore, in this Dissertation, some of the simple but industrially significant reactions including gasification of solid carbon by CO_2, calcination of $CaCO_3$ and sulphation of CaO, are considered for developing and verifying the theory of using an experimentally determined $f(X)$ function for the pore evolution.

1.3 Objectives and structure of this dissertation

The work in this Dissertation is a contribution towards the theoretical understanding of the reaction and diffusion phenomena during some of the industry's most important non-catalytic gas-solid reactions: gasification, calcination and sulphation. The overall objective of the research presented in this Dissertation was to develop and verify a general reaction and diffusion model for the non-catalytic gas-solid reactions using gasification, calcination and sulphation reactions as examples, where the

chemical kinetics, intraparticle heat and mass transfer processes and the evolution of pore structures are all considered in sufficient details. By developing such a model, new understandings of the reactions between gas and solid particles could be discovered. The specific objectives are:

1. To construct the mathematical frameworks of the general model for non-catalytic gas-solid reactions.
2. To develop and verify the theory that involves using an experimentally determined $f(X)$ function to describe the evolution of pore structure during reaction between gas and solid particle, using gasification of char as the model reaction.
3. To apply the model and the pore evolution theory to other non-catalytic gas-solid reactions involving different classes of pore evolution during reaction, using calcination of limestones and sulphation of calcined limestones as the model reactions.

The structure of this Dissertation is as follows. Chapter 1 presents a review of the background including the overall motivation of this Dissertation, an overview of modelling gas-solid reactions and the key objectives to achieve. Chapter 2 describes the principal experimental methodologies employed in this work, the arrangement and the specification of the experimental apparatus, and a description of the materials used. Chapter 3 illustrates the step-by-step derivation of the general reaction and diffusion model for gas-solid reactions and the numerical methods employed for solving the system. Chapter 4 develops and verifies the theory of using an experimentally determined $f(X)$ function for describing the evolution of pore structure during the gasification of chars by CO_2. Chapter 5 investigates the application of the general model and the pore evolution theory to the calcination of limestone particles subjected to a number of calcination and carbonation cycles. Chapter 6 further explores the application of the general reaction and diffusion model and the pore evolution theory to the sulphation of calcined limestone particles subjected to a number of calcination and carbonation cycles. Finally, conclusions from the current work are presented in Chapters 7.

Parts of the work presented in this Dissertation have been published, as listed below:

- Dai, P., Dennis, J. S., & Scott, S. A. (2016a). Using an experimentally-determined model of the evolution of pore structure for the gasification of chars by CO_2. *Fuel*, **171**, 29–43.
- Dai, P., González, B., & Dennis, J. S. (2016b). Using an experimentally-determined model of the evolution of pore structure for the calcination of cycled limestones. *Chemical Engineering Journal*, **304**, 175–185.

Chapter 2 Experimental methods

The general experimental techniques used in this thesis are described in this Chapter. The details of certain experiments and materials, which are specific to a study, are given in relevant chapters. Section 2.1 covers methods used for characterising the solid particles involved in the gas-solid reactions. Section 2.2 describes the apparatus for determining the rate of reaction and conversion. Finally, section 2.3 lists all the materials used in the experiments and their methods of preparation.

2.1 Characterisation of particles

2.1.1 Nitrogen adsorption analysis

The surface areas and pore size distributions of the solid particles were measured using a TriStar 3000 (Micrometrics, Serial No. 1001) gas adsorption analyser. During a typical measurement, the solid particles were first degassed *in vacuo* at room temperature to remove gas adsorbed on the internal surface. After degassing, N_2 was introduced steadily into the sampling chamber isothermally at 77 K so that the absolute pressure of the chamber increased incrementally from ~0.01 bar to 1 bar. On completion, N_2 was desorbed from the surfaces of the particle at a low pressure of ~0.14 bar. The amount of N_2 adsorbed and desorbed during the pressure swing was recorded and used to calculate the surface area of the sample using the Brunauer–Emmett–Teller (BET) theory (Brunauer *et al.*, 1938). The pore size distribution and pore volume (for pore diameter within 1.7 – 200 nm) were calculated using the Barrett-Joyner-Halenda (BJH) model (Barrett *et al.*, 1951).

2.1.2 Mercury intrusion porosimetry

A mercury porosimeter (Micromeritics' AutoPore IV 9500) was used to measure the porosity, bulk and skeletal densities, and pore size distribution (for pores within 5.5 – 6000 nm dia.) of the solid particles. This technique is based on the behaviour of mercury within a capillary. Mercury is a non-wetting liquid (*i.e.* contact angle > 90°) and has a surface tension in air of 0.48 N m^{-1} at 298 K. These properties mean that a force is required to make mercury penetrate a capillary (or pores). The porosimeter

measures the volume of mercury taken up by the solid at an increasing pressure. Based on a force balance and assuming cylindrical pores, the relationship between the pressure exerted and the diameter of a pore, d_{pore}, is generally assumed to be given by the Washburn's (1921) equation:

$$P = \frac{-4\xi_s \cos\vartheta}{d_{pore}} \tag{2-1}$$

Here, P is the pressure applied to the mercury reservoir, ξ_s is the surface tension of mercury and ϑ is the contact angle between the mercury and the solid. Using Eq. (2-1), the pore size distribution can be determined from the volume injected at each increment of pressure and the overall porosity from the total volume of mercury finally injected.

2.1.3 Optical Microscopy

The solid particles were examined using a Malvern Morphologi G3 microscope equipped with lenses of magnifications $2.5 \times (13 - 1000\ \mu m)$, $5 \times (6.5 - 420\ \mu m)$, $10 \times (3.5 - 210\ \mu m)$, $20 \times (1.75 - 100\ \mu m)$ and $50 \times (0.5 - 40\ \mu m)$. The sample of particles was dispersed on to a glass plate at 1 – 2 bar pressure following a pre-defined Standard Operating Procedure (SOP). The microscope had a 5M pixel colour CCD array detector and a Nikon CFI 60 optical system, where the images of individual particles were captured by scanning the sample with the microscope whilst keeping the particles in focus. Illuminating the sample from above and/or below while accurately controlling the light levels enabled optical images of the particle surface to be captured. A range of morphological properties including circular equivalent diameter, perimeter, circularity and aspect ratio were automatically measured from the image of each particle, which then produced distributions of the properties of the sample particles.

2.1.4 Scanning Electron Microscope (SEM)

The surfaces and morphologies of the solid particles were examined using a scanning electron microscope (SEM, JEOL 5800LV). To prepare particles, samples were placed on a piece of double-sided tape attached to a standard aluminium stub for SEM, which was then sputter-coated with a thin layer of gold (thickness < 100 nm) to prevent accumulation of electrical charges on the sample surface. The gold-coated sample was then put into the chamber of a SEM, where the scanning was performed under low vacuum and at room temperature with an accelerating voltage between 3 and

20 kV. A primary beam of electrons was used to scan the sample, and the secondary electrons generated by the interaction of this beam with the sample were detected and amplified to produce images of the surface morphology of the sample at different magnifications.

2.1.5 X-Ray Powder Diffraction (XRD)

X-ray diffraction studies of the solid samples were used to investigate the composition of the crystalline phases present. Firstly, the samples were crushed and grounded to fine powder, below a sieve size of 67 μm, using a pestle and mortar. The powder was then packed in to a sample holder made of highly crystalline Si and Pt. The sample holder, the beam gun and the detector were arranged in a Bragg-Brentano para-focusing geometry so that the sample holder was always stationary and oriented horizontally, whilst the detector and the generator rotated around the sample. A beam of Cu K-α radiation (wave length = 1.5418 Å) was generated by a Philips PW1820 HT generator operating at 40 kV and 40 mA, which passed through an anti-scatter slit of 1° and a divergence slit of 0.2 mm. The detector was fitted with a receiving slit of 1° angle, and the angle of reflection 2θ was varied between 10° and 90°, at a rate of 0.025° per second. The collection of the diffraction patterns was performed at room temperature and pressure. The collected diffractograms were processed using the open-source software – Maud, and phase identification was performed using the Inorganic Crystal Structure Database (ICSD) and Crystallography Open Database (COD).

2.2 Fluidised bed reactor

Batch experiments involving the gasification of chars, calcination of limestones or sulphation of limestones were performed in the fluidised bed reactor arranged as shown in Figure 2.1. The fluidised bed was a quartz reactor, internal diameter 30 mm and length 460 mm, provided with a porous frit (4 mm thick, pore size +100, -160 μm) as the distributor, situated 110 mm from the base of the reactor. By using pressure taps at the inlet and the outlet, the pressure drop across the distributor and a 20 ml bed of 355 – 425 μm dia. silica sand was measured to be 13 – 15 mbar between 800 and 1000°C, which was about 1.8 – 2.0 times of the weight of the sand per unit bed area. The reactor was externally heated by an electric furnace (LTF 12/38/250, Lenton Ltd.). The temperature of the bed was measured by a K-type thermocouple (1.5 mm dia.) inserted into the top, with its tip 20 mm above the distributor. The flowrates of the fluidising gas

were controlled by rotameters calibrated at 293 K and 1 bar for gasification experiments and by mass flow controllers (Brooks 5850) calibrated at 293 K and 1 bar for calcination and sulphation experiments. The off-gas leaving the fluidised bed was sampled at 16.7 mL s^{-1} (STP) through a quartz tube. To prevent elutriated particles, tars and water vapour in the sampled gas entering the analysers, the gas was passed through a glass wool filter and a drying tube filled with $CaCl_2$ in series.

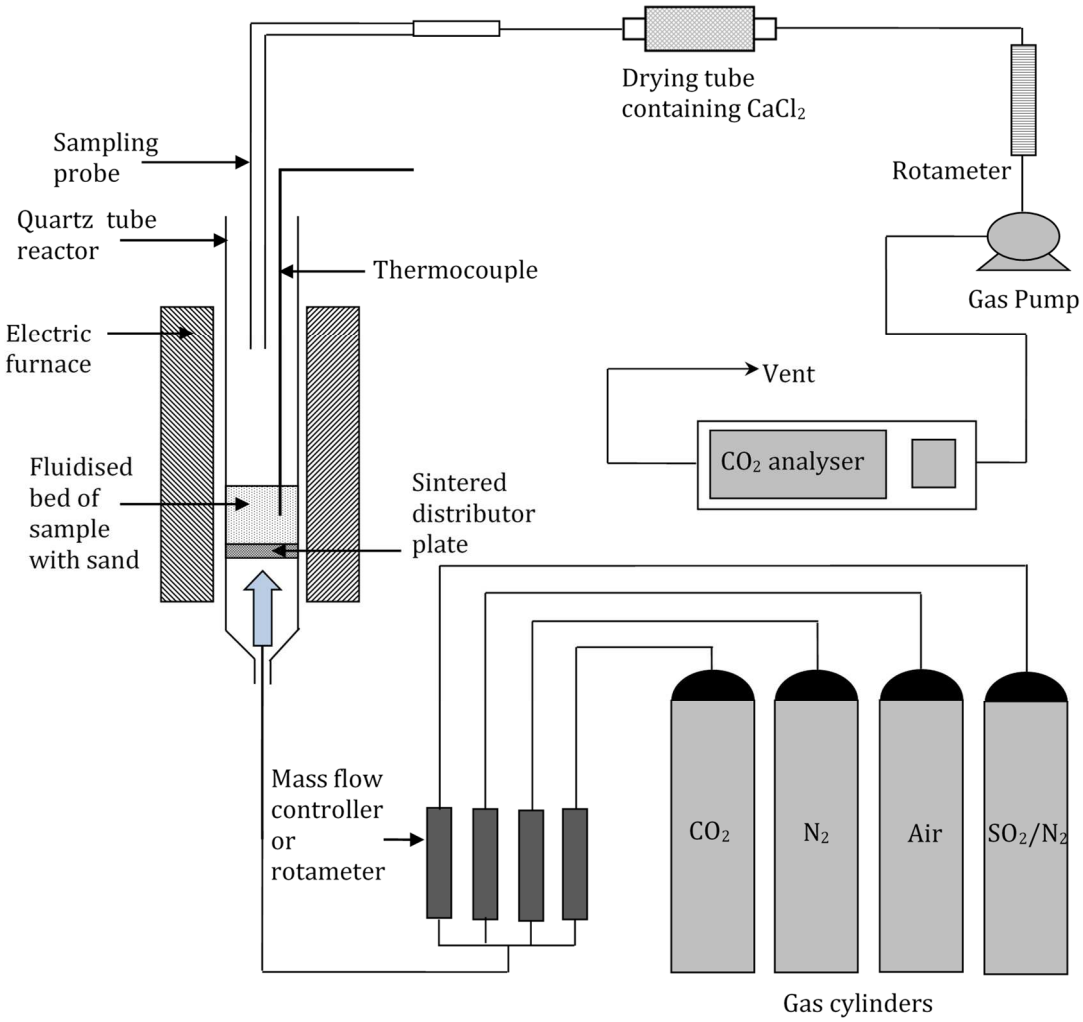

Figure 2.1. Schematic diagram of the experimental arrangement for experiments in a batch fluidised bed using a 30 mm i.d. quartz reactor.

The volume fractions of the gaseous species were measured by a non-dispersive infra-red gas analyser (ABB EL3020 – Uras26) coupled with a paramagnetic analyser (Magnos206) to measure O_2. The maximum measuring ranges of the gas analyser were 0 – 100 vol% CO_2, 0 – 30 vol% CO, 0 – 100 mol% O_2, 0 – 10,000 ppmv SO_2. The analyser contained internal calibration cells for each gas, with the mole fractions of gases being 88 mol%, 84 mol% and 7660 ppmv for CO, CO_2 and SO_2, respectively. The

oxygen analyser was calibrated using air, assuming a concentration of 20.9 mol%. For gasification experiments, the voltage output (0 – 10 V) from the analyser was transmitted to an analogue data acquisition card (USB- 1208LS, Measurement Computing) and recorded continuously at a frequency of 1 Hz. For calcination and sulphation experiments, the measurements of gas concentration was acquired directly by an Excel Macro through a RS-232 COM-port at a frequency of 1 Hz.

2.3 Materials

2.3.1 Gases

The gases used in the experiments were (i) N_2 (purity grade $\geqslant$ 99.9 vol%, oxygen $\leqslant$ 2 ppmv), (ii) CO_2 (purity grade $\geqslant$ 99.8 vol%), (iii) 3000 ppmv SO_2 in N_2, and (v) air (21 vol% O_2 in N_2). All gas cylinders were supplied by BOC or Air Liquide.

2.3.2 Sand

Natural, uncrushed silica sand (fraction C, David Ball Group plc., moisture content < 0.1% by dry mass, BS 1831-131:1998), sieved to a size fraction of 355 – 425 μm, was used as a fluidising bed material in the experiments unless otherwise specified. The effective particle density of the non-porous sand particles was ~2650 kg m^{-3}.

2.3.3 Chars

Two existing batches of solid fuels used by previous researchers in the group were used for the gasification study: i) char particles made from a low-rank Hambach lignite coal (Saucedo *et al.*, 2014) supplied by RWE Power AG, Germany, and ii) activated carbon particles (Sorbonorit B4, Norit) (Scott *et al.*, 2005). The lignite char was prepared by the pyrolysis of the parent coal in a bed of sand fluidised by pure N_2 at 1073 K; the detailed experimental method of preparing the chars is given by Dennis & Scott (2010) and Brown *et al.* (2010). The resulting char particles were sieved from the sand and recovered in four size fractions for the experiments: 0.36 - 0.50 mm, 0.60 - 1.00 mm, 1.00 - 1.40 mm and 1.70 - 2.56 mm. The activated carbon did not require pyrolysis: it was crushed and sieved into different size fractions, 0.36 - 0.43 mm, 0.71 - 1.25 mm and 1.70 - 2.36 mm.

2.3.4 Limestones

Two types of limestone particles were used in calcination and sulphation experiments: (i) a Spanish limestone (Compostilla), and (ii) a British limestone (Purbeck). The size fractions used in the calcination experiments were 710 – 850 µm and 1400 – 1700 µm, and those used in the sulphation experiments were 355 – 500 µm and 710 – 850 µm.

Some limestone particles were cycled between carbonated and calcined states a number of times before they were used for calcination and sulphation studies. The cycling of the limestone particles was conducted in a bed of sand fluidised by 15 vol% CO_2 balance N_2 at 1 bar, which used the same fluidised bed reactor as shown in Figure 2.1. During cycling, the limestone particles were calcined at 1173 K for 10 minutes and then carbonated at 923 K for 10 minutes. Here, the temperature at which a partial pressure of CO_2 of 0.15 bar is in thermodynamic equilibrium with a mixture of CaO and $CaCO_3$ was calculated to be 1053 K (Barin & Platzki, 1995). The resulting particles were cooled in a desiccator and then were sieved from the sand.

Chapter 3 Theoretical models

In this chapter, the detailed features of the reaction and diffusion model of a single particle are discussed. Aspects of the model, and its validation, have already been published in (Dai *et al.*, 2016a; Dai *et al.*, 2016b).

3.1 Introduction

The system considered is a spherical solid particle, initial porosity ε_0, reacting with a stream of gas whilst it is immersed in a fluidised bed of inert silica sand particles. A typical non-catalytic gas-solid reaction can be represented:

$$\nu_{S1}S1_{(s)} + \nu_{G1}G1_{(g)} \rightleftarrows \nu_{S2}S2_{(s)} + \nu_{G2}G2_{(g)} \qquad (3\text{-I})$$

where S1and G1 are the reacting solid and gaseous species, S2 and G2 are the product solid and gaseous species and ν is the stoichiometric coefficient of each species. The actual chemical reaction could involve one or more gaseous species, but, in the present model, it is assumed that there are no more than two solid species, namely reactant and product. There are many examples of chemical reactions that follow this arrangement, *e.g.* gasification of solid carbon by CO_2, calcination of $CaCO_3$ and sulphation of CaO.

The principal assumptions made were:

i) The solid particle of S1 contains uniform and cylindrical pores, initial radius $r_{pore,0}$.

ii) The material and energy balances inside and outside the particle are in pseudo-steady state, so that the gas concentrations, total fluxes, total pressure and temperature have no time dependence. As justified by Bischoff (1963), the profiles generated using this assumption will be achieved very quickly in a gas-solid system. For example, the thermal diffusivity of a typical solid is about 9×10^{-6} m^2/s at 800°C, so that for a 2 mm dia. particle, the time constant estimated from (particle radius)^2 / (2 × thermal diffusivity) is very small, ~ 0.06 s. The diffusion coefficient of CO in N_2 is 2×10^{-6} m^2/s at 800°C, so the time constant is 0.25 s. Wen (1968) also concluded that the pseudo-steady state solution was a

good approximation for most of the solid-gas reaction systems except for systems with extremely high pressure and very low solid reactant concentration. On the other hand, the mass and energy balances are affected indirectly by the solid conversion X which does have time dependence and affects the physical properties of the particle (*e.g.* porosity, pore diameter and particle size), but the time constant is usually much larger thus justifying the use of the pseudo-steady assumption.

iii) The fluidised bed is considered to have a constant local tortuosity and porosity around the solid particle, and there is no variation of total pressure outside the particle, since the net flux of gas leaving the particle and entering the bed is assumed to be low compared with the interstitial flow of fluidising gas.

iv) It is assumed that the radiative contribution to heat transfer were small.

3.2 Model equations

3.2.1 Intraparticle mass transfer

A model of multi-component diffusion based on the Stefan-Maxwell equations within a porous medium is needed to describe the intraparticle diffusion rigorously. The two principal flux models for non-equimolar, multi-component mass transfer are the Dusty Gas Model (DGM) (Evans *et al.*, 1961), and the Mean Pore Transport Model (MPTM) (Rothfeld, 1963; Schneider, 1978; Arnošt & Schneider, 1995). The DGM assumes that the flow of a gas mixture through a porous solid is similar to the flow through a random array of solid spheres fixed in space and obstructing the motion of the moving particles of gas, while the MPTM is based on the description of flows in a single straight capillary and relating these descriptions to flow in the porous medium as a whole, treated as a network of capillaries. Even though the assumptions for the MPTM approach stem from sounder physics, for a long time, the DGM approach has been the one most used in the literature. The relatively slow development of MPTM models is partly owing to confusion over the description of multi-component flow in the continuum regime, which, in turn, has led to difficulty in establishing reliable models for the intermediate regime (Dennis, 2017).

Given that both models are algebraically complicated, Young & Todd (2005) developed a new MPTM called the Cylindrical Pore Interpolation Model (CPIM), where the equations of flux for diffusion in the Knudsen regime and the Continuum

regime are in the same form except for the diffusivities. Therefore, by using an interpolated diffusivity between the Knudsen and the Continuum regimes for the transitional flow, the CPIM can be applied across all flow regimes. The largest difference between the CPIM and the DGM is the treatment of the diffusivity in intermediate regime. In the DGM, only the Knudsen diffusivity is present in the pressure gradient equation of the DGM, whereas the CPIM attempts to account for both the continuum and the Knudsen effects. Since binary diffusivity is inversely proportional to the total pressure, it is unsurprising that at a high pressure, both the DGM and the CPIM are dominated by Knudsen diffusivity, hence become similar. However, at low pressures, the values of binary diffusivity become comparable to Knudsen diffusivity, so that the disparity between the two models becomes much larger. It should be noted that the interpolation of the diffusivity prescribed in the CPIM is arbitrary and there is no priori theoretical reason for suggesting it provides a good representation in a transitional flow. The extension of the CPIM to flow in porous medium is achieved by introducing a factor combining the porosity and the tortuosity factor, as shown in the next paragraph. Unlike the usual treatments, this parameter is not absorbed into the gas diffusivities and flow permeability, since it can be eliminated from all but one of the equations and, with appropriate boundary conditions, the flux ratios can be obtained in terms of a mean pore radius only. The porosity–tortuosity parameter simply controls the absolute flux level and cab be best interpreted as a length scale-factor (Young & Todd, 2005).

Comparing all three models, the CPIM has a more rigorous treatment of continuum flow, a clearer interpolation procedure for transitional flow and a more compact form of the working equations which helps to clarify the roles of the governing parameters. Recent studies suggest that the CPIM is well suited to modelling multi-component diffusion in both catalyst pellets (Lim & Dennis, 2012) and in gasifying char particles (Saucedo *et al.*, 2014). For this reason, the CPIM was used to model intraparticle diffusion in the present work. The governing equations for *N* gas species are:

$$\frac{dy_n}{dr} = \frac{\tau^2 RT}{\varepsilon P} \sum_{m=1}^{N} \left(\frac{y_n J_m}{D_{A,mn}} - \frac{y_m J_n}{D_{A,nm}} \right) \qquad n = 1, 2 \ldots N \tag{3-2}$$

$$\frac{dP}{dr} = -\frac{\tau^2 A_A}{\varepsilon}\sum_{n=1}^{N}\left(\sqrt{M_n}\cdot J_n\right) \tag{3-3}$$

The boundary conditions for the above equations are given at the centre ($r = 0$) and the surface ($r = r_p$) of the particle:

$$r = 0: \quad J_n = 0 \tag{3-4}$$

$$r = r_p: \quad y_n = y_n^S, \qquad P = P^S \tag{3-5}$$

Here, y_n is the mole fraction of species n, J_n is the total molar flux of species n, τ^2 represents the tortuosity factor of the particle from mercury intrusion porosimetry measurements, ε is the porosity at the local point, which varies with conversion and is discussed later, and M_n is the molar mass of gas species n. The superscript S refers to particle surface.

The parameters $D_{A,nm}$ and A_A are found by interpolating between the extremes of continuum and Knudsen flow using the equations proposed by Young & Todd (2005):

$$\frac{1}{D_{A,nm}} = \frac{1}{D_{K,n}} + \frac{1}{D_{B,nm}} \qquad \frac{1}{A_A} = \frac{1}{A_K} + \frac{1}{A_C} \tag{3-6}$$

where $D_{K,n}$ is the Knudsen diffusivity and the parameters A_K and A_C are the coefficients in the pressure gradient equation in the continuum and Knudsen regime, given by (Cunningham & Geankoplis, 1968; Young & Todd, 2005)

$$D_{K,n} = \frac{2r_{pore}}{3}\sqrt{\frac{8RT}{\pi M_n}} \qquad A_K = \frac{3}{4r_{pore}}\sqrt{\frac{\pi RT}{2}}$$
$$A_C = 8\mu_{mix}RT \Big/ \left(Pr_{pore}^2 \sum_{n=1}^{N}\left(y_n\sqrt{M_n}\right)\right) \tag{3-7}$$

The viscosity of the gas mixture, μ_{mix}, is given by (Bird *et al.*, 2007)

$$\mu_{mix} = \sum_{n}^{N}\left(y_n\mu_n \Big/ \sum_{m}\left(y_m\Phi_{nm}\right)\right) \tag{3-8}$$

Here Φ_{nm} is a dimensionless parameter and μ_n represents the viscosity of the pure species *n*, and are calculated from Chapman-Enskog theory using the Lennard-Jones (6-12) potential (Bird *et al.*, 2007):

$$\Phi_{nm} = \frac{1}{\sqrt{8}}\left(1 + \frac{M_n}{M_m}\right)^{-0.5}\left[1 + (\frac{\mu_n}{\mu_m})^{0.5}\left(\frac{M_m}{M_n}\right)^{0.25}\right]^2 \tag{3-9}$$

$$\mu_n = 2.6693 \times 10^{-6}\sqrt{M_n T}/\left(\sigma_n{}^2 \Omega_\mu\right) \tag{3-10}$$

$$\Omega_\mu = \frac{1.16145}{(\kappa T/\epsilon_{nm})^{0.14874}} + \frac{0.52487}{\exp(0.77320\kappa T/\epsilon_{nm})} + \frac{2.16178}{\exp(2.43787\kappa T/\epsilon_{nm})} \tag{3-11}$$

$$\epsilon_{nm} = \sqrt{\epsilon_n \cdot \epsilon_m} \tag{3-12}$$

where Ω_μ is the collision integral for viscosity and has been curve-fitted for the experimentally-determined results of Monchick & Mason (1961) by Neufeld *et al.* (1972). The parameter ϵ_n is the maximum energy of attraction between two molecules of *n*, σ_n is a characteristic diameter of the molecule of *n*, often called the collision diameter, and κ is the Boltzmann constant. The values of the parameters σ_n and ϵ_n/κ for all the gas species used here are listed in Table 3.1. Going back to Eq. (3-6), $D_{B,nm}$ is the molecular diffusivity also calculated from the Chapman-Enskog theory using the Lennard-Jones (6-12) potential (Bird *et al.*, 2007):

$$D_{B,nm} = 0.0018583 \times 10^{-4}\sqrt{T^3\left(\frac{1}{M_n} + \frac{1}{M_m}\right)}\frac{1}{P\sigma_{nm}^2\Omega_D} \tag{3-13}$$

$$\Omega_D = \frac{1.06036}{(\kappa T/\epsilon_{nm})^{0.15610}} + \frac{0.19300}{\exp(0.47635\kappa T/\epsilon_{nm})} + \frac{1.03587}{\exp(1.52996\kappa T/\epsilon_{nm})} + \frac{1.76474}{\exp(3.89411\kappa T/\epsilon_{nm})} \tag{3-14}$$

$$\sigma_{nm} = \frac{1}{2}(\sigma_n + \sigma_m) \tag{3-15}$$

Here σ_{nm} is a parameter appearing in the Lennard-Jones (6-12) potential between one molecule of *n* and one of *m*. Similar to Ω_μ in Eq. (3-11), the collision integral for diffusivity, Ω_D, has also been curve-fitted for the experimentally determined results of Monchick & Mason (1961) by Neufeld *et al.* (1972).

Table 3.1. Lennard-Jones (6-12) potential parameters from the Appendix E in Bird *et al.* (2007).

	N_2	O_2	CO_2	CO	SO_2
σ_n (Å)	3.667	3.433	3.996	3.590	4.026
ϵ_n/κ (K)	99.8	113.0	190.0	110.0	363.0

The error in the predicted binary diffusivities by this method is ~ 7.3% (Green & Perry, 2007).

The porosity, ε, changes with the local conversion of the solid S1, X, during reaction and can be derived from the volume balance equation for a thin cylindrical shell inside the particle:

$$\varepsilon(X) = \varepsilon_0 + X(1-\varepsilon_0)\left(1 - \frac{\nu_{S1} V_{M,S2}}{\nu_{S2} V_{M,S1}}\right) \tag{3-16}$$

where $V_{M,S2}$ and $V_{M,S1}$ are the molar volume of the non-porous solid S2 and S1. As noted earlier, it was assumed that the particle has uniform cylindrical pores of initial diameter $d_{pore,0}$; the corresponding initial porosity of the particle is ε_0. Ignoring the small volume of crossing between pore channels, the local porosity can be estimated from

$$\varepsilon(r) \cdot \delta V = \pi d_{pore}^2 \sum_{i=1} L_i/4 \tag{3-17}$$

where δV is the volume of a differential element between r and $r + dr$ and $\sum_{i=1} L_i$ is the sum of the length of the cylindrical pores within the element. Assuming that the evolution of the internal pores (not on the particle surface) during reaction occurs only in a radial direction so that the pore diameter changes while the length of the pore remains constant, then:

$$\varepsilon(r)/\varepsilon_0 = \left(d_{pore}/d_{pore,0}\right)^2 \tag{3-18}$$

Substituting Eq. (3-16) into (3-18), the pore diameter at some time when the local conversion is *X* is:

$$d_{pore} = d_{pore,0}\sqrt{\left(\varepsilon_0 + X(1-\varepsilon_0)\left(1 - \frac{\nu_{S1}V_{M,S2}}{\nu_{S2}V_{M,S1}}\right)\right)\Big/\varepsilon_0} \tag{3-19}$$

3.2.2 External mass transfer

The particulate phase of the fluidised bed is considered to have a constant local tortuosity and porosity around the solid particle. It is also assumed that there is no variation of pressure with radial distance outside the particle, since the interstitial velocity of the fluidising gas is much larger than the mass average velocity of gas leaving the surface of a reacting particle. This suggests that there is no tendency to form voids or bubbles around the reacting particle in the case under consideration and that pressure variations outside the particle can be neglected. The general Stefan-Maxwell equations (Bird *et al.*, 2007) were used to model the external mass transfer within a diffusion boundary layer of thickness δ outside the particle:

$$\frac{dy_n}{dr} = \frac{\tau_{bed}^2 RT}{\varepsilon_{bed}P}\sum_{m=1}^{N}\left(\frac{y_n J_m - y_m J_n}{D_{B,nm}}\right) \qquad n = 1, 2 \ldots N$$
$$dP/dr = 0 \tag{3-20}$$

Here τ_{bed}^2 is the tortuosity factor of the sand bed. It was experimentally measured to be $1.34^2 = 1.80$ for a packed bed with 200 µm dia. quartz sand by Zoia & Latrille (2011). Also, ε_{bed} is the porosity of the bed, assumed to be 0.44, the same as the porosity at incipient fluidisation determined by Davidson & Harrison (1963) for a bubbling fluidised bed of silica sand. The parameter $D_{B,nm}$ refers to the binary molecular diffusivity of species *n* and species *m*. The boundary conditions at the particle surface ($r = r_p$) and the edge of boundary layer ($r = r_p + \delta$) are:

$$r = r_p: \quad J_n = J_n^S \tag{3-21}$$

$$r = r_p + \delta: \quad y_n = y_n^{\mathrm{B}} \quad \& \quad P = P^B \tag{3-22}$$

where the superscript B refers to the bulk conditions.

3.2.3 Equation of mass balance

A pseudo-steady mass balance over a spherical shell at radius r gives the flux equations for the gaseous species:

$$\frac{1}{r^2}\frac{d}{dr}(r^2 J_{\mathrm{n}}) = Q_n \qquad n = 1, 2 \ldots N \tag{3-23}$$

where J_n is the total flux (*i.e.* diffusive flux + advective flux) of species n. The parameter Q_n is the net rate of reaction of species n, in mol m^{-3} s^{-1}, which is positive for a net gain and negative for a net loss in species. Equation (3-23) holds under the pseudo-steady state assumption regardless of whether the reaction occurs inside or outside of the particle.

A material balance on the solid S1 across a differential element gives the variation of local conversion of S1 with respect to time:

$$\left.\frac{dX}{dt}\right|_r = -M_{\mathrm{S1}}\left(\frac{Q_{\mathrm{S1}}}{\rho_{e,0}}\right) \tag{3-24}$$

with initial condition:

$$t = 0: \quad X(r) = 0 \quad \text{for all } r \in [0, r_p] \tag{3-25}$$

where $\rho_{e,0}$ is the initial bulk density, the particle centre is $r = 0$ and its surface is $r = r_p$. The form of the expression of the rate of reaction depends on the specific reaction and will be discussed in the next three chapters.

3.2.4 Equation of energy balance

The standard form of equation of energy has been derived in Appendix A, where one of the complete forms is Eq. (A-19):

$$\rho C_p \frac{DT}{Dt} = -\nabla \cdot \boldsymbol{q} - \nabla \cdot \left[\underline{\boldsymbol{\tau}} \cdot \boldsymbol{v}\right] + \boldsymbol{v} \cdot \left[\nabla \cdot \underline{\boldsymbol{\tau}}\right] - \sum_{n=1}^{N}\left(\widehat{H_n} - \frac{v^2}{2}\right)R_n + \frac{DP}{Dt} \tag{A-19}$$

where the definition of the symbols can be found within the text in Appendix A. As justified by the time constant analysis in section 3.1, the fluxes, pressure and temperature can be assumed in pseudo-steady state:

$$\frac{dv}{dt} = \frac{dP}{dt} = \frac{dT}{dt} = 0 \tag{3-26}$$

Therefore, Eq. (A-19) can be simplified to obtain a pseudo-steady state form (see Eq. (A-19) to (A-25) for derivation), which is:

$$\frac{1}{r^2}\frac{d}{dr}\left(r^2\frac{dT}{dr}\right) = \frac{1}{\lambda_{\text{eff}}}\sum_{n=1}^{N}\left(H_n + \frac{{u_M}^2}{2}M_n\right)Q_n + \frac{1}{\lambda_{\text{eff}}}\frac{dT}{dr}\sum_{n=1}^{N}J_n C_{p,n} + \frac{1}{\lambda_{\text{eff}}}\sum_{n=1}^{N}M_n J_n u_M \frac{du_M}{dr} \tag{3-27}$$

where $C_{p,n}$ is the molar heat capacity of species *n* and λ_{eff} is the effective thermal conductivity. H_n is the partial molar enthalpy of species *n* at temperature *T*, and is calculated from standard enthalpy of formation $H_{f,n}^0$ by

$$H_n = H_{f,n}^0 + \int_{298}^{T} C_{p,n}dT \tag{3-28}$$

The last term in Eq. (3-27) makes specific allowance for the small change in momentum occurring as a result of the change in mass in the gas phase during the non-catalytic reaction of the solid, which is an additional term to the corresponding equation given by Bird *et al.* (2007). The calculation of the thermal parameters C_p and λ is discussed in section 3.2.4. Finally, u_M is the mass-averaged velocity of the mixture which is given by

$$u_M = \sum_{n=1}^{N} M_n J_n \Big/ \sum_{n=1}^{N} \rho_{\text{g},n} \tag{3-29}$$

where $\rho_{\text{g},n}$ is the density of gas species *n* from ideal gas law. The boundary conditions for the internal energy balance are:

$$r = 0: \quad dT/dr = 0 \qquad r = r_p: \quad T = T^S \tag{3-30}$$

3.2.5 Calculation of the physical parameters

The boundary layer thickness δ was given by Hayhurst & Parmar (2002):

$$\mathrm{Sh}_{\mathrm{EMCD}} = 2\varepsilon_{mf}(1 + r_p/\delta) \tag{3-31}$$

$$\mathrm{Sh}_{\mathrm{EMCD}} = 2\varepsilon_{mf} + 0.61\left(2r_p U_p/\upsilon_{\mathrm{mix}}\right)^{0.48}(\upsilon_{\mathrm{mix}}/D_B)^{0.33} \tag{3-32}$$

$$U_p = U_{mf}(1 - \varepsilon_b)\{1 - 0.5\pi\mathrm{Ln}(1 - 6\varepsilon_b/\pi)\} \tag{3-33}$$

where ε_{mf} is the voidage at incipient fluidisation for a bubbling fluidised bed with silica sand. Also, υ_{mix} is the kinematic viscosity of the gas mixture calculated using Chapman-Engskog theory and D_B is the binary molecular diffusivity for a chosen gas species in the fluidising gas. The bubble fraction ε_b is given by

$$\varepsilon_b = \left(U - U_{mf}\right)/U_b = \left(h - h_{mf}\right)/h \tag{3-34}$$

where the bubble velocity, U_b, is given by Davidson & Harrison (1963):

$$U_b = \left(U - U_{mf}\right) + 0.71\left(g\overline{d_b}\right)^{0.5} \tag{3-35}$$

The parameter h_{mf} is the bed height at incipient fluidisation and $\overline{d_b}$ is the mean bubble diameter estimated from the correlation of Darton *et al.* (1977):

$$\overline{d_b} = 0.54\left(U - U_{mf}\right)^{0.4} h^{0.8}/(2g^{0.2}) \tag{3-36}$$

where h is the expanded height of the bed when fluidised at superficial velocity U. Although Hayhurst and Parmar's (2002) correlation is based on equimolar counter-diffusion (EMCD), it has been shown that it will yield the correct value of δ from Eq. (3-31), even for non-EMCD (Hayhurst, 2000).

The effective thermal conductivity of the reacting particle was calculated from

$$\lambda_{\mathrm{eff}} = (1 - \varepsilon)\lambda_{\mathrm{solid}} + \varepsilon\lambda_{\mathrm{gases}} \tag{3-37}$$

$$\lambda_{\text{gases}} = \sum_{n=1}^{N} y_n \lambda_n \tag{3-38}$$

The thermal conductivities of the pure gaseous species n, λ_n, were obtained from

$$\lambda_n = C_1^n T^{C_2^n} / (1 + C_3^n / T + C_4^n / T^2) \tag{3-39}$$

where T is in K and $C_1^n - C_4^n$ are constants for species n (Green & Perry, 2007). The overall thermal conductivity is largely influenced by that of the solid. The specific heat capacity of each gas was estimated from,

$$C_P^n = B_1^n + B_2^n T + B_3^n / T^2 \tag{3-40}$$

where T is in K and $B_1^n - B_3^n$ are constants from Green & Perry (2007). The physical parameters of all the gas species involved in this thesis are listed in Table 3.2. The thermal conductivity of the fluidised bed was also calculated using Eq. (3-37), where λ_{solid} of the bed material and the porosity of the bed at incipient fluidisation was used.

Table 3.2 Physical parameters of gas species.

		CO_2	CO	O_2	SO_2	N_2
Molar mass / g mol^{-1}		44.01	28.01	15.9994	64.066	28.0
Standard enthalpy of formation / kJ mol^{-1}		-393.5	-110.5	0	-296.8	0
Heat capacity coefficients	B_1 / J mol^{-1} K^{-1}	3.96	6.60	8.27	7.70	6.50
	B_2 / J mol^{-1} K^{-2}	0.00274	0.0012	0.000258	0.0053	0.001
	B_3 / J K mol^{-1}	-1.955×10^5	0	-1.877×10^5	-8.3×10^{-7}	0
Thermal conductivity coefficient	C_1 / W m^{-1} K^{-1}	3.69	5.9882×10^{-4}	4.4994×10^{-4}	10.527	3.3143×10^{-4}
	C_2 / -	-0.3838	0.6863	0.7456	-0.7732	0.7722

	C_3 / -	964	57.13	56.699	-1333	16.323
	C_4 / -	1.86×10^6	501.92	0	1.5064×10^6	373.72

3.3 Non-dimensional model equations

The above equations were made dimensionless using the following non-dimensional variables:

$$\eta^I = \frac{r}{r_p}\left(0 \le r \le r_p\right) \qquad \eta^E = \frac{r - r_p}{\delta}\left(r_p \le r \le r_p + \delta\right)$$

$$D'_{B,nm} = \frac{D_{B,nm}}{D_{\mathrm{ref}}} \qquad D'_{A,nm} = \frac{D_{A,nm}}{D_{\mathrm{ref}}} \tag{3-41}$$

$$P' = \frac{P}{P^B} \qquad J'_n = \frac{r_p R T^B}{D_{\mathrm{ref}} P^B} J_n \qquad T' = \frac{T}{T^B}$$

The reference diffusivity, D_{ref}, was chosen arbitrarily as the molecular diffusivity of one gaseous species in the other, *e.g.* CO_2 in N_2, at the bulk condition. The superscript *I* and *E* indicate internal and external of the particle.

If the particle radius r_p decreases during the reaction, *e.g.* during the gasification of a reactive particle, the coordinates need to be transformed carefully. The transformation of the spatial coordinate from r to η is described in Appendix B and is given:

$$\frac{\partial}{\partial \eta}\Big|_t = r_p \frac{\partial}{\partial r}\Big|_t \qquad \frac{\partial^2}{\partial r^2} = \frac{1}{{r_p}^2}\frac{\partial^2}{\partial \eta^2} \tag{3-42}$$

There is an extra term for the time derivative, required for the equation describing rate of conversion:

$$\left.\frac{\partial}{\partial t}\right|_\eta = \left.\frac{\partial}{\partial t}\right|_r + \frac{\eta}{r_p}\dot{r_p}\left.\frac{\partial}{\partial \eta}\right|_t \tag{3-43}$$

3.3.1 Equations for the internal model

With the above transformations, the CPIM equations for intraparticle mass transfer become:

$$\frac{dy_n}{d\eta^I} = \frac{\tau^2 T'}{\varepsilon P'} \sum_{m=1}^{N} \left(\frac{y_n J'_m}{D'_{A,mn}} - \frac{y_m J'_n}{D'_{A,nm}} \right) \qquad n = 1, 2 \dots N \tag{3-44}$$

$$\frac{dP'}{d\eta^I} = -\frac{\tau^2 A_A D_{\text{ref}}}{\varepsilon R T^B} \sum_{n=1}^{N} \left(\sqrt{M_n} \cdot J'_n \right) \tag{3-45}$$

The dimensionless equations for the fluxes and the boundary conditions are given by

$$\frac{1}{{\eta^I}^2} \frac{d}{d\eta^I} \left({\eta^I}^2 J'_n \right) = {\phi_n}^2 = \frac{{r_p}^2 R T^B Q_n}{D_{\text{ref}} P^B} \tag{3-46}$$

$$\eta^I = 0: \quad J'_n = 0 \tag{3-47}$$

$$\eta^I = 1: \quad y_n = y_n^S \quad \& \quad P' = 1 \tag{3-48}$$

The Eq. (3-24) for local conversion of solid becomes:

$$\left. \frac{dX}{dt} \right|_{\eta^I} = \frac{\eta^I}{r_p} \dot{r_p} \left(\left. \frac{\partial X}{\partial \eta^I} \right|_t \right) - M_{\text{S1}} \left(\frac{Q_{\text{S1}}}{\rho_{e,0}} \right) \tag{3-49}$$

where $\dot{r_p}$ is the rate of change of particle radius arising from Eq. (3-43). The initial condition for local conversion changes to

$$t = 0: \quad X(\eta^I) = 0 \quad \text{for all } \eta^I \in [0, 1] \tag{3-50}$$

The non-dimensional energy equation inside the particle and its boundary conditions are:

$$\begin{aligned} &\frac{d^2 T'}{d{\eta^I}^2} + \left(\frac{2}{\eta^I} - \frac{D_{\text{ref}} P^B}{\lambda^I_{\text{eff}} R T^B} \sum_{n=1}^{N} C_{p,n} J'_n \right) \frac{dT'}{d\eta^I} \\ &\qquad = \frac{{r_p}^2}{\lambda^I_{\text{eff}} T^B} \sum_{n=1}^{N} \left(H_n + \frac{{u_M}^2}{2} M_n \right) Q_n \\ &\qquad + \frac{D_{\text{ref}} P^B}{\lambda^I_{\text{eff}} R {T^B}^2} \sum_{n=1}^{N} M_n J'_n u_M \frac{du_M}{d\eta^I} \end{aligned} \tag{3-51}$$

$$\eta^I = 0: \quad \frac{dT'}{d\eta^I} = 0 \tag{3-52}$$

$$\eta^I = 1: \quad T' = \frac{T^S}{T^B} \tag{3-53}$$

3.3.2 Equations for the external model

The transformed equations describing external mass transfer become:

$$\frac{dy_n}{d\eta^E} = \frac{\delta T'}{r_p P'} \sum_{m=1}^{N} \left(\frac{y_n J'_m - y_m J'_n}{D'_{B,nm}} \right) \qquad n = 1, 2, 3 \ldots N \tag{3-54}$$

$$\frac{dP'}{d\eta^E} = 0 \tag{3-55}$$

$$\frac{dJ'_n}{d\eta^E} + \frac{2}{r_p/\delta + \eta^E} J'_n = \frac{\delta r_p R T^B Q_n}{D_{\mathrm{ref}} P^B} \tag{3-56}$$

with boundary conditions:

$$\eta^E = 0: \quad J'_n = J'_{n,s} \tag{3-57}$$

$$\eta^E = 1: \quad y_n = y_n^S \quad \& \quad P' = 1 \tag{3-58}$$

The non-dimensional energy equation for energy balance outside the particle is:

$$\frac{d^2T'}{d{\eta^E}^2} + \left(\frac{2}{r_p/\delta + \eta^E} - \frac{\delta D_{\mathrm{ref}} P^B}{r_p \lambda^E_{\mathrm{eff}} R T^B} \sum_{n=1}^{N} C_{p,n} J'_n \right) \frac{dT'}{d\eta^E} = \frac{\delta^2}{\lambda^E_{\mathrm{eff}} T^B} \sum_{n=1}^{N} \left(H_n + \frac{{u_M}^2}{2} M_n \right) Q_n + \frac{\delta D_{\mathrm{ref}} P^B}{r_p \lambda^E_{\mathrm{eff}} R {T^B}^2} \sum_{n=1}^{N} M_n J'_n u_M \frac{du_M}{d\eta^E} \tag{3-59}$$

The boundary conditions are:

$$\eta^E = 0: \quad T' = \frac{T^S}{T^B} \tag{3-60}$$

$$\eta^E = 1: \quad T' = 1 \tag{3-61}$$

3.4 Model solutions

The system to be solved is described by Eqs. (3-44) to (3-61) and it is fully specified by the boundary and initial conditions. Both the intraparticle and external mass transfer models each have $(2N+1)$ 1st order ordinary differential equations (ODEs) in the space domain. Hence $(2N+1)$ boundary conditions are needed to solve the equations. The ODE for conversion is 1st order in the time domain, hence only one initial condition is required. The energy equation is a 2nd order ODE, hence two boundary conditions are required for both the internal and external cases. The main difficulty in solving the system lies with (i) dealing with parameters which vary with local conditions, and (ii) efficient solution of the large system of equations. A numerical algorithm called Orthogonal Collocation on Finite Element (OCFE) (Chang & Finlayson, 1978a) was written in MATLAB to solve the model, whose mathematical principles are describe in Appendix C.

The symbols used in the following section are specific to section 3.4 and Appendix C, and the definitions can be found within the text. Outside these two sections, please refer to the List of Abbreviations and Acronyms for definitions of symbols.

3.4.1 Solution to the internal model

For the internal reaction and diffusion model described in section 3.3.1, all the matrices of the dependent variables (*i.e.* y_n, J'_n, P' and T') and the independent spatial variables (*i.e.* η^I and w), have a dimension of $[NT \times 1]$. Using the coordinate transformation shown in Eq. (C-15), the equations of the internal model become:

$$\left.\frac{dy_n}{dw}\right|_i^v = \frac{\Delta\eta|^v \tau^2 T'}{\varepsilon P'} \sum_{m=1}^{N} \left(\frac{y_n J'_m}{D'_{A,mn}} - \frac{y_m J'_n}{D'_{A,nm}} \right) \equiv f{y_n}^I \tag{3-62}$$

$$\left.\frac{dP'}{dw}\right|_i^v = -\frac{\Delta\eta|^v \tau^2 A_A D_{\text{ref}}}{\varepsilon R T^B} \sum_{n=1}^{N} \left(\sqrt{M_n} \cdot J_n'\right) \equiv f{P^I} \tag{3-63}$$

$$\left.\frac{dJ_n'}{dw}\right|_i^v = \left(\frac{\Delta\eta|^v {r_p}^2 R T^B Q_n}{D_{\text{ref}} P^B} - \frac{2J_n'}{\frac{\eta|_1^v}{\Delta\eta|^v} + w|_i^v} \right) \equiv f{J_n}^I \tag{3-64}$$

$$\begin{aligned} \left.\frac{d^2T'}{d(w)^2}\right|_i^v + \left(\frac{2}{\frac{\eta|_1^v}{\Delta\eta|^v} + w|_i^v} - \frac{\Delta\eta|^v D_{\text{ref}} P^B}{\lambda_{\text{eff}} R T^B} \sum_{n=1}^{N} C_{p,n} J_n' \right) \left.\frac{dT'}{dw}\right|_i^v \\ = \frac{\left(r_p \Delta\eta|^v\right)^2}{\lambda_{\text{eff}} T^B} \sum_{n=1}^{N} \left(H_n + \frac{{u_M}^2}{2} M_n \right) Q_n \\ + \frac{D_{\text{ref}} P^B \Delta\eta|^v}{\lambda_{\text{eff}} {RT^B}^2} \sum_{n=1}^{N} M_n J_n' u_M \left.\frac{du_M}{dw}\right|_i^v \equiv f{T^I} \end{aligned} \tag{3-65}$$

where the right-hand side of each equation does not contain any derivative of the dependent variables and is represented in short by $f{y_n}^I$, $f{P^I}$, $f{J_n}^I$ and $f{T^I}$ respectively.

The derivatives of the dependent variables in the above equations can now be substituted by their corresponding matrix equations discussed in section 3.4, as follows:

$$\begin{aligned} &\left.\frac{dy_n}{dw}\right|_i^v = \sum_{i=1}^{NP} [A]_{j,i}\, y_n|_i^v \qquad \left.\frac{dP'}{dw}\right|_i^v = \sum_{i=1}^{NP} [A]_{j,i}\, P'|_i^v \\ &\left.\frac{dJ_n'}{dw}\right|_i^v = \sum_{i=1}^{NP} [A]_{j,i}\, J_n'|_i^v \\ &\left.\frac{dT'}{dw}\right|_i^v = \sum_{i=1}^{NP} [A]_{j,i}\, T'|_i^v \qquad \left.\frac{d^2T'}{d(w)^2}\right|_i^v = \sum_{i=1}^{NP} [B]_{j,i}\, T'|_i^v \end{aligned} \tag{3-66}$$

$$n = 1, 2 \ldots N; \quad j = 2 \ldots NP - 1; \quad v = 1 \ldots NE$$

Once again, $[A]_{j,i}$ and $[B]_{j,i}$ are the matrix cells at the j^{th} row and i^{th} column of the collocation matrices [A] and [B], calculated from the roots of the Legendre polynomials in Eq. (C-7) and (C-8). The reason why the index j ranges between 2 and $(NP - 1)$ is

that the boundary conditions and, or, continuity constraints are specified at the first and the last nodes of each finite elements. The system of equations to be solved for each of the dependent variables (*i.e.* y_n, J'_n, P' and T') is given by

$$\sum_{i=1}^{NP} [A]_{j,i}\, y_n|_i^v - f{y_n}^I = 0 \tag{3-67}$$

$$\sum_{i=1}^{NP} [A]_{j,i}\, P'|_i^v - fP^I = 0 \tag{3-68}$$

$$\sum_{i=1}^{NP} [A]_{j,i}\, J'_n|_i^v - f{J_n}^I = 0 \tag{3-69}$$

$$\sum_{i=1}^{NP} [B]_{j,i}\, T'|_i^v + \left(\frac{2}{\frac{\eta|_1^v}{\Delta\eta|^v} + w|_i^v} - \frac{\Delta\eta|^v D_{\text{ref}} P^B}{\lambda_{\text{eff}} R T^B} \sum_{n=1}^{N} C_{p,n} J'_n \right) \sum_{i=1}^{NP} [A]_{j,i}\, T'|_i^v - fT^I = 0 \tag{3-70}$$

The above equations are called the interior residual equations, which are defined at the interior collocation points (nodes other than the element boundaries) of each finite element and are solved by minimising the residual of the left-hand side to a value suitably close to 0.

The system boundary conditions at the centre of particle ($\eta^I = 0$) are given by the following equation at the 1st collocation point of the 1st finite element:

$$At\ \eta^I = 0: \quad J'_n|_{i=1}^{v=1} = 0 \qquad \left.\frac{dT'}{d\eta^I}\right|_{i=1}^{v=1} = 0 \tag{3-71}$$

The boundary conditions at the particle surface ($\eta^I = 1$) are specified at the last collocation point of the last finite element:

$$At\ \eta^I = 1: \quad y_n|_{i=NP}^{v=NE} = y_n^S \qquad P'|_{i=NP}^{v=NE} = 1 \qquad T'|_{i=NP}^{v=NE} = \frac{T^S}{T^B} \tag{3-72}$$

The continuity constraints on the values and the gradients of the dependent variables, shown in Eq.(C-18), are specified at all finite elements' boundary nodes, except for the very first and the very last ones where boundary conditions are defined.

For the internal model, there are $2n + 2$ unknowns (y_n, J'_n, P' and T') at each collocation point. Hence, each unknown requires $NT = NE \times (NP - 1) + 1$ equations to be solved. Table 3.3 shows the number of equations of different categories and the total number does sum to NT for each dependent variable as expected.

Table 3.3. Number of equations to be solved for each dependent variables

Variables	Interior residual equations	Continuity constraints	Boundary conditions	Boundary condition type
y_n	$NE(NP-2)$	$(NE-1)$	1 at $\eta^I = 1$	Dirichlet
P	$NE(NP-2)$	$(NE-1)$	1 at $\eta^I = 1$	Dirichlet
J_n	$NE(NP-2)$	$(NE-1)$	1 at $\eta^I = 0$	Dirichlet
T	$NE(NP-2)$	$(NE-1)$	2 at $\eta^I = 0$ & 1	Neumann /Dirichlet

Finally, the matrix forms of Eqs. (3-67) to (3-72) are stacked together following the method described in section 3.4.2 and 3.4.3, and can be solved simultaneously using the subroutine *fsolve* in MATLAB together with the adaptive meshing algorithm discussed in section C.4 to find the values of the dependent variables at each collocation points. The results from this solution give the profile of gas mole fractions, total pressure, total fluxes and temperature within the particle.

3.4.2 Solution to the external model

The same coordinate transformation, described by Eq. (C-15), was applied to the equations of the external model shown in section 3.3.2, as follow:

$$\left.\frac{dy_n}{dw}\right|_i^v = \frac{\Delta\eta|^v \delta T'}{r_p P'} \sum_{m=1}^{N} \left(\frac{y_n J'_m - y_m J'_n}{D'_{B,nm}}\right) = f{y_n}^E \tag{3-73}$$

$$\left.\frac{dP'}{dw}\right|_i^v = 0 = fP^E \tag{3-74}$$

$$\left.\frac{dJ_n'}{dw}\right|_i^v = \left(\frac{\Delta\eta|^v \delta r_p R T^B Q_n}{D_{\text{ref}} P^B} - \frac{2J_n'}{\frac{r_p}{\delta\Delta\eta|^v} + \frac{\eta|_1^v}{\Delta\eta|^v} + w|_i^v}\right) = f{J_n}^E \tag{3-75}$$

$$\begin{aligned}\left.\frac{d^2T'}{d(w)^2}\right|_i^v + \left(\frac{2}{\frac{r_p}{\delta\Delta\eta|^v} + \frac{\eta|_1^v}{\Delta\eta|^v} + w|_i^v} - \frac{\Delta\eta|^v \delta D_{\text{ref}} P^B}{r_p \lambda_{\text{eff}} R T^B} \sum_{n=1}^{N} C_{p,n} J_n'\right) \left.\frac{dT'}{dw}\right|_i^v \\ = \frac{\delta^2 \Delta\eta|^{v2}}{\lambda_{\text{eff}} T^B} \sum_{n=1}^{N} \left(H_n + \frac{{u_M}^2}{2} M_n\right) Q_n \\ + \frac{\Delta\eta|^v \delta D_{\text{ref}} P^B}{r_p \lambda_{\text{eff}} R {T^B}^2} \sum_{n=1}^{N} M_n J_n' u_M \left.\frac{du_M}{dw}\right|_i^v = fT^E\end{aligned} \tag{3-76}$$

The derivatives in the above equations can be substituted in the same way as shown by Eq. (3-66) from the previous section. The system of equations was then organised in the same way as in Eqs. (3-67) to (3-70):

$$\sum_{i=1}^{NP} [A]_{j,i}\, y_n|_i^v - f{y_n}^E = 0 \tag{3-77}$$

$$\sum_{i=1}^{NP} [A]_{j,i}\, P'|_i^v - fP^E = 0 \tag{3-78}$$

$$\sum_{i=1}^{NP} [A]_{j,i}\, J_n'|_i^v - f{J_n}^E = 0 \tag{3-79}$$

$$\sum_{i=1}^{NP}[B]_{j,i}\,T'|_i^v + \left(\frac{2}{\frac{r_p}{\delta\Delta\eta|^v}+\frac{\eta|_1^v}{\Delta\eta|^v}+w|_i^v} - \frac{\Delta\eta|^v\delta D_{\mathrm{ref}}P^B}{r_p\lambda_{\mathrm{eff}}RT^B}\sum_{n=1}^{N}C_{p,n}J_n'\right)\sum_{i=1}^{NP}[A]_{j,i}\,T'|_i^v - fT^E = 0 \tag{3-80}$$

The boundary conditions will be defined at the particle surface ($\eta^E = 0$) and the edge of the diffusion boundary layer ($\eta^E = 1$):

$$At\ \eta^E = 0: \quad J_n'|_{i=1}^{v=1} = \frac{r_pRT^B}{D_{\mathrm{ref}}P^B}J_n^S \qquad T'|_{i=1}^{v=1} = \frac{T^S}{T^B} \tag{3-81}$$

$$At\ \eta^E = 1: \quad y_n|_{i=NP}^{v=NE} = y_n^B \qquad P'|_{i=NP}^{v=NE} = 1 \qquad T'|_{i=NP}^{v=NE} = 1 \tag{3-82}$$

The continuity equation between two neighbouring elements is exactly the same as Eq. (C-18).

For the external model, there are also $2n + 2$ unknowns (*i.e.* y_n, J_n', P' and T') at each collocation point for *n* species. Hence, the number of equations from the interior residual, continuity and boundary conditions categories is the same as shown in Table 3.3. To achieve continuity between the internal and external models, the total fluxes of gases at the particle surface, J_n^S, calculated from the internal model were used as an initial guess of the flux boundary conditions, Eq. (3-81), for the external model. Together with the bulk conditions, Eq. (3-82), at the edge of diffusion boundary layer, the system of equations was solved simultaneously by using the subroutine *fsolve* in MATLAB to find the values of the dependent variables at each collocation point. The results from this solution give values of gas concentration, pressure and temperature at the particle surface to be used as the updated boundary conditions of the internal model. The internal model was then solved to yield the new boundary conditions for the external model. The iteration proceeded until the differences in values of gas concentration, flux, pressure and temperature at the particle surface given by the internal and external models were smaller than 0.1%.

3.4.3 Time progression of the system

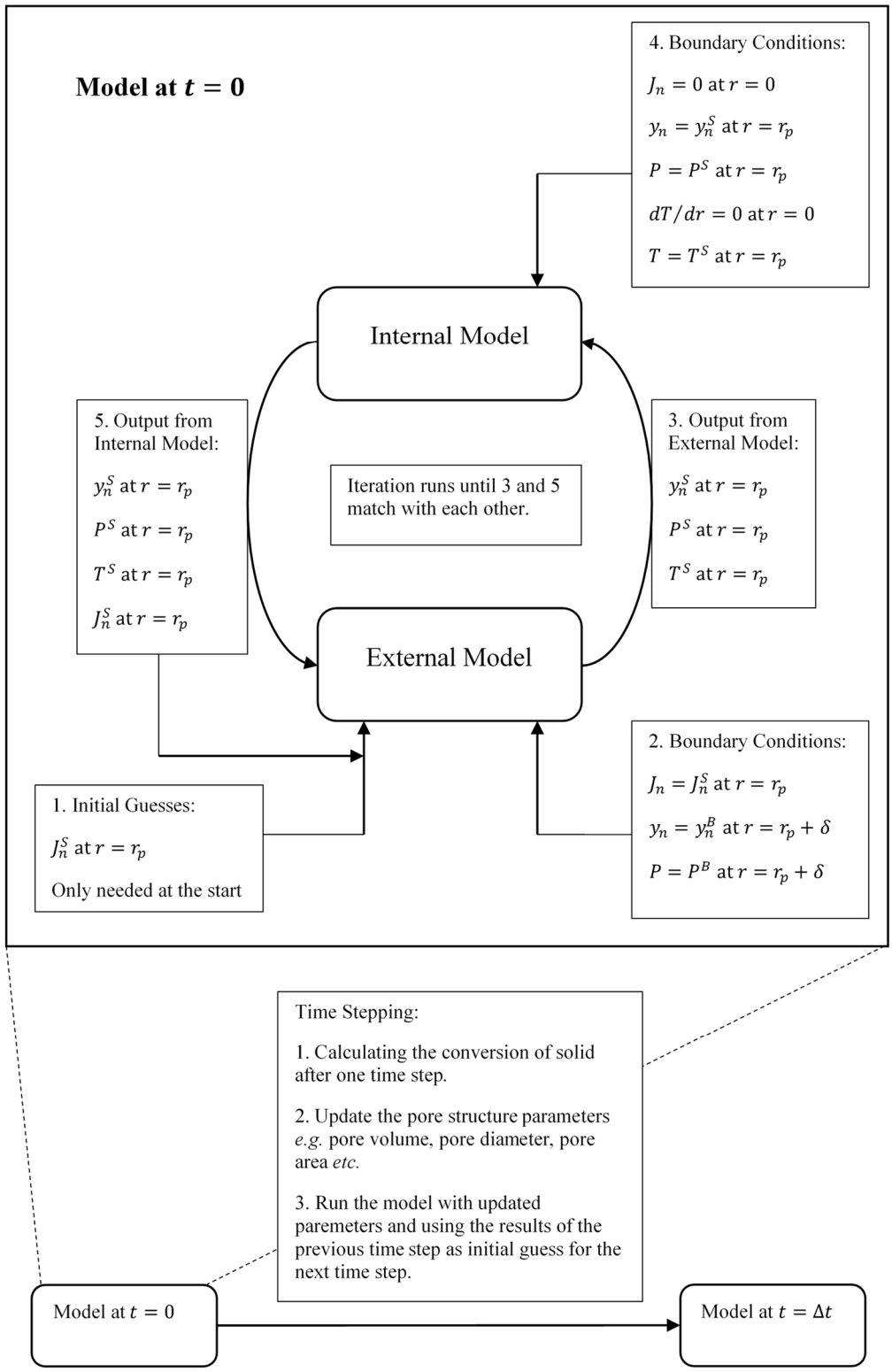

Figure 3.1 Schematic flow diagram showing the algorithm for solving the internal and external models and time stepping procedures.

Pseudo-steady state has been assumed for all the variables except the conversion X. Using the initial condition, Eq. (3-50), the 1st order time-dependent ODE of local

conversion X, Eq. (3-49), has to be solved. The numerical subroutine *ode45* in MATLAB was used to calculate the values of $X(\eta^I)$ at time $t + \Delta t$ based on $X(\eta^I)$ and dX/dt at time t. The relevant model parameters, *e.g.* porosity and pore diameter, were updated with the new value of $X(\eta^I)$, and then the internal model and external model solved for results at time $t + \Delta t$. The iterative process was stopped when reaching the target time. Figure 3.1 shows the flow diagram of the algorithm described here and in the previous section.

For some reacting systems, the rate of reaction slows as conversion increases so that the gradient of the conversion with respect to time reduces. Hence it makes sense to ensure that the time step Δt is small at the start and gradually increases as reaction proceeds, so that the computational cost is minimal. There are several simple strategies to achieve this: (i) constant time step, (ii) linearly increasing time step, (iii) geometrically increasing time step. Here (i) and (iii) were implemented for a total simulation time of t_{Total} and Z time steps as follows:

$$\Delta t_i = \Delta t_0 {\alpha_t}^{i-1} \qquad i = 1,2 \dots Z \tag{3-83}$$

where the initial time step Δt_0 is

$$\begin{aligned} &\alpha_t \neq 1: \quad \Delta t_0 = t_{Total}\left(\frac{1-\alpha_t}{1-{\alpha_t}^Z}\right) \\ &\alpha_t = 1: \quad \Delta t_0 = \frac{t_{Total}}{Z} \end{aligned} \tag{3-84}$$

The parameter α_t is an input which can take any positive value: (i) a value between 0 and 1 means the time step is reduced after each iteration, suitable for reactions where the rate increases with conversion; (ii) a value equals to 1 means uniform time step, applicable to all types of reactions but does not give the optimum efficiency; (iii) a value exceeding 1 means that the time step is increased after each iteration, suitable for reactions where the reaction rate reduces with conversion.

3.4.4 Input parameters

Table 3.4 Input parameters of the model for simulating the calcination of limestone particles.

Configuration	Parameter	Value
(1) Bulk conditions	Temperature, T^B / K	1073
	Pressure, P^B / Bar	1.013
	Mole fraction of CO_2, $y^B_{CO_2}$	0.05
	Mole fraction of N_2, $y^B_{N_2}$	0.95
(2) Solid particle	Particle diameter / µm	500
	Mass fraction of $CaCO_3$	1
	Mass fraction of CaO	0
	Skeletal density / kg m^{-3}	2710
	Pore volume / cm^3 g^{-1}	0.02
	Pore diameter / nm	50
	BET area / m^2 g^{-1}	2.0
	Tortuosity factor	1.41
(3) Fluidised bed	Fluidising gas flow rate (STP) / ml s^{-1}	80
	Particle diameter / µm	400
	Particle density / kg m^{-3}	2648
	Bed diameter / mm	30
	Voidage at incipient fluidisation, ε_{mf}	0.44
	Bed height at incipient fluidisation, H_{mf} / mm	29
	Tortuosity factor	1.34
(4) Time grid	Total simulation time, t_{Total} / s	200
	Number of time steps, Z	200
	Time step growth factor, α_t	1.02
(5) Spatial grid	Number of collocation points, NP (internal model)	7
	Number of finite elements, NE (internal model)	15
	Element spacing decay factor, α_x (internal model)	1.0
	Number of collocation points, NP (external model)	5
	Number of finite elements, NE (external model)	15
	Element spacing decay factor, α_x (external model)	1.0

The input parameters required by the model were categorised as shown in Table 3.4 under (1) bulk conditions; (2) solid particle properties; (3) fluidised bed properties; (4) time grid and (5) spatial grid. To be specific, an example of the configurations for simulating the calcination of limestone particles is shown in Table 3.4, which will be discussed in Chapter 5. Configuration (1) – (2) are specific to the reactions studied and will be set in the corresponding chapters, while (3) – (5) are constant throughout the entire thesis unless specified otherwise, except for the total simulation time in (4).

Chapter 4 Using an experimentally-determined model of the evolution of pore structure for the gasification of chars by CO_2

4.1 Introduction

During the gasification of a batch of char, the rate of reaction increases, from time $t = 0$, to a maximum and thereafter drops continuously with time as conversion increases. This has been attributed to the change in the pore structure of the particle during reaction. At the start, new gas-solid interface area is created as the small pores grow during gasification, but, at larger conversions, the internal area falls as large pores coalesce (Kawahata & Walker, 1963; Bhatia & Perlmutter, 1980). Hence, many have sought to model the change of internal pore structure with conversion during reactions. For example, Bhatia & Perlmutter (1980) and Gavalas (1980) developed random pore models (RPM), using different approaches, to model the total surface area at any conversion as a function of the initial morphological parameters, *e.g.* the initial porosity and surface area. Gavalas (1980) reported a reasonable agreement between the model and experimental measurements of char gasification at low temperature, but observed some degree of deviation at high temperature where intraparticle diffusion limitations became significant within a char particle. Similar behaviour was also observed for the RPM of Bhatia & Perlmutter (1980) by Lin & Strand (2013). Often the correlation between the total surface area, as measured by Brunauer–Emmett–Teller (BET) N_2 or CO_2 adsorption, and reactivity is weak. This is because the BET area does not account for the nature of the surface, or the concentration of active sites there (Radovic *et al.*, 1985; Lizzio *et al.*, 1990). Hence the applicability of complex mathematical models of pore structure does not always capture all the features of the reaction.

In a review of early works, Laurendeau (1978) concluded that the overall kinetics of char gasification were often correlated by an expression of the form of $r = K_0 C_{CO_2}^n$, where K_0 is the overall rate constant and the order of reaction n is between 0 and 1. However, many (*e.g.* Reif, 1952; Ergun, 1956; Strange & Walker, 1976) agree

that the intrinsic rate of reaction follows Ergun's oxygen-exchange mechanism (Ergun, 1956). If detailed descriptions of the intraparticle and external diffusion processes and energy balance are included in the model, then it is more realistic to use the intrinsic kinetics for the reaction rate rather than using the overall kinetics. Saucedo (2014) and Saucedo *et al.* (2014) took the equations for the diffusion of gaseous reactants and products within a particle of char and coupled them, locally, with an expression describing the chemical kinetics of gasification within the char in the form $r = g(C_i, T, P) \times f(X)$. Clearly, this meant that the conversion would vary across the radius of the particle. However, Saucedo (2014) assumed that X could be replaced by its average for the particle at a particular time, $\overline{X}$, thus reducing the computational complexity of marching forward local values of X at each radial grid point.

In this study, Saucedo's (2014) problem has been solved rigorously by applying the reaction and diffusion model developed in Chapter 3 which tracks the evolution of the pore structure based on the local conversion within a particle. The theory has then been investigated experimentally to determine how far the use of an arbitrary $f(X)$ can be applied to the reaction of similar particles, but of different size and being gasified at conditions different to those used to determine $f(X)$. Aspects of this chapter have been published (Dai *et al.*, 2016a).

4.2 Experimental methods

4.2.1 Materials

Table 4.1 Analysis of the char particles used in the experiments.

Fuel	Ultimate Analysis (wt%)[a]				Density (kg m^{-3})	
	C	H	N	Balance	Bulk	Skeletal
Hambach lignite char	85.69	0.82	0.84	12.65	831	1310
Activated carbon	87.80	0.64	0.37	11.19	703	1076

[a] From Saucedo *et al.* (2014) and Scott *et al.* (2005).

The gases used were N_2, CO_2 and air, as described in section 2.3.1. Silica sand sieved to 355 – 425 μm, was used as a fluidised bed material. Two solid fuels were used: i) char particles made from a low-rank Hambach lignite coal, and ii) activated

carbon particles. The preparation of the char particles was described in section 2.3.3. The lignite char particles were sieved into four size fractions for the experiments: 0.36 - 0.50 mm, 0.60 - 1.00 mm, 1.00 - 1.40 mm and 1.70 - 2.56 mm. The activated carbon did not require pyrolysis: it was crushed and sieved into different size fractions, 0.36 - 0.43 mm, 0.71 - 1.25 mm and 1.70 - 2.36 mm. The composition and density of the fuel particles are listed in Table 4.1.

4.2.2 Fluidised bed experiments

Batch experiments were performed in the fluidised bed described in section 2.2. In an experiment, the reactor was filled with 20 ml of silica sand and heated to the desired temperature, *viz.* 1073 – 1273 K. For gasification, the fluidising gas was typically 30 mol% CO_2, balance N_2. The total volumetric flowrate was 50 mL s^{-1} (STP), giving U/U_{mf} ~ 4.2 – 5.0, with U being the superficial velocity at the temperature of the bed and U_{mf} being the value at incipient fluidisation. The value of U_{mf} was determined by a pressure sensor measuring the pressure drop between the reactor inlet and outlet as a function of the gas flow rate. Experimental measurements gave the flowrate at U_{mf} of 10 and 12 mL s^{-1} (STP) for 1273 and 1073 K, respectively, whereas the correlation of Wen & Yu (1966) gave values of 9 and 12 mL s^{-1} (STP). About 0.05 g of fuel were added to the reactor and allowed to gasify to the point where the concentration of CO in the off-gas was measured as ~ 0. Then the reactor was purged with pure nitrogen before burning off the residual carbon in air. Each experiment was repeated at least 3 times. The mass of fuel added to the bed was chosen to be small to avoid complications arising from rate of mass transfer between the bubble and the particulate phases (Saucedo, 2014). The overall rate of production of CO from gasification in mol s^{-1} g^{-1} is

$$R'_g = 2 \times \frac{\left[\dot{n}_{out}\left(y_{CO,out} + y_{CO_2,out}\right) - \dot{n}_{in}\left(y_{CO,in} + y_{CO_2,in}\right)\right]}{m_{batch}} \qquad (4\text{-}1)$$

where m_{batch} is the initial mass of char. The $\dot{n}_{out}$ and $\dot{n}_{in}$ are the total molar flows leaving and entering the reactor at the exit and entrance conditions, where $\dot{n}_{out}\left(1 - y_{CO,out} - y_{CO_2,out}\right) = \dot{n}_{in}\left(1 - y_{CO,in} - y_{CO_2,in}\right)$ from the mass balance of nitrogen. The raw measurements were deconvoluted to account for the mixing and delay in the sampling line using the methods described in Appendix D.

4.3 Theoretical methods

4.3.1 Modelling the kinetics of gasification

The model described in this work retained all of the assumptions described in Chapter 3, applied to a spherical carbon particle gasified in a stream of CO_2, diluted by N_2 in the batch fluidised bed reactor. The only reaction occurring is:

$$\mathrm{C_{(s)} + CO_{2(g)} \rightleftharpoons 2CO_{(g)}} \qquad \Delta H^0_{298} = +173 \text{ kJ mol}^{-1} \tag{4-II}$$

Although the study focused on gasification by CO_2; of course, steam is also an important gasifying agent. The most widely-used reaction scheme is that of Ergun (1956) in which gaseous CO_2 is adsorbed on an active site, C^*, on the surface of the char followed by desorption of the CO produced:

$$\mathrm{C^* + CO_{2(g)} \underset{k_{-1}}{\overset{k_1}{\rightleftharpoons}} C(O) + CO_{(g)}} \tag{4-III}$$

$$\mathrm{C(O) \overset{k_2}{\rightarrow} C^* + CO_{(g)}} \tag{4-IV}$$

The intrinsic rate of CO production per unit mass of carbon, $R'_{g,0}$, can be expressed as

$$R'_{g,0} = \frac{2c_0k_2\left(p_{\mathrm{CO_2}} - \frac{p^2_{\mathrm{CO}}}{K_P}\right)}{p_{\mathrm{CO_2}} + \frac{k_2}{k_1} + \left(\frac{k_{-1}}{k_1}\right)p_{\mathrm{CO}}} \tag{4-5}$$

using Langmuir-Hinshelwood (L-H) kinetics and assuming a pseudo-steady state for the number of occupied sites C(O). Ergun (1956) proposed this equation without the term p^2_{CO}/K_P. The extra term was added to allow reaction (4-IV) to be reversible (Dennis & Scott, 2010). Here c_0 is the initial number of active sites per unit mass of char, k_1, k_{-1} and k_2 are rate constants, p_{CO} and $p_{\mathrm{CO_2}}$ are the partial pressures of CO and CO_2, and K_P is the equilibrium constant for the overall gasification reaction (4-II). Both the equilibrium constant for reaction (4-III), given by k_{-1}/k_1, and the combined parameter c_0k_2 were found (Ergun, 1956) to be independent of the type of carbon used. The values of k_{-1}/k_1 and c_0k_2 were fitted by Arrhenius equations with constant activation energies of -95 kJ/mol and 247 kJ/mol respectively (Ergun, 1956). In fact, experiments

have shown that k_2 is independent of partial pressure of CO_2, thus confirming the L-H kinetics used by Ergun (Hüttinger & Nill, 1990; Hüttinger & Fritz, 1991). Accordingly, the rate of reaction of species n, Q_n in mol m^{-3} s^{-1}, appearing in the reaction and diffusion model in Chapter 3 is given by

$$Q_n = \nu_n Q_C = \frac{\nu_n}{2}\left(R'_{g,0}\rho_{e,0}\right) f(X) \qquad n = 1,2,3 \tag{4-6}$$

$$\rho_{e,0} = \rho_m(1-\varepsilon_0) \tag{4-7}$$

Here Q_C is the rate of reaction of the solid carbon in mol m^{-3} s^{-1} and ν_n is the stoichiometric coefficient of species n representing CO, CO_2, and N_2 respectively. Finally, $\rho_{e,0}$ is the initial bulk density, ρ_m is the skeletal density and ε_0 is the local porosity in a particle. Given that the total flux J_3 (diffusive flux + advective flux) of the inert nitrogen is zero, an elemental mass balance on oxygen gives:

$$J_1 + 2J_2 = 0 \qquad J_3 = 0 \tag{4-8}$$

A material balance on carbon across a differential element gives the variation of local conversion of carbon with respect to time as a function of the carbon consumption rate Q_C:

$$\left.\frac{dX}{dt}\right|_r = -M_C\left(\frac{Q_C}{\rho_e}\right) = -12\left(\frac{Q_C}{\rho_{e,0}}\right) \qquad Q_C = Q_2 = -\frac{Q_1}{2} \tag{4-9}$$

the initial condition being

$$t = 0: \quad X(r) = 0 \quad \text{for all } r \in [0, r_p] \tag{4-10}$$

4.3.2 Evolution of pore structure

The porosity, ε, changes with the local conversion of carbon, X, during reaction and can be derived from the carbon balance equation over a thin cylindrical shell inside the particle, which also corresponds to Eq. (3-16) in chapter 3:

$$\varepsilon(X) = \varepsilon_0 + X(1-\varepsilon_0) \tag{4-11}$$

From Eq. (3-17) to (3-19) in Chapter 3, the pore diameter at some time when the local conversion is X is:

$$d_{pore} = d_{pore,0}\sqrt{(\varepsilon_0 + X(1-\varepsilon_0))/\varepsilon_0} \tag{4-12}$$

The change of radius of the particle during the reaction occurs in two stages: i) prior to the overall conversion reaching a critical value, the particle shrinks as its density decreases, and ii) at a critical overall conversion, the particle disintegrates from the outside owing to a loss of structural integrity (Gavalas, 1980; Singer & Ghoniem, 2013). During the second stage, the change of radius is usually extremely rapid and is a complicated process occurring at a conversion close to 100%. The present study focused on the first stage. When a particle shrinks with decreasing density, the loss of elemental carbon in solid and gas phases within a char particle is equal to the net carbon transferred out of the particle by the fluxes of CO and CO_2, at pseudo-steady conditions. This gives the following equations:

$$-\frac{d}{dt}\left(\frac{4\pi}{3}{r_p}^3(1-\bar{\varepsilon})\frac{\rho_m}{M_c}+\frac{4\pi}{3}{r_p}^3\overline{\varepsilon\cdot[\mathrm{C}]}\right) = 4\pi{r_p}^2(J_1^S + J_2^S) \tag{4-13}$$

$$\bar{\varepsilon} = 3\int_0^1 {\eta^I}^2\varepsilon\, d\eta^I \qquad \overline{\varepsilon\cdot[\mathrm{C}]} = 3\int_0^1 {\eta^I}^2\varepsilon([\mathrm{CO_2}]+[\mathrm{CO}])\, d\eta^I \tag{4-14}$$

where η^I is the dimensionless radius. The above equations can be rearranged:

$$-\left(3(1-\bar{\varepsilon})\frac{\rho_m}{M_c}+3\overline{\varepsilon\cdot[\mathrm{C}]}\right)\frac{dr_p}{dt}+r_p\frac{\rho_m}{M_c}\frac{d\bar{\varepsilon}}{dt}-r_p\frac{d}{dt}\left(\overline{\varepsilon\cdot[\mathrm{C}]}\right) = 3(J_1^S+J_2^S) \tag{4-15}$$

The initial condition is

$$t=0: \quad r = r_{p,0} \tag{4-16}$$

In Eq. (4-15), $d\bar{\varepsilon}/dt$ and $d\left(\overline{\varepsilon\cdot[\mathrm{C}]}\right)/dt$ can be estimated by numerically differentiating the outputs of Eq. (4-14). The above equation (4-13) is a 1st order ODE in r_p and was solved numerically in MATLAB. In addition, Eq. (4-15) could be simplified to describe a shrinking core model at constant density by setting $d\bar{\varepsilon}/dt = 0$. In practice, the initial particle diameter, $r_{p,0}$, was more of a variable input around its estimated value rather than a constant owing to the uncertainties in using a mean value for the size distribution measurement.

4.4 Results

4.4.1 Particle characterisation

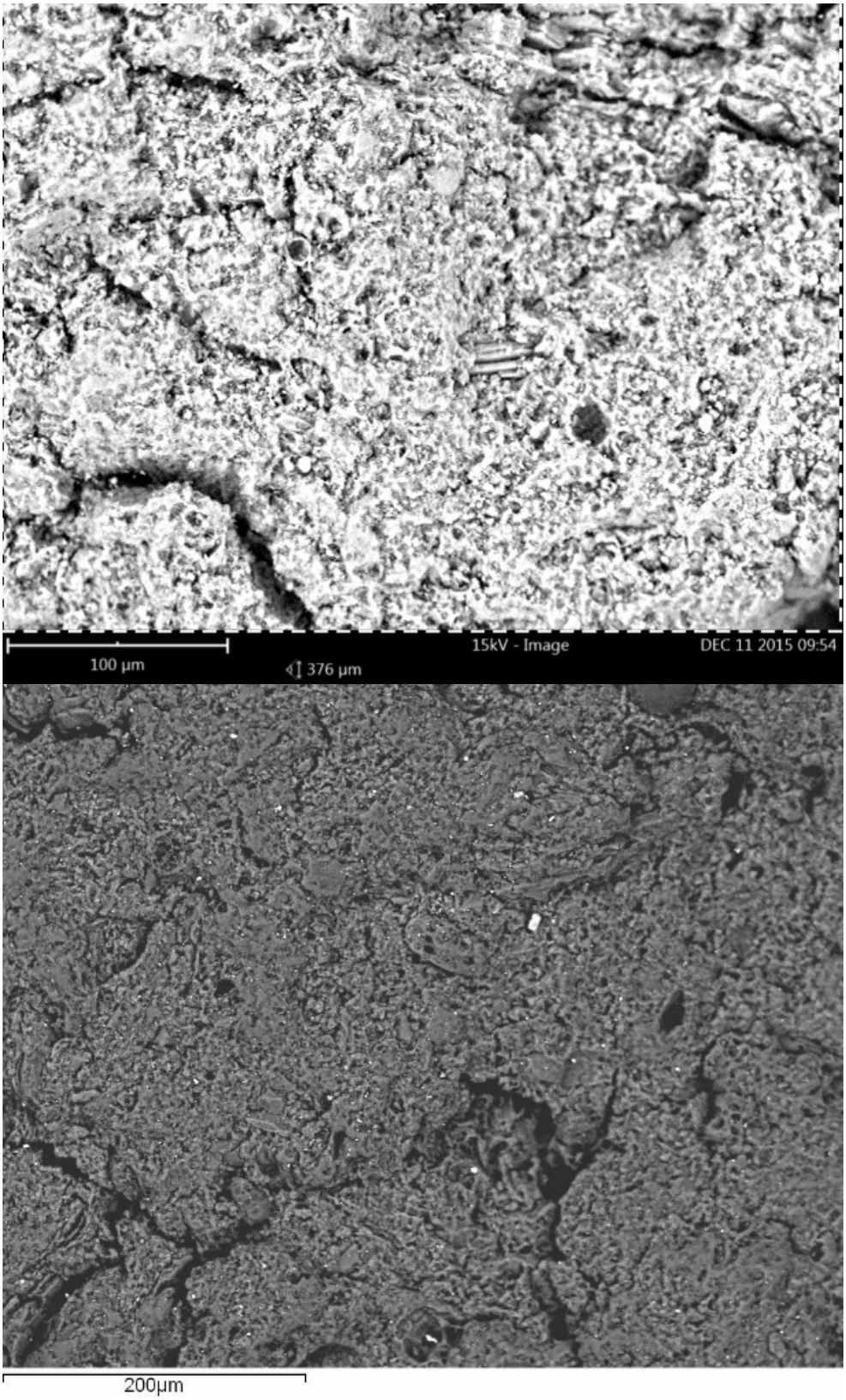

Figure 4.1 SEM images of the lignite char particles.

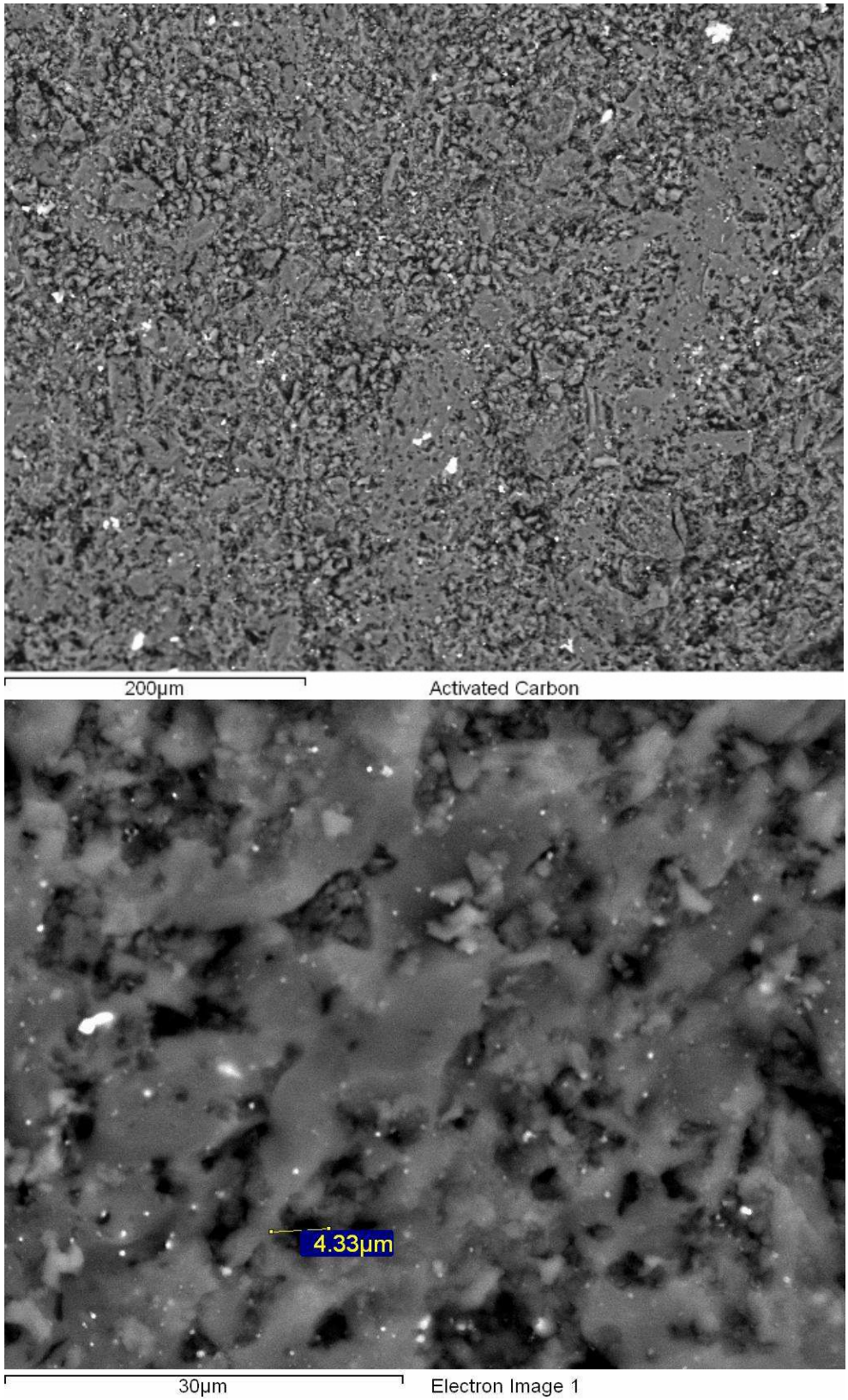

Figure 4.2 SEM images of activated carbon particles.

Figure 4.1 and 4.2 show Scanning Electron Microscope (SEM) images of the polished surfaces of, respectively, lignite char and activated carbon particles, where huge voids and cracks > 100 μm were present in the lignite chars but not in the activated carbon. Figure 4.3 shows the pore size distribution measurements from BJH adsorption analysis and mercury intrusion porosimetry, the key parameters of which are summarised in Table 4.2 and 4.3. The measurements show similar values of parameters for the same fuel indicating that the pore structures of particles of different sizes are the same. Comparing the two sets of analyses, it can be concluded that most of the surface area exists in small pores (d_{pore} < 10 nm) while the majority of the pore volume is contained in large pores (d_{pore} > 100 nm). It was, of course, possible that the fuel particles had considerable unmeasured surface area and pore volume in the microporous range (d_{pore} < 2 nm), as the BET and mercury intrusion analyser were unable to measure pores below a diameter of 1.7 nm and 3 nm respectively. In the subsequent modelling, the mean pore diameter $d_{pore} = 4V/A$ from mercury porosimetry was used as the initial pore diameter of the fuel particles, where V was the total intrusion volume and A was the total pore area.

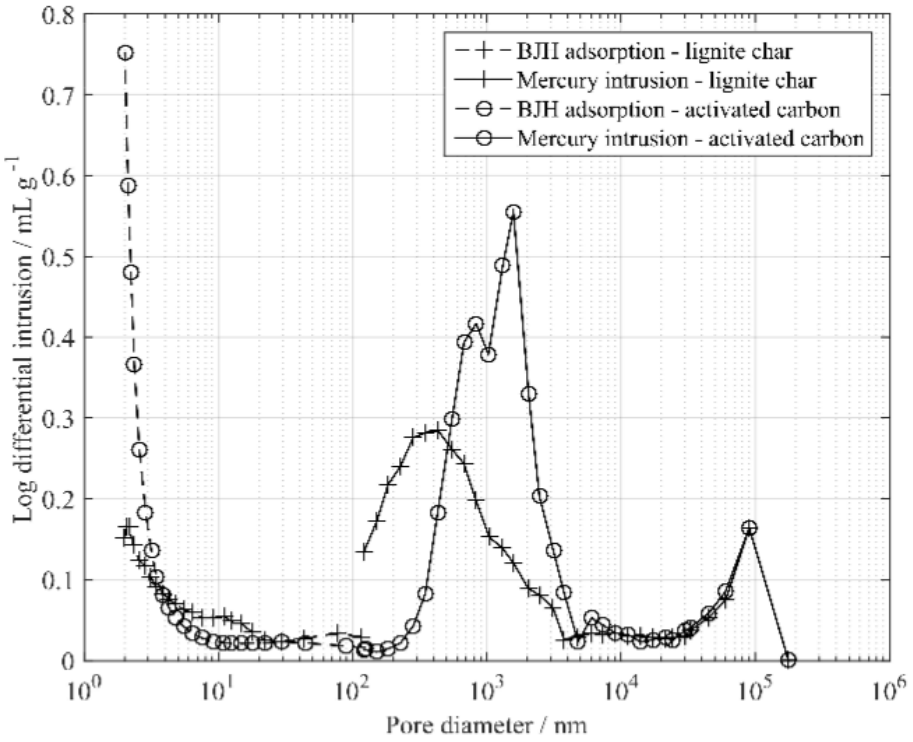

Figure 4.3 Pore size distributions of the 0.60 – 1.00 mm dia. lignite char and the 0.71 – 1.25 mm dia. activated carbon particles from BJH adsorption analysis and mercury intrusion porosimetry.

Table 4.2 Characterisation of the fuel particles by BET analysis.

Fuel particles	BET area / $m^2\ g^{-1}$	BJH volume / $cm^3\ g^{-1}$	BJH adsorption mean pore diameter / nm
Lignite char, 0.60 – 1.00 mm	178	0.113	5.6
Lignite char, 1.70 – 2.56 mm	160	0.103	6.4
Activated carbon, 0.71 – 1.25 mm	1019	0.130	3.3
Activated carbon, 1.70 – 2.36 mm	947	0.122	3.5

Table 4.3 Characterisation of the fuel particles by mercury porosimetry.

Fuel particles	Porosity	Total pore area / $m^2\ g^{-1}$	Total intrusion volume / $cm^3\ g^{-1}$	Mean pore diameter / nm	Bulk density / $kg\ m^{-3}$	Tortuosity factor / -
Lignite char, 0.60 – 1.00 mm	0.31	10.70	0.428	160	874	1.9
Lignite char, 1.70 – 2.56 mm	0.33	10.56	0.452	171	788	1.9
Activated carbon, 0.71 – 1.25 mm	0.36	14.75	0.492	133	703	1.9

Optical microscopy allowing a maximum measurable dimension of 1000 µm was used to measure the size distribution and the shape of the particles. Figure 4.4 shows distributions of the probability density function (left *y*-axis) and the cumulative density function (right *y*-axis) measured for 0.36 – 0.50 mm and 0.60 – 1.00 mm dia. lignite char particles; the main parameters from size distribution measurements are summarised in Table 4.4. No measurements were made on the activated carbon particles because their size fractions (0.71 – 1.25 mm and 1.70 – 2.36 mm) exceeded the measuring range. For the lignite chars, the mode of the main peak occurred at a size close to the Sauter mean diameter, $D(3,2)$. The values of Sauter mean diameter are larger than the upper mesh size, because the particles have large aspect ratios and pass through the sieves by their smallest dimension. In the model, the particle diameter, d_p,

was calculated from the geometric mean of the sieves d_p = (lower mesh × upper mesh)$^{0.5}$. It gave values close to those given by $D(3,2) \times \psi$, where $\psi = 4\pi S_p / P^2$. Here S_p is the mean of measured area and P is the mean of measured perimeter of the particle sample, both of which are estimated from the on-board image analysis software of the equipment.

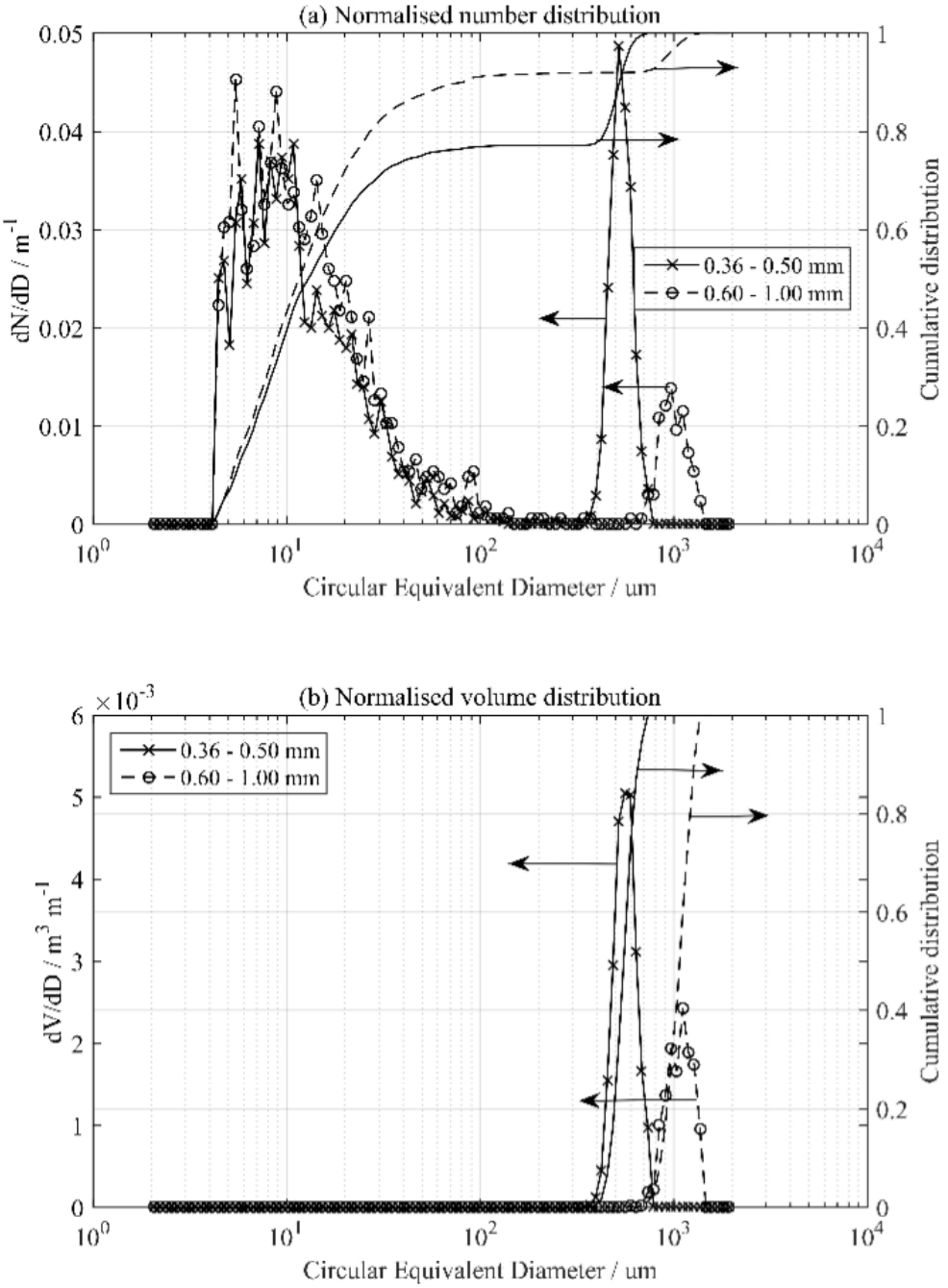

Figure 4.4 Particle size distribution measurements of 0.36 – 0.50 mm and 0.60 – 1.00 mm dia. lignite chars: (a) distribution based on the number of particles and (b) distribution based on the volume of the particles.

Table 4.4 Summary of particle size distribution for lignite chars.

Parameter	0.36 – 0.50 mm	0.60 – 1.00 mm
10% of total volume below this size, $D10$ / µm	466	856
50% of total volume below this size, $D50$ / µm	551	1070
90% of total volume below this size, $D90$ / µm	653	1268
Sauter mean diameter, $D(3,2)$ / µm	574	1100
Average high sensitivity circularity, ψ / -	0.74	0.75
$D(3,2) \times \psi$ / µm	425	825
Geometric mean diameter used in model, d_p / µm	421	775

4.4.2 Mass balance

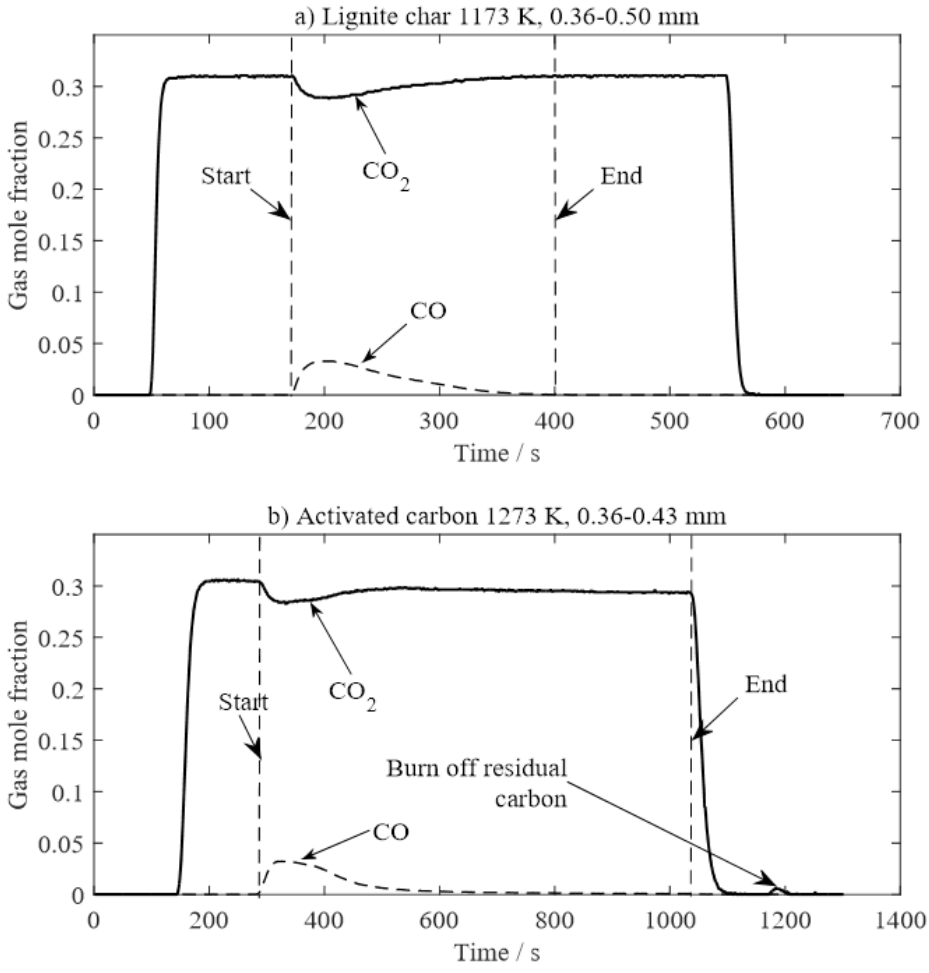

Figure 4.5 Raw measurements of gas mole fraction during gasification experiments in a bubbling fluidised bed, where the U/U_{mf} is ~ (a) 4.9 and (b) 4.2.

The statistical analysis of the mass balance of carbon within the reactor is shown in Table 4.5, where 4 different sizes of lignite char and 3 different sizes of activated carbon were gasified at 3 different temperatures. Experiments were replicated 3 times at each condition. The table shows that an almost complete closure of the mass balance was achieved in the reactor within the accuracy of the experiments.

Table 4.5 Yield of carbon converted to CO from the complete gasification of the fuels.

Statistical parameter	Lignite char	Activated carbon
Mass fraction of solid carbon in the chars converted into	1.01	0.98
Standard deviation in fraction of sample mass	0.05	0.07
Number of experiments × 3 replicates at each condition	36	27

4.4.3 Gasification of fuel particles at different temperatures

Since the model predicts the local reaction rate and conversion across the radius of a particle, the overall values of rate and conversion need to be obtained from integration across the particle radius. For a distribution of the variable χ (*e.g.* S_C and X), its volume-averaged value can be calculated from

$$\bar{\chi} = 3\int_0^1 (\eta^{I\,2}\chi)d\eta^I \qquad (4\text{-}17)$$

where η^I is the dimensionless radius of the particle. The integral was evaluated numerically.

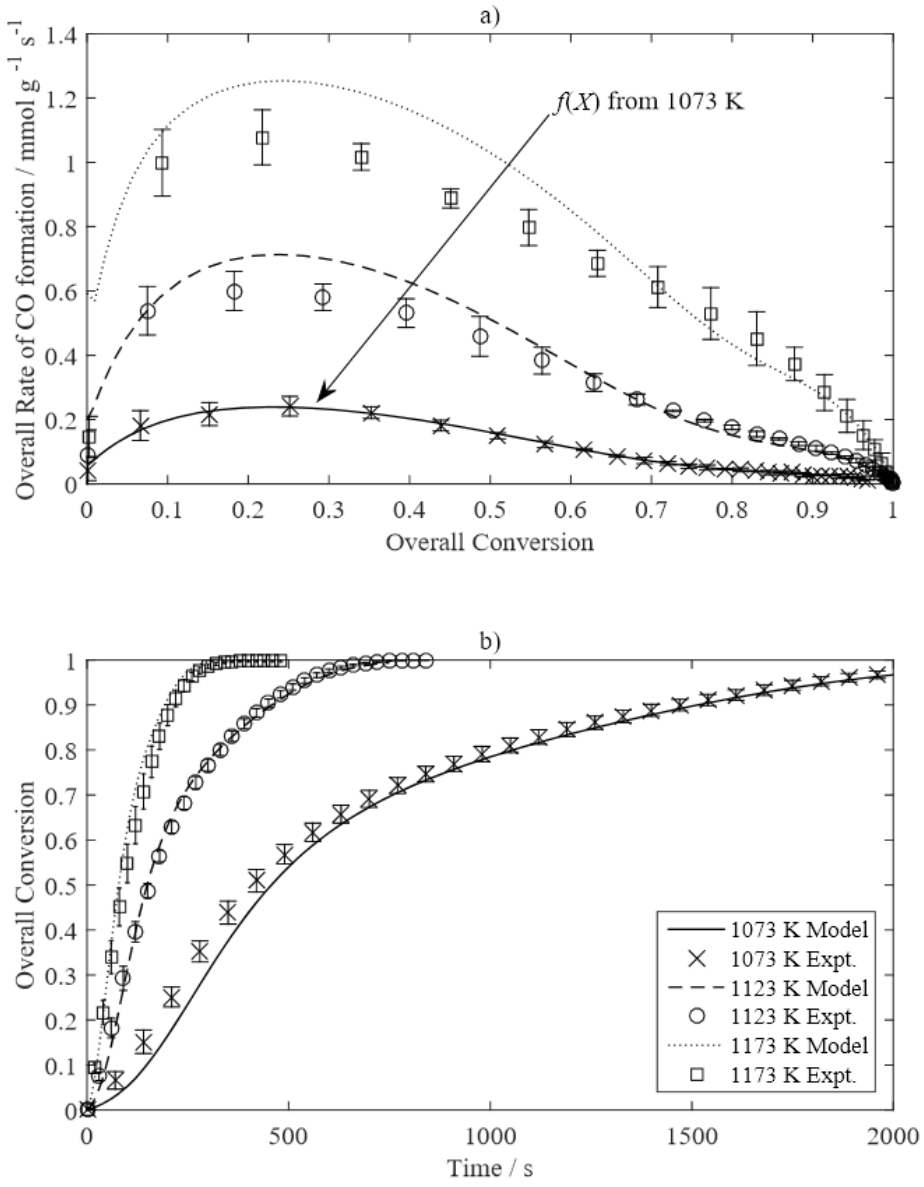

Figure 4.6 Comparison of model results with experimental measurements of the gasification of 0.60 – 1.00 mm lignite char particles by 30 vol% CO_2 balance N_2. The chars were gasified at three different temperatures: 1073 K (×), 1123 K (○) and 1173 K (□). The error bars of the experimental measurements indicate the 95% confidence interval obtained from a *t* – distribution of three repeated measurements of each sample.

Initially, a constant arbitrary function $f(X)$, appearing in Eq. (4-6), was used in the simulations at different temperatures. The $f(X)$ was determined from experimental measurements of gasification rate *vs.* conversion conducted under conditions where the reaction was controlled by intrinsic chemical kinetics. Given the high reactivity of the lignite chars, this necessitated experiments at relatively low temperatures. For example, for lignite char, 0.60 – 1.00 mm dia. particles were gasified by 30 vol% CO_2 balance N_2 at 1073, 1123 and 1173 K. The $f(X)$ was determined from the result of experiments at 1073 K, at which temperature the effectiveness factor κ_{eff} ~ 0.94, and applied to the

simulations of reaction at 1123 K (where κ_{eff} ~ 0.92) and 1173 K (κ_{eff} ~ 0.82). The calculation of the initial effectiveness factors is discussed later in section 4.5.2, with values at other conditions depicted in Figure 4.12. The comparison between theory and experiment is shown in Figure 4.6, which exhibits increasing disagreement between the two as temperature increases. Although the rate of gasification at the peak was over-predicted for 1123 K and 1173 K, the overall conversion *vs.* time matched well the experimental results for all temperatures.

For activated carbon, 0.36 – 0.43 mm dia. particles were gasified in 30 vol% CO_2, balance N_2 at 1173, 1223 and 1273 K. The $f(X)$ was determined from the results at 1173 K, at which κ_{eff} ~ 0.97, and applied to the simulations at 1223 K (κ_{eff} ~ 0.95) and 1273 K (κ_{eff} ~ 0.92). The comparison between the model and the experimental measurements is shown in Figure 4.7. Since the reaction was stopped when the rate of gasification became very slow at high conversion, the experiments at 1173 K only had measurements of gasification rate up to an overall conversion of 0.8. Thus the $f(X)$ determined from it could not be extrapolated beyond 80% of conversion and so the figure shows no theoretical predictions beyond this point. Model and experiment matched well at 1173 K and 1223 K, but differed somewhat for 1273 K even though all three experiments were fairly close to being controlled by intrinsic chemical kinetics.

It was concluded that using a constant $f(X)$ for all temperatures gave an imperfect fit between the model and the measurements for both lignite char and activated carbon. One possible cause of this could be that the particles contained multiple types of active sites, whose contributions to the overall gasification rate changed with temperature. Therefore, the $f(X)$ determined at low temperature would not correctly reflect the change of number of active sites due to changes of internal morphology. Thus, it was necessary to examine whether a constant $f(X)$ was applicable to simulating the experiments affected by intraparticle mass transfer, by using particles of different sizes, at the same temperature. Since the arbitrary function $f(X)$ was to be determined from the measurements conducted under conditions where the reaction was controlled by intrinsic chemical kinetics, at the given temperature, it necessitated using particles sufficiently small in size to evaluate the $f(X)$. So, at each temperature, the $f(X)$ was obtained from the measurements on the smallest particles and then applied to the simulations of the larger ones.

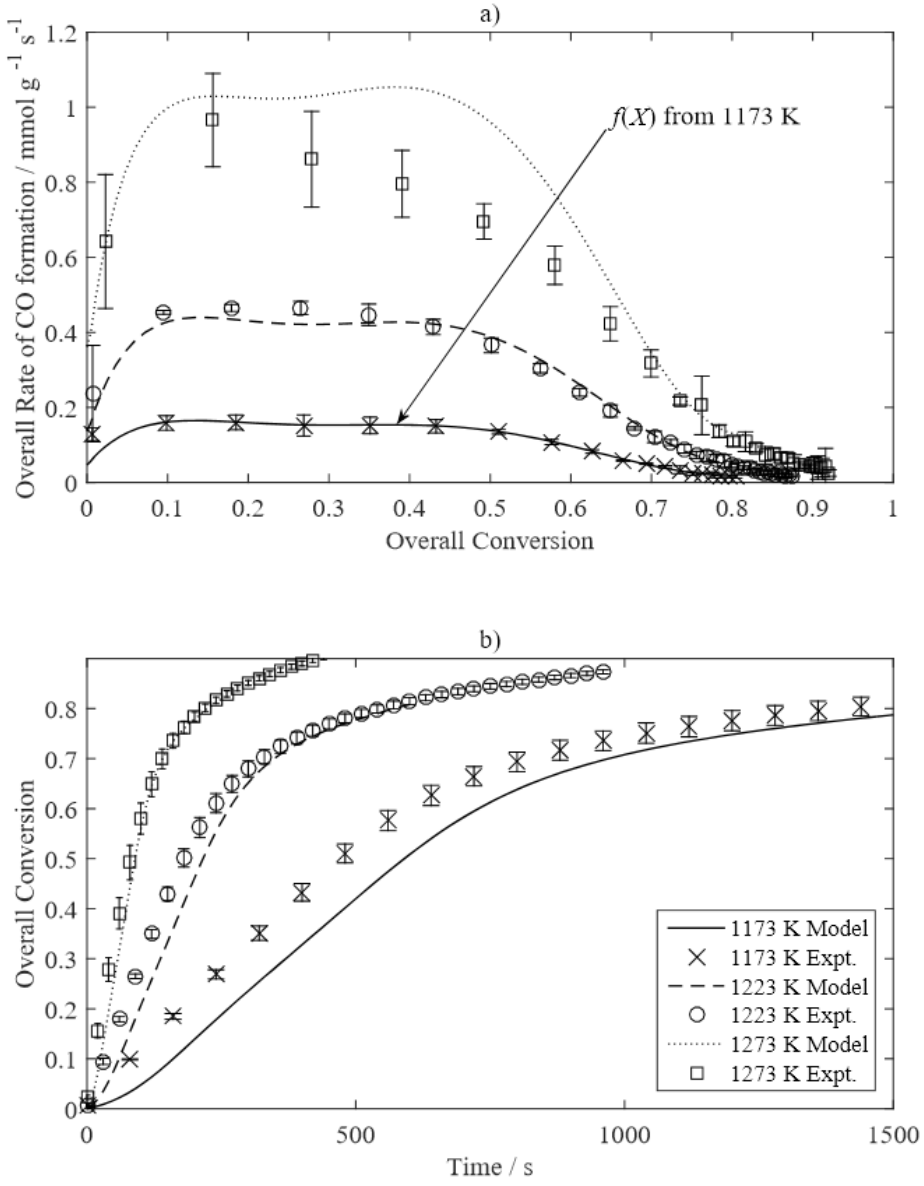

Figure 4.7 Comparison of model results with experimental measurements of the gasification of 0.36 – 0.43 mm activated carbon particles by 30 vol% CO_2 balance N_2. The chars were gasified at three different temperatures: 1173 K (×), 1223 K (○) and 1273 K (□). The error bars attached to the experimental points indicate the 95% confidence interval obtained from a *t* – distribution of three repeated measurements of each sample.

4.4.4Gasification of fuel particles of different sizes

Experiments with lignite char were performed using different sizes of particles (0.60 – 1.00 mm, 1.00 – 1.40 mm and 1.70 – 2.56 mm), at 1073 K, 1123 K and 1173 K. Additional particles with a sieve size of 0.36 – 0.50 mm were used at 1173 K, because at this temperature the kinetics are fast and lead to significant gradients in intraparticle gaseous diffusion in particles of 0.60 – 1.00 mm dia. Hence, in summary, the *f*(*X*) was determined from the measurements at 1073 K on 0.60 – 1.00 mm particles, at 1123 K

on 0.60 – 1.00 mm particles and at 1173 K on 0.36 – 0.50 mm particles. The derived $f(X)$ were then applied to reaction and diffusion in larger particles, at the corresponding temperature. Figure 4.8 compares the overall rate of CO production *vs.* overall carbon conversion from both experiment (points) and theory (line) for lignite chars gasified in 30 vol% CO_2, balance N_2 at 1073 – 1173 K. Judging from the plots of conversion *vs.* time, there is an excellent fit between measurements and model results. The plots of rate *vs.* conversion show deteriorating agreement between experiments and model as the particle diameter increases. Nonetheless, the agreement between model and experiment is satisfactory.

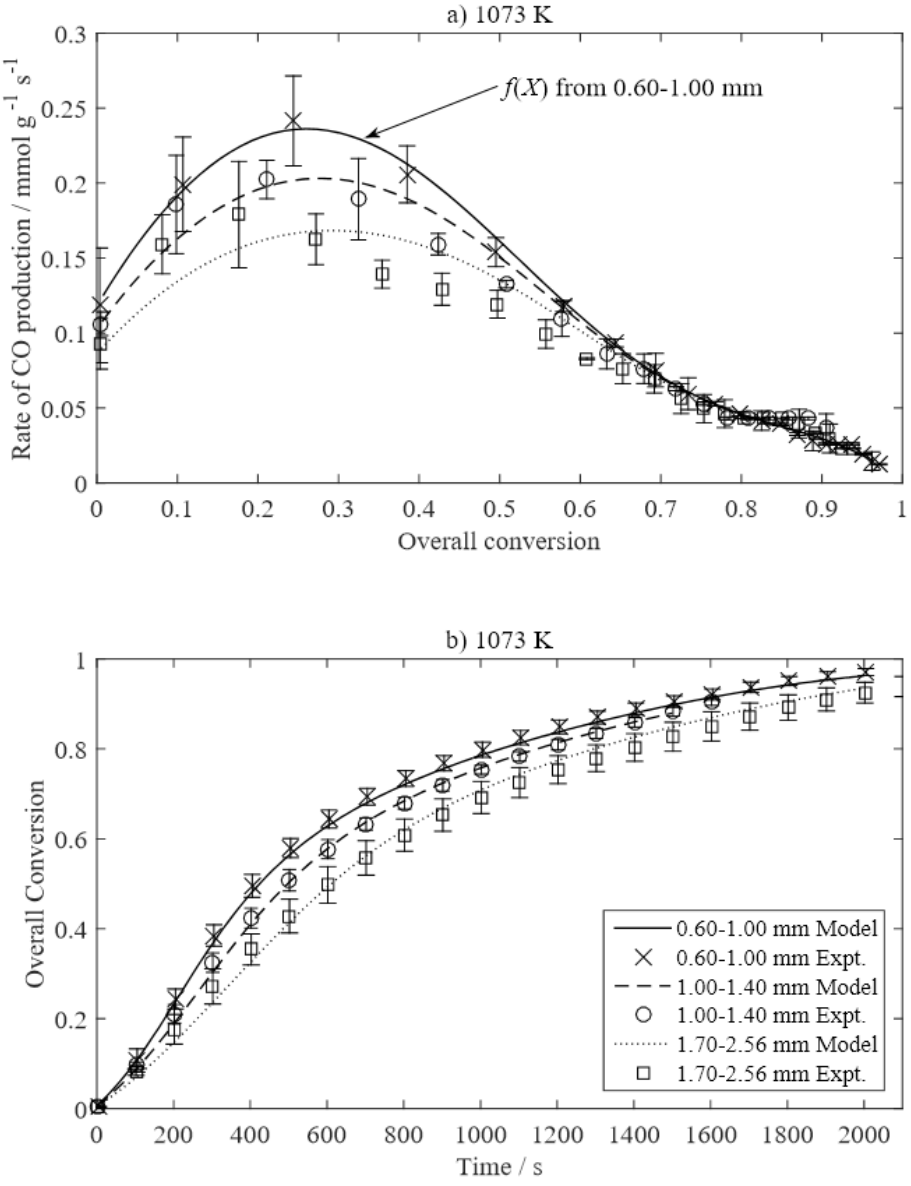

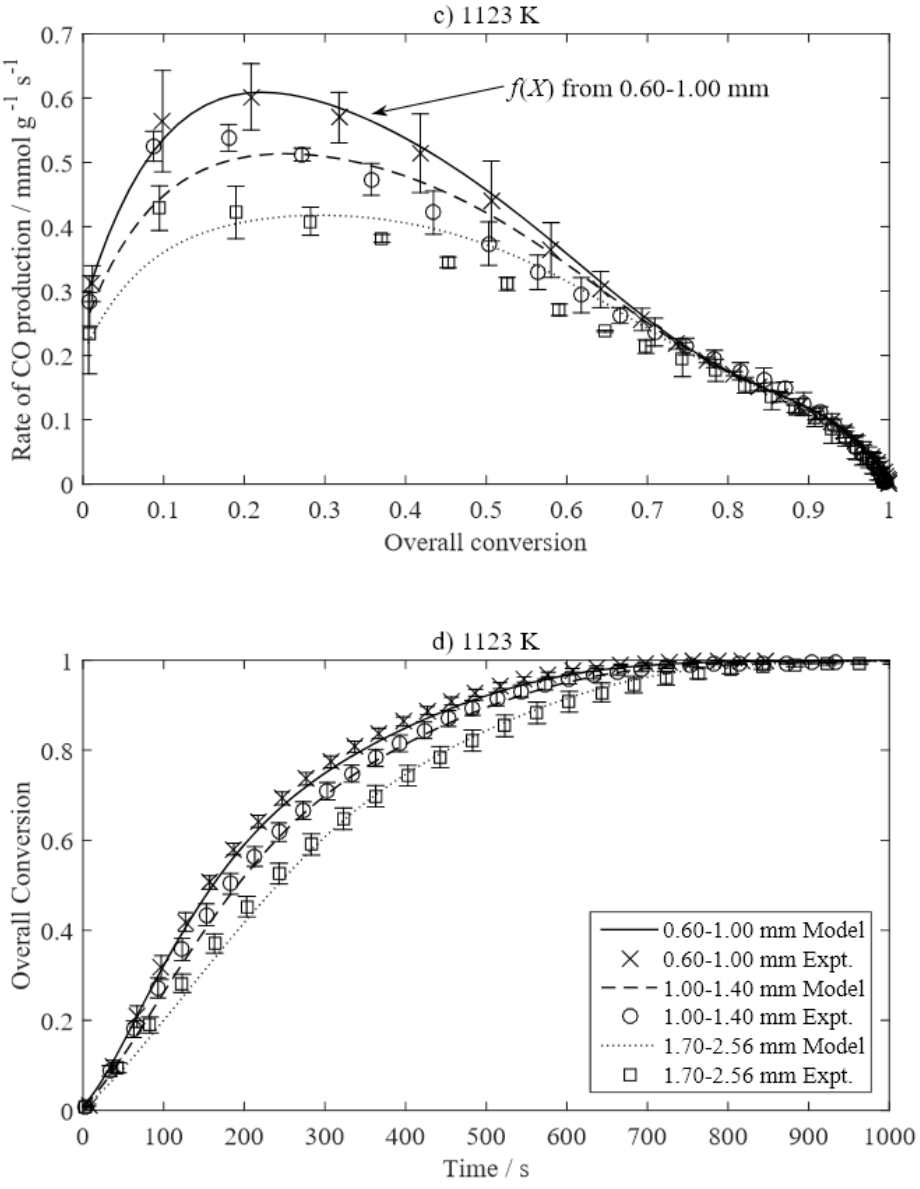
c) 1123 K
Rate of CO production / mmol g-1 s-1
Overall conversion
f(X) from 0.60-1.00 mm
d) 1123 K
Overall Conversion
Time / s
0.60-1.00 mm Model
0.60-1.00 mm Expt.
1.00-1.40 mm Model
1.00-1.40 mm Expt.
1.70-2.56 mm Model
1.70-2.56 mm Expt.

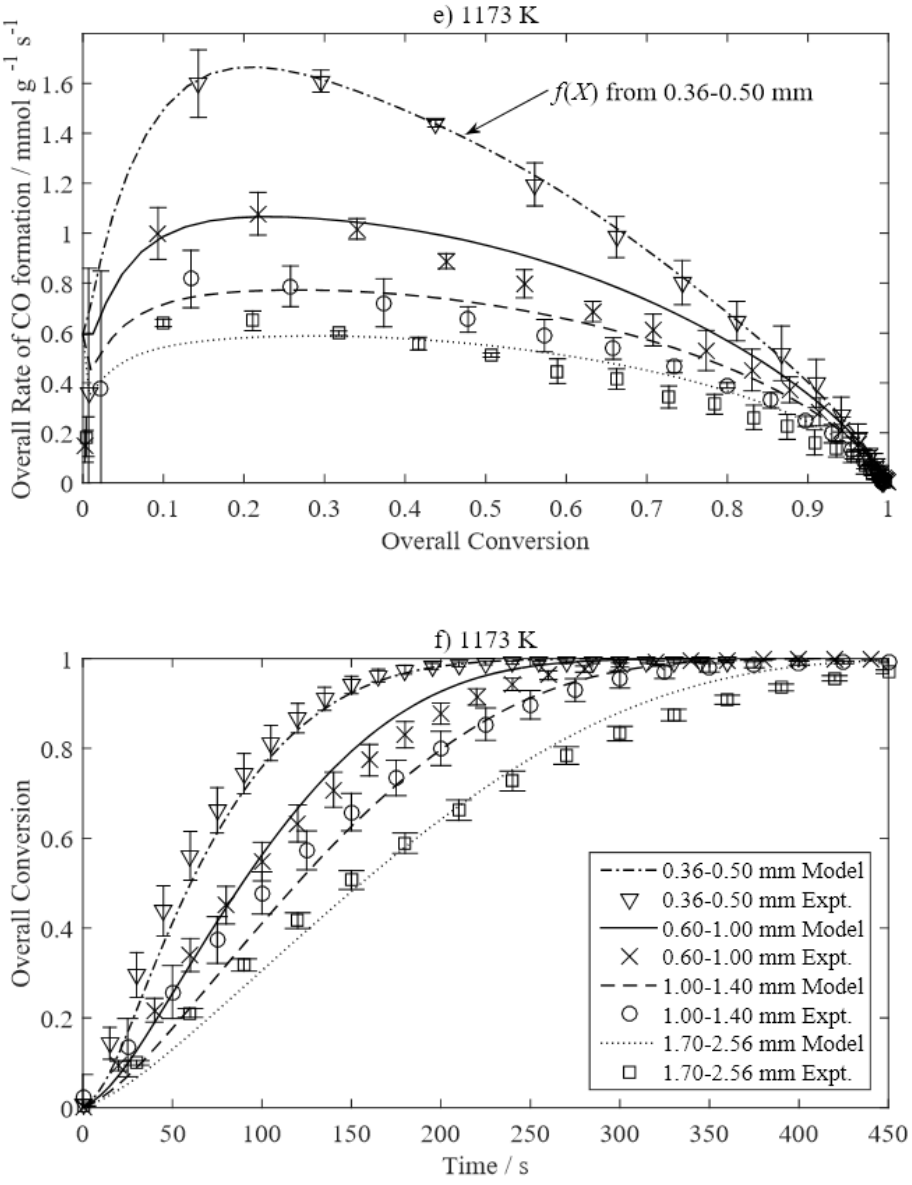

Figure 4.8 Comparison of model results with experimental measurements of the gasification of lignite char by 30 vol% CO_2 balance N_2 at 1073 K, 1123 K and 1173 K. Three different size fractions of lignite char were used at 1073 K and 1123 K: 0.60 – 1.00 mm (×), 1.00 – 1.40 mm (○) and 1.70 – 2.56 mm (□). Additional particles with size of 0.36 – 0.50 mm (∇) were used for 1173 K experiments. The error bars on the experimental points indicate the 95% confidence interval obtained from a *t* – distribution of three repeated measurements of each sample.

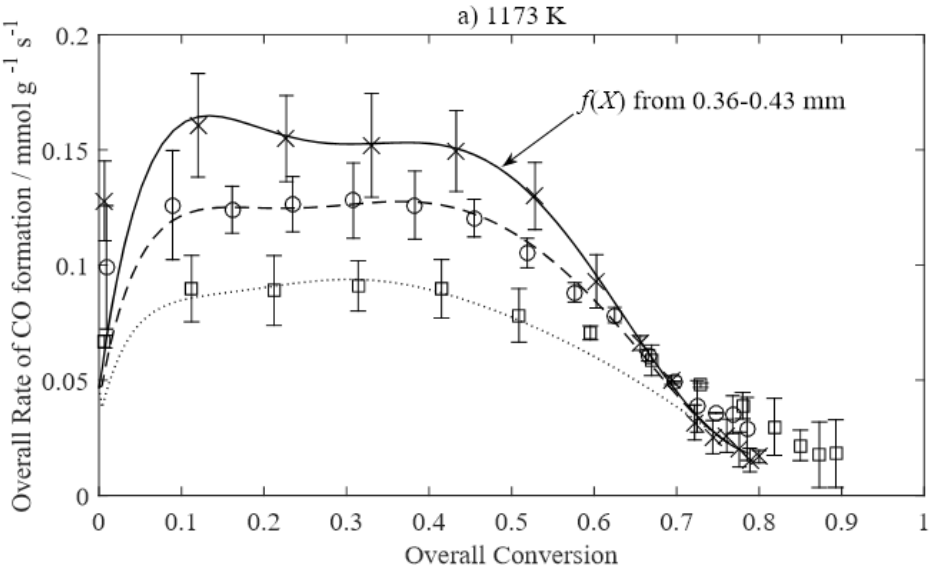
a) 1173 K
Overall Rate of CO formation / mmol g -1 s -1
Overall Conversion
f(X) from 0.36-0.43 mm
0
0.05
0.1
0.15
0.2
0.1
0.2
0.3
0.4
0.5
0.6
0.7
0.8
0.9
1

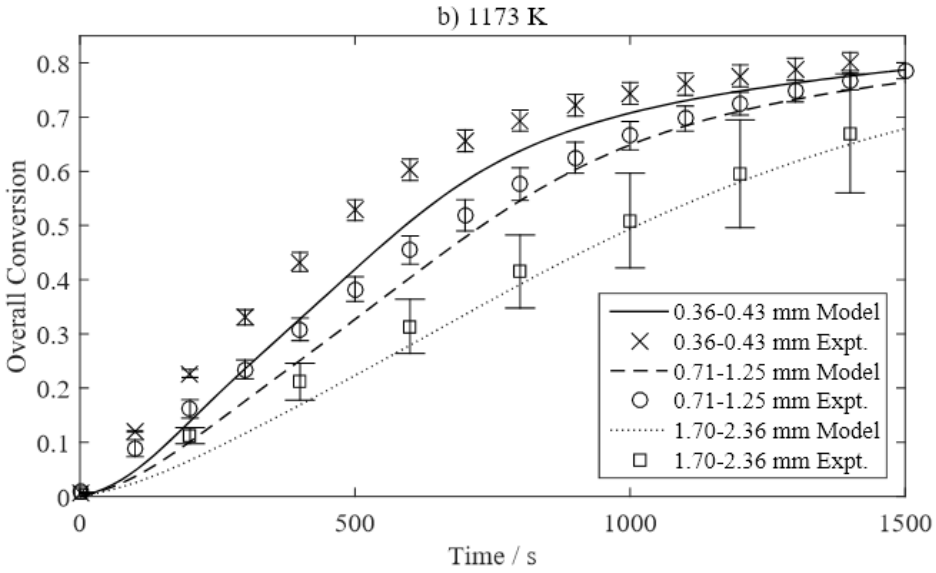
b) 1173 K
Overall Conversion
Time / s
0.36-0.43 mm Model
0.36-0.43 mm Expt.
0.71-1.25 mm Model
0.71-1.25 mm Expt.
1.70-2.36 mm Model
1.70-2.36 mm Expt.
0
0.1
0.2
0.3
0.4
0.5
0.6
0.7
0.8
500
1000
1500

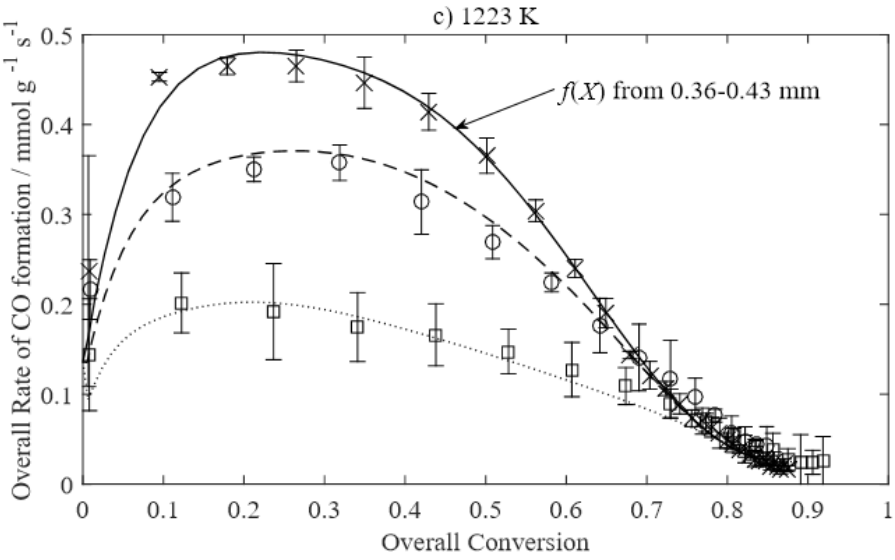
c) 1223 K
Overall Rate of CO formation / mmol g -1 s-1
f(X) from 0.36-0.43 mm
Overall Conversion

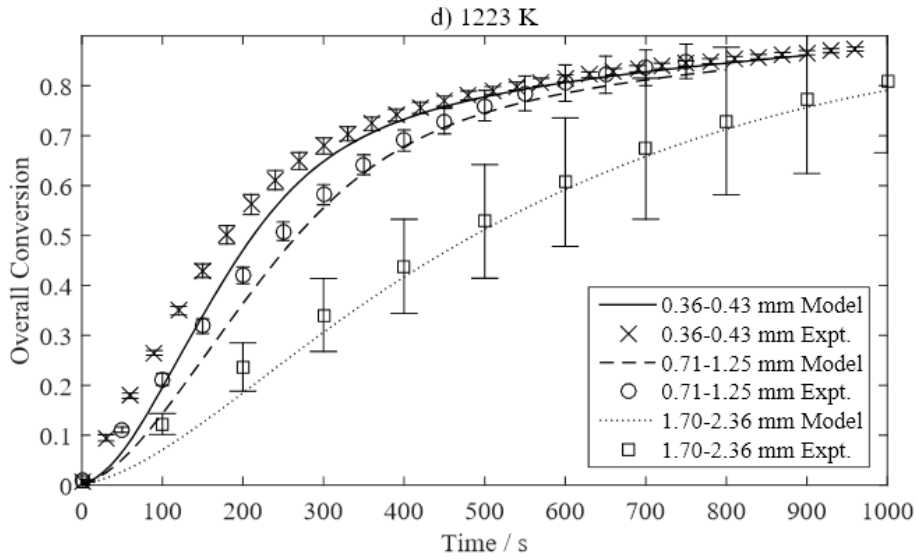
d) 1223 K
Overall Conversion
Time / s
0.36-0.43 mm Model
0.36-0.43 mm Expt.
0.71-1.25 mm Model
0.71-1.25 mm Expt.
1.70-2.36 mm Model
1.70-2.36 mm Expt.

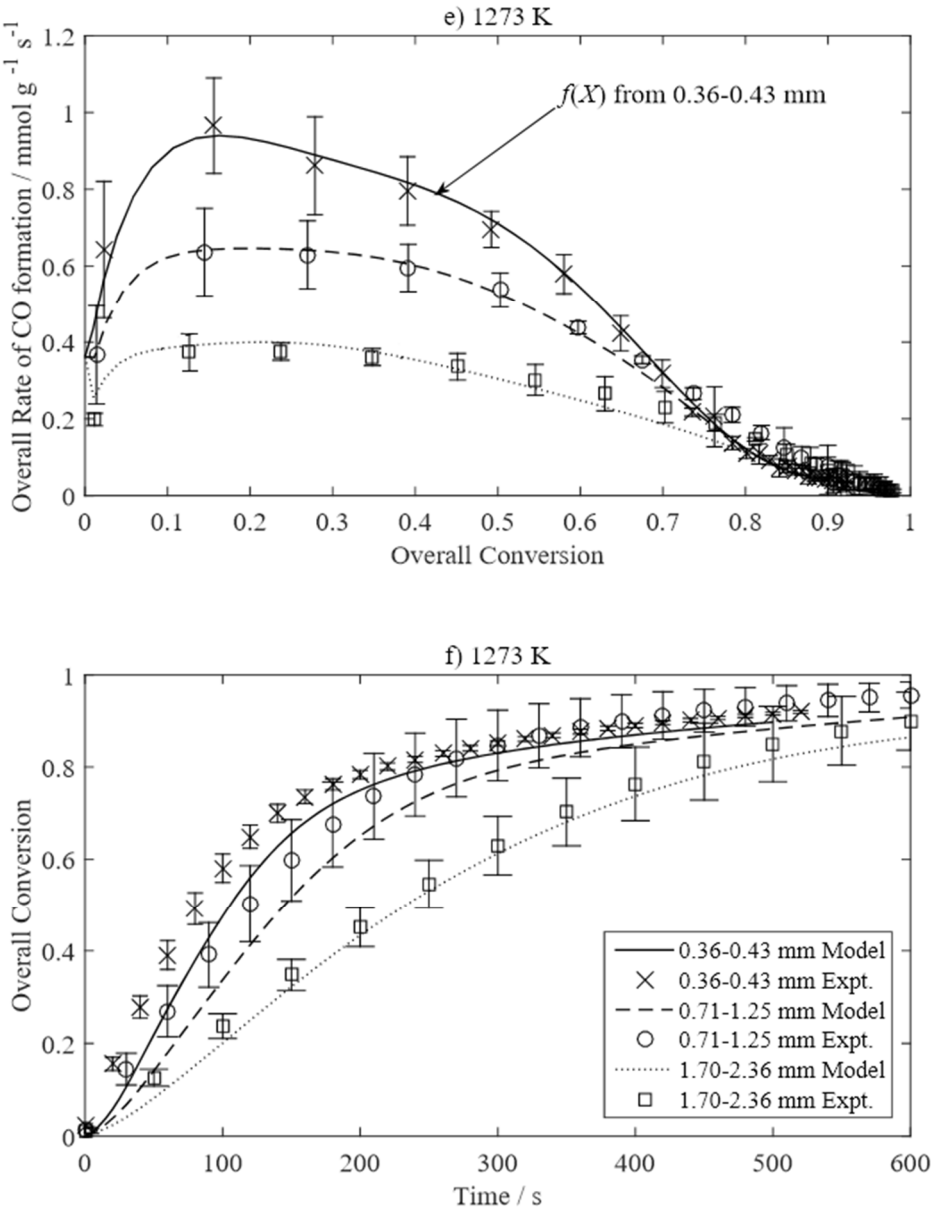

Figure 4.9 Comparison of model with experiment for the gasification of activated carbon by 30 vol% CO_2 balance N_2 at 1173 K, 1223 K and 1273 K. Three different size fractions of activated carbon were used: 0.36 – 0.43 mm (×), 0.71 – 1.25 mm (○) and 1.70 – 2.36 mm (□). The on the experimental points indicate the 95% confidence interval obtained from a *t* – distribution of three repeated measurements of each sample.

Experiments with activated carbon were performed at 1173 K, 1223 K and 1273 K, using particle sieve sizes of 0.36 – 0.43 mm, 0.71 – 1.25 mm and 1.70 – 2.36 mm. At each temperature, the $f(X)$ was determined from the experimental measurements made with particles of sieve size 0.36 – 0.43 mm and applied to the simulations of larger particles, at the corresponding temperatures. Figure 4.9 shows the results. The low reactivity of activated carbon has resulted in noisy measurements and large error bars. Despite this, the figure shows excellent agreement between measurements and the

model predictions up to 60% conversion. Afterward, the rate soon dropped as pores coalesced and internal reactive surface area commenced to fall.

4.5 Discussion

4.5.1 The *f*(*X*) hypothesis

The original *f*(*X*) hypothesis, proposed by Saucedo (2014) and Saucedo *et al.* (2014), assumed that the variation in the rate of reaction due to pore structure changes at any temperature could be modelled by an arbitrary *f*(*X*) function obtained from reaction in the absence of intraparticle gradients in gas concentration at one temperature. One implicit assumption in the original hypothesis was that the solid surface was homogeneous and that all the particle reacted with the same rate parameters. However, there is a significant amount of evidence to indicate that many carbons and chars possess multiple types of active sites with different energetic distribution. For example, Radović *et al.* (1983) suggested that there is a distribution of site activities on the carbon surface: the very active sites might be unavailable for reaction because of the formation of a stable carbon-oxygen complex; the sites of lower activity have difficulty in forming the carbon-oxygen reaction intermediate; and it is the optimum sites that are important, *i.e.*, sites that are both active and available, for the gasification reactivity. Hüttinger & Nill (1990) characterised the energetic surface heterogeneity and extract kinetic parameters for the active sites using temperature-programmed desorption. Considerable work has been done on characterising and modelling the effect the active sites on the carbon reactivity for gasification (Calo & Perkins, 1987; McEnaney, 1991; Xu *et al.*, 2013; Roberts *et al.*, 2015) and oxidation (Montoya *et al.*, 2001; Sendt & Haynes, 2005, 2011; Senneca *et al.*, 2017). In particular, Calo & Perkins (1987) analysed the data from published works based on heterogeneous surface model and showed that the actual behaviour exhibited by any particular set of gasification rate data in the chemically-controlled regime was dependent on the surface heterogeneity, as well as temperature and the relative amounts of CO_2 and CO. They further concluded that there might not be any truly intrinsic rate parameters for the gasification reaction, since the activation energy of the kinetic parameters, *e.g.* k_1 and k_{-1}, are functions of the active site distribution function, which depends on the nature of the char, its thermal history, and perhaps even the history of exposure to certain gaseous species which may adsorb on and/or react with selected portions of the active site distribution. Therefore,

the kinetic rate parameters were often applied within a relatively narrow range of experimental conditions. In the context of this work, the use of an overall activation energy of 247 kJ/mol for the rate parameter c_0k_2 in Eq. (4-5) seems to be an oversimplification, which could mean that the $f(X)$ function determined at one temperature would not be applicable at a different temperature due to the additional change of the "intrinsic" rate resulted from the distribution of active sites.

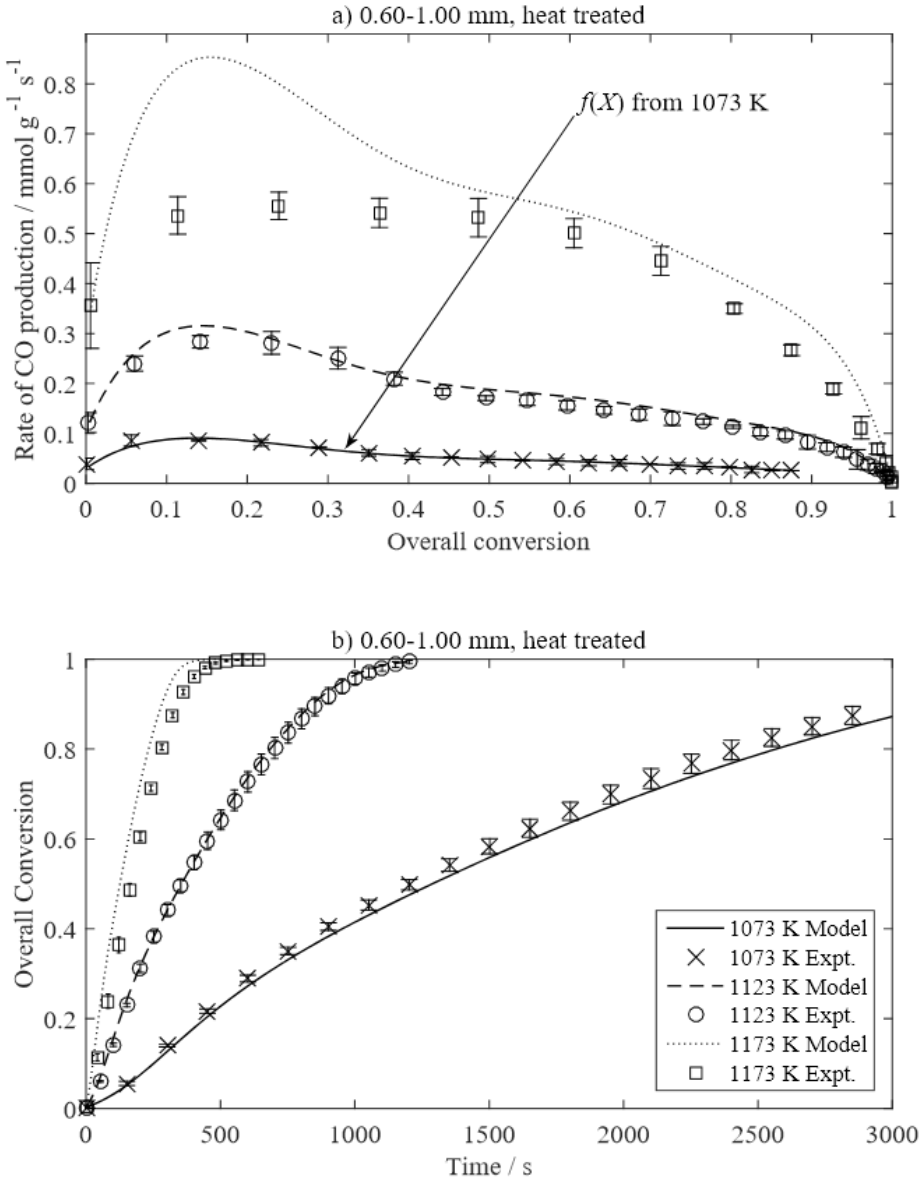

Figure 4.10 Comparison of model results with experimental measurements of the gasification of 0.60 – 1.00 mm lignite char particles, heat treated at 1273 K for 1 hour, by 30 vol% CO_2 balance N_2. The chars were gasified at three different temperatures: 1073 K (×), 1123 K (○) and 1173 K (□). The error bars on the experimental points indicate the 95% confidence interval obtained from a t – distribution of three repeated measurements of each sample.

The results in section 4.4.3 showed that a constant $f(X)$ function obtained from low temperature experiments was relatively poor in predicting the value and shape of the rate *vs.* conversion curve for higher temperature experiments. This might be because both the lignite char and the activated carbon contained multiple types of active sites. To attempt to eliminate the effect of different active sites, the lignite chars were subjected to heat treatment. Previous studies (Hüttinger & Fritz, 1991) have found that c_0 in Eq. (4-5) decreases exponentially with temperature. It was surmised that the reactivity of heat-treated chars might be nearly constant because of a more homogeneous carbon structure (Laurendeau, 1978). In a previous study (Senneca *et al.*, 1998) the chars were treated at 900 – 1200 °C for 1 – 300 minutes, and it was found that their reactivity decreased considerably with increasing temperature and time. Hence the lignite char particles were heat-treated in a sand bed fluidised by a stream of pure N_2 at 1273 K for 1 hour and cooled to room temperature before gasification by CO_2. The results, in Figure 4.10, showed a significant reduction of reactivity compared to Figure 4.6. In order to match the initial rate of reaction at 1073 K, the activation energy of the kinetic parameter c_0k_2 was arbitrarily increased to 317 kJ/mol, a 27 kJ/mol increase due to the thermal deactivation. The figure shows an excellent fit between the model results and experimental measurements at 1073 K and 1123 K. At 1173 K, the shape of the $f(X)$ curve could no longer capture the change of the reaction rate, but it still shows a good agreement between model and experiment when conversion > 0.5. Compared to Figure 4.6, the fit between model predictions and experimental measurements here is better at 1123 K but poorer at 1173 K. Figure 4.11 compares the $f(X)$ curve for both normal and heat-treated lignite char particles and shows a complete change of shape of $f(X)$ curves, suggesting that thermal deactivation of active sites did change the $f(X)$ curve.

Thus, it can be concluded that the model utilising $f(X)$ determined from the measurements on small particles at one temperature (Regime I) could be used for the simulation of larger particles at the same temperature (Regime II) with excellent accuracy; the existence of multiple types of active sites prevents, in accurate work, the use of $f(X)$ across temperatures due to the change of rate contributions from each species. However, even if it is applied across a range of temperatures, the agreement between model and experiment is still reasonable.

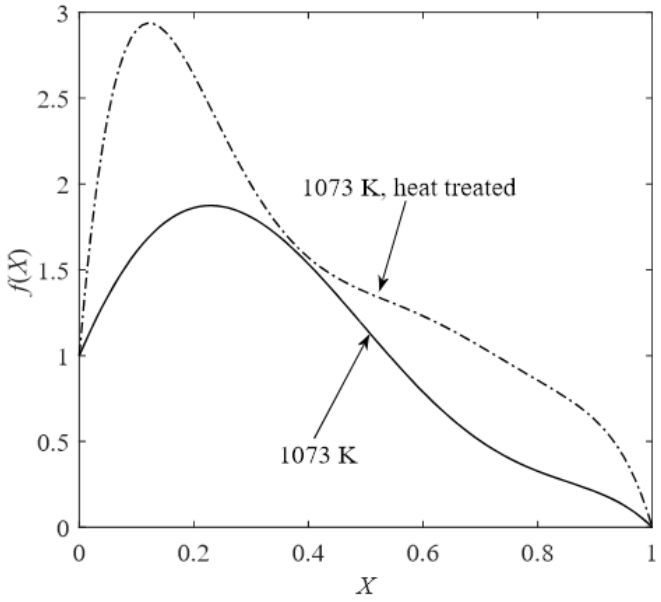

Figure 4.11 The $f(X)$ function curves for the normal 0.60 – 1.00 mm lignite char particles and the heat treated (1273 K, 1 hour) particles fitted from the gasification measurements at 1073 K by 30% CO_2 balance N_2.

4.5.2The fuel particles

The lignite chars contained very large pores and cavities that could potentially act as feeder pores to the small pores. The reacting CO_2 probably diffused quickly through the large feeder pores, but diffused more slowly into the smaller pores which contained most of the surface area. Reducing the size of a char particle, *e.g.* by grinding, would have little effect on mass transfer, until the particles were small enough to eliminate the large pores (Scott, 2004). On this basis, the char particle could be viewed as an agglomerate of several small particles with large voids in between. Thus, the mean particle diameter of the char particle, obtained from the particle size distribution measurement, might not be a realistic reflection of the true particle size in mass transfer. In addition, the particle diameter used in the model was estimated from the geometric mean of the sieve sizes, which introduces an approximation. Therefore, the uncertainties in initial particle diameters used in the model might be significant. In practice, changing the particle diameter had no significant effect on the predicted rate of reaction for particles in Regime I, as expected. As the reaction of the particles moved to Regime II, the change of particle diameter had a larger effect on the predicted rate, *e.g.* smaller particle diameters gave higher rates and larger diameters resulted in lower rates. Therefore, it was possible to adjust the particle diameter used in the model to match the

measurements of the rate. However, the shape of the overall rate *vs.* conversion curve could not be altered by changing the particle diameter used in the model.

For lignite chars, an average of 165 nm from the measured mean pore diameters was used to give the results shown in section 4.4.3 and 4.4.4. However, the pore diameter of activated carbon, 133 nm, determined by the mercury porosimetry in Table 4.3, did not give a good fit between experimental measurements and the model results. The value of the pore diameter for activated carbon was varied during the fitting process. As a result, a pore diameter in the relatively narrow range of 20 – 40 nm gave the best fits, as shown in Figure 4.7 and Figure 4.9. The equation for diffusivity – Eq. (3-7) shows that the Knudsen diffusivity, D_K, is proportional to the pore diameter. In mass transfer controlled regime, the overall interpolated diffusivity, D_A, is ~ D_K. Slight change in pore diameter will alter the intraparticle diffusion process, and thus the rate of reaction. In kinetically controlled regime, the reaction becomes insensitive to the change in pore diameter unless the change is so significant that the reaction becomes diffusion limited. In the next Chapter, section 5.5.3 included a simulation study of the sensitivity of the shape of the rate *vs.* conversion curve to pore diameter, where the shape of the apparent $f(X)$ function, *i.e.* reaction rate normalised by the initial rate *vs.* conversion, can change significantly due to change in pore diameter. Therefore, the use of a single average pore diameter in the model might be an oversimplification in precise work, which might have contributed to the increasing disagreement between the model and the experimental measurements across temperature shown in Figure 4.6 and Figure 4.7. In addition, the use of Eq. (4-12) for the evolution of the pore diameter with conversion merits further discussion. The simplification of assuming a non-overlapping pore structure during the derivation of Eq. (4-12) is of course unrealistic for coal chars. For a real char particle, as the gasification of the char proceeds, the pores of the particle enlarges at first then coalesces and the intraparticle diffusion resistance reduces accordingly. Without considering the overlapping volume between pores, the model might have overestimated the increase in the pore diameter compared to the actual case for the same increase in conversion, hence overestimating the reduction in the mass transfer resistance. The effect of overestimating the increase in pore diameter should make no difference if the reaction is initial controlled by the chemical kinetics and will remain so as gasification proceeds. However, if the reaction is not in kinetically controlled regime at the start, the model will overpredict the increase in pore diameter thus the reaction rate, which would contribute to the increasing discrepancy between the

model and the experimental measurements observed at higher temperature and for larger particles in Figure 4.6 to Figure 4.9.

Lignite char was very reactive when gasified with CO_2, whilst the activated carbon was much less so. Comparing the rates of reaction of the smallest particles (lignite char: 0.36 – 0.43 mm and activated carbon: 0.36 – 0.50 mm) at 1173 K, the peak rate of gasification of lignite char was ~ 10 times that of the activated carbon. Since activated carbon had ~ 5 times more BET area than lignite, this difference in rate indicates that the correlation between BET area and reactivity is poor. It also meant that the mathematical pore models predicting the rate of reaction based on total surface area would have limited application in simulating the reaction and diffusion inside the particles during char gasification. The reason for these differences in kinetics, apart from the form of the carbon present in the fuel particles, might be that the lignite, a low rank coal, tends to contain more metal elements than does activated carbon. The metal impurities, especially the alkali metals, *e.g.* potassium, sodium and calcium, could catalyse the reaction of carbon. Saucedo (2014) reported that calcium, presumably as CaO, was found to catalyse the rate of reaction in the later stages of conversion (*i.e.* $X > 0.4$) increasing the rate by as much as 25% over untreated char. Experiments performed in the present work, using scanning electron microscopy coupled with electron diffraction scattering (SEM-EDS), have confirmed that i) lignite char contains Na, Ca and Mg and ii) activated carbon contains Na, Ca and Mg. Although this does not unequivocally prove the difference is due to the metals loading, it does confirm the higher content of potentially catalytic metals in the lignite.

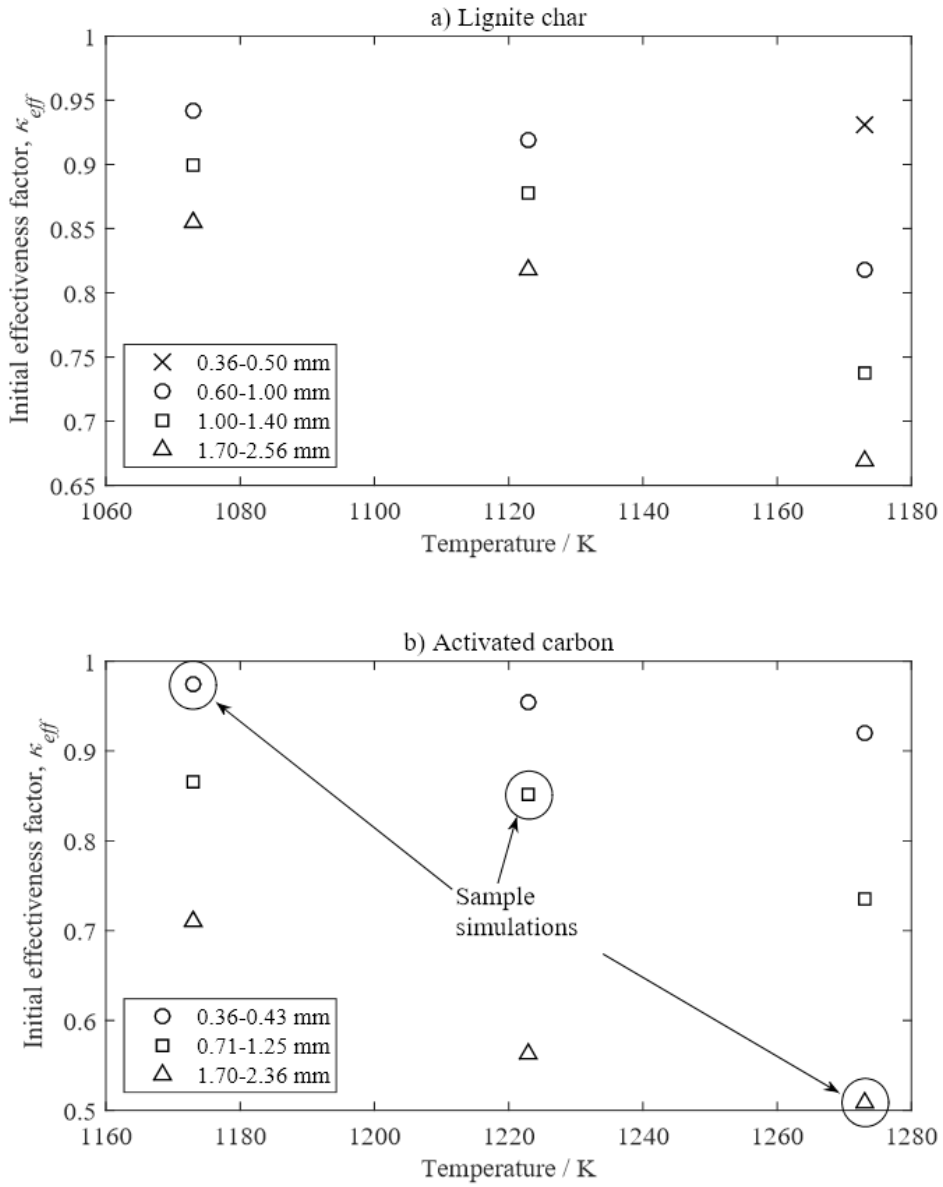

Figure 4.12 Initial effectiveness factor of the samples: a) lignite char particles at 1073 K, 1123 K and 1173 K; b) activated carbon at 1173 K, 1223 K and 1273 K. Three samples, highlighted in b), are selected for comparison.

Figure 4.12 shows the initial effectiveness factor calculated for the experiments of each particle size at different temperatures using $\kappa_{eff} = \tanh(\gamma\varphi/\varphi^*)$, which was applicable to a catalytic reaction following a Langmuir-Hinshelwood mechanism (Meenakshi Sundaram, 1982). Here, κ_{eff} is the effectiveness factor, φ is the Thiele modulus and the detailed definitions of the correction factor γ and the normalised Thiele modulus φ^* were summarised in Appendix E. Figure 4.12 confirms that the smallest particles used at each temperature were all in the kinetically-controlled regime (Regime I), because their κ_{eff} was close to unity. As both the temperature and the particle size increase, the effectiveness factor drops, indicating a growing intraparticle

mass transfer limitation to the rate of reaction (Regime II). As the diffusional flux increases during reaction due to growing pores, the effectiveness factor will gradually increase with conversion. To visualise the profiles of conversion, gas concentration, pressure and temperature and compare the model results in different regimes, three experiments of the activated carbon particles were selected for further simulation study: i) 0.36 – 0.43 mm dia. particles at 1173 K, $\kappa_{eff} = 0.97$ (Regime I); ii) 0.71 – 1.25 mm dia. particles at 1223 K, $\kappa_{eff} = 0.85$ (Regime II); iii) 1.70 – 2.36 mm dia. particles at 1273 K, $\kappa_{eff} = 0.51$ (well within Regime II).

4.5.3 Local conversion

Figure 4.13 shows the simulated profiles of local conversion *vs.* dimensionless radius for the three experiments selected in Figure 4.12(b), where the gradient of the conversion profile becomes steeper in particles experiencing severer intraparticle mass transfer limitation, as expected. Moving from a) to c), the initial gradient becomes steeper when the effectiveness factor is lower. As the overall conversion increases, the resistance to intraparticle mass transfer falls because of the opening and coalescence of pores, hence the gradient of conversion gradually reduces. Plot b) shows that even when the effectiveness factor is as high as 0.85, there is a difference of 0.2 – 0.3 in conversion between the surface and the centre of the particle.

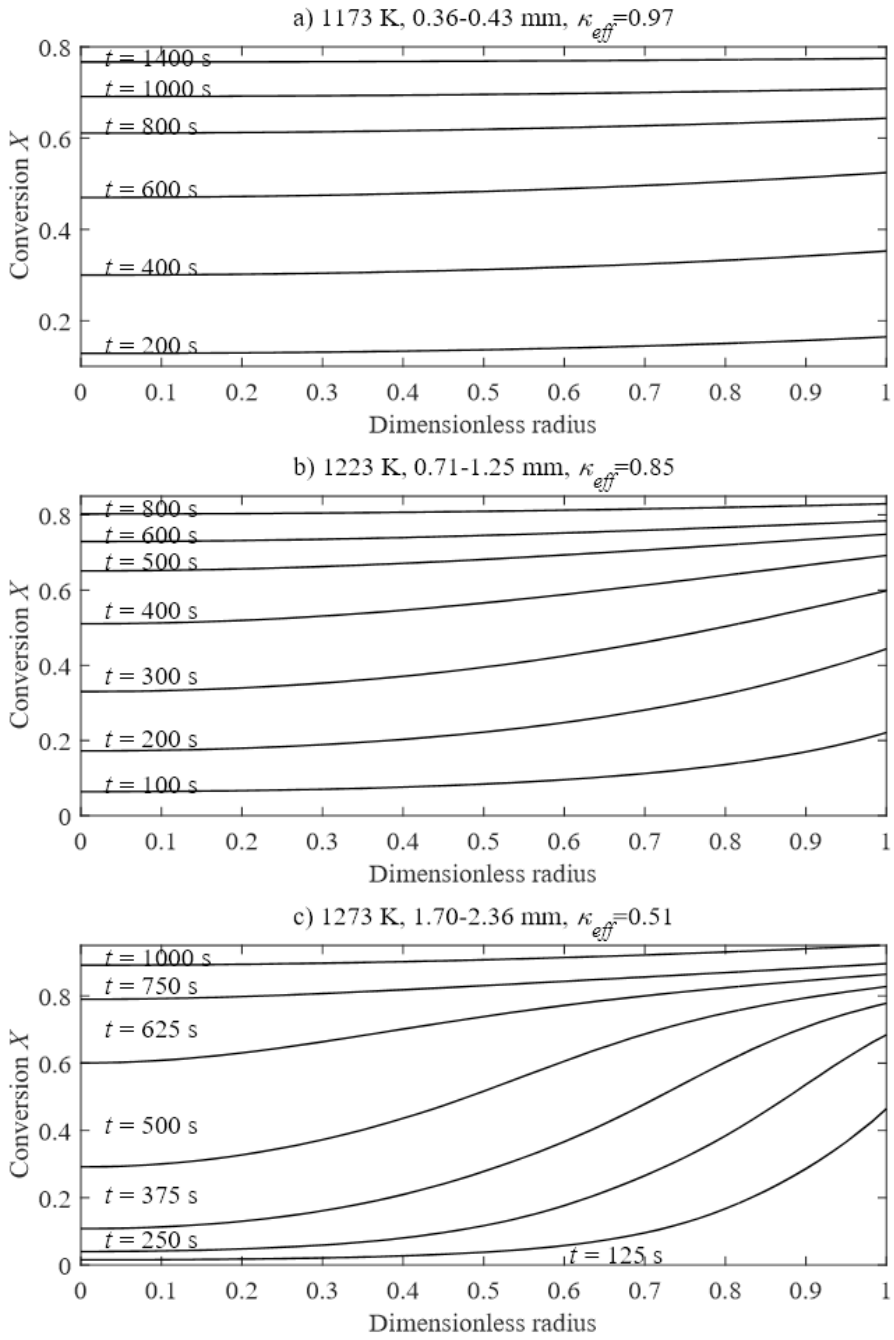

Figure 4.13 Local conversion profile of three different sizes of activated carbon particles gasified by 30 vol% CO_2 balance N_2 at various temperature.

4.5.4 Gas concentration and total fluxes

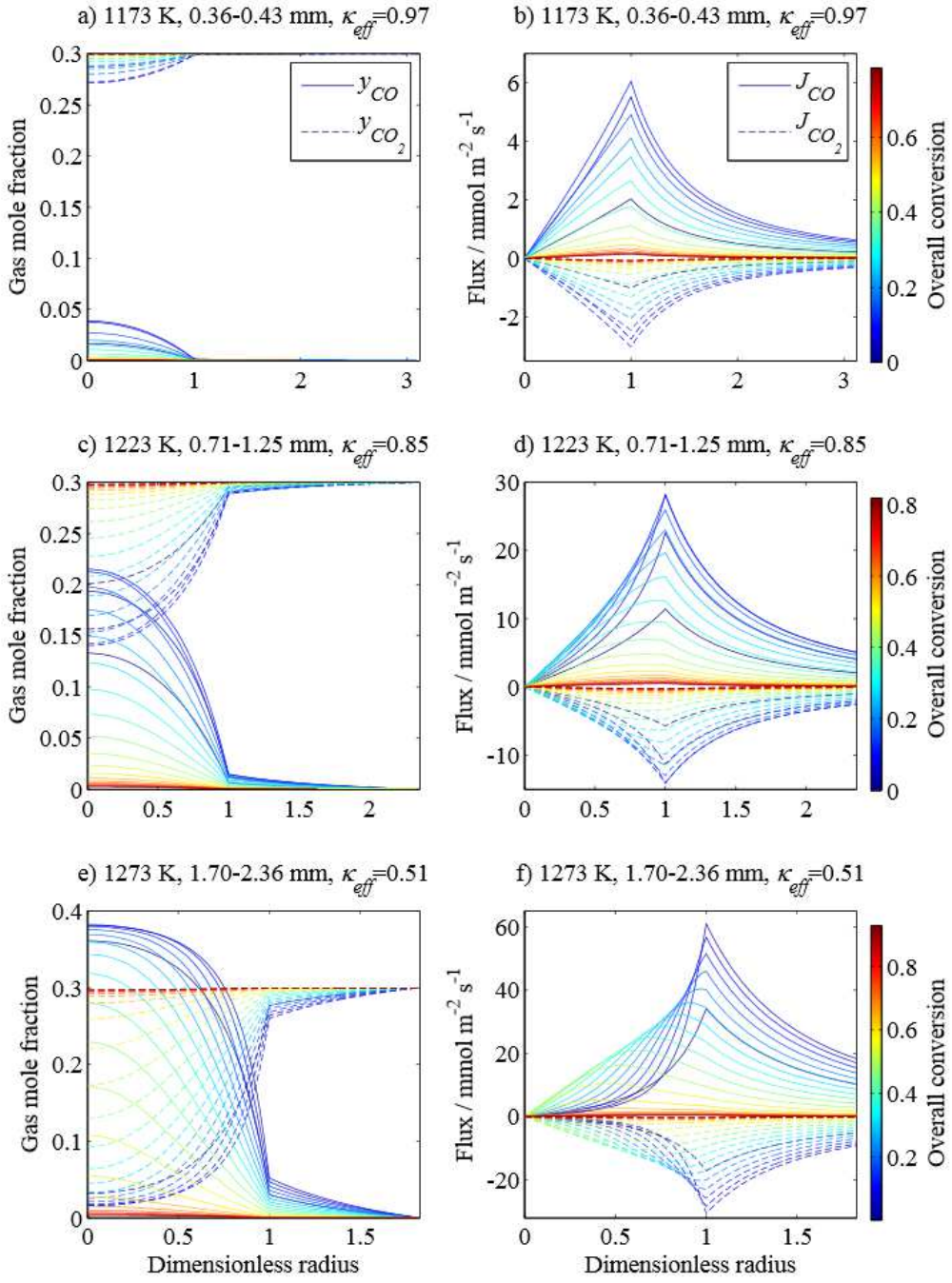

Figure 4.14 Model predicted profiles of gas concentration and total flux of activated carbon particles gasified by 30 vol% CO_2 balance N_2. Radius 0 – 1 is inside the particle; radius > 1 is outside the particle. A positive value of flux means the direction of the flux is pointing outwards from the centre, and a negative value means the flux is directed inwards.

Figure 4.14 shows three sets of simulations of the gas concentration and total fluxes with radial distance from the centre of the particle at different overall conversions. Moving vertically from a) to e), the initial gradient in concentration of gas becomes steeper, meaning that the internal mass transfer limitation is severer for bigger

particles at higher temperature. At the start of the reaction (X < ~ 0.2), the pores open up, the porosity increases and reactive surface area grows. Thus, the rate of carbon gasification increases, which reduces the concentration of CO_2 and increases that of CO. The total fluxes of CO_2 and CO increase as a result of the higher gasification rate. As conversion increases (X > ~ 0.2), the pores start to coalesce with each other and the reactive surface area falls. The rate of reaction also drops, resulting in decreases in total fluxes. The concentration of CO_2 then increases while that of CO drops. Similar trends can also be observed for pressure and temperature variation, discussed in section 4.5.6.

Moving vertically from plot a) to e), the figure also shows that the boundary layer thickness relative to the particle diameter δ/r_p reduces: a) ~ 2.12; b) ~ 1.36; c) ~ 0.83. This is because the Sh_{EMCD}, appeared in Eq. (3-31) in Chapter 3, is proportional to $r_p^{0.48}/T^{0.5}$, where the temperature dependence comes from the diffusivity $D_{B,23}$, and the large increase in r_p has dominated over the influence of the relatively small change in T. In addition, the gradient of external gas concentration increases as the effectiveness factor reduces as expected.

4.5.5 Change in particle diameter

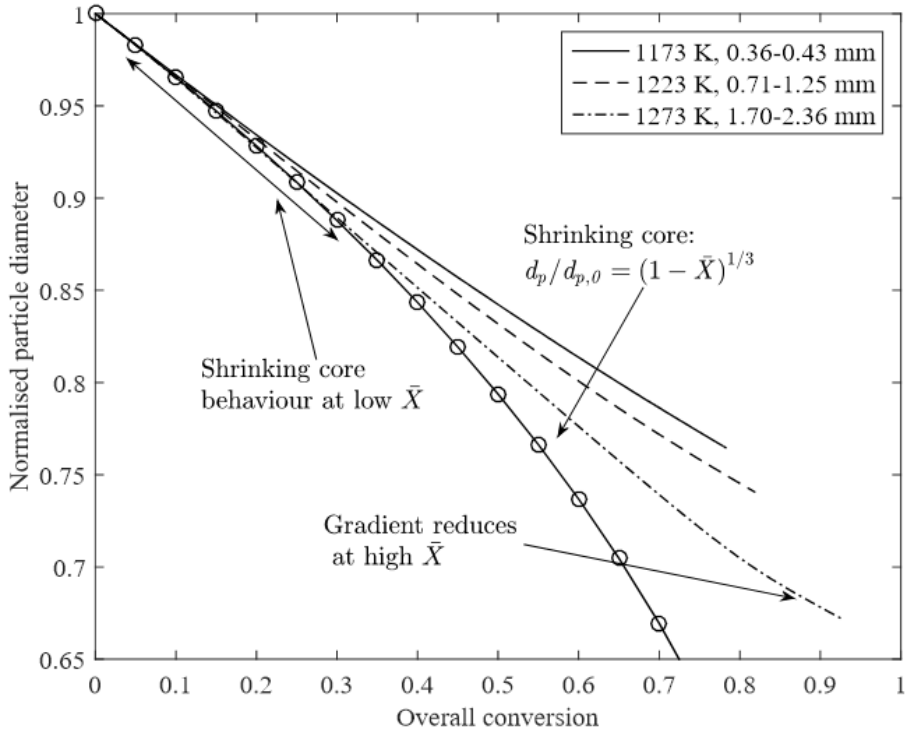

Figure 4.15 Model predicted change of particle diameter for three different sizes of activated carbon particles gasified by 30 vol% CO_2 balance N_2 at various temperature.

Changes in particle diameter with conversion, calculated from Eq. (4-15), are shown in Figure 4.15. They are compared with the curve for a shrinking core model, where $d_p/d_{p,0} = (1 - \bar{X})^{1/3}$. The highlighted area in the figure shows that all three cases had some degree of shrinking core behaviour when conversion was low. The particle of activated carbon, 1.70 – 2.36 mm dia., at 1273 K displays the shrinking core behaviour up to 30% conversion while the two other cases diverge from the shrinking core curve after a conversion of 10%. As conversion increases and pores open up, the gas concentation gradient within the particle flattens and the rate of particle shrinking reduces. At high conversions ~ 0.8, the rate of particle shrinking further reduces as indicated in the figure.

It has been suggested that a carbon particle would start to shrink when the porosity at the surface reached ~ 0.8 during combustion in air (Gavalas, 1980). This corresponds to a conversion of ~ 0.7 at the particle surface for activated carbon particles. However, Figure 4.15 shows that all three particles start to shrink at the beginning of gasification. Looking at the conversion profiles in Figure 4.13, none of the three simulations gave such a high conversion as 0.7 at the surface when gasification had just started.

4.5.6 Pressure and temperature variation

Figure 4.16 shows the predicted profiles of pressure for the three sets of simulations, calculated using Eq. (3-3) of the CPIM model in chapter 3. As the rate of reaction passes through a maximum at about 15% – 20% conversion, the pressure profile reached a maximum as shown in the figure. However, the effects are slight and would be undetectable, experimentally. The magnitude of the difference in total pressure between the inside of a particle and the outside is small, *e.g.* a maximum ~ 14% of the bulk pressure for activated carbon gasified at 1273 K and 30% CO_2.

Since the gasification of carbon with CO_2 is endothermic, the temperature inside the particle will always be lower than the outside. The differences in temperature between the bulk and the centre of the particle increased with increase in particle sizes and temperature as the influence of intraparticle mass transfer became more significant, but the overall magnitude was very small. The model predicted a maximum temperature difference of ~ 2°C for activated carbon gasified at 1273 K and 30% CO_2. This value is in line with the conclusion by Scott (2004) that the temperature difference

between the particle and the bed was < 4°C, when a reactive char was gasified at 1273 K in 100% CO_2. In addition, the model showed that the temperature gradient across the particle was small, which also agrees with the isothermal assumption used in many gasification studies.

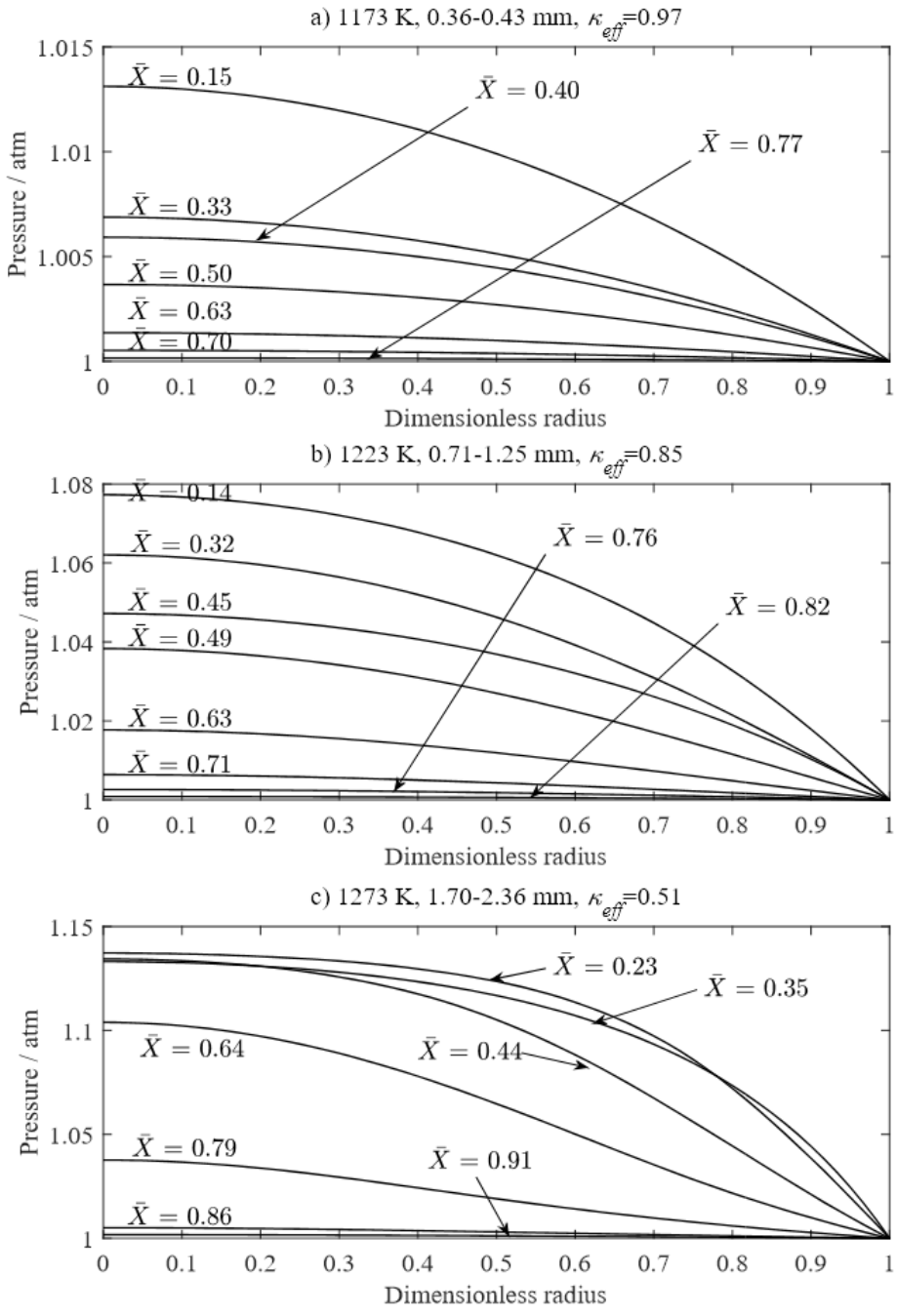

Figure 4.16 Model predicted pressure profiles for three different sizes of activated carbon particles gasified by 30 vol% CO_2 balance N_2 at various temperature.

4.6 Conclusions

It has been proposed that a simple arbitrary function $f(X)$, determined from experimental measurements of rate *vs.* conversion in the kinetically-controlled regime, could be used in place of mathematical pore models, to describe the evolution of pore structure during a reaction influenced by intra-particle gas mass transfer. The reaction and diffusion model developed in Chapter 3 using the Cylindrical Pore Interpolation Model for intraparticle mass transfer, the Stefan-Maxwell equations for external mass transfer and the equations of energy were applied here together with Ergun's kinetic rate equation to test the applicability to the gasification of char particles with CO_2.

Two different fuel particles were used in the experiments, where the lignite chars were ~ 10 times more reactive than the activated carbon particles even though the latter had a pore area ~ 5 times bigger than the former. The results show that for the gasification of chars, the $f(X)$ predicts the rate of reaction of particles of various sizes well, all being at the same temperature. However, for chars and gasification at least, an $f(X)$ evaluated at one temperature does not predict experimental measurements perfectly at other temperatures, possibly because there are contributions from multiple types of active sites within the particles. Heat treatment was applied to the lignite char particles in order to eliminate the effect of different active sites, which enabled a better fitting between the model and the experiments across different temperatures. Hence, the application of the $f(X)$ function across temperature did seem to be affected by the multiple types of active sites during char gasification.

The significance of this research is that the $f(X)$ hypothesis presents a simple solution for modelling the evolution of pore structures during reactions of particles. Instead of using complicated mathematical pore models, one could determine the $f(X)$ from the experiments used for kinetic studies. This idea could be further applied to many other gas-solid reactions that involve change of pore structures during reactions. However, one needs to be aware that the presence of multiple types of active sites could lead to incorrect predictions (multiple sites are also not reflected in most published pore models).

Chapter 5 Using an experimentally-determined model of the evolution of pore structure for the calcination of cycled limestones

5.1 Introduction

In Chapter 4, it was concluded that the application of the $f(X)$ concept to the gasification of chars by CO_2 suffered the complication of there being multiple types of active sites for adsorption on the surface of char so that a single $f(X)$ determined from experimental measurements at a low temperature was unable to fit satisfactorily to all the measurements made at a substantially higher temperature. Accordingly, to investigate the basic hypothesis that a gas-solid reaction can be characterised by $r = g(C_i, T, P) \times f(X)$, it is important to identify a solid which is unlikely to contain sites which vary in relative activity with temperature. In addition, one important class of non-catalytic gas – solid reactions not touched on yet is where a solid product is laid down in the pores. The conversion of calcium carbonate to calcium oxide via calcination reaction does not involve gas adsorption as a rate-controlling process and the product CaO will build up in the newly formed pores, thus calcination of limestone is a potential candidate for the study. Of course, virgin limestone ($CaCO_3$) is almost non-porous, and the calcination reaction usually follows the Shrinking Core Mechanism (SCM) (Dennis & Hayhurst, 1987; García-Labiano *et al.*, 2002), unsuitable for the application of the $f(X)$ concept. However, limestones which have been successively calcined to CaO and carbonated in CO_2 back to $CaCO_3$ many times, present a different type of porous solid, which can be described by the Continuous Reaction Model (CRM). Such particles are created when raw limestone particles have been subjected to a history of cycling between the calcined and carbonated states in a fluidised bed or a fixed bed reactor. This typically would occur when using such Ca-based materials for removing CO_2 from the flue gas of plants such as those producing electricity, cement or steel in proposed schemes for carbon capture and storage. In those cases, the recarbonation stage is never

complete and so after many cycles, the starting, carbonated material is, in fact, quite porous and so provides an appropriate candidate for testing the $f(X)$ hypothesis.

The study in this chapter was therefore to examine if the $f(X)$ concept could be applied to such a type of reactions, where the solid product was formed in the pores using calcination as an example for different particle sizes and over a range of temperatures. In addition, the evolution of the pore structure during calcination of limestone particles will be different compared to the gasification of chars. A success in modelling the calcination of limestone with the reaction and diffusion model developed earlier would significantly expand the potential application of the model. The content of this chapter has been published (Dai *et al.*, 2016b).

5.2 Experimental methods

5.2.1 Materials

The gases used in the experiments were N_2 ($\geq$ 99.9 vol%, oxygen $\leq$ 2 ppmv) and CO_2 ($\geq$ 99.8 vol%). All gases were supplied by either BOC or Air Liquide. Natural, uncrushed silica sand (fraction C, David Ball Group plc., dry), sieved to 355 – 425 μm, was used as a fluidised bed material. The density of the non-porous sand particles was ~ 2690 kg m^{-3}. Two types of limestone particles were used: (i) a Spanish limestone (Compostilla) after 8 cycles of calcination and carbonation, and (ii) a British limestone (Purbeck) after 6 such cycles. The chemical compositions of the corresponding virgin limestones are shown in Table 5.1. The cycling of the limestone particles was conducted in a bed of sand fluidised by 15 vol% CO_2 balance N_2 at 1 bar. The limestone particles were calcined at 1173 K for 10 minutes and then carbonated at 923 K for 10 minutes. Here, the temperature at which a partial pressure of CO_2 of 0.15 bar was in thermodynamic equilibrium with a mixture of CaO and $CaCO_3$ was calculated to be 1053 K (Barin & Platzki, 1995). The resulting carbonated particles were cooled in a desiccator and then were sieved from the sand. Two sieve size fractions were used in the experiments for each type of limestone: 710 – 850 μm and 1400 – 1700 μm. These sizes were selected in order to recover the cycled particles effectively from the sand and to compare the theoretical predications across different particle sizes. The number of cycles was chosen so that the conversion of CaO of the limestone during a particular cycle was close to that of the previous cycle, as shown in Figure 5.1, but not so many

that the pore area and volume had been markedly destroyed by sintering. After cycling, the internal pores of the limestone, even at the start in the fully-carbonated state, could be macro-pores (> 50 nm) so that the calcination probably occurred continuously throughout the entire particle if it was not limited by heat transfer.

Table 5.1 Composition of the fresh limestones in wt%.

	Ca	Fe	Mg	Al	K	Mn	Si	S	Zr	Ti
Compostilla	89.7	2.5	0.76	0.16	0.46	0	0.07	0	0	0.37
Purbeck	97.67	0.49	0.61	0.21	0.09	0.14	0.65	0.11	0.05	0

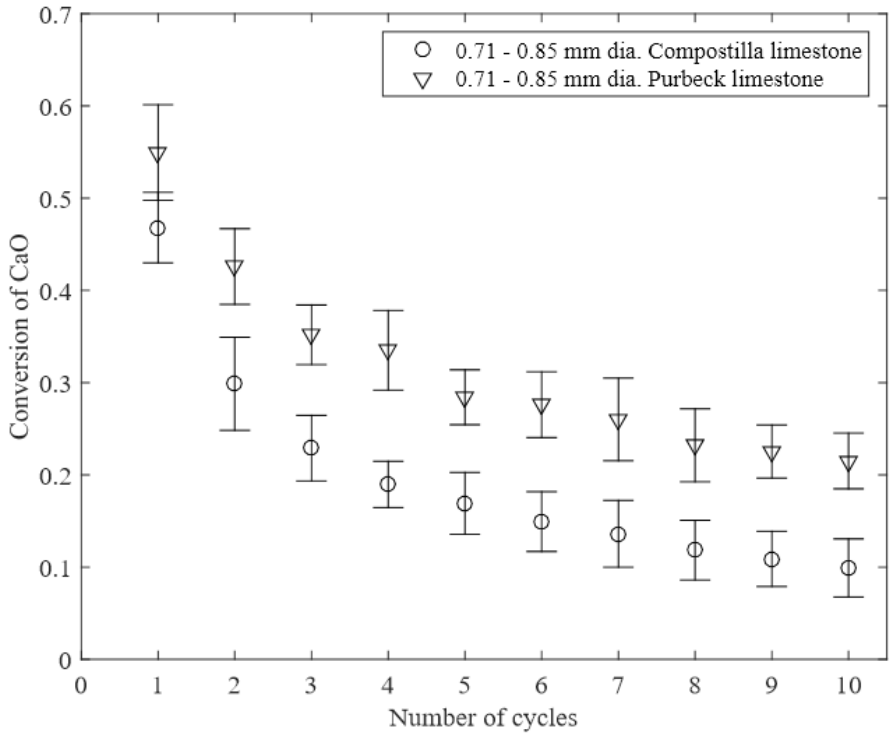

Figure 5.1 The conversion of CaO during the cycling of 710 – 850 μm dia. particles of Compostilla and Purbeck limestones. The error bar corresponded to the 95% confidence interval from a *t*-distribution based on five repeated measurements.

5.2.2 Fluidised bed experiments

Batch experiments were performed in the fluidised bed described in Chapter 2. In an experiment, the reactor was filled with 20 ml of silica sand and heated to the desired temperature, *viz.* 1023 – 1173 K. For calcination, the fluidising gas was 100 mol% N_2. The total volumetric flowrate was 80 mL s^{-1} (STP), giving U/U_{mf} ~ 6.3 – 7.9, with U being the superficial velocity at the temperature of the bed and U_{mf} being the

value at incipient fluidisation predicted from the correlation of Wen & Yu (1966). From experimental measurements using different sample masses, a sample mass of 0.30 g limestone added to the bed was chosen to avoid complications arising from mass transfer between the bubble and the particulate phases. Each experiment was repeated at least 3 times. To ensure complete calcination of the limestones, the experiment was terminated 10 seconds after the measured concentration of CO_2 of the off-gas had returned to zero.

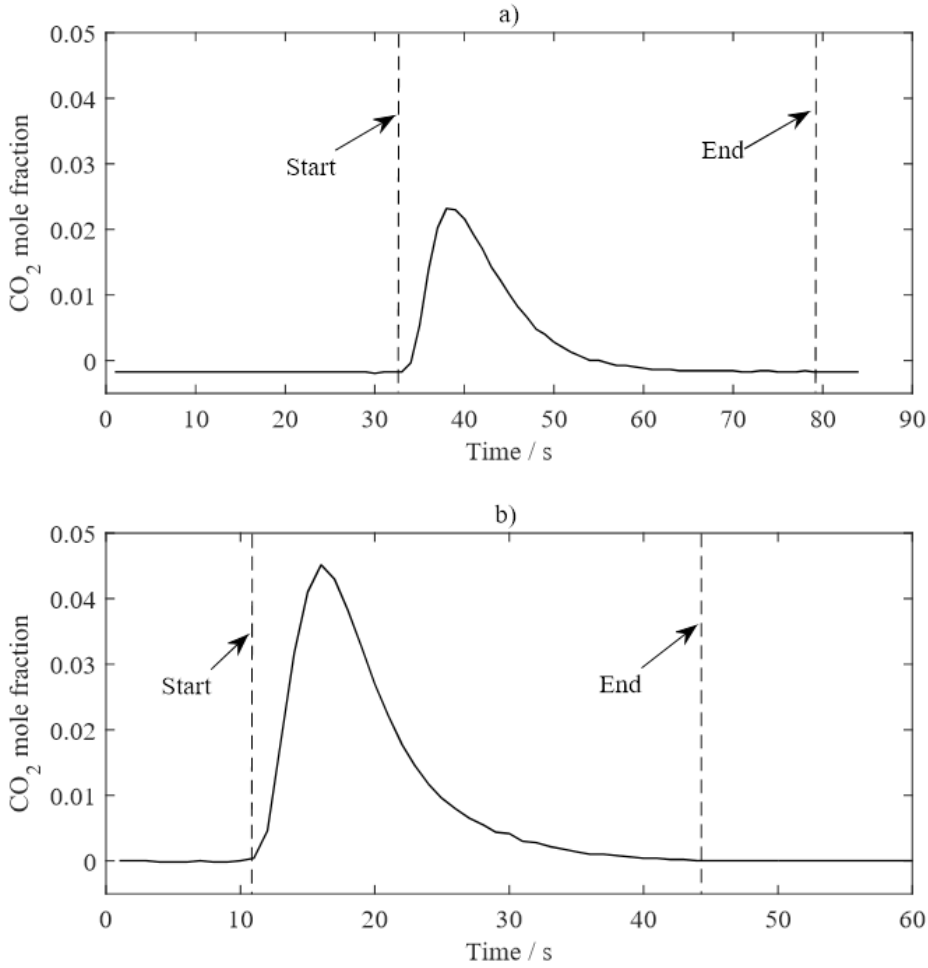

Figure 5.2 Measurements of CO_2 mole fraction during calcination of cycled limestones at atmospheric pressure: a) Compostilla 0.71 – 0.85 mm at 1173 K; b) Purbeck 0.71 – 0.85 mm at 1173 K.

Figure 5.2 shows the raw measurements of CO_2 mole fraction in the off-gas during the calcination of cycled Compostilla (plot a) and Purbeck limestone particles (plot b) in a bed of silica sand fluidised by pure N_2. The figure suggests that the calcination of Compostilla at 1173 K was completed after ~ 50 s while Purbeck at 1173 K finished calcining after 35 s. The peak concentration of CO_2 from Compostilla was about half that of Purbeck, hence the reactivity of Compostilla was significantly less

than that of Purbeck. The equilibrium partial pressure of CO_2 at 1173 K is about 1.087 bar, so the concentration driving force $p_{CO_2}/p_{CO_2}^{eq} < 5\%$. Hence this confirms that the fluidised bed was close to a differential reactor, and it is reasonable to use 0% CO_2 as the bulk concentration in the model.

The overall rate of production of CO_2 from calcination in s^{-1} is $dX/dt = \left(\dot{N}_{out}y_{CO_2,out} - \dot{N}_{in}y_{CO_2,in}\right)/\int\left(\dot{N}_{out}y_{CO_2,out} - \dot{N}_{in}y_{CO_2,in}\right)dt$. The parameters $\dot{N}_{out}$ and $\dot{N}_{in}$ are the total molar flows leaving and entering the reactor at the exit and entrance conditions, where $\dot{N}_{out}\left(1 - y_{CO_2,out}\right) = \dot{N}_{in}\left(1 - y_{CO_2,in}\right)$ from the mass balance of nitrogen. The raw measurements were deconvoluted to account for the mixing and delay in the sampling line using the method described in Appendix D, where the mean residence times for the two CSTRs were found to be 3.38 s and 3.39 s.

5.3 Theoretical methods

5.3.1 Modelling the kinetics of calcination

The model described in this study assumed that the limestone particle was spherical and was calcined in a bed of silica sand fluidised by a stream of N_2. The only reaction occurring was:

$$CaCO_{3(s)} \rightleftharpoons CaO_{(s)} + CO_{2(g)} \qquad \Delta H^0_{298K} = +178 \text{ kJ mol}^{-1} \qquad \text{(5-I)}$$

The assumptions made in Chapter 3 when developing the general reaction and diffusion model also applied here, except that the temperature of the particle surface was assumed to be close to the temperature of the bulk as the heat transfer coefficient between the particulate phase of the fluidised bed and the surface of the particle was large. Since outside the solid particle, the convective heat transfer in a bubbling fluidised bed involved packets of sand particles coming into contact with the particle for a short time, then quickly moving away to be replaced by other packets. Following the study of gasification of chars, the evolution of the internal morphology of a limestone particle during calcination was hypothesised to be described by an arbitrary *f*(*X*). The *X* here corresponds to the local conversion of the maximum available $CaCO_3$ content within the particle after cycling, where the $CaCO_3$ formed during the last carbonation stage was assumed to be uniformly distributed across the particle. The assumption of uniformly distributed $CaCO_3$ across the particle will be discussed further in section 5.5.1. The

reason for such a definition of conversion was that the limestone particle was only partially carbonated and the maximum CO_2 uptake decayed gradually with the number of cycles, as shown in Figure 5.1. As assumed in Chapter 4, the *f*(*X*) function was taken to be capable of being applied at any point in a particle and to be independent of temperature. The value of *f*(*X*) changes with the local conversion, which will vary with distance from the centre of the particle. Similar to gasification, the form of *f*(*X*) should be obtainable from a plot of the experimental rate of calcination against conversion in experiments in which the rate is controlled *solely* by intrinsic chemical kinetics.

The intrinsic rate of reaction per unit of surface area for reaction (5-I) was given by Dennis & Hayhurst (1987):

$$-q_{\mathrm{c}} = k_c - \bar{k} C_{\mathrm{CO_2}} = k_c - \bar{k}\, p_{\mathrm{CO_2}}/RT \tag{5-2}$$

where k_c is the rate constant of the calcination reaction (here, in mol m^{-2} s^{-1}), $\bar{k}$ is the rate constant of the reverse, carbonation reaction (m s^{-1}) and $p_{\mathrm{CO_2}}$ is the partial pressure of CO_2. At equilibrium, the rate $q_{\mathrm{c}} = 0$, so that $k_c - \bar{k}\, p^{eq}_{\mathrm{CO_2}}/RT = 0$. Therefore, the ratio of rate constants is:

$$k_c/\bar{k} = p^{eq}_{\mathrm{CO_2}}/RT \tag{5-3}$$

Substituting Eq. (5-3) into Eq. (5-2),

$$-q_{\mathrm{c}} = k_c\left(1 - p_{\mathrm{CO_2}}/p^{eq}_{\mathrm{CO_2}}\right) \tag{5-4}$$

Here $p^{eq}_{\mathrm{CO_2}}$ is the equilibrium partial pressure of CO_2 at local conditions. Barin & Platzki (1995) gave the following expression for $p^{eq}_{\mathrm{CO_2}}$:

$$p^{eq}_{\mathrm{CO_2}} = 4.083 \times 10^7 \exp(-20474/T) \tag{5-5}$$

The rate constant k_c was assumed to be an activated quantity, thus

$$k_c = \Lambda_{k_c} \exp(-E_a/RT). \tag{5-6}$$

The rate of reaction per unit volume of particle, Q_C, is therefore given by:

$$Q_C = q_{\mathrm{c}} A_{s,0} \rho_{e,0} f(X) = -k_c\left(1 - p_{\mathrm{CO_2}}/p^{eq}_{\mathrm{CO_2}}\right) A_{s,0} \rho_{e,0} f(X) \tag{5-7}$$

where the parameter $A_{s,0}$ is the initial pore area per unit mass and $\rho_{e,0}$ is the initial bulk density of the particles.

A pseudo-steady mass balance over a spherical shell at radius *r* gives the flux equations for CO_2 and N_2:

$$\frac{1}{r^2}\frac{d}{dr}(r^2 J_{\mathrm{n}}) = Q_{\mathrm{n}} = -\nu_n Q_C = -\nu_n q_{\mathrm{c}} A_{s,0}\rho_{e,0} f(X) \qquad n = 1,2 \tag{5-8}$$

where J_n is the total flux (*i.e.* diffusive flux + advective flux) of species *n*. The parameter Q_n is the net rate of reaction of species *n*, in mol m^{-3} s^{-1}, which is positive for a net gain and negative for a net loss in species, and ν_n is the stoichiometric coefficient of species *n* in reaction (5-I). The subscripts 1 and 2 are used to represent, respectively, CO_2 and N_2. A material balance on carbon across a differential element gives the variation of local conversion of $CaCO_3$ with respect to time:

$$\left.\frac{dX}{dt}\right|_r = -M_{\mathrm{CaCO_3}}\left(\frac{Q_C}{\rho_{e,0}}\right) = k_c A_{s,0} M_{\mathrm{CaCO_3}}\left(1 - p_{\mathrm{CO_2}}/p_{\mathrm{CO_2}}^{eq}\right) f(X) \tag{5-9}$$

with initial condition

$$t = 0: \quad X(r) = 0 \quad \text{for all } r \in [0, r_p] \tag{5-10}$$

where the particle centre is at $r = 0$ and the particle surface at $r = r_p$. Since $A_{s,0}M_{\mathrm{CaCO_3}}$ is the initial pore area per unit volume of particle and is constant, the product of the parameters $k_c A_{s,0} M_{\mathrm{CaCO_3}}$ can be replaced by a modified rate constant k_c' to simplify the equation:

$$\left.\frac{dX}{dt}\right|_r = k_c'\left(1 - p_{\mathrm{CO_2}}/p_{\mathrm{CO_2}}^{eq}\right) f(X)$$
$$k_c' = \Lambda_{k_c} A_{s,0} M_{\mathrm{CaCO_3}} \exp(-E_a/RT) = k_0 \exp(-E_a/RT) \tag{5-11}$$

Here the activation energy of k_c' is the same as that of k_c, but the pre-exponential becomes $k_0 = \Lambda_{k_c} A_{s,0} M_{\mathrm{CaCO_3}}$.

5.3.2 Evolution of pore structure

The porosity, ε, changes with the local conversion of $CaCO_3$, *X*, during reaction and can be derived from the volume balance equation for a thin cylindrical shell inside the particle:

$$\varepsilon(X) = \varepsilon_0 + X(1-\varepsilon_0)\left(1 - V_{M,\mathrm{CaO}}/V_{M,\mathrm{CaCO_3}}\right) \quad (5\text{-}12)$$

where $V_{M,\mathrm{CaO}}$ and $V_{M,\mathrm{CaCO_3}}$ are the molar volume of the non-porous CaO and $CaCO_3$ solids. In terms of the pore diameter, it was assumed that the particle has uniform cylindrical pores of initial diameter $d_{pore,0}$; the corresponding initial porosity of the particle was ε_0. From Eq. (3-17) to (3-19) in Chapter 3, the pore diameter at some time when the local conversion is *X* is:

$$r_{pore} = r_{pore,0}\sqrt{\left(\varepsilon_0 + X(1-\varepsilon_0)\left(1 - V_{m,\mathrm{CaO}}/V_{m,\mathrm{CaCO_3}}\right)\right)/\varepsilon_0} \quad (5\text{-}13)$$

In terms of the particle size, Wu *et al.* (2010) reported only 2 – 7% reduction in particle diameter after 10 calcination – carbonation cycles. Hence the overall particle size was assumed to be constant during calcination. Any change of the solid volume due to the difference in molar volumes of $CaCO_3$ and CaO was taken only to affect the pore structure parameters *e.g.* porosity and pore diameter.

5.4 Results

5.4.1 Characterisation of the limestone particles

The measurements from the Brunauer–Emmett–Teller (BET) analysis and mercury intrusion porosimetry of the carbonated limestone particles are shown in Table 5.2 and Table 5.3, both of which produce a pore size distribution of the particles shown in Figure 5.3. It is clear that these cycled particles have substantial pore volume, even in their fully-carbonated state, in contrast to virgin limestone, which has negligible porosity. For both the Compostilla and the Purbeck limestone particles, most of the pore volume measured seemed to come from pores bigger than 200 nm, although the particles may still have considerable unmeasured pore volume in the micro-porous range (d_{pore} < 2 nm), because the BET and mercury intrusion analyser were unable to measure pore diameters smaller than 1.7 nm and 3 nm respectively. In the subsequent modelling, the mean pore diameter $d_{pore} = 4V/A$ from mercury porosimetry was used as the initial pore diameter of the particles, where *V* is the total intrusion volume and *A* is the total pore area.

Table 5.2 BET analysis of the 0.71 – 0.85 mm dia. carbonated limestone particles.

Limestone	BET area / $m^2\ g^{-1}$	BJH volume / $cm^3\ g^{-1}$	BJH adsorption mean pore diameter / nm
Compostilla, 8 cycles	0.33	7.2×10^{-3}	72
Purbeck, 6 cycles	1.58	9.9×10^{-3}	21

Table 5.3 Mercury porosimetry of the 0.71 – 0.85 mm dia. carbonated limestone particles.

Limestone	Porosity	Total pore area / $m^2\ g^{-1}$	Total intrusion volume / $cm^3\ g^{-1}$	Mean pore diameter / nm	Bulk density / $kg\ m^{-3}$	Tortuosity factor / -
Compostilla, 8 cycles	0.16	0.46	0.07	608	2235	2.8
Purbeck, 6 cycles	0.34	3.88	0.19	196	1811	2.1

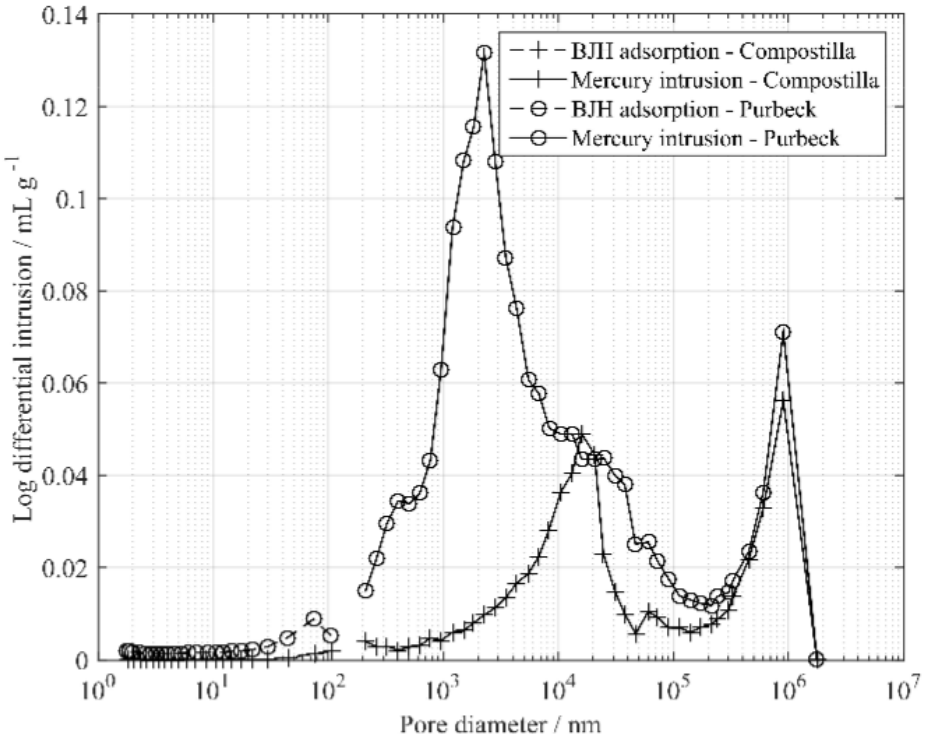

Figure 5.3 Pore size distributions of the 8 cycles Compostilla and the 6 cycles Purbeck carbonated limestone particles from BJH adsorption analysis and mercury porosimetry.

Optical microscope was used to determine the particle size distribution of the 0.71 – 0.85 mm diameter Purbeck limestones shown in Figure 5.4, which gives a relative narrow volume weighted distribution above 600 μm in plot (b) and a number weighted distribution for fine particles less than 10 μm in plot (a). Similar to the finding

in chapter 4, Table 4.4 shows that the geometric mean diameter of the sieve sizes can be a reasonably close estimate of the product of the Sauter mean diameter and the circularity of the particle, $D(3,2) \times \psi$. Hence for particles of the Compostilla limestone and the 1.40 – 1.70 mm dia. Purbeck limestone, which did not have the particle size distribution measurements, the geometric mean diameter could be used for the mean diameter in the model.

Table 5.4 Summary of particle size distribution for the Purbeck limestone.

Parameter	0.71 – 0.85 mm
10% of total volume below this size, $D10$ / μm	772
50% of total volume below this size, $D50$ / μm	924
90% of total volume below this size, $D90$ / μm	1097
Sauter mean diameter, $D(3,2)$ / μm	959
Average high sensitivity circularity, ψ / -	0.88
$D(3,2) \times \psi$ / μm	844
Geometric mean diameter used in model, d_p / μm	777

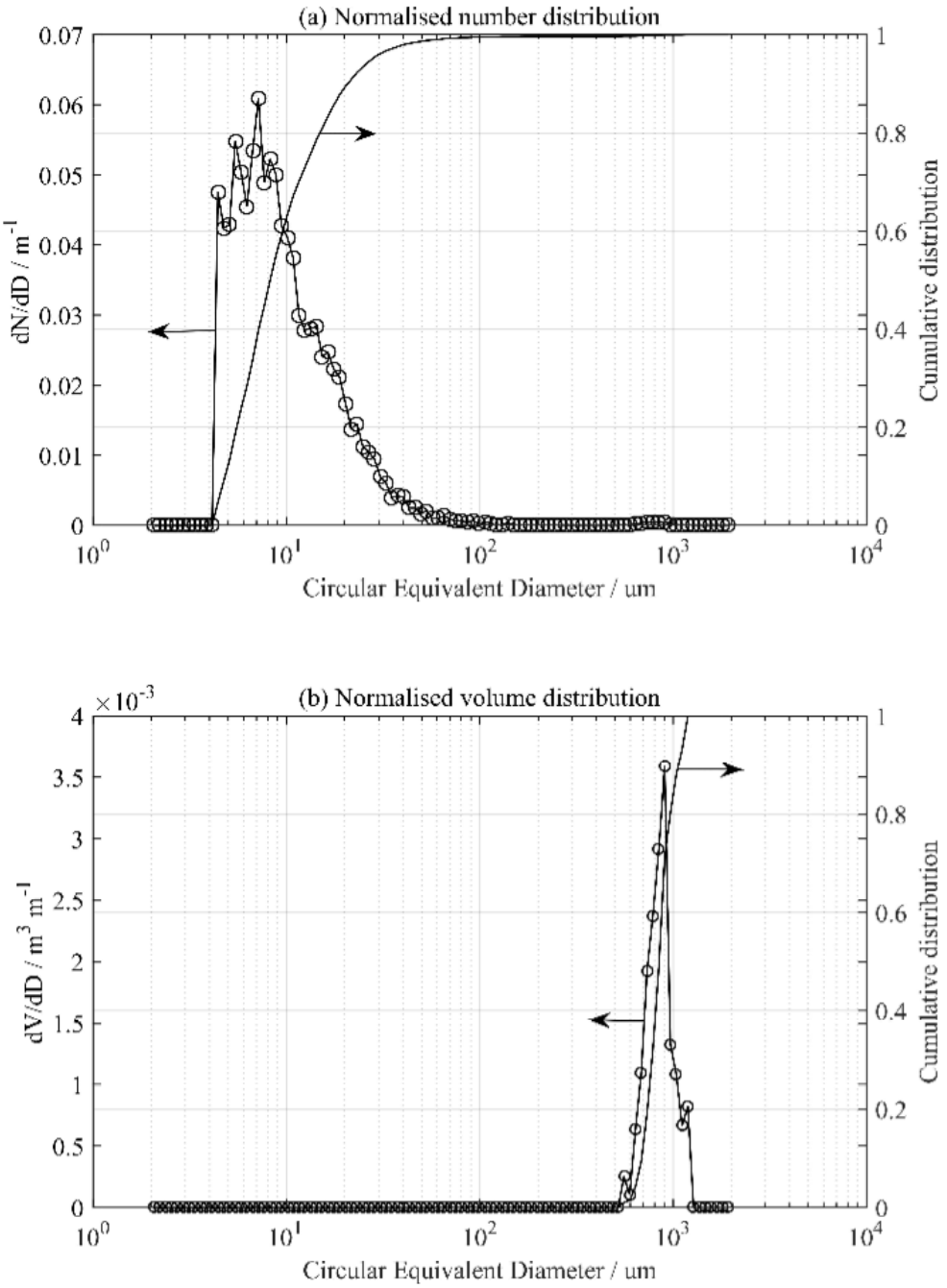

Figure 5.4 Particle size distribution measurements of the 0.71 – 0.85 mm dia. Purbeck 6 cycles limestone particle: (a) distribution based on the number of particles and (b) distribution based on the volume of the particles.

5.4.2Kinetic parameters

The Arrhenius coefficients and activation energies of the kinetic parameter k_c' in Eq. (5-I), were determined from the initial rate extrapolated from the experimental measurements, as shown in Figure 5.5. At the start of reaction, the particle conversion is 0 and $f(X) = 1$, and Eq. (3-I) can be rearranged

$$\mathrm{Ln}(dX/dt\,|_{t=0}) = -E_a/RT + \mathrm{Ln}(k_0) + \mathrm{Ln}\left(1 - p_{\mathrm{CO_2}}/p_{\mathrm{CO_2}}^{eq}\right) \quad (5\text{-}14)$$

If the value of $p_{\mathrm{CO_2}}/p_{\mathrm{CO_2}}^{eq}$ is much smaller than 1, which was the case in the experiments used here, then

$$\mathrm{Ln}(dX/dt\,|_{t=0}) = \mathrm{Ln}(k_c') = -E_a/RT + \mathrm{Ln}(k_0) \quad (5\text{-}15)$$

A plot of $\mathrm{Ln}(dX/dt\,|_{t=0})$ *vs.* $1/T$ should therefore yield the activation energy E_a and the Arrhenius coefficient k_0. The results of the kinetic parameters of the limestones used here are shown in Table 5.5.

In the subsequent Figure 5.6 and Figure 5.9 in section 5.4.3 and 5.4.4, the linearity of the plots show that the calcination of the limestone was indeed controlled by chemical kinetics at low temperature, hence confirming the use of Eq. (5-15) for the determination of the kinetic parameters. The errors associated with the kinetic parameters mainly come from extrapolating the initial rates from measurements, and using a limited number of measurements for linear regression analysis. The 95% confidence intervals of the kinetic parameters are shown in Figure 5.6 and Figure 5.9.

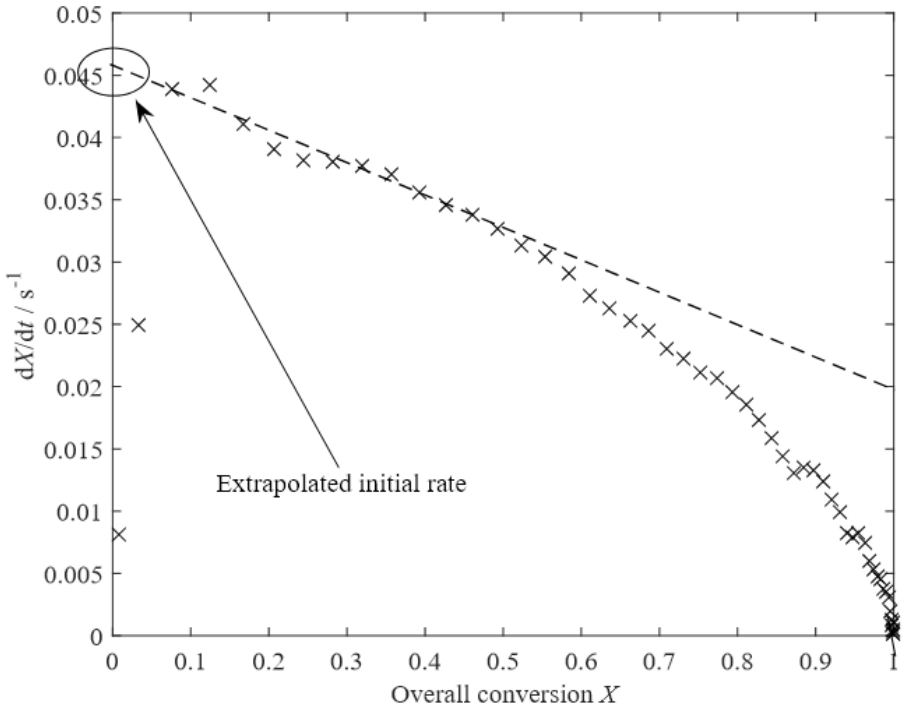

Figure 5.5 Determining initial rate of reaction using linear extrapolation (--) on rate and conversion measurements (×) of Compostilla 0.71 – 0.85 mm particles at 1073 K.

Table 5.5 Kinetic parameters of the calcination of 0.71 – 0.85 mm dia. limestone particles.

Limestone particles	k_0 / s^{-1}	E_a / kJ mol^{-1}
Compostilla, 8 cycles	1.72×10^7	175 ± 12
Purbeck, 6 cycles	6.50×10^7	186 ± 5

5.4.3 Calcination of Compostilla limestone particles

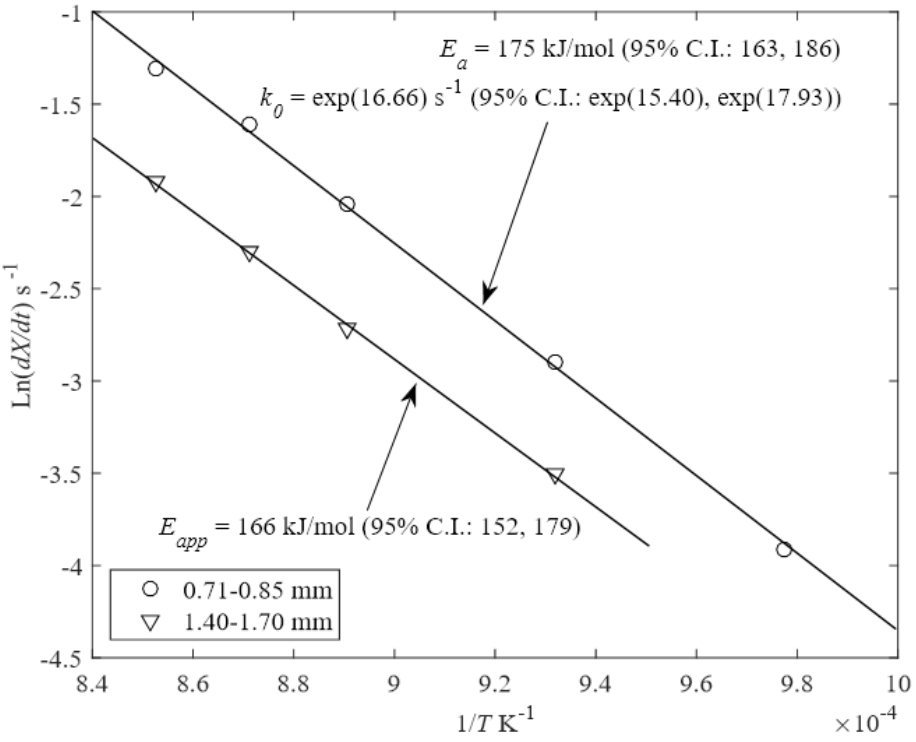

Figure 5.6 Determining the kinetic parameters of Compostilla limestone particles. The measurements were obtained from the calcination of the limestone particles at 1023 K (0.71 – 0.85 mm only), 1073 K, 1123 K, 1148 K and 1173 K. The values of the kinetic parameters of the rate constant are shown with 95% confidence interval (C.I.).

Particles of Compostilla limestone with diameters of 0.71 – 0.85 mm and 1.40 – 1.70 mm were calcined at 1023 K (0.71 – 0.85 mm only), 1073 K, 1123 K, 1148 K and 1173 K. Using the initial rate extrapolated to zero conversion, Figure 5.6 shows that the plot of $\mathrm{Ln}(dX/dt)$ *vs.* $1/T$ of each particle forms straight lines. The values of the kinetic parameters in Eq. (3-I) were determined from a linear regression analysis, yielding an activation energy of $E_a = 175 \pm 12$ kJ/mol and $k_0 = 1.72 \times 10^7$ s^{-1} for 0.71 – 0.85 mm dia. particles. For 1.40 – 1.70 mm dia. particles, the reaction rates were lower than those of 0.71 – 0.85 mm dia. particles and the apparent activation energy was 166 ± 14 kJ/mol, representing a 9 kJ/mol reduction but within the error band of

± 12 kJ/mol. It is expected that the gradient of a best fit line would approach one half its intrinsic value if the reaction rate were significantly limited by intraparticle mass transfer (Levenspiel, 1999). However, this is not observed in Figure 5.6. In literature, the reported activation energy of calcination was between 160 and 210 kJ/mol (Fuertes *et al.*, 1993; Borgwardt, 1985; Dennis & Hayhurst, 1987; García-Labiano *et al.*, 2002; Murthy *et al.*, 1994). Hence, the activation energy of 175 ± 12 kJ/mol are sufficiently high to suggest that the reactions could not have been in mass transfer limited regime. It can be concluded that (i) the calcination of 0.71 – 0.85 mm dia. particles was controlled by intrinsic chemical kinetics; (ii) the reactions of 1.40 – 1.70 mm dia. particles were possibly affected by intraparticle mass transfer but not severely so.

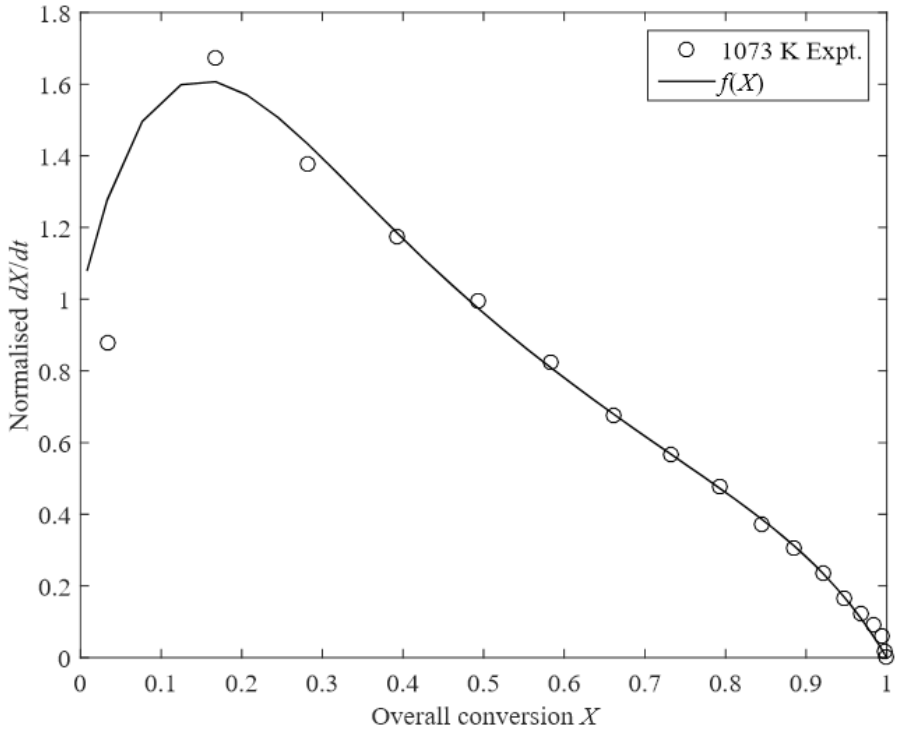

Figure 5.7 Determining the function $f(X)$ from the plot of normalised rate of calcination *vs.* conversion measurement of 0.71 – 0.85 mm dia. Compostilla at 1073 K.

The form of $f(X)$ needs to be determined from experimental measurements of calcination rate *vs.* conversion conducted under conditions where the reaction is controlled by intrinsic chemical kinetics. Owing to the low rate of reaction at 1023 K, the percentage fluctuation caused by random noise in the measurements of CO_2 concentration was very large. The resulting $f(X)$ was not a smooth function, as expected. However, since experiments at both 1023 K and 1073 K appear to be in the regime of chemical kinetic control, as shown in Figure 5.6, the $f(X)$ function was determined from the measurements at 1073 K instead. Figure 5.7 shows the plot of $f(X)$, a 6th order

polynomial of X, determined from the normalised rate *vs.* conversion measurements of Compostilla limestone of sieve diameter 0.71 – 0.85 mm, calcined at 1073 K. Using this $f(X)$, the model was able to fit well the experimental results at 1023 K, as seen in Figure 5.8(a). This strongly suggests that the $f(X)$ was not merely a fit valid for one particular experimental condition.

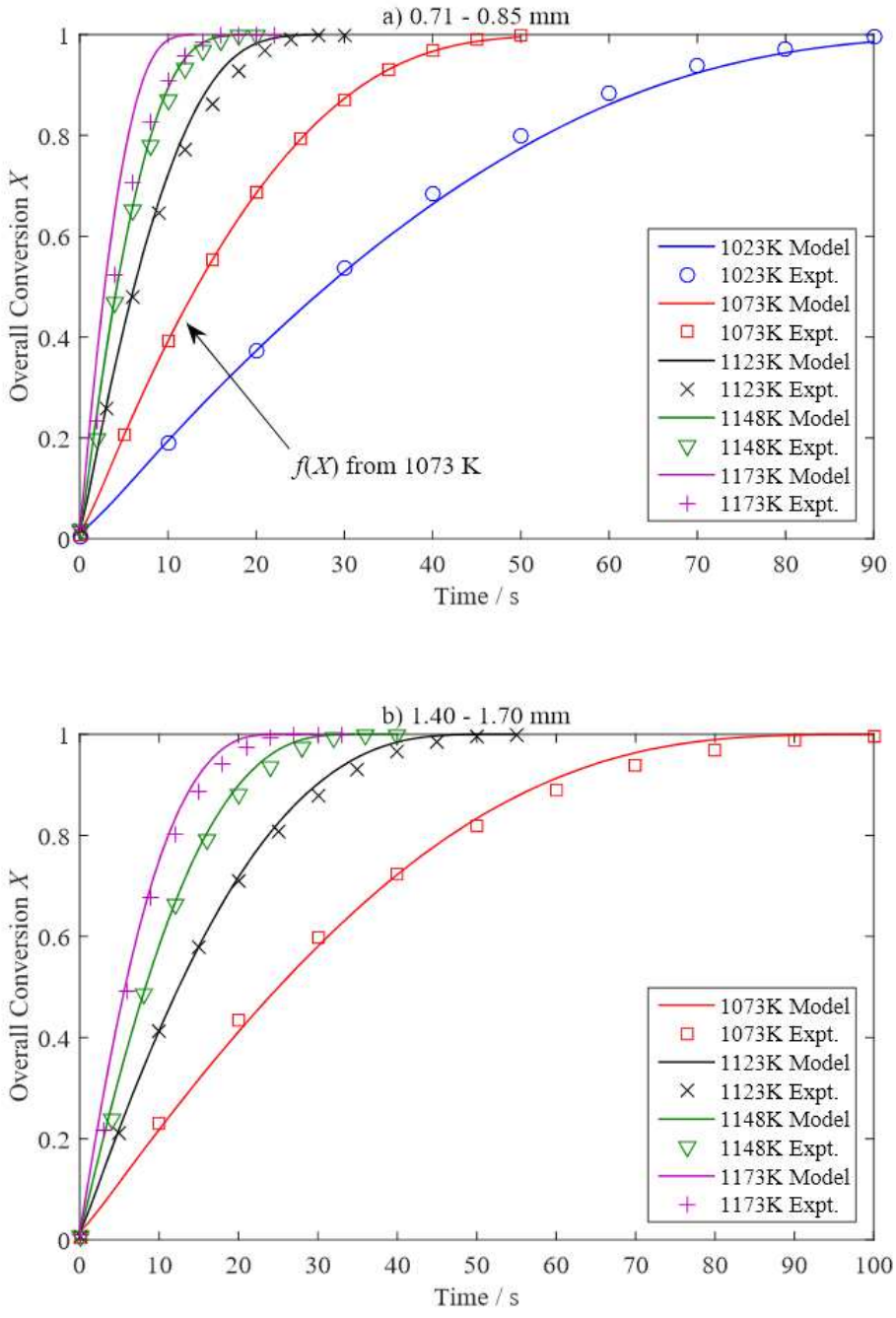

Figure 5.8 Comparison of model results (lines) with experimental measurements (points) of the calcination of Compostilla limestone particles (8 cycles) by 100% N_2: a) 0.71 – 0.85 mm; b) 1.40 – 1.70 mm. The $f(X)$ was determined from the rate *vs.* conversion measurements of 0.71 – 0.85 mm particles at 1073 K, and was applied to all cases.

Further comparisons between model predictions and experimental measurements for Compostilla limestone of 0.71 – 0.85 mm dia. and 1.40 – 1.70 mm dia. are shown in Figure 5.8, with generally good agreement being seen between experiment and theory. However, the experimental measurements for the 0.71 – 0.85 mm dia. particle at 1173 K were almost identical to those at 1148 K, which indicates either a severe limitation by external mass transfer or an error in deconvolution of the measurements to correct for mixing in the sampling line due to the rapidity of the reaction. Figure 5.6 shows that even for the larger particles at higher temperature, the rate of reaction was not limited by intraparticle mass transfer as the gradients of the two measurements are almost the same. Therefore, it can be concluded that the unexpected behaviour of the rate of 0.71 – 0.85 mm dia. at 1173 K is due to error in deconvolution.

5.4.4 Calcination of Purbeck limestone particles

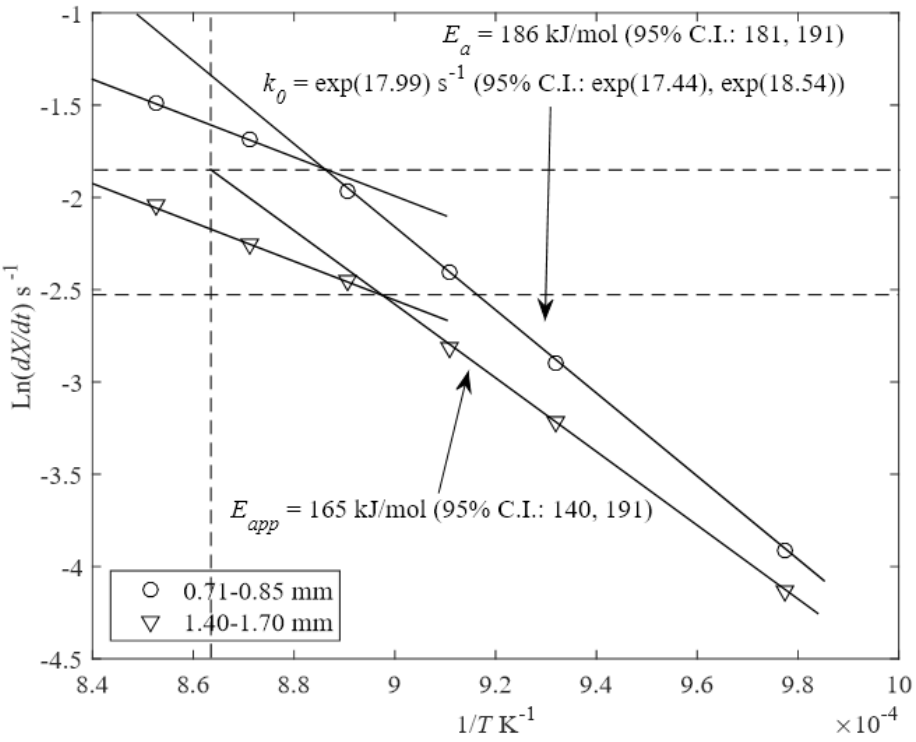

Figure 5.9 Determining the kinetic parameters of Purbeck limestone particles. The measurements are from calcination of 0.71 – 0.85 mm and 1.40 – 1.70 mm particles at 1023 K, 1073 K, 1098 K, 1123 K, 1148 K and 1173 K. The gradient of the linear regression line for both particles reduced by ~ 50% at 1098 – 1173 K. The values of the kinetic parameters are shown with 95% confidence interval (C.I.).

Experiments with Purbeck limestone were performed using 0.71 – 0.85 mm and 1.40 – 1.70 mm dia. particles at 1023 K, 1073 K, 1098 K, 1123 K, 1148 K and 1173 K. The same kinetic analysis was performed on the experimental measurements and the

results are shown in Figure 5.9. A linear regression line of the plot of $\mathrm{Ln}(dX/dt)$ *vs.* $1/T$ gives an activation energy $E_a = 186 \pm 5$ kJ/mol and the rate constant $k_0 = 6.50 \times 10^7\ \mathrm{s}^{-1}$, where the activation energy seems in line with the 160 – 210 kJ/mol range reported in the literature (Fuertes *et al.*, 1993; Borgwardt, 1985; Dennis & Hayhurst, 1987; García-Labiano *et al.*, 2002; Murthy *et al.*, 1994). At 1098 – 1173 K, the gradient of the regression lines fitted to the measurements, effectively $-E_a/R$, is reduced by about half at $T > 1098$ K. Hence, this figure suggests that the transition of the reaction regime from chemical kinetic control to internal mass transfer control starts at ~ 1098 K. Figure 5.9 also shows that the rates of reaction of the 1.40 – 1.70 mm dia. particles are lower than those of the 0.71 – 0.85 mm dia. particles; the linear regression lines of the 1023 – 1098 K measurements show a 21 kJ/mol decline, larger than the ± 5 kJ/mol error, in the apparent activation energy, probably owing to a growing influence of internal mass transfer limitation for larger particles. At $T > 1098$ K, the slope of the points for the 1.40 – 1.70 mm dia. particles is almost the same as that for the 0.71 – 0.85 mm particles, suggesting that the reaction becomes limited by mass transfer. Furthermore, for the 1.40 – 1.70 mm dia. particles the transition of the reaction regime occurs at a temperature lower than that of the 0.71 – 0.85 mm dia. particle, a consequence of the increased mass transfer limitation in larger particles.

Figure 5.10 compares the rates of conversion *vs.* time from experimental measurements (points) with the theory (line) for Purbeck limestone calcined in 100% N_2 at 1023 – 1173 K. Interestingly, the $f(X)$ determined previously from the measurements on Compostilla limestone of 0.71 – 0.85 mm dia. at 1073 K, shown in Figure 5.7, was successfully applied here for both size fractions of Purbeck limestone. The result shows that the model fits perfectly with the experimental measurements even for measurements at 1173 K.

Given the results, it can be concluded that using a constant $f(X)$ across different temperatures gives a satisfactory agreement between the model and the measurements for both Compostilla and Purbeck limestone. The fact that the $f(X)$ obtained from measurements of Compostilla could be successfully applied to the modelling of Purbeck suggests that the two limestone particles experienced similar changes of internal morphology during calcination. One reason that could explain this is that both particles had been periodically cycled several times before the final calcination reaction, which could have reduced the effect of initial differences in pore structures thus making the

two types of limestone particles more similar in terms of internal morphology. In addition, after a number of calcination – carbonation cycles, the reactivity of the particles approached an asymptotic value. It might also be the case that the internal pore structure had developed into an "asymptotic" stage, where the original variations in pore structures between the two limestones had become slight during cycling.

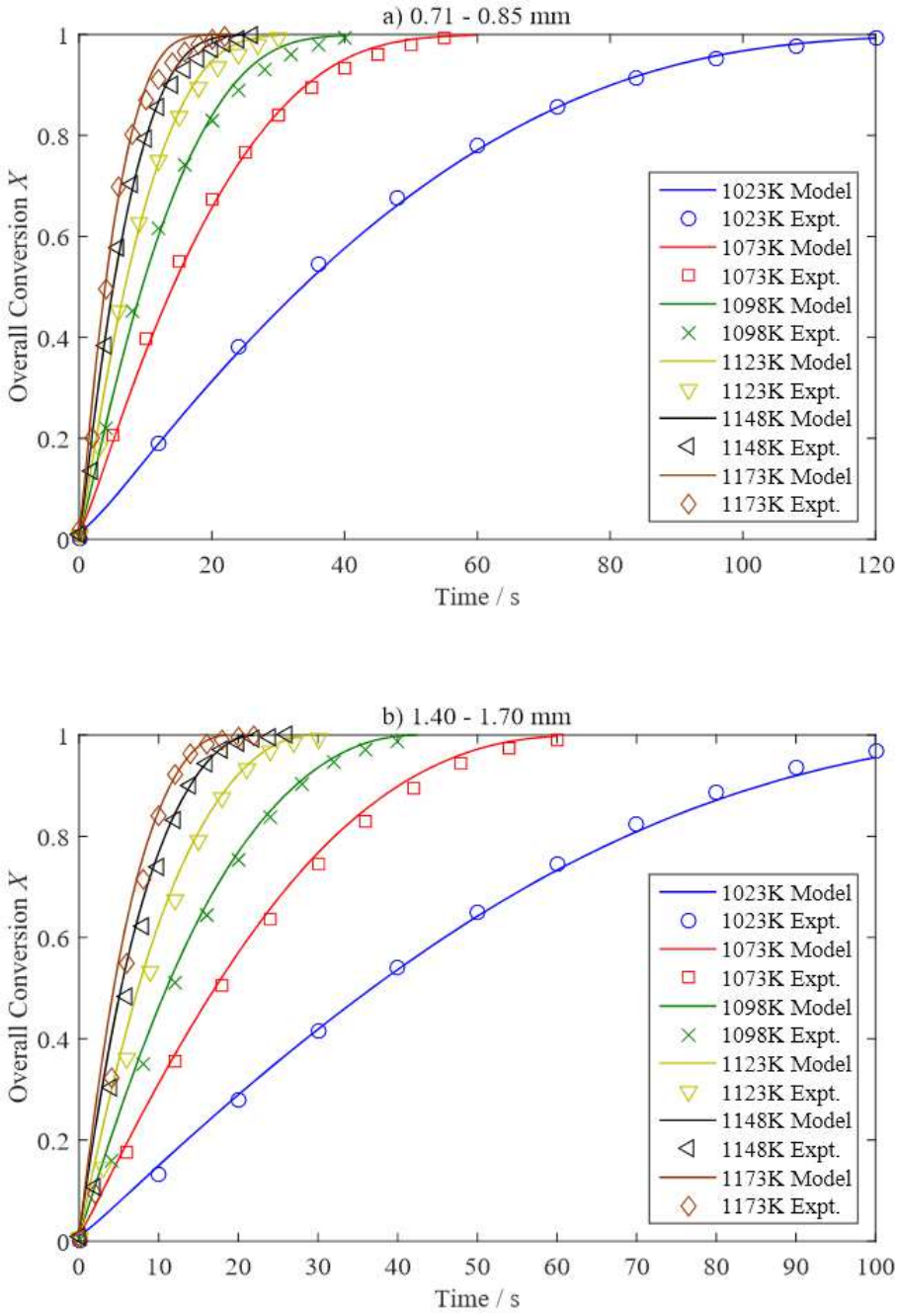

Figure 5.10 Comparison of model results (lines) with experimental measurements (points) of the calcination of Purbeck limestone particles (6 cycles) by 100% N_2: a) 0.71 – 0.85 mm; b) 1.40 – 1.70 mm. The $f(X)$ determined from Compostilla 710 – 850 µm particles at 1073 K was used here.

5.4.5 Effect of pressure on calcination rate

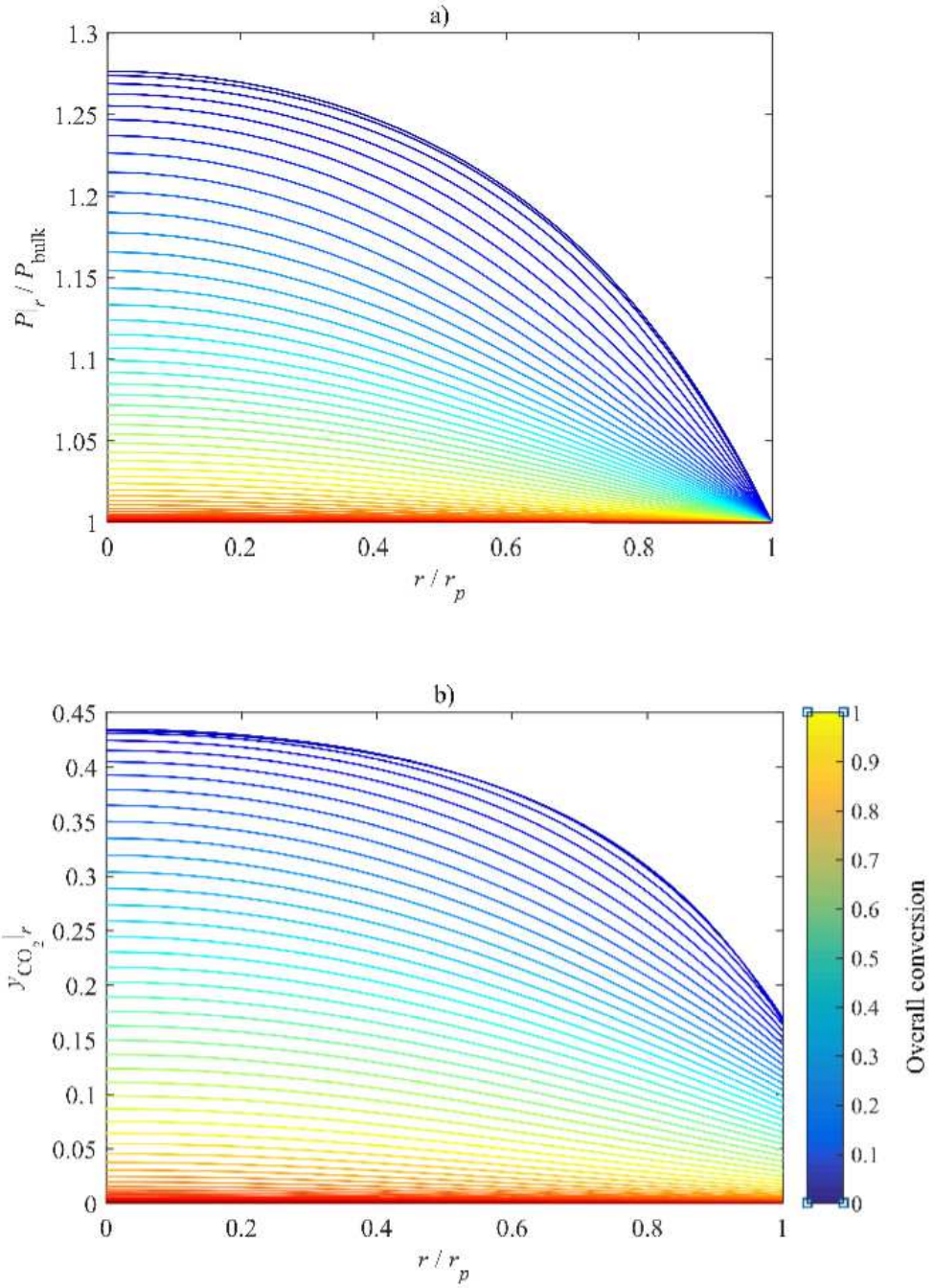

Figure 5.11 Profiles of normalised local pressure and CO_2 mole fraction inside the particle from simulation result of calcination of 0.71 – 0.85 mm dia. Purbeck limestone at 1 bar and 1148 K in pure N_2. The radius is normalised by the particle radius, so $r/r_p = 1$ is the particle surface. The colour bar indicates the conversion of the particle.

The results presented in this section and the following two were obtained from the simulation of the calcination of particles of Purbeck limestone diameter 0.71 – 0.85 mm dia. which had been cycled 6 times in a fluidised bed at various pressures, temperatures and CO_2 mole fractions in the bulk. A typical evolution of the intraparticle profiles of total pressure and CO_2 mole fraction is shown in Figure 5.11, where the

profiles flatten as conversion increases. The initial values at the particle centre are basically the maximum points on the profiles, which are good indicators of the intraparticle gradients of the local pressure and CO_2 mole fraction. All the results presented here are based on the initial values of the partial pressure of CO_2 at particle centre, $p_{CO_2}|_{r=0} = (P \cdot y_{CO_2})|_{r=0}$. Table 5.6 shows the initial values of $P|_{r=0}/P^{bulk}$ and $y_{CO_2}|_{r=0}$ at the particle centre when the bulk is 0% CO_2.

Table 5.6 Simulation results of the initial values of the total pressure and CO_2 mole fraction at the particle centre for 0% CO_2 in the bulk.

$P\|_{r=0}/P_{bulk}$					$y_{CO_2}\|_{r=0}$				
	P_{bulk} / bar					P_{bulk} / bar			
T_{bulk} / K	0.1	1.0	2.0	3.0	T_{bulk} / K	0.1	1.0	2.0	3.0
1048	1.57	1.04	1.02	1.01	1048	0.399	0.080	0.048	0.035
1098	2.48	1.11	1.04	1.02	1098	0.645	0.187	0.115	0.085
1148	4.47	1.26	1.10	1.05	1148	0.828	0.370	0.244	0.186
1198	8.42	1.57	1.22	1.12	1198	0.928	0.603	0.446	0.357

Figure 5.12 shows the initial values of $p_{CO_2}|_{r=0}$ as a function of the bulk pressure. At a constant temperature and bulk CO_2 mole fraction, higher bulk pressure leads to a larger local partial pressure of CO_2. Since the equilibrium partial pressure of CO_2 is fixed at constant temperature, higher local partial pressures result in smaller driving forces $(p_{CO_2}^{eq} - p_{CO_2}|_r)$ which can be seen from the decreasing distance between the calculated points and the broken line. Therefore, the calcination rate is reduced at high pressure even when the bulk CO_2 mole fraction is 0%. This observation has been reported in the literature (Dennis & Hayhurst, 1987; García-Labiano *et al.*, 2002). When the bulk CO_2 mole fraction is high, the local partial pressure could easily exceed the equilibrium partial pressure, which means carbonation would occur.

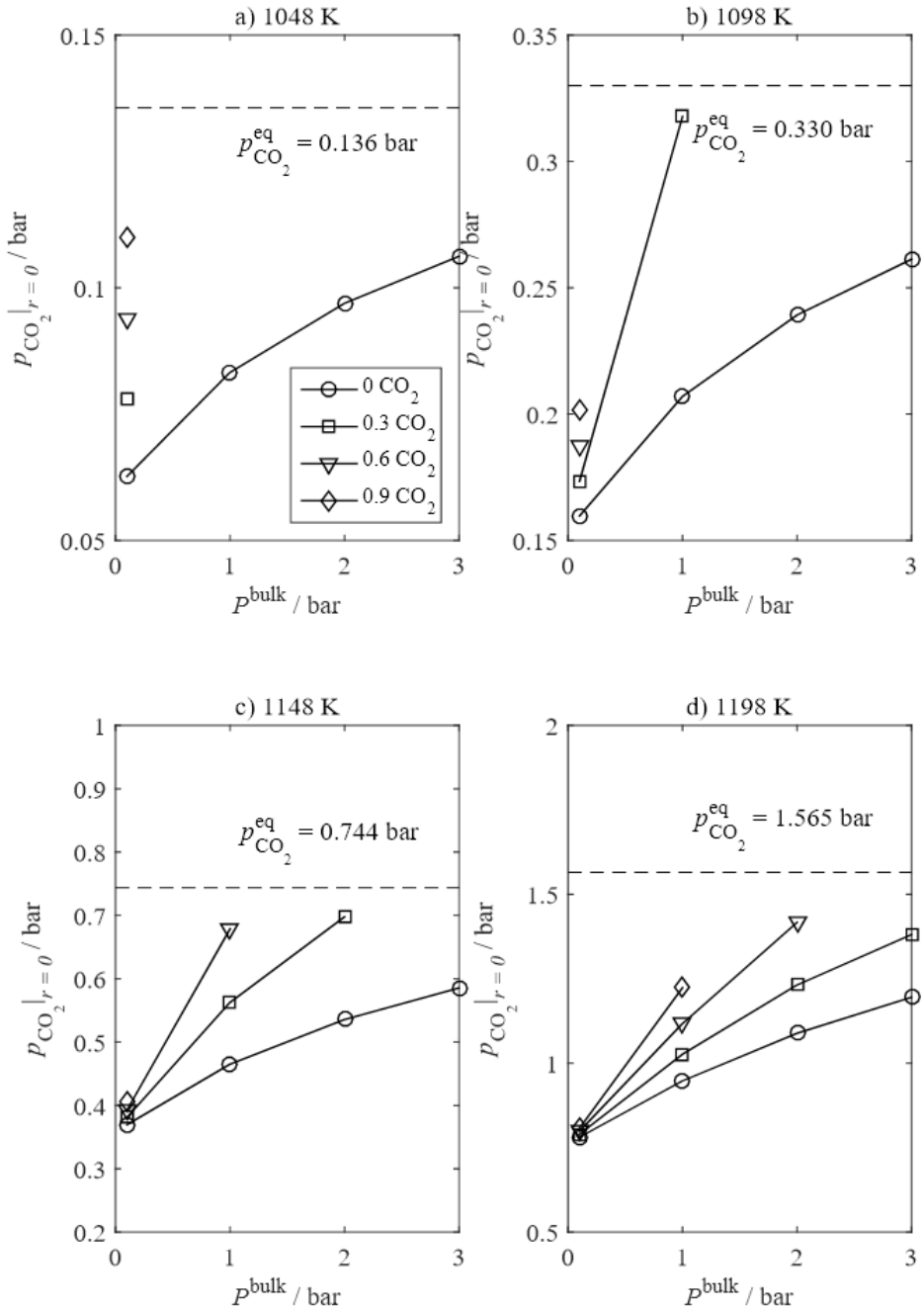

Figure 5.12 Simulation results of the initial $p_{CO_2}|_{r=0}$ as a function of the bulk pressure at different $y^{bulk}_{CO_2}$ and T^{bulk} for the calcination of 0.78 - 0.85 mm dia. Purbeck limestones. The bulk pressure is 0.1, 1.0, 2.0 and 3.0 bara and the bulk CO_2 mole fractions are 0, 0.3, 0.6 and 0.9. The equilibrium partial pressure $p^{eq}_{CO_2}$ at each temperature is indicated as broken lines.

5.4.6 Effect of temperature on calcination rate

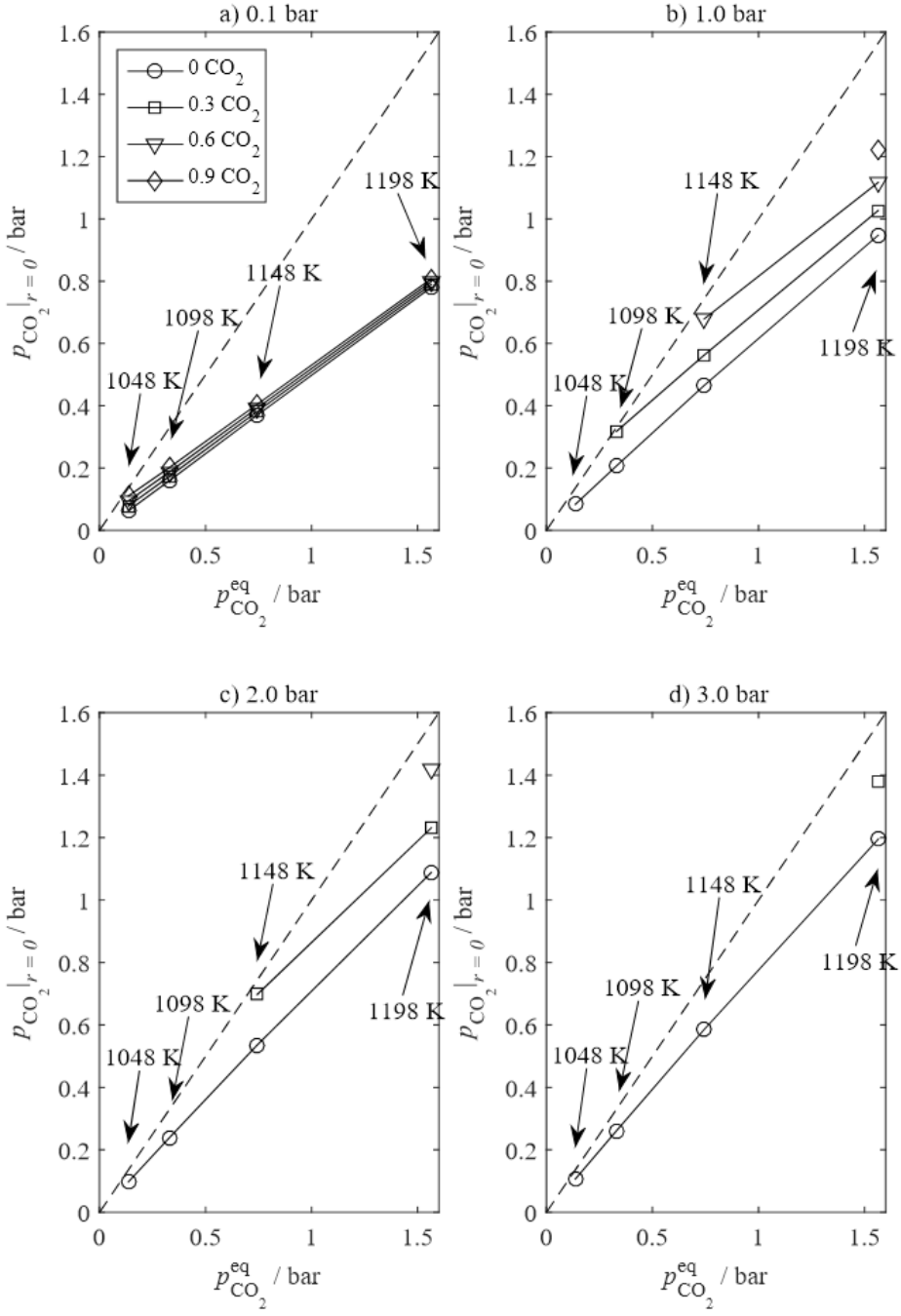

Figure 5.13 Simulation results of the initial $p_{CO_2}|_{r=0}$ as a function of $p^{eq}_{CO_2}$ at different $y^{bulk}_{CO_2}$ and P_{bulk} for the calcination of 0.78 - 0.85 mm dia. Purbeck limestones. The equilibrium partial pressure of CO_2 is 0.136, 0.330, 0.744 and 1.565 bar and the bulk CO_2 mole fractions are 0, 0.3, 0.6 and 0.9. The temperature at which the $p^{eq}_{CO_2}$ is calculated is indicated on the plots. The broken lines indicate the level where the local partial pressure $p_{CO_2}|_{r=0}$ equals to the equilibrium partial pressure $p^{eq}_{CO_2}$.

Figure 5.13 shows the initial values of $p_{CO_2}|_{r=0}$ as a function of the equilibrium partial pressure of CO_2, which varies with temperature according to Eq. (5-5). At a

constant pressure and bulk CO_2 mole fraction, a higher temperature leads to both a larger local partial pressure and a larger equilibrium partial pressure of CO_2. However, the increase in $p_{CO_2}^{eq}$ is greater than the increase in $p_{CO_2}|_r$ so that the gaps between the broken lines and the solid lines widen as temperature increases. It means that the partial pressure driving force of the calcination reaction $\left(p_{CO_2}^{eq} - p_{CO_2}|_r\right)$ increases, thus the rate of calcination increases with temperature, a fact observed experimentally.

5.4.7 Effect of CO_2 mole fraction on calcination

Figure 5.14 shows the initial values of $p_{CO_2}|_{r=0}$ as a function of the bulk CO_2 mole fraction. At a constant temperature and pressure, a higher bulk CO_2 mole fraction leads to larger local partial pressure of CO_2 inside the particles, which reduces the partial pressure driving force. This effect has also been reported in the literature (Dennis & Hayhurst, 1987; García-Labiano *et al.*, 2002). In addition, at higher pressure, the increase in $p_{CO_2}|_r$ with $y_{CO_2}^{bulk}$ is much more significant than that at lower pressure, while the change of $p_{CO_2}|_r$ due to change of $y_{CO_2}^{bulk}$ is only slightly more than that at lower temperature. In the other words, i) high pressure results in a more significant effect of $y_{CO_2}^{bulk}$ on $p_{CO_2}|_r$ compared to low pressure; ii) low temperature leads to a slight effect of $y_{CO_2}^{bulk}$ on $p_{CO_2}|_r$ compared to high temperature. Also, as the total pressure increases, the local partial pressure could become higher than equilibrium partial pressure so that no calcination occurs. Those data points above the equilibrium partial pressure are not shown in Figure 5.14, which is why some data series only have one data point.

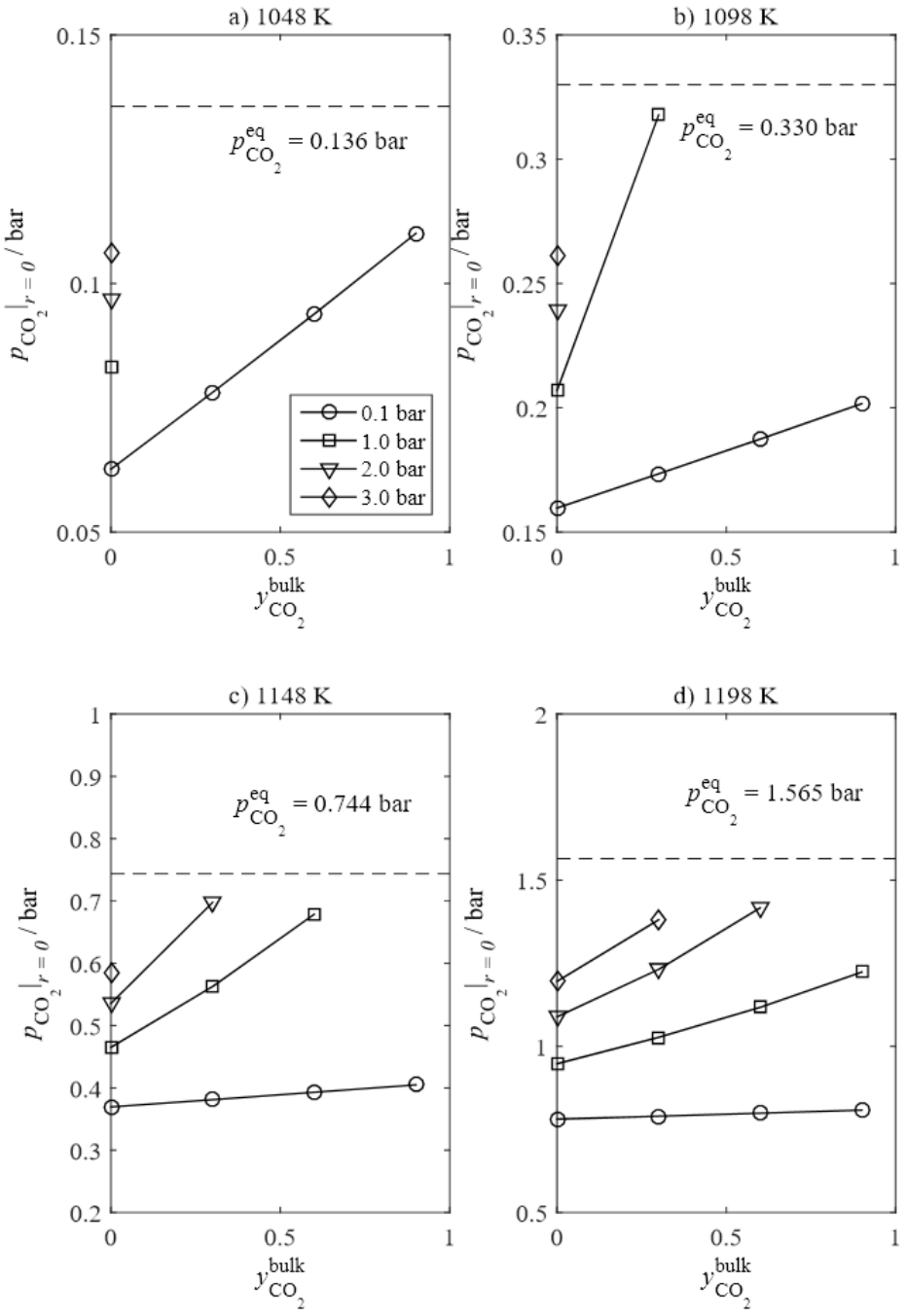

Figure 5.14 Simulation results of the initial $p_{CO_2}|_{r=0}$ as a function of $y^{bulk}_{CO_2}$ at different P_{bulk} and T_{bulk} for the calcination of 0.78 - 0.85 mm dia. Purbeck limestones. The equilibrium partial pressure of CO_2 is 0.136, 0.330, 0.744 and 1.565 bar and the bulk CO_2 mole fractions are 0, 0.3, 0.6 and 0.9. The temperature at which the $p^{eq}_{CO_2}$ is calculated is indicated on the plots. The broken lines indicate the level where the local partial pressure $p_{CO_2}|_{r=0}$ equals to the equilibrium partial pressure $p^{eq}_{CO_2}$.

5.5 Discussion

5.5.1 Comparison between the experiment and the model

The study in this chapter has focused on the calcination of two different limestone particles which have been successively calcined and carbonated several times prior to the calcination. Comparing the reaction rates of both limestones in Figure 5.6 and Figure 5.9, the reactivity of Compostilla is slightly lower than that of Purbeck for 0.71 – 0.85 mm dia. particles. In addition, Table 5.3 and Figure 5.3 show that the mean pore diameter of Purbeck limestones is smaller, being ~1/3 that of Compostilla limestones. With higher reactivity and smaller pore diameter, Purbeck limestone is indeed expected to experience more significant effects of intraparticle mass transfer on observed rate of reaction, as shown in Figure 5.6 and Figure 5.9 at higher temperature. Experimentally, the observed activation energies for the calcination of cycled, carbonated material were reasonably close to values in the literature for the calcination of virgin limestones, being 175 ± 12 kJ/mol and 186 ± 5 kJ/mol, respectively, for the Compostilla and Purbeck. These values, being close to the standard enthalpy of calcination, +178 kJ/mol, suggest that the activation energy for the reverse, carbonation reaction is small, being ~ -3 kJ/mol for Compostilla and ~ +8 kJ/mol for Purbeck. Thus, the intrinsic rate of carbonation changes little with temperature. Zawadzki & Bretsznajder (1935) found that the rate of carbonation varies linearly with the difference between the partial pressure of CO_2 and its equilibrium value at 328 – 368ºC, which suggested that the rate constant was the same for all temperature thus a zero activation energy of the carbonation rate. Nitsch (1962) also concluded that the rate of carbonation has an activation energy close to zero because the rate *versus* partial pressure difference gave a single linear line for measurements at 800 – 850ºC. The same conclusions were also reached by Bhatia & Perlmutter (1983) and Dennis & Hayhurst (1987) for carbonation experiments at 823 – 998 K and 1073 – 1248 K respectively.

One of the assumptions mentioned earlier was that the $CaCO_3$ formed during the last carbonation stage was uniformly distributed across the limestone particles. This was an important assumption because if $CaCO_3$ did not form uniformly across the particle, then the initial porosity and the pore diameter of the carbonated particle could not be expected to be uniform anywhere in the particle as suggested by Eq. (5-12) and (5-13) when $X = 0$. Unlike calcination of $CaCO_3$, the carbonation reaction of CaO usually becomes limited by the diffusion through the $CaCO_3$ product layer soon after the pore

surface is covered with a thin layer of product. During cycling of the limestone particles, the carbonation stage occurred at 923 K. Hence for the 710 – 850 μm dia. Compostilla after 6 cycles, the maximum Thiele modulus given by the initial rate was $\varphi|_{X=0} = \frac{r_p}{3}\sqrt{\frac{\bar{k}A_{s,0}\rho_{e,0}}{D_{\text{eff}}}} = \sim 1$, where $r_p = 390 \times 10^{-6}$ m, $\bar{k}A_{s,0}\rho_{e,0} = 280\ \text{s}^{-1}$ and $D_{\text{eff}} = 4.62 \times 10^{-6}\ \text{m}^2/\text{s}$ at the carbonation conditions, giving an effectiveness factor of ~ 0.8. As carbonation continues, the reaction soon becomes limited by the product layer diffusion, which further reduces the Thiele modulus. Thus, the limestone particles only experienced limited pore diffusion resistance and was likely to form a uniform product layer during the carbonation stage of the cycling at 923 K. In addition, Pacciani (2008) analysed particles of 500 – 710 μm dia. virgin limestone calcine being carbonated at similar conditions and concluded that CO_2 penetrated the whole particle and the product $CaCO_3$ built up uniformly across the particle. Therefore, the assumption of $CaCO_3$ being uniformly formed across the cycled particles during the carbonation stage seems to be fine.

An interesting result from this study was that the *f*(*X*) function determined from the measurements on the Compostilla limestone has been applied successfully in modelling the conversion of the Purbeck limestone. This implies that the evolution of the pore structure of both limestone particles are similar during calcination. One hypothetical reason for this observation is related to the cycling process of the limestones, where the change of pore structure become more stable as number of cycles increases. In fact, a study of the sulphation rate of cycled lime particles showed that different limestones followed a very similar conversion *vs.* time evolution after 50 cycles (Arias *et al.*, 2012), which indicates that the cycling process does affect how the pore structure evolves with conversion.

5.5.2 The effect of pressure and concentration

The isobaric assumption within a porous particle has often been taken in order to simplify the model of intraparticle diffusion. However, Table 5.6 shows that the variation of total pressure needs to be considered for a more rigorous description of diffusion within the particle. For example, at 1198 K and atmospheric pressure, the initial total pressure at the particle centre can be 1.57 times of the bulk pressure. Therefore, the intraparticle pressure gradient should not be neglected without good

justification, especially at low pressure or high temperature. This is in general agreement with the conclusions of Khinast *et al.* (1996). However, the variation of total pressure has been found to be more significant than that reported by Khinast *et al.* (1996), possibly owing to their use of the Dusty Gas Model.

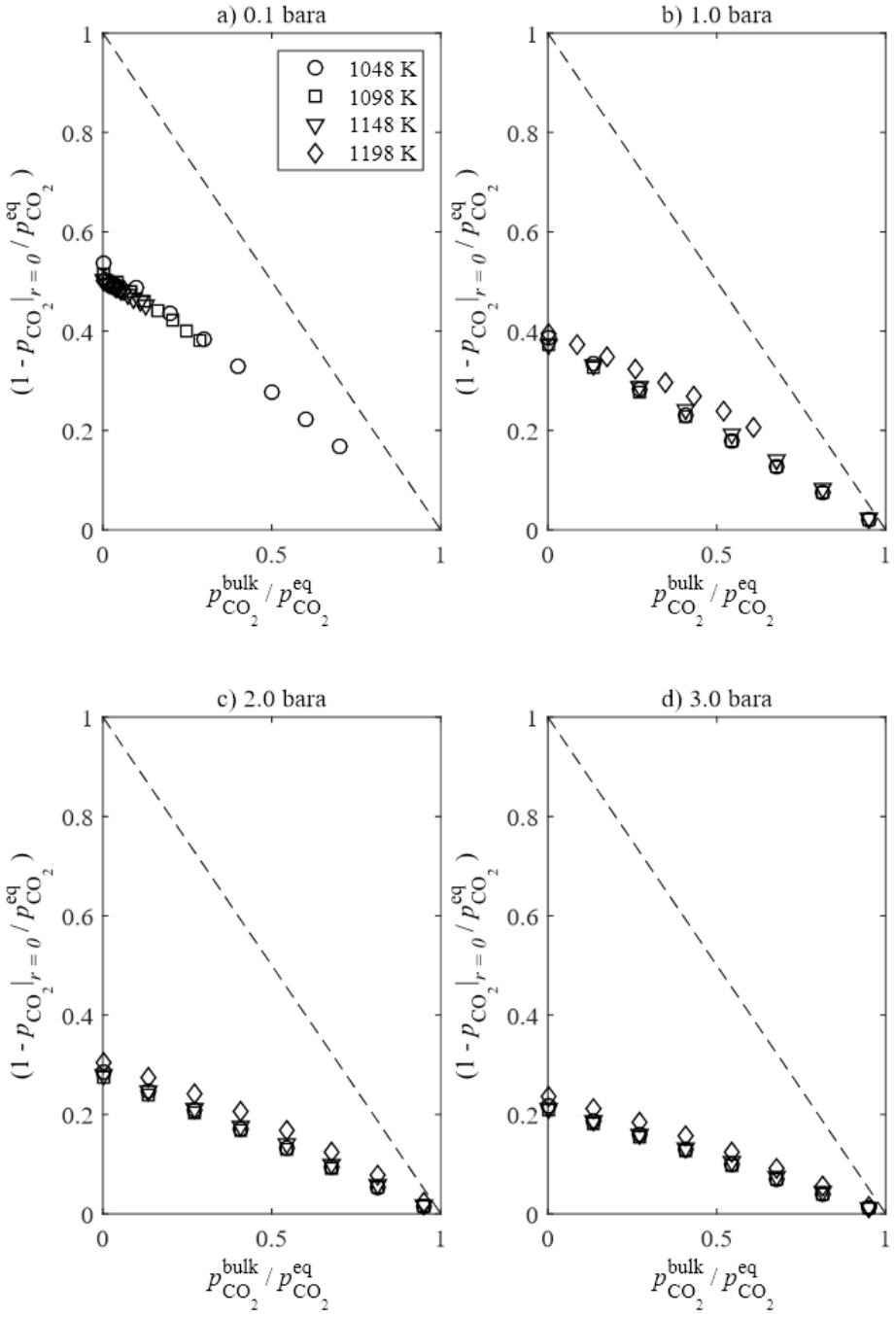

Figure 5.15 Plot of $\left(1 - p_{CO_2}|_{r=0}/p^{eq}_{CO_2}\right)$ *vs.* $p^{bulk}_{CO_2}/p^{eq}_{CO_2}$ for simulations at 0.1 – 3.0 bara and 1048 – 1198 K. The broken line indicates the ideal case where $p_{CO_2}|_{r=0} = p^{bulk}_{CO_2}$.

Figure 5.15 shows a plot of the normalised partial pressure driving force $\left(1 - p_{CO_2}|_{r=0}/p^{eq}_{CO_2}\right)$ against normalised bulk partial pressure $p^{bulk}_{CO_2}/p^{eq}_{CO_2}$. Even though

the points produced by the model show a curved trend, a straight line of $\left(1 - p_{\mathrm{CO_2}}|_{r=0}/p^{\mathrm{eq}}_{\mathrm{CO_2}}\right) = m\left(1 - p^{\mathrm{bulk}}_{\mathrm{CO_2}}/p^{\mathrm{eq}}_{\mathrm{CO_2}}\right)$, where *m* is the intercept at y-axis, would have fitted them well. Khinast *et al.* (1996) proposed an exponentially-decaying function $\exp(-a\, p^{\mathrm{bulk}}_{\mathrm{CO_2}}/p^{\mathrm{eq}}_{\mathrm{CO_2}})$ with $a = 11.92$ to describe how the $p^{\mathrm{bulk}}_{\mathrm{CO_2}}$ influences the driving force when $0 < y^{\mathrm{bulk}}_{\mathrm{CO_2}} \leq 0.065$ at 1053 K and 1 bara. Other workers have used a power law function $\left(1 - p^{\mathrm{bulk}}_{\mathrm{CO_2}}/p^{\mathrm{eq}}_{\mathrm{CO_2}}\right)^b$ with b ranging from 1 to 2 (Rao *et al.*, 1989; Silcox *et al.*, 1989; Fuertes *et al.*, 1993; Hu & Scaroni, 1996). It should be noted that neither the exponentially-decaying function nor the power law function matches the results in Figure 5.15, because the shape of both functions is different from that of the simulated results.

Interestingly, all the data points at different temperatures cluster closely around a single line, indicating that the effect of $p^{\mathrm{bulk}}_{\mathrm{CO_2}}$ on the partial pressure driving force is almost unchanged at different temperatures. Figure 5.15 confirms that higher $p^{\mathrm{bulk}}_{\mathrm{CO_2}}$ leads to lower normalised driving force $\left(1 - p_{\mathrm{CO_2}}|_{r=0}/p^{\mathrm{eq}}_{\mathrm{CO_2}}\right)$ hence lower calcination rate. In addition, the trend shows that the driving force $\left(1 - p_{\mathrm{CO_2}}|_{r=0}/p^{\mathrm{eq}}_{\mathrm{CO_2}}\right)$ is always smaller than, and diverging from, the line representing $\left(1 - p^{\mathrm{bulk}}_{\mathrm{CO_2}}/p^{\mathrm{eq}}_{\mathrm{CO_2}}\right)$ as bulk pressure increases. This behaviour was observed by Dennis & Hayhurst (1987), where they proposed that the rate of calcination, per unit area of reacting interface, q_{c}, was controlled by intrinsic chemical kinetics at the interface, and not by diffusional resistances to flow through the porous oxide. Accordingly,

$$q_{\mathrm{c}} = \bar{k}\left(p^{eq}_{\mathrm{CO_2}} - p^{\mathrm{bulk}}_{\mathrm{CO_2}} - P_{\mathrm{bulk}} y_I\right) \tag{5-16}$$

where $p^{eq}_{\mathrm{CO_2}}$ is the equilibrium partial pressure of CO_2 at the temperature concerned, P_{bulk} is the bulk pressure of the system and $\bar{k}$ is the intrinsic rate constant for the carbonation reaction (*viz.* the reverse of reaction (5-I)) per unit area of interface. The term $P_{\mathrm{bulk}} y_I$, where y_I was a constant at a given temperature, was an empirical factor introduced to account for the fact that, when $p^{\mathrm{bulk}}_{\mathrm{CO_2}} = 0$, the rate of calcination was still affected by the overall pressure of the system, as if a fictitious mole fraction, y_I, existed at the reaction interface. They concluded that very complex processes must occur at the interface.

Although, Dennis & Hayhurst (1987) reported that the calcination of their fresh limestones followed a shrinking core mechanism and was kinetically controlled, it was likely that the limestones experienced some degree of intraparticle mass transfer limitation. Hence the partial pressure of CO_2 at the surface of the unreacted core of limestone was greater than in bulk partial pressure, as a result of the intraparticle gradient of the CO_2 partial pressure across the porous product layer of CaO. In addition, the reaction zone inside the limestone was very likely to be wider than a sharp interface, especially if there were pores inside the unreacted core allowing CO_2 to escape. Hence the unreacted core of the limestone would actually experience a partial pressure of CO_2 very close to the equilibrium partial pressure. Therefore, it seems clear that the spurious partial pressure of CO_2, $P^{\text{bulk}}y_I$, introduced by Dennis & Hayhurst (1987) represents an overall average value over the entire particle during the period of the calcination of the particle. The value of y_I can be calculated by

$$y_I = \frac{1}{P_{\text{bulk}} t_c} \int_0^{t_c} \left(\int_0^1 3{\eta_r}^2 \left(p_{\text{CO}_2}|_r - p_{\text{CO}_2}^{\text{bulk}} \right) d\eta_r \right) dt \tag{5-17}$$

where η_r is the dimensionless radius and t_c is the time for complete calcination of the particle. Further simulations based on the particle parameters reported by Dennis & Hayhurst (1987) were run to estimate the values of y_I, the results of which are shown in Table 5.7 and Figure 5.16. At low temperature, the value of y_I from the simulation is very close to that reported by Dennis & Hayhurst (1987). As the temperature increases, the simulation predicts somewhat larger values of y_I. In addition, there is a highly linear trend shown in Figure 5.16 between the value of y_I estimated from the simulation and that obtained by Dennis & Hayhurst (1987).

Table 5.7 Comparison of the values of y_I.

T_{bulk} / K	$p_{\text{CO}_2}^{\text{eq}}$ / bar	y_I from Dennis & Hayhurst (1987)	y_I from simulation
1098	0.330	0.07	0.09
1148	0.744	0.10	0.18
1198	1.565	0.17	0.29

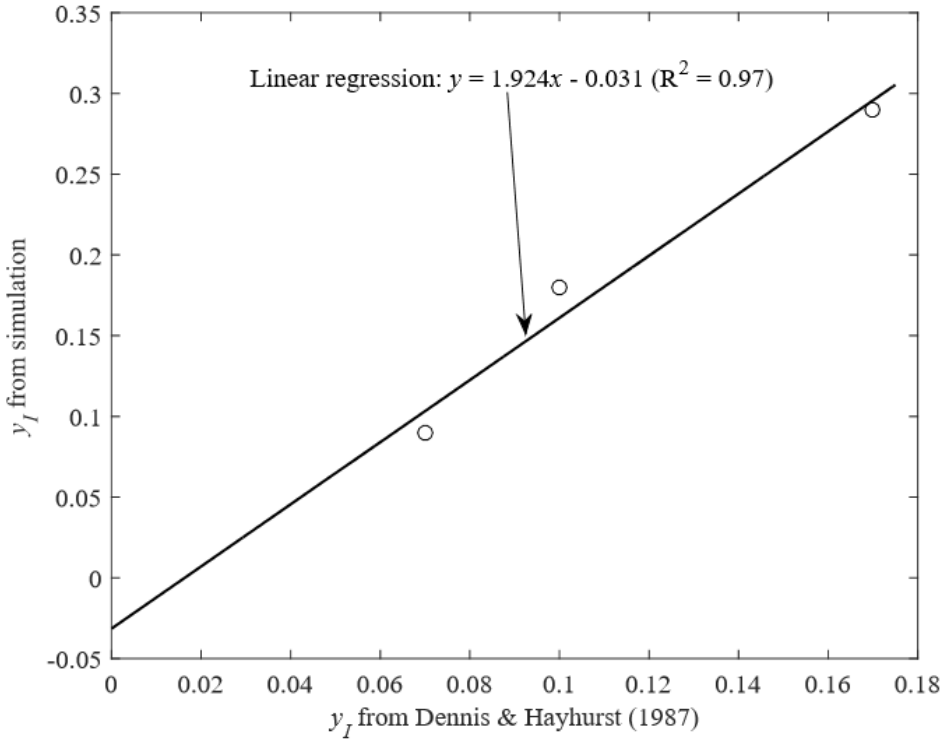

Figure 5.16 Comparing the values of y_I estimated from simulation results using Eq. (5-17) and that of Dennis & Hayhurst (1987). A linear regression of the two sets of values gives a high goodness of fit ~ 0.97.

The values of y_I reported by Dennis & Hayhurst (1987) were originally obtained by plotting $\left(p_{\mathrm{CO_2}}^{\mathrm{eq}} - p_{\mathrm{CO_2}}^{\mathrm{bulk}}\right)/P_{\mathrm{bulk}}$ against $r_p/t_c P_{\mathrm{bulk}}$. This followed from the justification that the reaction occurred as a shrinking core mechanism and was kinetically controlled, giving

$$t_{\mathrm{c}} = \frac{r_p}{\bar{k} V_{M,\mathrm{CaCO_3}} \left(p_{\mathrm{CO_2}}^{\mathrm{eq}} - p_{\mathrm{CO_2}}^{\mathrm{bulk}} - P_{\mathrm{bulk}} y_I\right)} \tag{5-18}$$

where $V_{M,\mathrm{CaCO_3}}$ is the molar volume of $CaCO_3$. The general increase in the values of y_I with temperature, shown in Table 5.7, agrees with the experimental observation by Dennis & Hayhurst (1987), who noted that y_I depends only on the temperature of the fluidised bed reactor. While the current model predicts some changes in y_I when $y_{\mathrm{CO_2}}^{\mathrm{bulk}}$ and P_{bulk} are changed, the effects of $y_{\mathrm{CO_2}}^{\mathrm{bulk}}$ are small compared to the effects of temperature and pressure. It should be noted that the vertical distance between the data points and the broken line is significantly smaller at high $p_{\mathrm{CO_2}}^{\mathrm{bulk}}$ in Figure 5.15, which indicates that the values of y_I reduce considerably with increasing $p_{\mathrm{CO_2}}^{\mathrm{bulk}}$. This is in line

with the observations of Dennis & Hayhurst (1987) who found departures from their proposed model when the experimental values of $p_{CO_2}^{bulk}$ were large.

García-Labiano *et al.* (2002) attempted to explain the effect of CO_2 concentration by using the Freundlich isotherm and a modified Langmuir-Hinshelwood adsorption model for the rate expression. To explain the effects of bulk pressure, they modified the equation for molecular diffusivity by Fuller *et al.* (1966) by introducing a fitting parameter, *m*, to the pressure term. While there was fair agreement with their experimental results, there was little justification given towards the physical interpretation of the fitting parameters, introduced in their rate expressions and models diffusivity. While it is recognised that complex processes occur at the calcination interface, it has been demonstrated that by using a more rigorous description of reaction and diffusion through the porous particle, the experimentally observed effects of CO_2 mole fraction and bulk pressure observations can, at least to some extent, be explained.

5.5.3 Sensitivity of the apparent *f*(*X*)

Assuming the intrinsic *f*(*X*) function is known, then an apparent *f*(*X*) function could be determined from the plot of the normalised rate against conversion at any condition. The apparent *f*(*X*) function should be the same as the intrinsic *f*(*X*) function when the reaction is kinetically controlled, whereas it will be different from the intrinsic *f*(*X*) function when there is significant intraparticle mass transfer resistance. The mass transfer resistance is affected by the particle properties and reaction conditions. Here, the sensitivities of the apparent *f*(*X*) function to the particle size, pore diameter, porosity and reaction temperature are studied, through simulation studies using the calcination reaction as an example. The variable input parameters are listed in Table 5.8 and the constant input parameters required by the model are shown in Table 5.9.

Table 5.8 The parameters to be varied during simulation.

Parameter	Temperature / K	Particle size / μm	Pore diameter / nm	Pore volume / cm^3 g^{-1}
Value 1	973	100	25	0.025
Value 2	1223	1600	200	0.2

Table 5.9 Input parameters of the model for simulating the calcination of $CaCO_3$.

Configuration	Parameter	Value
(1) Bulk conditions	Pressure, P^B / Bar	1.013
	Mole fraction of CO_2, $y^B_{CO_2}$	0
	Mole fraction of N_2, $y^B_{N_2}$	1
(2) Solid particle	Mass fraction of $CaCO_3$	1
	Mass fraction of CaO	0
	Skeletal density / kg m^{-3}	2710
	BET area / m^2 g^{-1}	2.0
	Tortuosity factor	1.41
(3) Fluidised bed	Fluidising gas flow rate (STP) / ml s^{-1}	80
	Particle diameter / μm	400
	Particle density / kg m^{-3}	2648
	Bed diameter / mm	30
	Voidage at incipient fluidisation, ε_{mf}	0.44
	Bed height at incipient fluidisation, H_{mf} / mm	29
	Tortuosity factor	1.34

Figure 5.17 and Figure 5.18 show the simulation results of the apparent *f*(*X*) function for calcination reaction occurring at 973 K and 1273 K, where a simple function of $f(X) = 1 - X$ is used as the intrinsic *f*(*X*) function. Figure 5.19 and Figure 5.20 show the case where the intrinsic *f*(*X*) function is $f(X) = (1 - X)^2$. Comparing the four figures, some general patterns can be recognised:

i) As expected, in kinetically controlled regime, *e.g.* initial effectiveness factor ≥ 0.9, the apparent *f*(*X*) functions coincide with the intrinsic *f*(*X*) functions, regardless of the reaction temperature and the particle properties.

ii) The effect of temperature: for small particles, the apparent *f*(*X*) function at a high temperature changes more from the intrinsic *f*(*X*) function than that at a low temperature. Whereas it becomes the opposite for the large particles – the apparent *f*(*X*) function at a low temperature differs more from its intrinsic form than that at a high temperature.

iii) The effect of pore diameter: for small particles, the apparent $f(X)$ function generally becomes closer to the intrinsic $f(X)$ function as the pore diameter increases. However, for large particles, this only occurs to the front end of the apparent $f(X)$ function. The back end could either moves further away or show no change as the pore diameter increases. The shape of the apparent $f(X)$ function can change significantly due to the change in pore diameter.

iv) The effect of pore volume: the apparent $f(X)$ function of particles with a large pore volume is generally lower than that of particles with a small pore volume. Note here, a pore volume of 0.2 cm^3/g corresponds to a porosity of 0.35 and a pore volume of 0.025 cm^3/g corresponds to a porosity of 0.06. The shape of the apparent $f(X)$ function can also change significantly due to the change in pore volume.

v) The effect of particle size: with the large particle, the apparent $f(X)$ function generally increases in magnitude and becomes further away from the intrinsic $f(X)$ function. The most significant increase in the apparent $f(X)$ function seems to be within 0.1 – 0.2 conversion. Large particles seem to amplify the effect of other factors.

vi) The initial effectiveness factor was not a consistent indicator for the changes in the apparent $f(X)$ function, since the change of the apparent $f(X)$ function does not seem to follow a uniform trend as the effectiveness factor reduces.

vii) Regardless of the shape of the intrinsic $f(X)$ function, the shapes of the apparent $f(X)$ function for particles with the initial effectiveness factor < 0.3 all become similar *i.e.* rising rapidly toward a peak at ~10 – 20% conversion and then gradually reducing to 0 at 100% conversion. However, the magnitude of the apparent $f(X)$ function does show difference *e.g.* the apparent $f(X)$ functions in Figure 5.18b are noticeably higher than those in Figure 5.20b.

In conclusion, the intrinsic $f(X)$ function is important when reaction is kinetically controlled, since it governs the evolution of the rate and conversion of the reaction. As the mass transfer limitation increases, either by changing the reaction conditions or the particle properties, the apparent $f(X)$ function will evolve into a more complex shaped curve and become very different from the shape of the intrinsic $f(X)$ function. Although, it can be argued that the exact form of the intrinsic $f(X)$ function in mass transfer limited regime might not be as important as in kinetically controlled regime, the simulation results here show that intrinsic $f(X)$ function does seem to still affect the absolute path of

the evolution of the rate and conversion of the reaction. The reason is that the particle becomes more porous during calcination, which results in less resistance from mass transfer as reaction proceeds. Hence, the intrinsic $f(X)$ function becomes more and more important at the later stage of the reaction.

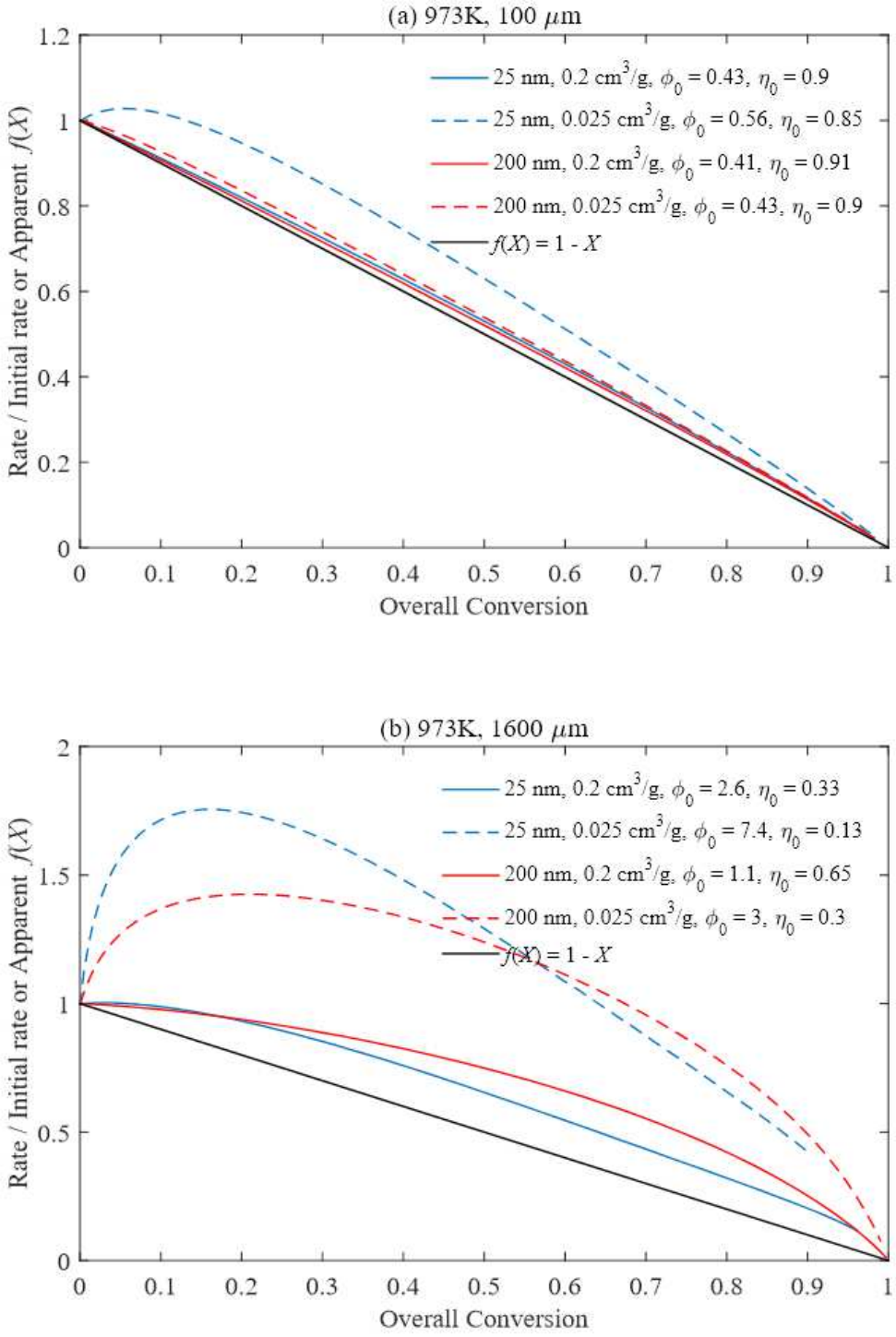

Figure 5.17 The apparent $f(X)$ function of calcination of $CaCO_3$ at 973 K, with different particle size (unit: μm), pore diameter (unit: nm) and pore volume (unit: cm^3/g). The value of ϕ_0 is the initial Thiele modulus and η_0 is the initial effectiveness factor. The intrinsic $f(X)$ function is $f(X) = 1 - X$.

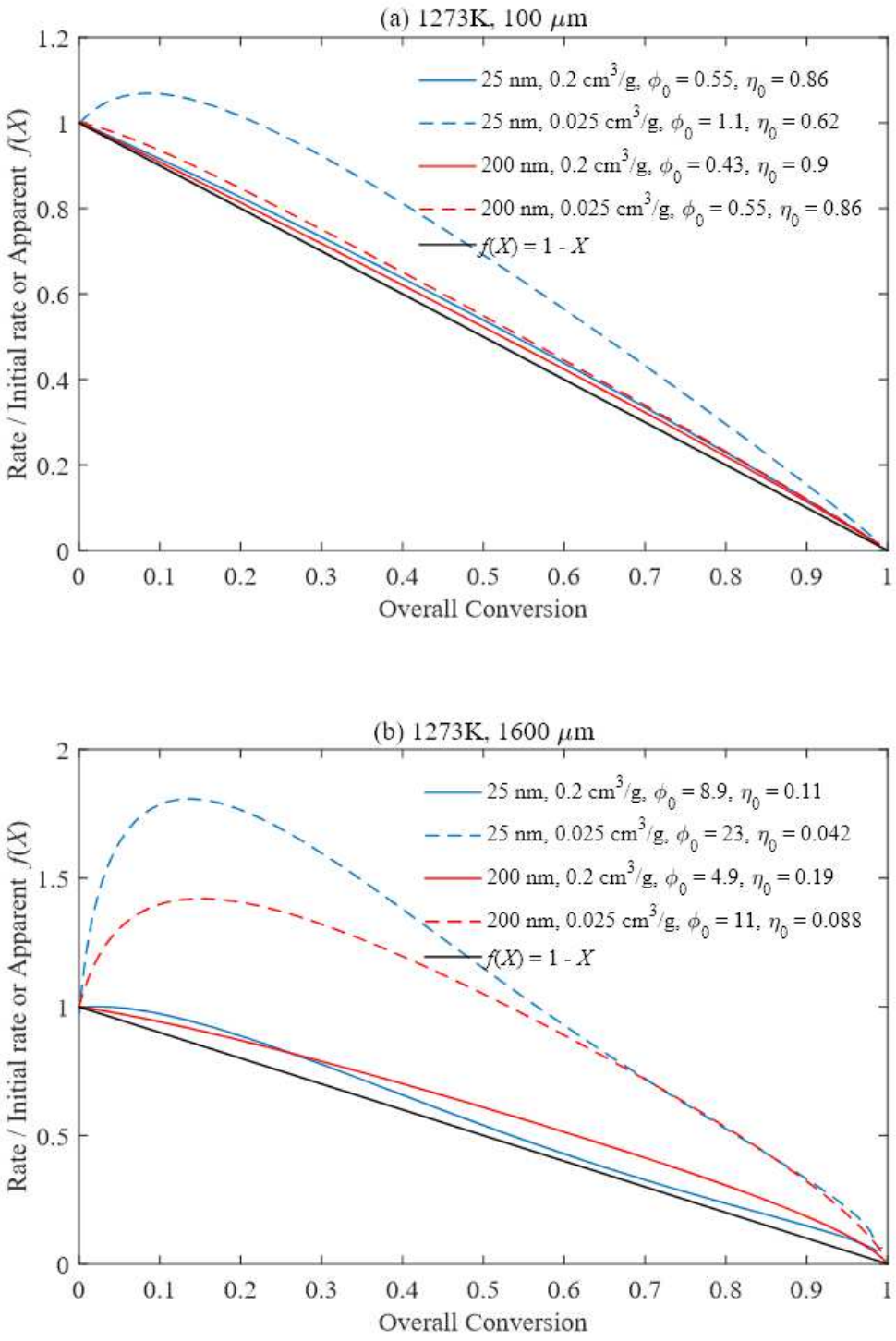

Figure 5.18 The apparent $f(X)$ function of calcination of $CaCO_3$ at 1273 K, with different particle size (unit: μm), pore diameter (unit: nm) and pore volume (unit: cm^3/g). The value of ϕ_0 is the initial Thiele modulus and η_0 is the initial effectiveness factor. The intrinsic $f(X)$ function is $f(X) = 1 - X$.

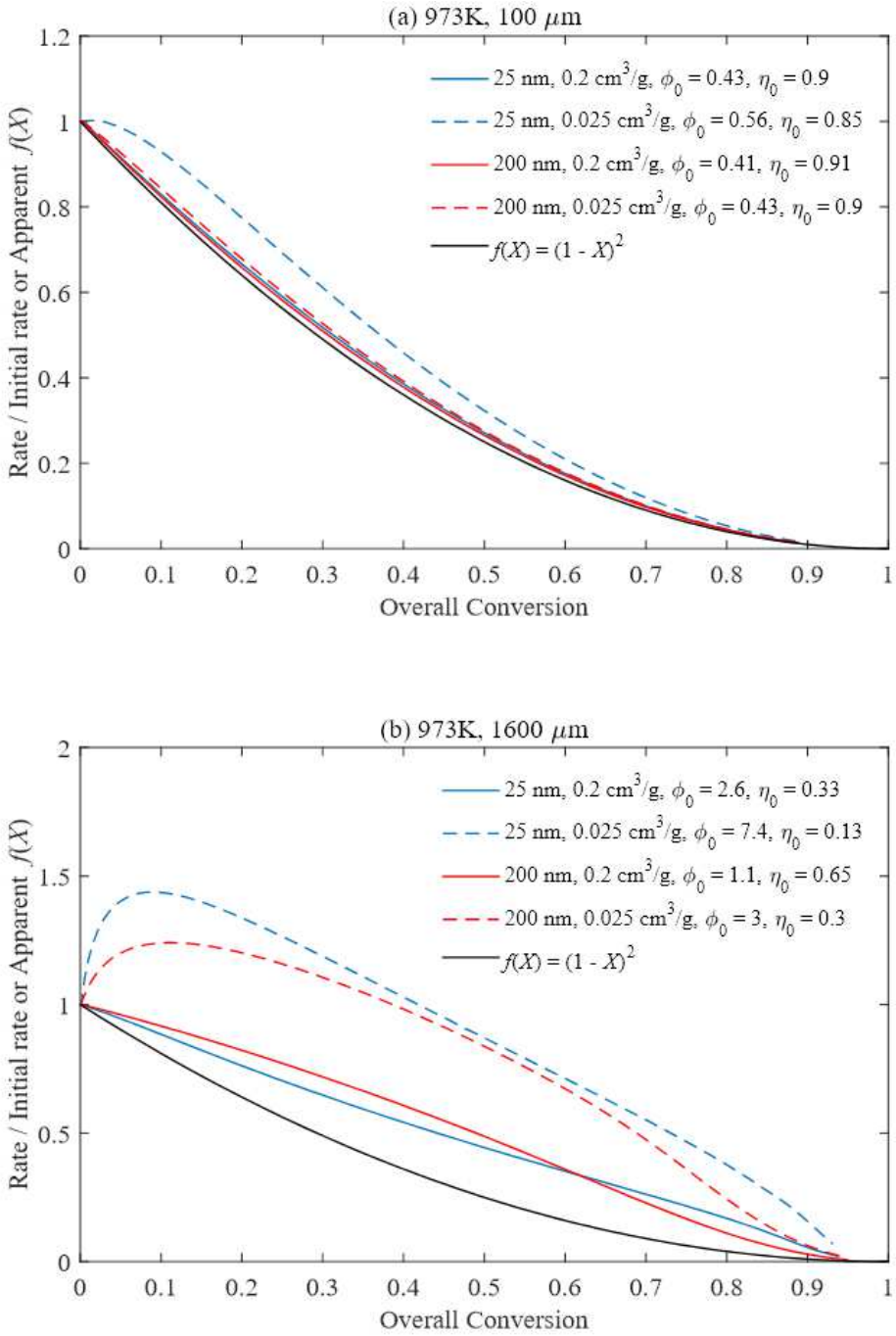

Figure 5.19 The apparent $f(X)$ function of calcination of $CaCO_3$ at 973 K, with different particle size (unit: μm), pore diameter (unit: nm) and pore volume (unit: cm^3/g). The value of ϕ_0 is the initial Thiele modulus and η_0 is the initial effectiveness factor. The intrinsic $f(X)$ function is $f(X) = (1 - X)^2$.

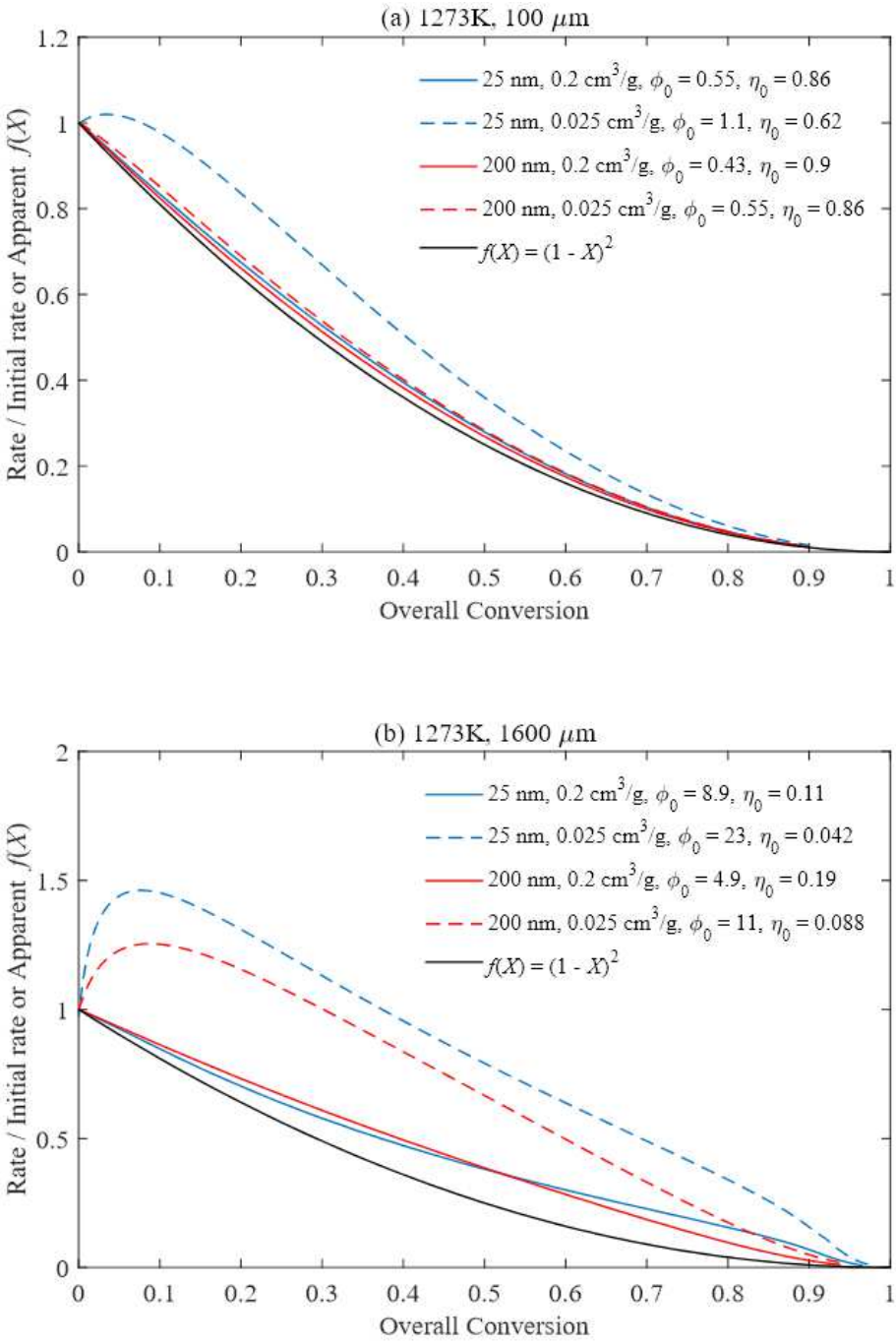

Figure 5.20 The apparent $f(X)$ function of calcination of $CaCO_3$ at 1273 K, with different particle size (unit: μm), pore diameter (unit: nm) and pore volume (unit: cm^3/g). The value of ϕ_0 is the initial Thiele modulus and η_0 is the initial effectiveness factor. The intrinsic $f(X)$ function is $f(X) = (1 - X)^2$.

5.6 Conclusions

The reaction and diffusion model developed in Chapter 3 was applied to a different type of non-catalytic gas-solid reaction here – the calcination of limestones. The limestones were subjected to a history of cycling between the calcined and carbonated states in a fluidised bed reactor in order to create a pore structure that would

allow the calcination reaction to occur continuously across the particle rather than occurs on a sharp front. The experimentally-determined function, $f(X)$, which has been shown to be effective in describing the change in the pore structure during gasification across different particle sizes, was applied to two different limestones, each with two particle sizes, across different temperature. Excellent agreement between experiment and theory was obtained, and the model using the $f(X)$ approach predicted the conversion of particles of various sizes well at temperatures different to that at which the function was derived, thus indicating that the $f(X)$ is solely dependent on the evolution of the morphology of the particle. In addition, it was found that the $f(X)$ determined from Compostilla limestone was successful in predicting the conversion of Purbeck limestones, which indicated that the two limestones had a similar evolution of pore structure after the first carbonation. This observation was attributed to the hypothesis that the calcination – carbonation cycling process might have significantly reduced the difference in the pore structures of the limestone particles and made them more homogenous.

This study also investigated the reasons behind the experimentally-observed effects of bulk pressure, temperature and CO_2 mole fraction on the rate of calcination of limestone particles in a fluidised bed. It could be concluded that the rate of reaction was proportional to the difference between equilibrium partial pressure of CO_2 and the local partial pressure of CO_2 inside the particle. A rise in either the bulk pressure or the bulk CO_2 mole fraction would increase the local partial pressure of CO_2 inside the particle, which reduced the partial pressure driving force and hence the rate of reaction. Moreover, the effect of bulk CO_2 mole fraction on the local partial pressure of CO_2 was most significant at high pressure. When temperature increased, the equilibrium partial pressure of CO_2 grew at a higher rate than the local partial pressure of CO_2, so the partial pressure driving force increased. Hence, the observed rate of reaction was larger at high temperature. It was demonstrated that in order to describe the diffusion of CO_2 through the porous particle, the variation of both bulk pressure and CO_2 concentration needed to be considered. The partial pressure driving force of the reaction rate displayed almost a linear relationship with the bulk partial pressure of CO_2, which varied little with the temperature. The previously reported parameter y_I of Dennis & Hayhurst (1987) was better explained as the difference between an average value of the local partial pressure of CO_2 inside the particle and that of the bulk environment, normalised

by the bulk pressure. The value of y_I decreased significantly when the bulk partial pressure of CO_2 became close to the equilibrium partial pressure.

Through simulation, it was shown that as the mass transfer limitation increases, the apparent $f(X)$ function would evolve into a more complex shaped curve and became very different from the shape of the intrinsic $f(X)$ function. The intrinsic $f(X)$ function was important in both the kinetically controlled and the mass transfer controlled regimes.

Chapter 6 Modelling the reaction and diffusion processes of the sulphation of limestone calcines

6.1 Introduction

A third type of non-catalytic gas-solid reaction involves the formation of a solid product which takes up more volume than the initial reacting solid, hence resulting in a lower surface area, smaller pore volume and more closed pore structure. This type of reaction can be extremely difficult to simulate owing to increased intraparticle resistance to mass transfer arising from the complicated changes in the pore structure. The sulphation of calcined limestone with SO_2 and O_2 is one such reaction and represents an industrial process for removing sulphur from flue gases, particularly in fluidised bed combustion.

The aim of the present chapter was to (i) investigate whether the reaction and diffusion model developed in this Dissertation can be applied to systems where the product is a solid, using sulphation of CaO as an important example, and (ii) explain the reasons for the commonly observed temperature maxima of CaO's absorption capacity of SO_2.

6.2 Experimental methods

6.2.1 Materials

Two different types of particles of the Purbeck limestone (~ 98 wt% $CaCO_3$ for the virgin uncalcined particles) were used in the experiments: (i) 355 – 500 μm dia. virgin calcine (1 calcination, 0 carbonation) and (ii) 710 – 850 μm dia. particles which had been subjected to cycles of calcination and carbonation (21 calcinations, 20 carbonations). A smaller size fraction was chosen for the virgin calcine to reduce the external mass transfer resistance since the virgin calcine generally had much bigger pore area than the cycled calcine and was substantially more reactive.

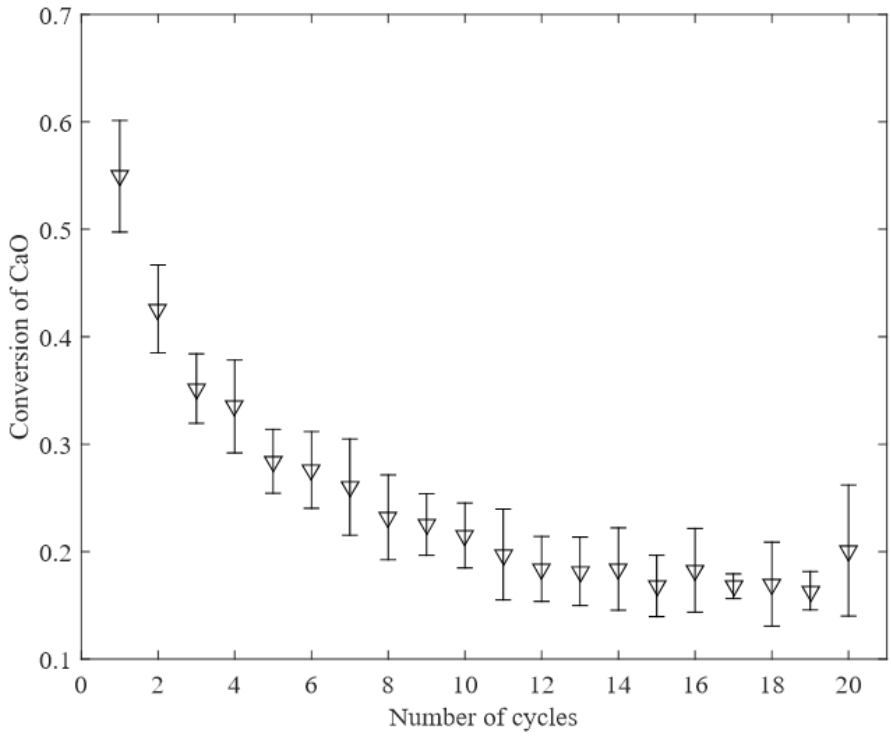

Figure 6.1 The conversion of CaO during the cycling of the 710 – 850 μm dia. Purbeck limestone particles. The error bar corresponded to the 95% confidence interval from a *t*-distribution based on five repeated measurements.

The cycling of the limestone particles was conducted in a bed of sand fluidised by 15 vol% CO_2 balance N_2 at 1 bar. In a cycling experiment, a known mass of sorbent was subjected to repeated cycles of treatments, where a single cycle consisted of the calcination of the limestone particles at 1173 K followed by the carbonation at 923 K. Both the calcination and the carbonation steps had a duration of 600 s, with a target heating rate of 30°C/min between the two temperatures. Typically, a bed containing 20 mL of 355 – 425 μm dia. silica sand, and approximately 4 g of virgin limestones was placed in the reactor. The flow rate of the fluidising gas was 41 mL/s (STP) throughout the entire cycling process, which gave a U/U_{mf} ratio of 3.4 at 923 K. To start the cycling process, the limestone particles were added to the reactor after it was filled with the sand and heated to 923 K, then the temperature control programme was switched to cycling mode to heat the reactor to the calcination temperature. The concentration of CO_2 in the exhaust gases was continuously recorded during the experiment. After the last calcination, the sample bed was removed and placed in a crucible within a desiccator and finally sieved when cool. To eliminate the absorption of moisture from the environment, the calcined samples were kept in small bottles within an air-tight container which was half filled with $CaCl_2$ sorbent. Figure 6.1 shows the CaO conversion on each cycle, which was defined as the number of mole of CO_2 absorbed

per mole of CaO present in the limestone particles during the carbonation stage and was calculated using the CO_2 concentration measurements during the calcination stage. The conversion of CaO to carbonate in the Purbeck limestone was almost constant after 20 cycles. The pore structure of the particles was characterised by BET analysis and the mercury porosimetry, as described in Chapter 2, and the results are shown in the section 6.4.1.

6.2.2 Fluidised bed experiments

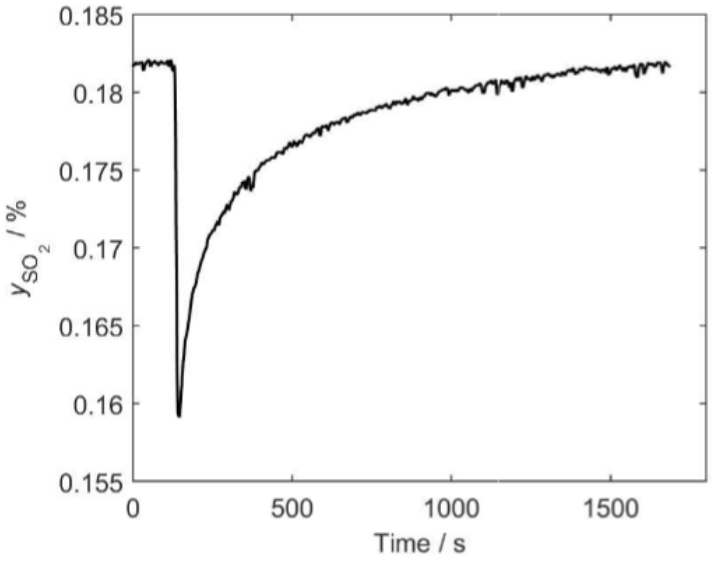

Figure 6.2 The measurement of the concentration of SO_2 during the sulphation of the 710 – 850 μm dia. Purbeck cycled calcine in 1800 ppm SO_2, 5.2 vol% O_2 balance N_2 at 1223 K.

Batch experiments were performed in the fluidised bed described in Chapter 2. In an experiment, the reactor was filled with 20 mL of silica sand and heated to the desired temperature, *viz.* 973 – 1223 K. This range of temperature was chosen to ensure that $CaSO_4$ was the only thermodynamically-stable product. The fluidising gas was 1800 ppm SO_2 and 5.2 vol% O_2 balance N_2 and the total volumetric flowrate was 80 mL s^{-1} (STP), giving U/U_{mf} ~ 5.8 – 8.4, with U being the superficial velocity at the temperature of the bed and U_{mf} being the value at incipient fluidisation predicted from the correlation of Wen & Yu (1966). A known mass of limestone particles was added to the bed 1 minute after the bed temperature had reached the target level and the gas concentration had stabilised. To ensure complete sulphation of the limestones, the experiment was terminated 10 seconds after the measured concentration of SO_2 of the off-gas had returned to its initial value. Each experiment was repeated at least 3 times.

An example of the raw measurement of the SO_2 concentration during the sulphation of the cycled calcine at 1223 K is shown in Figure 6.2.

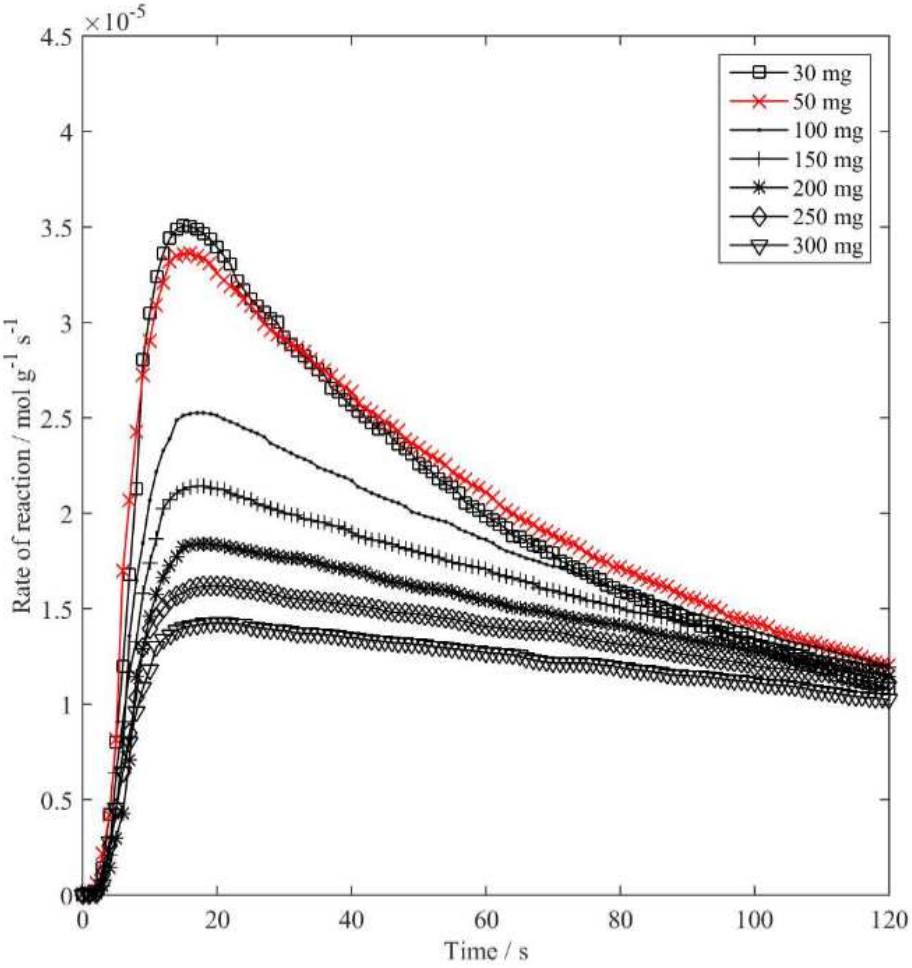

Figure 6.3 The experimental measurements of the rate of reaction of the Purbeck virgin calcine at 1173 K with 10 – 300 mg of sample mass. The 50 mg curve was shown in red.

Experimental measurements using different sample masses of the 355 – 500 μm dia. Purbeck virgin calcine ranging from 10 – 300 mg at 1173 K were conducted to determine the appropriate sample mass and the results are shown in Figure 6.3. The reaction rate appears to decrease when the sample mass was bigger than 50 mg due to complications arising from mass transfer between the bubble and the particulate phases. Hence a sample mass of 50 mg was chosen for all experiments.

The rate of the reaction and the conversion were calculated from the measurements of [SO_2] by:

$$\hat{Q}_{\mathrm{CaSO_4}} = \frac{1}{m_{\mathrm{CaO}}}\left(\frac{\dot{N}_{in} y_{\mathrm{N_2},in}}{y_{\mathrm{N_2},out}} y_{\mathrm{SO_2},out} - \dot{N}_{in} y_{\mathrm{SO_2},in}\right) \tag{6-1}$$

where $\hat{Q}_{\mathrm{CaSO_4}}$ was the rate of sulphation in mol g^{-1} s^{-1}, m_{CaO} was the mass of CaO in the sample batch, $\dot{N}_{in}$ was the total mole of gas fed into the bed and y was the mole fraction of gas species. The molar conversion to $CaSO_4$ was calculated from

$$X = M_{\mathrm{CaO}} \int \hat{Q}_{\mathrm{CaSO_4}}\, dt = 56 \int \hat{Q}_{\mathrm{CaSO_4}}\, dt \qquad (6\text{-}2)$$

The rate measurements were deconvoluted using the model described in Appendix D, consisting of 2 constant stirred tank reactors (CSTR) in series with a plug flow reactor (PFR), to account for the mixing and delay in the sampling line. The mean residence times for the two CSTRs were found to be 3.38 s and 3.39 s. Compared to the time scale of sulphation reaction, ~ 1000 – 3000 s, the time constants of the CSTRs were negligible.

6.3 Theoretical methods

6.3.1 Modelling the kinetics of sulphation

The assumptions made in Chapter 3 when developing the general reaction and diffusion model also applied here, except that the temperature of the particle surface was assumed to be close to the temperature of the bulk as the heat transfer coefficient between the particulate phase of the fluidised bed and the surface of the particle was large. Since outside the solid particle, the convective heat transfer in a bubbling fluidised bed involved packets of sand particles coming into contact with the particle for a short time, then quickly moving away to be replaced by other packets. The overall reaction occurring in the reactor was:

$$\mathrm{CaO_{(s)}} + \mathrm{SO_{2(g)}} + \frac{1}{2}\mathrm{O_{2(g)}} \rightleftharpoons \mathrm{CaSO_{4(s)}} \quad \Delta H^0_{1123} = -481.4\ \mathrm{kJ\ mol^{-1}} \qquad (6\text{-III})$$

Following the studies of gasification and calcination, the evolution of the internal morphology of a calcined limestone particle during sulphation was also assumed to be described by an arbitrary *f*(*X*). The *f*(*X*) function was taken to be capable of being applied at any point in a particle and to be independent of temperature. Following gasification and calcination, the form of *f*(*X*) for sulphation should be obtainable from a plot of the experimental rate of sulphation against conversion in experiments in which the rate is controlled *solely* by intrinsic chemical kinetics. Normally, the *X* here would

be defined as the local conversion of $CaSO_4$ within the calcined limestone particle. The value of $f(X)$ changes with the local conversion, which will vary with distance from the centre of the particle. However, the conversion to $CaSO_4$ usually cannot reach 100% during the sulphation of calcined limestones, because in theory the reaction will stop once all the pore volume are filled with the $CaSO_4$ product, which has a molar volume ~3 times of that of CaO. This means an alternative definition of the conversion is needed for the $f(X)$ function so that the value of $f(X)$ can be 1 and 0 at conversions of 0 and 1, respectively. Therefore, X', defined as the conversion normalised by the theoretical maximum conversion when all the pore volume is filled with $CaSO_4$, was used in the $f(X')$ function. The $f(X')$ function should be capable of being determined from experimental measurements of the rate and conversion of the virgin calcine particles in the regime where internal mass transport is not rate-controlling. In this case, the conversion of $CaSO_4$ should be uniform across the particle and the reaction should reach 100% of the theoretical maximum conversion given by Eq. (6-25). However, in all the experiments undertaken in the relevant regime, the sulphation reactions stopped before the theoretical maximum conversion was reached despite a long reaction time. Thus it was not possible to determine the $f(X')$ function from experiments. This issue can be resolved by using a predefined $f(X')$ function such as $f(X') = 1 - X'$ across all temperatures.

There are two thermodynamically-feasible routes that the sulphation process could follow:

$$(a):\ \mathrm{CaO_{(s)}} + \mathrm{SO_{2(g)}} \rightleftharpoons \mathrm{CaSO_{3_{(s)}}} \tag{6-IV}$$

$$\mathrm{CaSO_{3_{(s)}}} + \frac{1}{2}\mathrm{O_{2(g)}} \rightleftharpoons \mathrm{CaSO_{4_{(s)}}} \tag{6-V}$$

or

$$(b):\ \mathrm{SO_{2(g)}} + \frac{1}{2}\mathrm{O_{2(g)}} \rightleftharpoons \mathrm{SO_{3_{(g)}}} \tag{6-VI}$$

$$\mathrm{SO_{3_{(g)}}} + \mathrm{CaO_{(s)}} \rightleftharpoons \mathrm{CaSO_{4_{(s)}}} \tag{6-VII}$$

The majority of the studies in literature have favoured route (*a*) (Dennis & Hayhurst, 1990; Hansen *et al.*, 1993; Allen & Hayhurst, 1996a, 1996b) whilst some have supported route (*b*) (Burdett, 1983; Lin, 1994). In a review of sulphation in fluidised beds, Anthony & Granatstein (2001) concluded that the work of Dennis & Hayhurst (1990) was definitive in proving that SO_3 was not a necessary precursor and the initial rate of reaction was independent of O_2 concentration for the sulphation of limestones. Dennis & Hayhurst (1990) and Allen & Hayhurst (1996a) also concluded that $CaSO_3$ would decompose at higher temperature through

$$4CaSO_3 \rightleftharpoons 3CaSO_4 + CaS \qquad \text{(6-VIII)}$$

where the CaS would be readily oxidised by O_2, thus

$$CaS + 2O_2 \rightleftharpoons CaSO_4 \qquad \text{(6-IX)}$$

Reactions (6-IV) and (6-IX) become more important at temperatures above 773 K (Zawadzki, 1932) and no $CaSO_3$ is observable in the presence of O_2 above 1123 K (Allen & Hayhurst, 1996a). Figure 6.4 shows a phase diagram for $CaSO_4$ from which it can be deduced that, under the experimental conditions used in the present research, *viz.* 1800 ppm SO_2, 5.2% O_2, balance N_2 at 973 – 1223K, $CaSO_4$ is the main product of reaction between SO_2 and CaO. Hence in this study, the mechanism of the sulphation reaction was assumed to follow route (*a*) given by reactions (6-IV) and (6-V), where $CaSO_3$ and $CaSO_4$ would be formed below 973 K and only $CaSO_4$ above 973 K. In fact, the solid species present in the sulphated particles of the 20 times cycled calcine was examined by XRD and the result is shown in Figure 6.5, which confirms that only $CaSO_4$ existed as the product of the reaction.

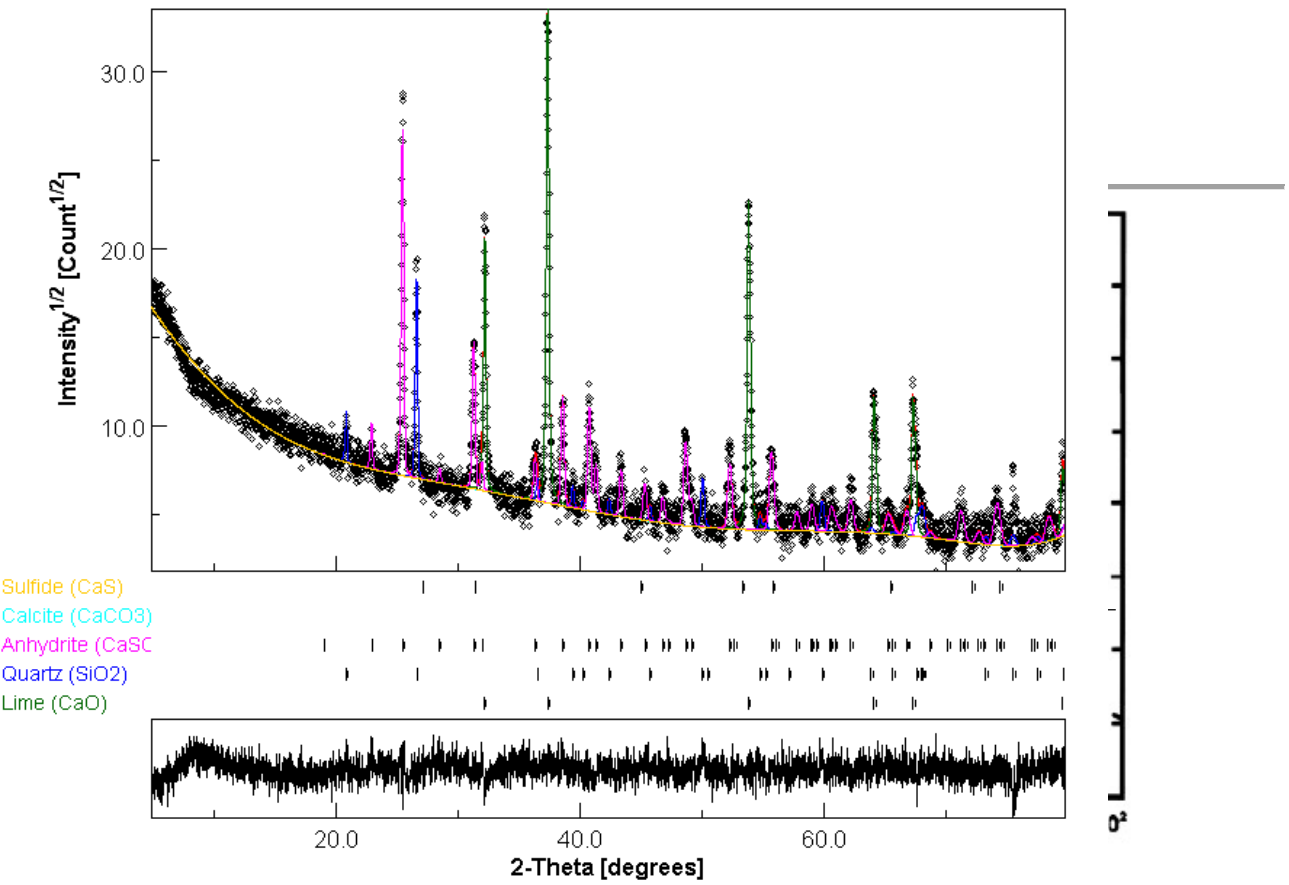

Figure 6.4 Phase diagram of the $CaSO_4$ stability (Anthony & Granatstein, 2001) with the experimental conditions of the current study marked by the black circle.

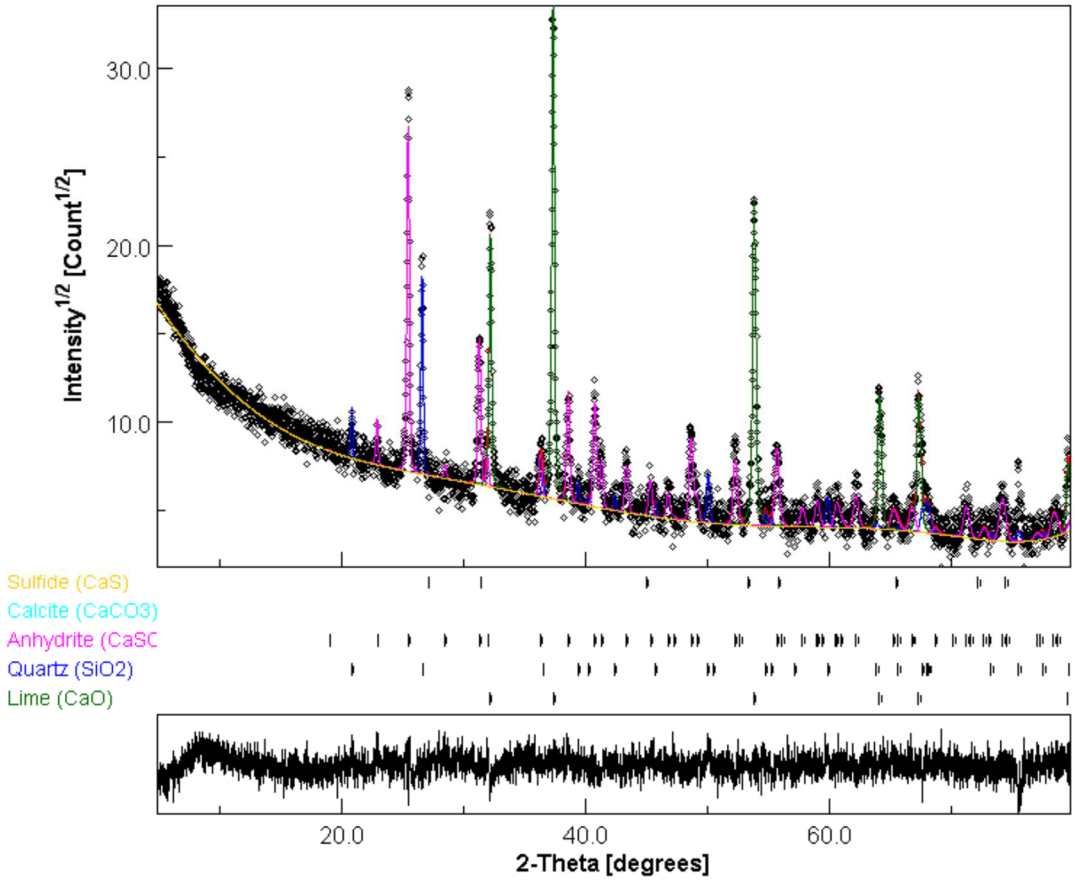

Figure 6.5 XRD measurement of the sulphated particles of the 710 – 850 µm dia. Purbeck cycled calcine at 973 K, only CaO, $CaSO_4$ and the inert impurity SiO_2 were present in the sample.

The intrinsic rate of reaction per unit internal surface area for sulphation has been found to be first order with respect to [SO_2] and independent of [O_2] (Borgwardt, 1970; Dennis & Hayhurst, 1987; Allen & Hayhurst, 1996a). Generally, product layer diffusion soon becomes rate limiting just after the pore surface has become covered by a sufficient amount of $CaSO_4$. This product-deposition aspect of gas-solid reactions was not considered in the general reaction and diffusion model presented in Chapter 3. The following addresses this omission, because the overall reaction rate should take into account diffusion through a thickening product layer. The rate equation could be written

$$Q_{\mathrm{CaSO_4}} = k_{Avg}\left(\frac{p_{\mathrm{SO_2}}}{RT}\right)A_{s,0}\rho_{e,0}f(X') \qquad X' = \frac{X}{X_{max}} \tag{6-10}$$

where $Q_{\mathrm{CaSO_4}}$ is the rate of reaction (mol m^3 s^{-1}), $p_{\mathrm{SO_2}}$ is the local partial pressure of SO_2 within the particle (Pa), $A_{s,0}$ is the initial pore area (m^2 kg^{-1}), $\rho_{e,0}$ is the initial bulk density of the particles (kg m^{-3}) and $f(X')$ describes how the rate of reaction evolves with the normalised conversion due to changes in pore structure. The maximum absorption capacity of SO_2, X_{max}, is estimated by filling all the pore volume with $CaSO_4$. The overall rate constant, k_{Avg}, given by Eq. (6-11) below in m s^{-1}, can be determined from the mass balance over a cylindrical pore in its radial direction:

$$\frac{1}{k_{Avg}} = \frac{1}{k_s} + \frac{r_{pore,0}}{D_P}\mathrm{Ln}\left(\frac{r_{pore,0}}{r_{pore,0} - \Delta h}\right) \tag{6-11}$$

Here k_s is the intrinsic rate constant for sulphation in $\mathrm{m/s}$, D_P is the product layer diffusivity in $\mathrm{m^2/s}$ and Δh is the product layer thickness. The product layer diffusivity D_P follows the Arrhenius equation with the activation energy, E_{D_P}, and the pre-exponential factor, D_{P0},

$$D_P = D_{P0}\exp\left(-\frac{E_{D_P}}{RT}\right) \tag{6-12}$$

In the model, the product layer diffusivity was used as an adjustable parameter to fit the model predictions to the experimental results across temperatures, which then gave an estimate of its activation energy.

The classical picture of the product layer diffusion involves SO_2 diffusing through the $CaSO_4$ product to reach unreacted CaO. This has been assumed in many previous studies of limestone sulphation, although the high values quoted (Pigford &

Sliger, 1973; Bhatia & Perlmutter, 1981a; Anthony & Granatstein, 2001) for the activation energy in Eq. (6-12) for diffusion are inconsistent with gaseous diffusion. Borgwardt & Bruce (1986) studied the reactivity of calcines of pulverised limestone with SO_2 and suggested that the high sensitivity of the rate of reaction to temperature, taken together with the experimental apparent order of reaction with respect to [SO_2] being less than unity, implied an ionic diffusion process through the product layer. Iisa *et al.* (1992) reported the apparent activation energy of product layer diffusion to be 100 – 200 kJ mol^{-1}, and concluded that diffusion must occur *via* solid state diffusion rather than gaseous diffusion. Using a Pt-based marker on the surface of a compressed CaO tablet, Hsia *et al.* (1993) proposed that the sulphation reaction proceeded by the outward diffusion of Ca^{2+} ions through the $CaSO_4$ product layer and that the reaction occurred, in fact, at the interface between the $CaSO_4$ product and the gas in the pore. The reason given for assuming a higher mobility of the calcium ions was that smaller Ca^{2+} ion (~ 1.8 Å) is inherently more mobile than the SO_4^{2-} ion (~ 4.5 Å). In a later isotopic study using $^{32}SO_2$ and $^{34}SO_2$, it was further concluded that the Ca^{2+} and the O^{2-} ions diffused in a coupled manner from the CaO/$CaSO_4$ interface to the $CaSO_4$/gas interface when the product formed (Hsia *et al.*, 1995).

6.3.2 Evolution of pore structure

The symbols used in the following section are specific to section 6.3.2, and the definitions can be found within the text. In a limestone particle, there initially exists $CaCO_3$ and CaO, which can describe a general case for limestones after a number of carbonation and calcination cycles. The following subscripts are used in the development below to represent different solid phases: (i) $_S$ – overall particle solid, (ii) $_{CC}$ – calcium carbonate ($CaCO_3$), (iii) $_{CO}$ – calcium oxide (CaO) and (iv) $_{CS}$ – calcium sulphate ($CaSO_4$). The volume of the solids per unit mass, V_S, is given by

$$V_S = n_{CC}V_{M,CC} + n_{CO}V_{M,CO} + n_{CS}V_{M,CS} \tag{6-13}$$

where V_M is the molar volume of different solids and n is the number of mole of calcium per unit mass of particle. The total amount of calcium per unit mass, n_{TC}, is

$$n_{TC} = n_{CC} + n_{CO} + n_{CS} = n_{CC,0} + n_{CO,0} \tag{6-14}$$

Here the subscript 0 means at the start. Differentiating Eq. (6-13),

$$dV_S = V_{M,CC}dn_{CC} + V_{M,CO}(-dn_{CC} - dn_{CS}) + V_{M,CS}dn_{CS} = (V_{M,CC} - V_{M,CO})dn_{CC} + (V_{M,CS} - V_{M,CO})dn_{CS} \quad (6\text{-}15)$$

Let the conversion of $CaCO_3$, X_{CC}, and the conversion of $CaSO_4$, X_{CS}, be defined as follows:

$$X_{CC} = 1 - \frac{n_{CC}}{n_{CC,0}} \qquad X_{CS} = \frac{n_{CS}}{n_{TC}} \quad (6\text{-}16)$$

where $n_{CC,0}$ is the initial amount of the $CaCO_3$ present in the particle and would be 0 for fully-calcined limestones. Then Eq. (6-15) becomes

$$dV_S = -n_{CC,0}(V_{M,CC} - V_{M,CO})dX_{CC} + n_{TC}(V_{M,CS} - V_{M,CO})dX_{CS} \quad (6\text{-}17)$$

Hence the volume of the solid per unit mass as a function of X_{CC} and X_{CS} is

$$V_S = V_{S,0} - n_{CC,0}(V_{M,CC} - V_{M,CO})X_{CC} + n_{TC}(V_{M,CS} - V_{M,CO})X_{CS} \quad (6\text{-}18)$$

$$V_{S,0} = n_{CC,0}V_{M,CC} + n_{CO,0}V_{M,CO} \quad (6\text{-}19)$$

Similarly, the volume of the pores per unit mass is

$$V_{pore} = V_{pore,0} + n_{CC,0}(V_{M,CC} - V_{M,CO})X_{CC} - n_{TC}(V_{M,CS} - V_{M,CO})X_{CS} \quad (6\text{-}20)$$

Therefore, if $\varepsilon_0 > 0$, the porosity of the whole particle is given by

$$\varepsilon = \varepsilon_0 + \frac{1}{V_{S,0} + V_{pore,0}}\left[n_{CC,0}(V_{M,CC} - V_{M,CO})X_{CC} - n_{TC}(V_{M,CS} - V_{M,CO})X_{CS}\right] \quad (6\text{-}21)$$

If $\varepsilon_0 = 0$ and $V_{pore,0} = 0$, the porosity of the whole particle is given by

$$\varepsilon = \frac{1}{V_{S,0}}\left[n_{CC,0}(V_{M,CC} - V_{M,CO})X_{CC} - n_{TC}(V_{M,CS} - V_{M,CO})X_{CS}\right] \quad (6\text{-}22)$$

For fully-calcined limestone particles with no $CaCO_3$ present prior to sulphation, $n_{CC,0} = 0$ and the porosity becomes

$$\varepsilon = \varepsilon_0 - \frac{\varepsilon_0}{V_{pore,0}}\left[n_{CO,0}(V_{M,CS} - V_{M,CO})X_{CS}\right] \quad (6\text{-}23)$$

The maximum value of X_{CS} is reached when $\varepsilon = 0$, hence the theoretical maximum capacity of SO_2 uptake allowed by the pore volume is given by

$$X_{CS,max} = \frac{V_{\text{pore},0}}{n_{CO,0}\left(V_{M,CS} - V_{M,CO}\right)} \tag{6-24}$$

Substituting $V_{M,CS} = 46.0 \times 10^{-6}$ m^3 mol^{-1}, $V_{M,CO} = 16.9 \times 10^{-6}$ m^3 mol^{-1} and $n_{CO,0} = x_{CO,0}/(56 \times 10^{-3}$ kg mol$^{-1})$ into Eq. (6-24), where $x_{CO,0}$ is the initial mass fraction of CaO in the solid particles, gives

$$X_{CS,max} = 1924.4\left(V_{\text{pore},0}/x_{CO,0}\right) \tag{6-25}$$

Often, the molar volume of $CaSO_4$, is reported as 52.2×10^{-6} m^3 mol^{-1} which is ~3.09 times that of CaO. This value is correct for temperatures less than 473 K where the low density (2610 kg/m^3) $CaSO_4$ crystal structure is stable. For sulphation of CaO above 473 K, the density of the stable form of $CaSO_4$ should be 2960 kg/m^3, which gives a molar volume of 46.0×10^{-6} m^3 mol^{-1} (Milne *et al.*, 1990). Hence, if the other common value of $CaSO_4$ molar volume, 52.2×10^{-6} m^3 mol^{-1}, is used, the constant 1924.4 in Eq. (6-25) will become 1586.4. For a particle consisting of 100% CaO, which can be assumed for both of the Purbeck limestone calcines, Eq. (6-25) gives $V_{\text{pore},0} = 0.52 \times 10^{-6}$ m^3 kg^{-1} $= 0.52$ cm^3 g^{-1} for $X_{CS,max} = 1$, which means that the theoretical SO_2 uptake capacity can reach 100% only if the initial pore volume is bigger than 0.52 cm^3 g^{-1}.

In practice, the maximum conversion achieved during experiment is usually smaller than the theoretical value, *i.e.* there is incomplete conversion, owing to reaction being severely limited by solid state diffusion through the product layer and, or, complete blocking of the pore entrances. Hence, the pore volume being occupied by the product layer during the sulphation reaction could be much smaller than the actual total volume. In the subsequent modelling, the pore volume of the particles was treated as an adjustable parameter rather than a fixed physical constant when comparing model results to the experiments.

6.4 Results

6.4.1 Characterisation of the particles

The particle characterisation results from BET analysis and mercury intrusion porosimetry are shown in Table 6.1 and Table 6.2, and the pore size distributions are plotted in Figure 6.6. The results confirm that the surface area and the pore volume of particles which had been subjected to 20 cycles of calcination and carbonation are smaller than those of the virgin particles, calcined once, and the pores are correspondingly larger than those of the virgin particles. This is commonly observed with particles subjected to long periods of sintering.

Table 6.1 Characterisation of limestone particles by BET analysis.

Limestone	BET analysis		
	BET area / $m^2\ g^{-1}$	BJH volume / $cm^3\ g^{-1}$	BJH adsorption mean pore diameter / nm
Purbeck virgin calcine	10.53	0.19	79
Purbeck cycled calcine	3.04	0.07	114

Table 6.2 Characterisation of limestone particles by mercury porosimetry.

Limestone	Mercury intrusion porosimetry					
	Porosity	Total pore area / $m^2\ g^{-1}$	Total intrusion volume / $cm^3\ g^{-1}$	Mean pore diameter / nm	Bulk density / $kg\ m^{-3}$	Tortuosity factor / -
Purbeck virgin calcine	0.33	9.54	0.15	63	2035	2.1
Purbeck cycled calcine	0.31	2.11	0.09	171	2070	2.1

The total pore volume, estimated by summing values from the BJH analysis and mercury porosimetry, gave 0.34 $cm^3\ g^{-1}$ for the Purbeck virgin calcine and 0.16 $cm^3\ g^{-1}$ for the cycled material in its calcined state. From Eq. (6-25), the theoretical maximum conversion of the virgin calcine, based on these results, should be 0.65, where the contribution from the volume of the 2 – 200 nm dia. pores, estimated from the BJH

analysis, is 0.37 and that from the volume in pores of diameter ranging from 200 nm – 100 μm pores, measured from mercury porosimetry, is 0.29. The theoretical maximum conversion of the cycled calcine would be 0.31, where 0.13 is from pore volumes estimated by BJH analysis and 0.17 is from pore volume measured by mercury porosimetry. In the subsequent modelling work, the mean pore diameters of the virgin and cycled calcines were taken to be 60 nm and 170 nm respectively. Note that the limestone particles may have considerable unmeasured surface area and pore volume in the micro-porous range (d_{pore} < 2 nm), as the BET and mercury intrusion analyser were unable to measure pore diameters smaller than 1.7 nm and 3 nm respectively.

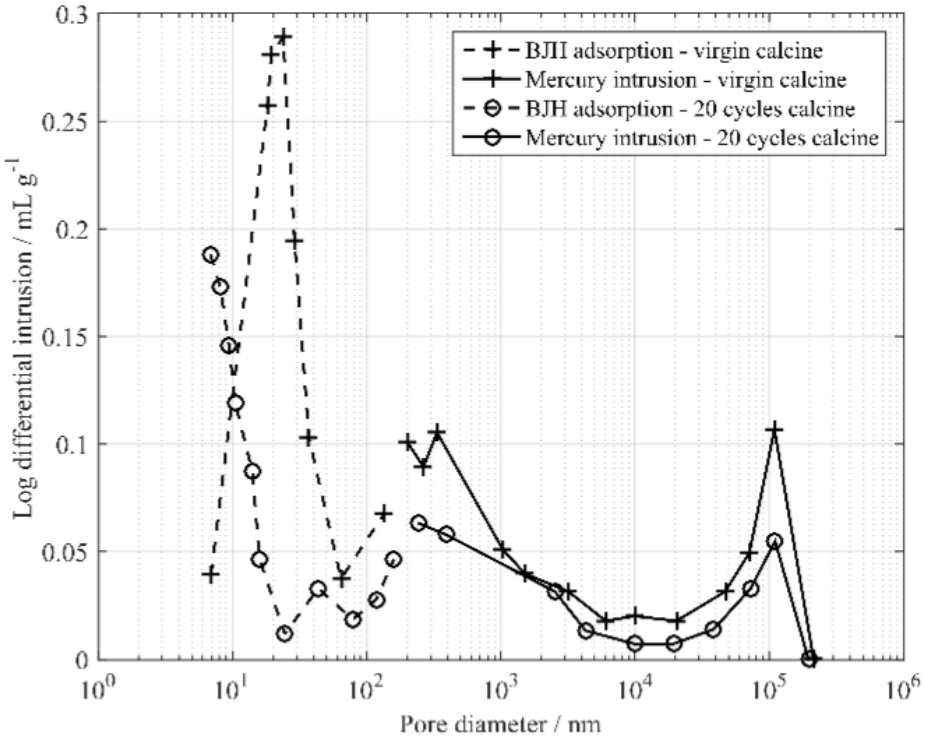

Figure 6.6 Pore size distribution of the Purbeck virgin and cycled calcines. BJH analysis results are shown below 200 nm and mercury porosimetry results are shown above 200 nm.

6.4.2 Kinetic parameters

The activation energy of the intrinsic rate constant k_s was measured from the initial rate of reaction which was extrapolated from the plot of the experimental measurements of the rate *vs.* conversion. When sulphation just starts, *i.e.* $X = 0$, the product layer thickness Δh is close to zero, and the overall rate constant k_{Avg} is equal to the intrinsic rate constant k_s, where

$$k_s = k_{s0}\exp(-\frac{E_a}{RT}) \tag{6-26}$$

In addition, $f(X') = 1$ when $X' = 0$, hence the initial rate becomes

$$Q_{\mathrm{CaSO_4}}\big|_{X'=0} = k_{s0}\exp(-\frac{E_a}{RT})\left(\frac{p_{\mathrm{SO_2}}}{RT}\right)A_{s,0}\rho_{e,0} \tag{6-27}$$

which can be rearranged:

$$\mathrm{Ln}\left(Q_{\mathrm{CaSO_4}}\big|_{X'=0}\cdot T\right) = -\frac{E_a}{RT} + \mathrm{Ln}\left(k_{s0}\left(\frac{p_{\mathrm{SO_2}}}{R}\right)A_{s,0}\rho_{e,0}\right) \tag{6-28}$$

Hence, by plotting $\mathrm{Ln}\left(Q_{\mathrm{CaSO_4}}\big|_{X'=0}\cdot T\right)$ against $1/T$, the activation energy can be determined from the gradient of the best fitted line of the experimental results. The initial rate of reaction $Q_{\mathrm{CaSO_4}}\big|_{X'=0}$ was extrapolated from the plot of the rate against conversion using the cubic interpolation method in MATLAB, as shown in Figure 6.7. The peak of the deconvoluted rate is slightly higher than the estimated initial rate in Figure 6.7, which is a usual feature for the deconvolution process using a non-linear mixing model *e.g.* 2 CSTR in series with a PFR. The deconvoluted rate almost coincidences with the experimentally measured rate, suggesting that the mixing effect in the sampling line was relatively fast compare to the sulphation reaction.

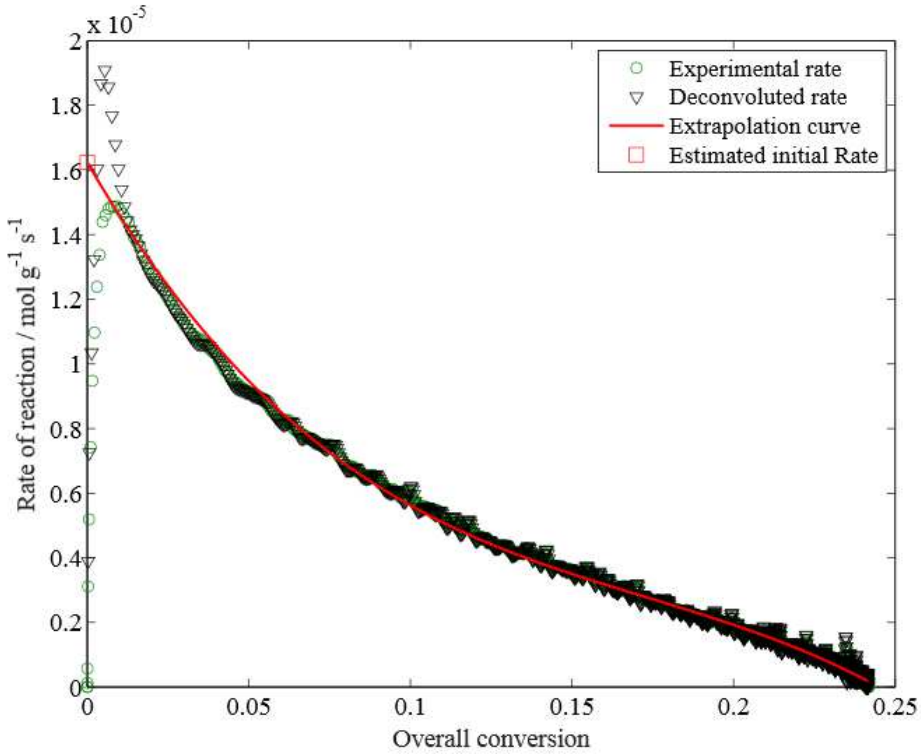

Figure 6.7 Extrapolating initial rate of reaction from the deconvoluted rate for a calcined particle using the cubic interpolation method in MATLAB. The material was 710 – 850 µm dia.

Purbeck limestone, cycled 20 times and sulphated with 1800 ppm SO_2, 5.2% O_2 balance N_2 at 1223 K. The original experimental rate prior to deconvolution is also plotted for comparison.

Figure 6.8 shows the plot of Ln $\left(Q_{\mathrm{CaSO_4}}\big|_{X'=0} \cdot T\right)$ against $1/T$ and the estimated values of the activation energies for the two limestone calcines, where the virgin calcine and the cycled calcine have a very similar activation energy of ~40 kJ mol^{-1}. A range of activation energies of k_s have been reported in the literature: Borgwardt (1970) reported 34 – 76 kJ mol^{-1} depending on the type of limestone whilst Bhatia & Perlmutter (1981) calculated it to be 56 kJ mol^{-1} using their random pore model. Borgwardt (1970) and Dennis & Hayhurst (1990) found values around 38 ± 5 kJ mol^{-1} for calcined virgin limestone. For cycled material, Cordero *et al.* (2014) estimated the value to be about 42 kJ mol^{-1} for material purged from a calcium looping process after a long residence time in the reactor, whilst Cordero & Alonso (2015) measured 22 – 26 kJ mol^{-1} for limestone calcines after 50 cycles of carbonation and calcination.

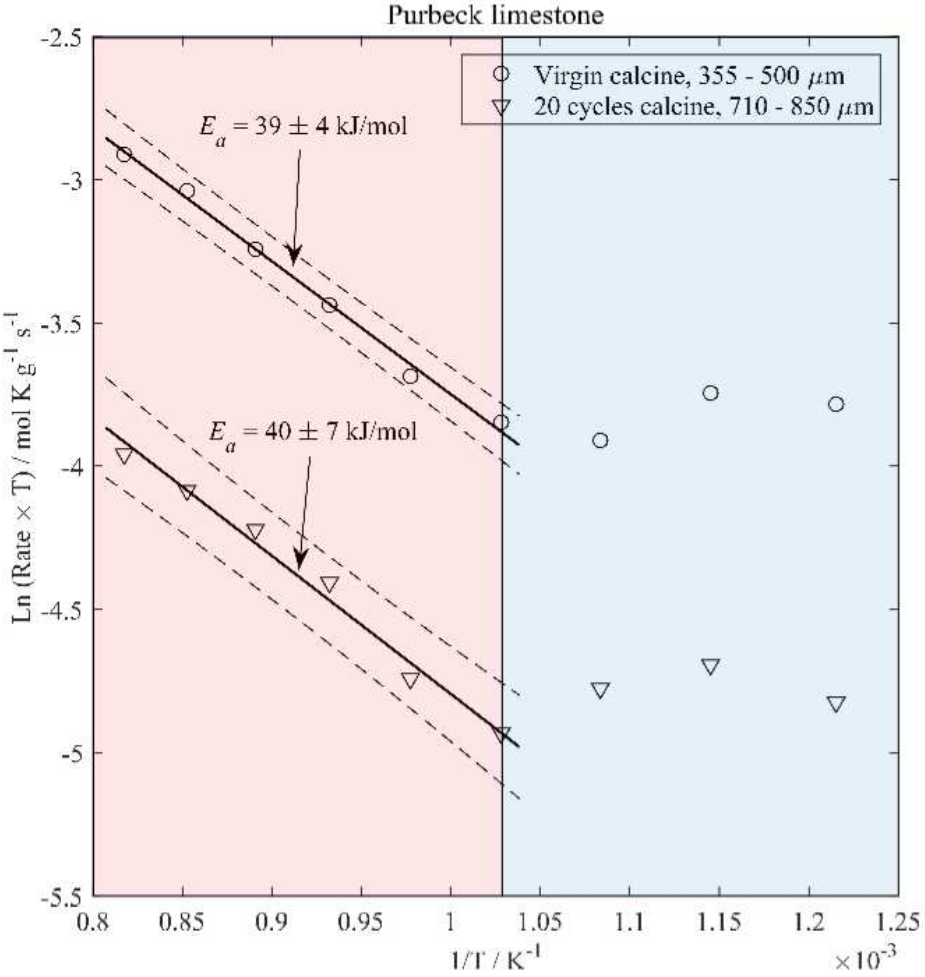

Figure 6.8 Determining the activation energy of the intrinsic rate constant of sulphation of the Purbeck limestones from measurements at 823 K, 873 K, 923 K, 973 K, 1023 K, 1073 K, 1123

K, 1173 K to 1223 K with 1800 ppm SO_2, 5.2% O_2 balance N_2. Measurements above 973 K are shaded in red and measurements below 973 K are shaded in blue.

A summary of the kinetic parameters is shown in Table 6.3, where the values of k_s at 1123 K are also given. In the literature, various values of k_s have been reported at 1123 K, thus: 128×10^{-5} m/s by Bhatia & Perlmutter (1981), 34×10^{-5} m/s by Dennis & Hayhurst (1990), 17×10^{-5} m/s by Allen & Hayhurst (1996a) and 68 – 135×10^{-5} m/s by Cordero & Alonso (2015). Therefore, the results obtained in this study are in line with the values reported in the literature. Above 973 K, there is no clear reduction in the activation energy due to mass transfer resistance in Figure 6.8, thus the sulphation reaction was initially controlled by the intrinsic chemical kinetics. Below 973 K, the reaction mechanism might have been different from that at higher temperature, which could account for the changes in the gradient shown in the blue region.

Table 6.3 Summary of the kinetic parameters determined from the experiments.

Particles	E_a / kJ mol^{-1}	k_{s0} / m s^{-1}	k_s at 1123 K / m s^{-1}
Virgin calcine	39 ± 4	0.011	16×10^{-5}
Cycled calcine (20 times)	40 ± 7	0.015	21×10^{-5}

6.4.3 Product layer diffusivities

The product layer diffusivity in Eq. (6-11) is an adjustable parameter when fitting the predicted rates and conversions of sulphation to those measured in the experiments, which are plotted as $\log(D_P)$ *vs.* $1/T$ in Figure 6.9 for the virgin and the cycled calcines. The activation energies of the product layer diffusivity were estimated to be 102 ± 7 kJ mol^{-1} and 130 ± 15 kJ mol^{-1}; in the literature it has been variously reported to be 120 kJ mol^{-1} (Bhatia & Perlmutter, 1981a), 138 kJ mol^{-1} (Borgwardt *et al.*, 1987), 147 kJ mol^{-1} (Fuertes *et al.*, 1994), 150 kJ mol^{-1} (Iisa *et al.*, 1992) and 165 kJ mol^{-1} (Duo *et al.*, 2004). A summary of the parameters is shown in Table 6.4, where the values of D_p at 1123 K are also given.

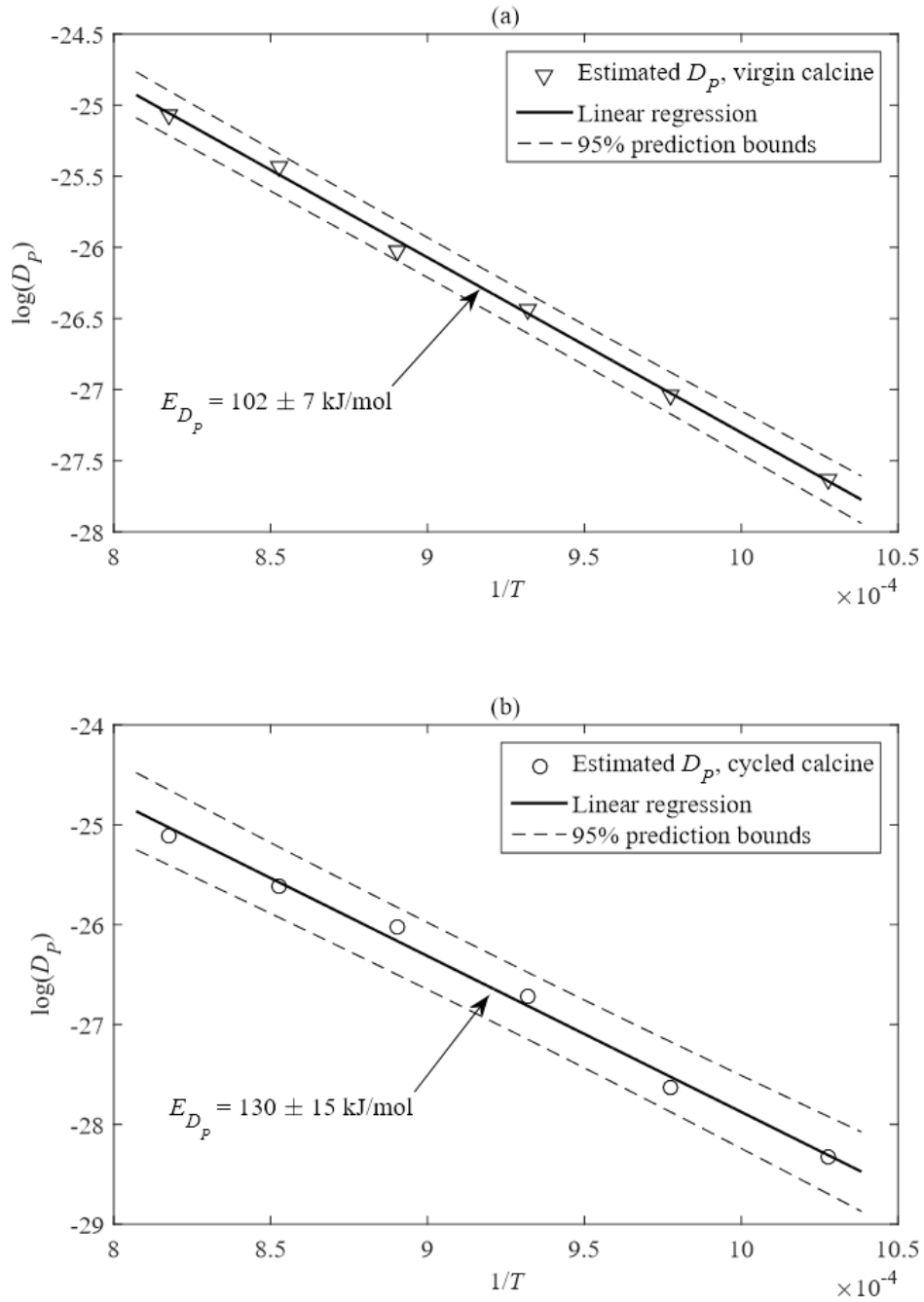

Figure 6.9 Estimating activation energies of the product layer diffusivities for the virgin and the cycled calcines sulphated with 1800 ppm SO_2, 5.2% O_2 balance N_2.

Table 6.4 Summary of the product layer diffusivity parameters determined from the model.

Particles	E_{D_P} / kJ mol^{-1}	D_{P0} / m^2 s^{-1}	D_P at 1123 K / m^2 s^{-1}
Virgin calcine	102 ± 7	0.31×10^{-6}	56×10^{-13}
Cycled calcine (20 times)	130 ± 15	4.74×10^{-6}	43×10^{-13}

6.4.4 Sulphation of virgin calcine particles

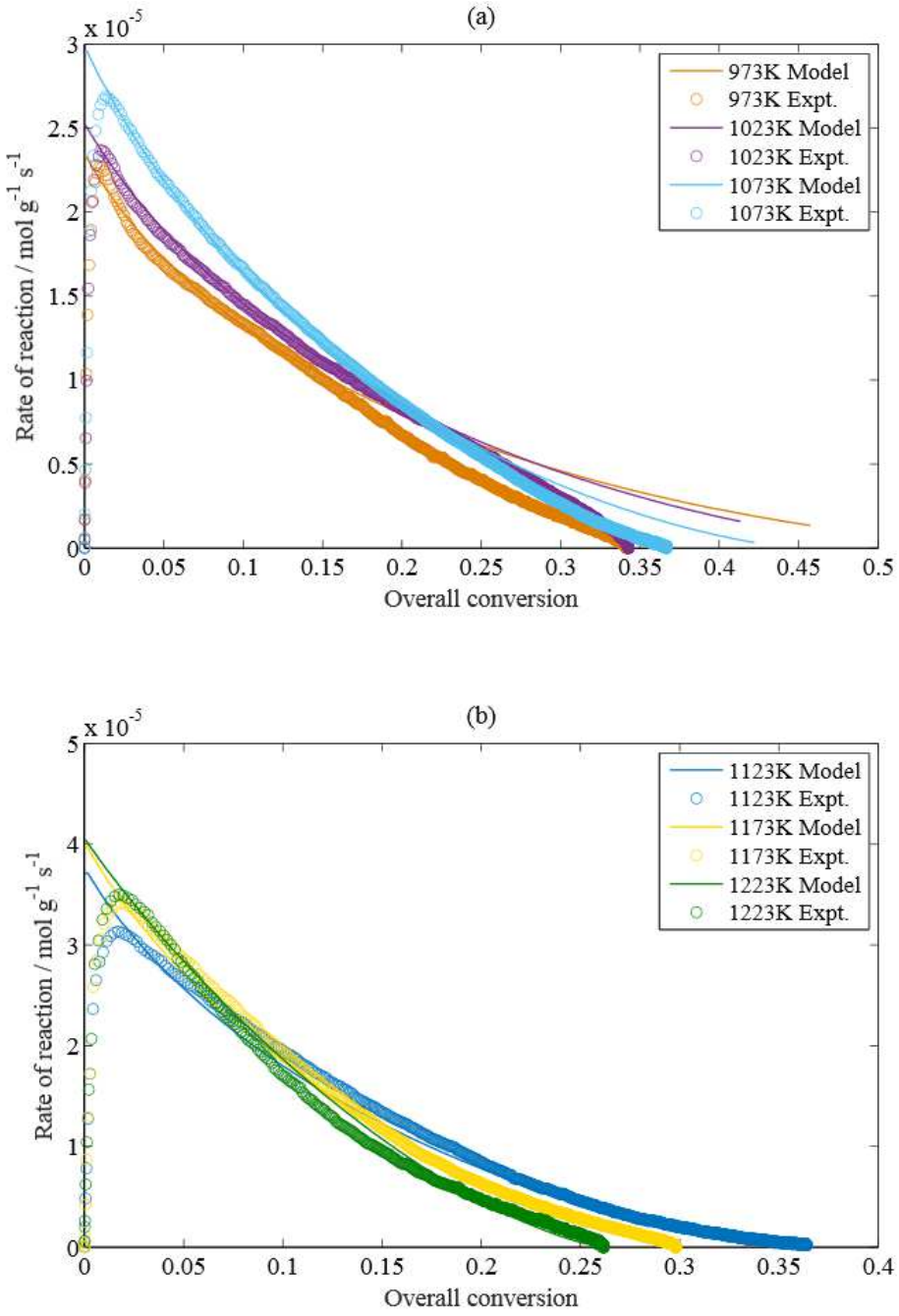

Figure 6.10 Comparison of model results (lines) with experimental measurements (points) of the sulphation of 355 – 500 µm dia. Purbeck virgin calcine by 1800 ppm SO_2, 5.2% O_2 balance N_2 at 973 – 1223 K. The simple $f(X') = 1 - X'$ function was used in all cases.

The experiments with the virgin calcine did not achieve 100% of the theoretical maximum conversion given by Eq. (6-25), hence it was not possible to determine the $f(X')$ function. Instead, the function was arbitrarily set to $f(X') = 1 - X'$ and used in the model for all temperatures to compare to the experimental measurements of the rate and conversion. Comparisons between the model predictions and the experimental

measurements of sulphation of the 355 – 500 μm dia. Purbeck virgin calcine at 973 – 1223 K are shown in Figure 6.10. This figure includes plots of the rate *vs.* conversion at (a) 973 – 1073 K and (b) 1123 – 1223 K. Good agreement between the experiments and the model is seen for 973 – 1123K up to an overall conversion of 0.25 in Figure 6.10(a), after which the experimental rates fall faster with conversion than the model predicts. For experiments at 1123 – 1223 K in Figure 6.10(b), the model agrees well with the experiments for all conversions. In addition, the model accurately predicted the decline in the ultimate conversion of $CaSO_4$ with temperature at 1123 – 1223 K.

The ultimate conversion of $CaSO_4$ predicted by the model was higher than that measured by the experiments. Figure 6.10 also shows that the maximum conversions start to drop rapidly at temperatures above 1123 K, which will be discussed in detail in section 6.5.2. The highest conversion of $CaSO_4$, ~0.35, was obtained during experiments at 1073 K, which was less than the theoretical maximum capacity of 0.65 calculated from Eq. (6-25) using the sum of the pore volume from BJH analysis and mercury porosimetry. However, a conversion of $CaSO_4$ of 0.35 corresponds to a pore volume of 0.18 $cm^3\ g^{-1}$, which, interestingly, is very close to the value of 0.19 $cm^3\ g^{-1}$ estimated from the BJH analysis in Table 6.1.

6.4.5 Sulphation of calcined, cycled particles

The experiments using the cycled calcines also did not achieve 100% of the theoretical maximum conversion given by Eq. (6-25), hence it was not possible to determine the $f(X')$ function. Again, the arbitrary choice of $f(X') = 1 - X'$ was used in the model for all temperatures to compare to the experimental measurements of the rate and conversion. Comparisons between the model predictions and the experimental measurements of sulphation of 710 - 850 μm dia. particles of cycled, calcined Purbeck limestone at 973 – 1223 K are shown in Figure 6.11, which includes plots of the rate *vs.* conversion at (a) 973 – 1073 K and (b) 1123 – 1223 K. Reasonable agreement between the experiments and the model can be found for 973 – 1173K in Figure 6.11(a) below a conversion of 0.05, above which the experimental rates fall much faster with conversion than the model predicts. In Figure 6.11(a), there is almost a perfect agreement between the model results and the experiments at 1123 – 1223 K.

The reactions stopped at different ultimate conversions of $CaSO_4$ for different temperatures in the experiments, being ~ 0.08 for 973 – 1023 K, ~ 0.15 at 1073 K and ~

0.25 for 1123 – 1223K. This is different from the behaviour of the virgin calcine, which will be discussed in section 6.5.2. The highest conversion to $CaSO_4$ in the experiments was obtained at 1123 K, ~0.25, which was close to the theoretical maximum capacity of 0.31 calculated from Eq. (6-25) using the sum of the pore volume from BJH analysis and mercury porosimetry. A conversion of 0.25 corresponded to a pore volume of 0.13 $cm^3\ g^{-1}$ using Eq. (6-25).

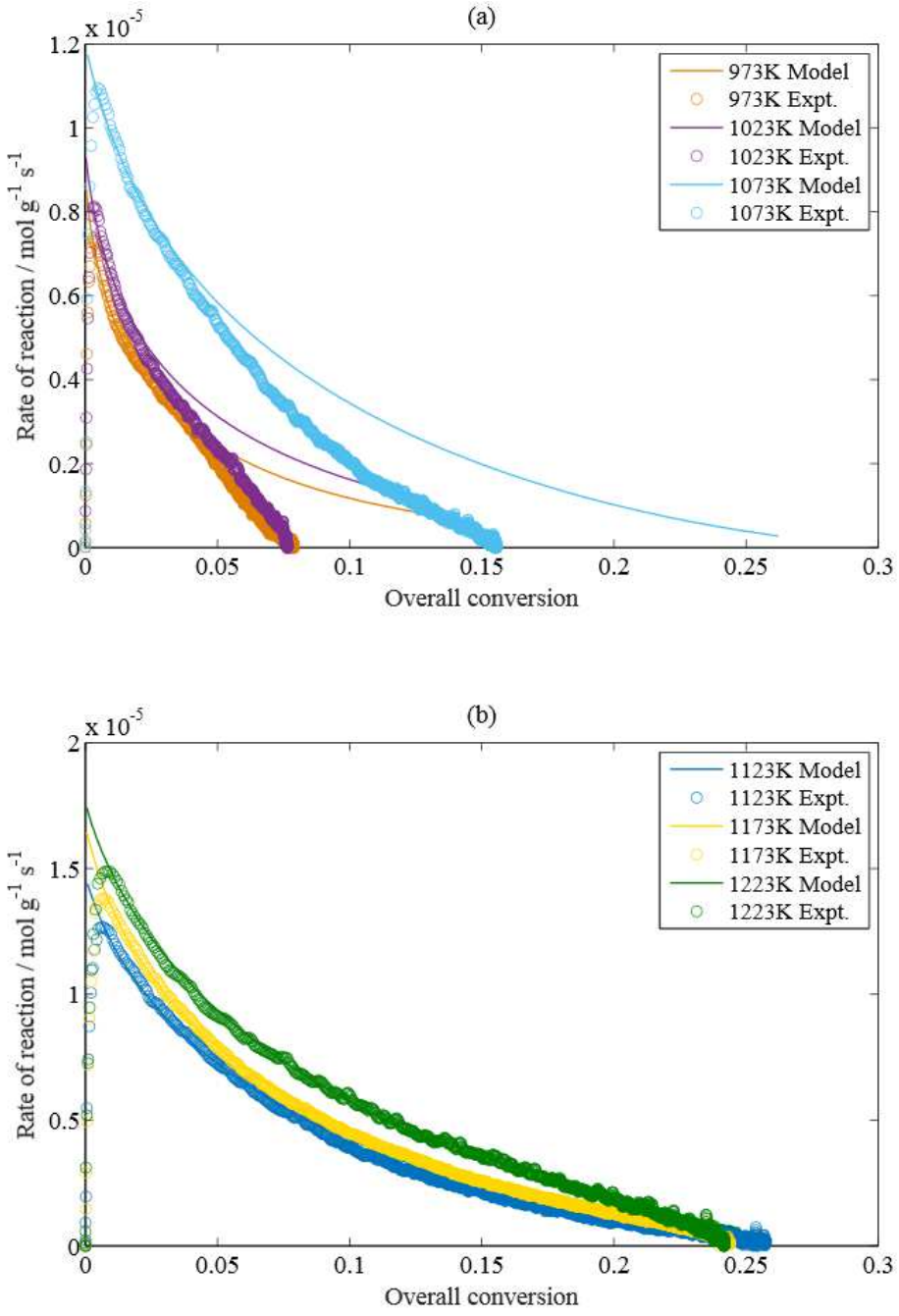

Figure 6.11 Comparison of model results (lines) with experimental measurements (points) for the sulphation of 710 – 850 µm dia. cycled Purbeck limestone calcine by 1800 ppm SO_2, 5.2% O_2 balance N_2. The simple $f(X') = 1 - X'$ function was used in all cases.

6.4.6 The ultimate conversion to $CaSO_4$ at different temperatures

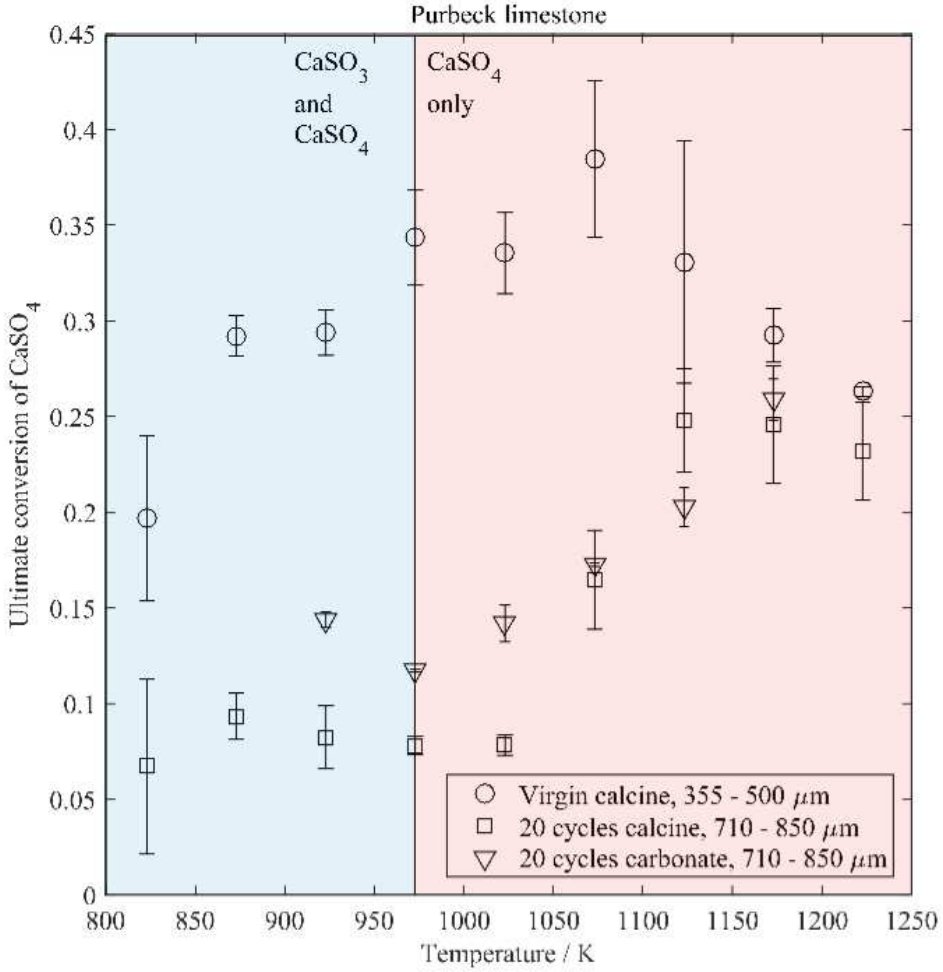

Figure 6.12 The ultimate conversion to $CaSO_4$ at different temperatures. The region where $CaSO_3$, $CaSO_4$ and CaS could exist thermodynamically is shaded below 973 K and the region where only $CaSO_4$ could exist is shaded above 973 K. At 1073 K, there are inflection points and a maximum.

The ultimate conversions to $CaSO_4$, *i.e.* the maximum absorption capacity of the material for SO_2, of the 0.36 – 0.50 mm dia. virgin and the 0.71 – 0.85 mm dia. cycled calcines were measured at 823 K – 1223 K. Additional measurements were made using cycled particles of 0.71 – 0.85 mm dia. in the carbonated state (20 calcinations, 20 carbonations) between 923K and 1173 K for comparison. The results are shown in Figure 6.12, where the region below 973 K is shaded blue and the region above 973 K red. Between 973 K and 1073 K, the virgin calcine and the cycled calcine behave similarly, insofar as the respective conversions to $CaSO_4$ were roughly constant between 973 and 1023 K and increased from 1023 to 1073 K. For the range 1073 – 1123 K, the trends between the two materials are different. Thus, the conversion to $CaSO_4$ of the virgin calcine decreases with increase in temperature while that of the

cycled calcine increases. Above 1123 K, the conversion of the virgin calcine continues to decline with increase in temperature, whilst that of the cycled calcine declines only very slightly. There is a distinct maximum at 1073 K for the virgin calcine and at 1123 K for the cycled calcine. On the other hand, the conversion to $CaSO_4$ of the cycled material in its carbonated state increases with increase in temperature monotonically above 973 K. Since no experiments were performed above 1173 K for the cycled material in its carbonated state, it cannot be deduced where any maximum would be. However, it can be concluded that the peak conversion to $CaSO_4$ of the carbonated material would appear at a temperature no lower than those of the virgin calcine and the cycled calcine. The behaviour of the carbonated material can be attributed to the effect of calcination on the pore structure during the sulphation reaction, where additional pore volume and potentially a porous product layer are created during the process (Hajaligol *et al.*, 1988).

6.5 Discussion

6.5.1 Comparison between model and experiment

The sulphation experiments undertaken on particles of the 355 – 425 μm dia. virgin calcine and the 710 – 850 μm dia. cycled calcine were analysed to give estimates of the intrinsic rate constant, both materials giving a value of the activation energy close to ~ 40 kJ mol^{-1} with pre-exponential factors were 0.011 and 0.015 m/s, respectively. The values were within the range of the values reported in several different kinetic studies of the sulphation of limestones. At 973 K, the Thiele modulus, given by $\varphi = \frac{r_p}{3}\sqrt{\frac{k_S A_{s,0} \rho_{e,0}}{D_{\text{eff}}}}$, was 1.34 for the virgin calcine and 1.10 for the cycled calcine, which indicated that the initial reaction of both particles was affected by, but not significantly limited by, the pore diffusion resistance. Figure 6.13 shows the local conversion profiles of the virgin and cycled calcines at 973 K predicted by the model, where the gradients of conversion across both particles are flat. Furthermore, the evolution of the effectiveness factors with conversion in Figure 6.14 shows a steep rise just after reaction begins. Therefore, the initial intraparticle diffusion resistance reduces rapidly as the solid diffusion becomes the limiting step. Nevertheless, Figure 6.10 and Figure 6.11 did show a reasonable agreement between the model using the $f(X')$ functions and the experiments across all temperature.

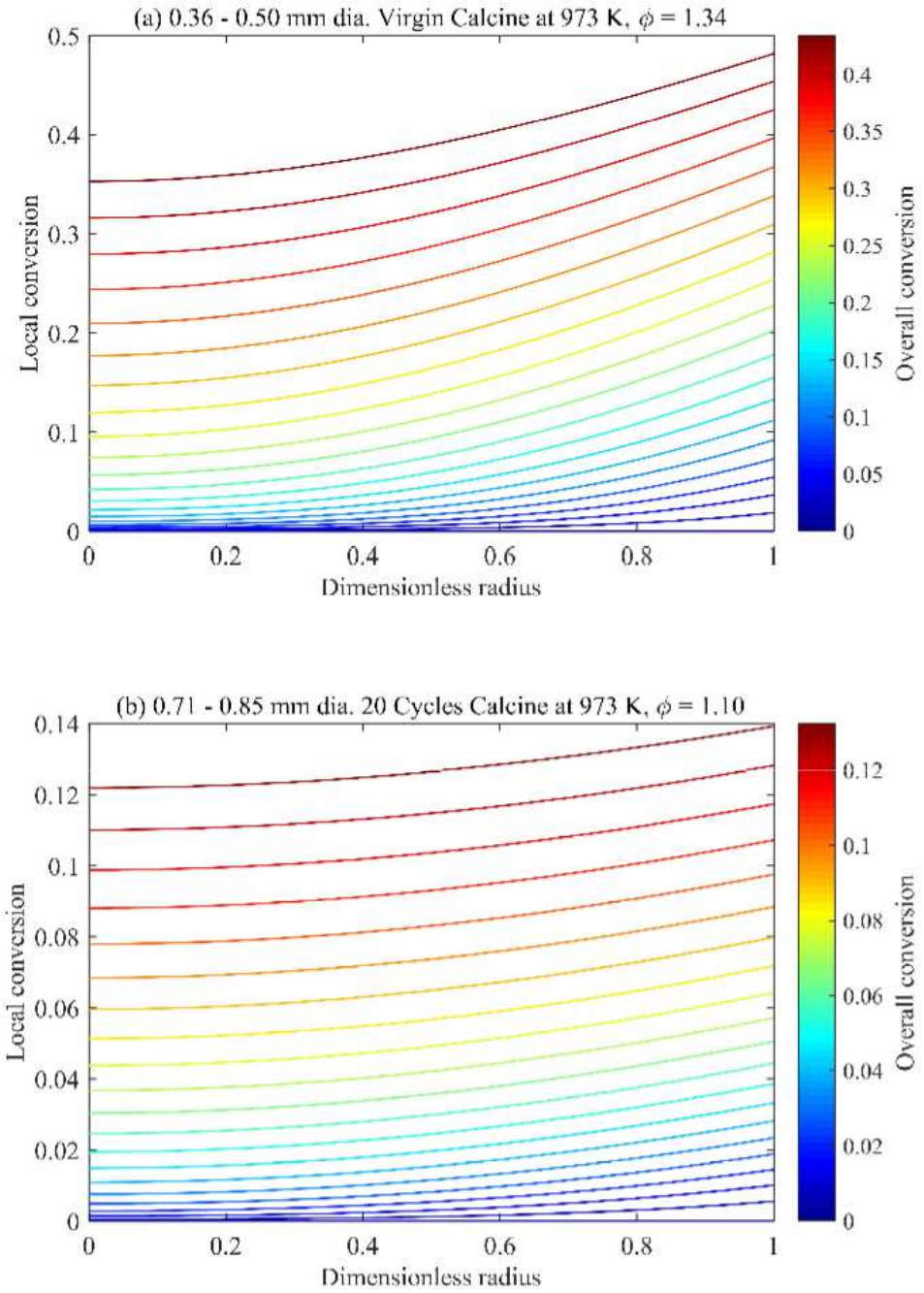

Figure 6.13 The predicted local conversion profiles of the 355 – 500 μm dia. virgin calcine and the 710 – 850 μm dia. cycled calcine reacting with 1800 ppm SO_2, 5.2% O_2 balance N_2 at 973 K. The colour bar indicates the overall conversion of $CaSO_4$.

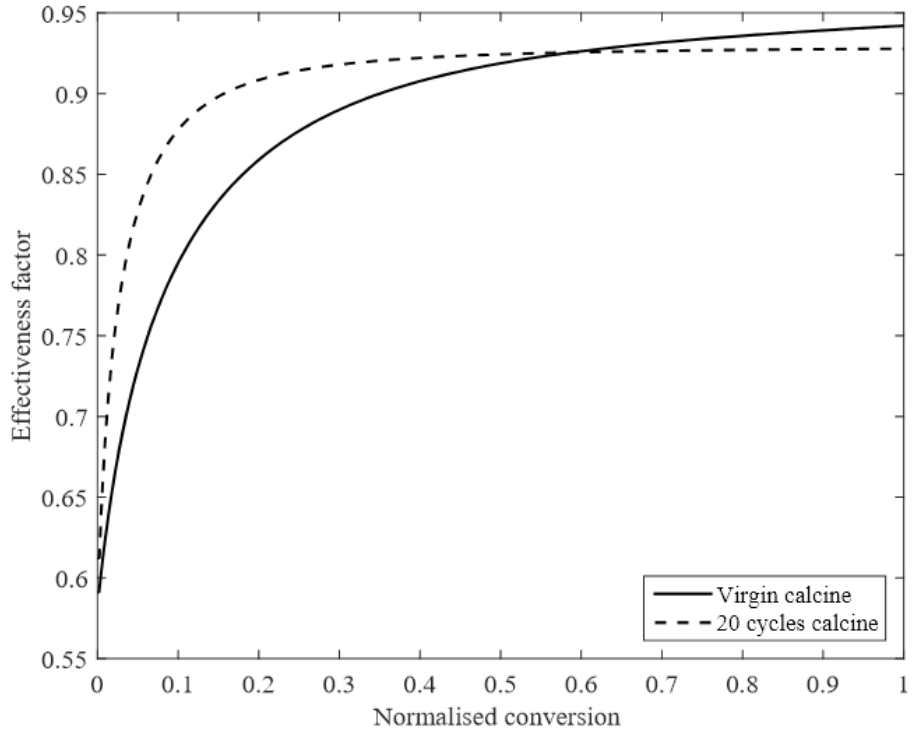

Figure 6.14 The predicted evolution of the effectiveness factor against the normalised conversion of $CaSO_4$ of the 355 – 500 μm dia. virgin calcine and the 710 – 850 μm dia. cycled calcine reacting with 1800 ppm SO_2, 5.2% O_2 balance N_2 at 973 K. The conversion is normalised by the experimental maximum conversion of $CaSO_4$.

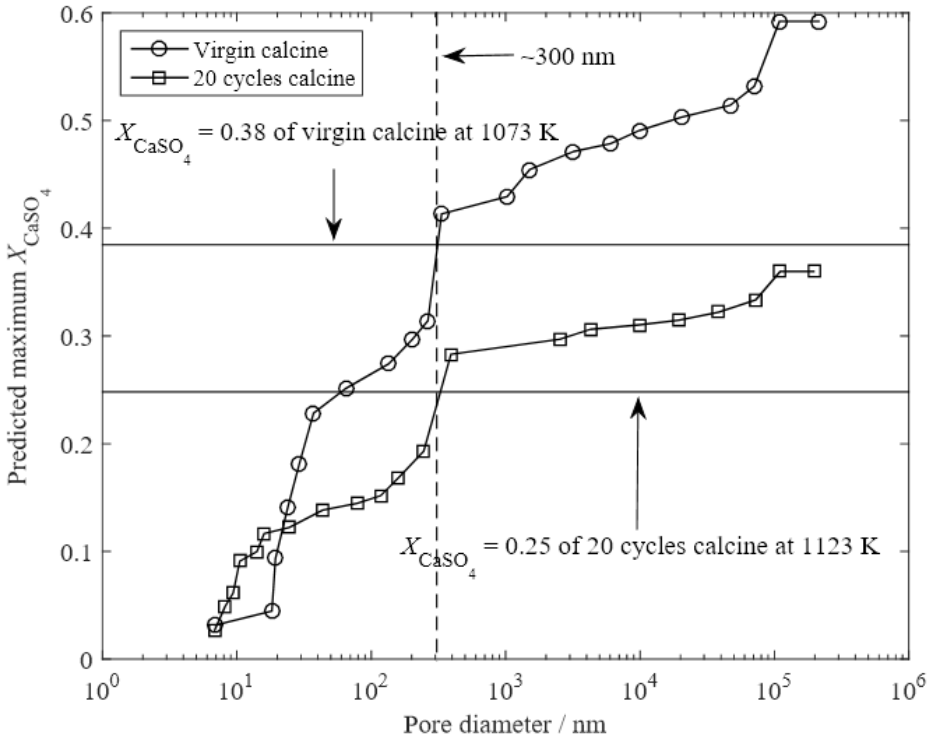

Figure 6.15 Predicted maximum conversion to $CaSO_4$ against pore diameter for Purbeck limestone calcines based on the experimental pore size distribution of the particles. The experimental maximum conversions of $CaSO_4$ of the virgin calcine at 1073 K and that of the cycled calcine at 1123 K are indicated, both of which intersect with the curve at ~300 nm.

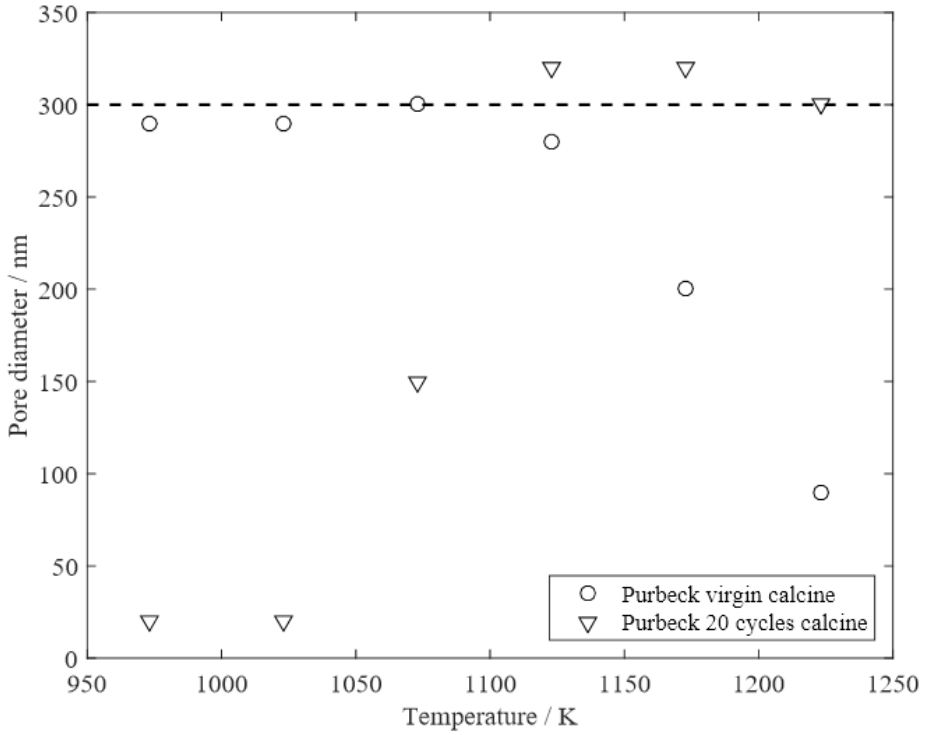

Figure 6.16 The range of pore sizes responsible for the absorption capacity of SO_2 determined from the experimental maximum conversion to $CaSO_4$ at different temperatures. The dashed line indicates an estimated limit of pore diameter ~300 nm.

The maximum conversion predicted by the model was determined by the pore volumes of the particles based on Eq. (6-25). The effective pore volume of the Purbeck virgin calcine, calculated by substituting the experimental maximum conversion of $CaSO_4$ into Eq. (6-25), was very close to the pore volume estimated from the BJH analysis for pores smaller than 200 nm. In their work on the cycling of limestones between the calcined and carbonated state, Fennell *et al.* (2007) found that absorption capacity for CO_2 was proportional to the volume of pores below 150 nm diameter and the initial reaction was rapid when filling up those pores. A distribution of the cumulative pore volume was obtained from the pore size distribution shown in Figure 6.6, which was used to plot the hypothetical maximum conversion to $CaSO_4$ if the volume of the pores were to be filled up, starting from the smallest pores up to a given size of pores. As shown in Figure 6.15, the cumulative pore volume distributions for both virgin and cycled calcined particles give the predicted maximum conversion to $CaSO_4$ against the pore diameter. Examples are shown for the virgin calcine at 1073 K and the cycled calcine at 1123 K, where the maximum conversion are the highest across all temperatures and both intersect with the curve at a pore diameter of ~300 nm. Similar calculations were done for all the other measurements of the maximum

conversion to $CaSO_4$ and are shown in Figure 6.16, where the volume below 300 nm seems to be the limit for the maximum conversion for both Purbeck limestone calcines.

6.5.2 The maximum conversion to $CaSO_4$

There have been considerable discussions over the existence of temperature maxima in the capture of SO_2 by calcined limestone. For sulphation under oxidising conditions, the optimum temperature for the conversion to $CaSO_4$ has been explained by different theories:

(i) At higher temperatures, the limestone particles experience severer sintering resulting in lower porosity and surface area, hence reducing the overall conversion of limestone. This has been dismissed by Anthony & Granatstein (2001) since sintering should not have a significant effect with a short residence time ~1 h and a small temperature span ~50°C.

(ii) The equilibrium between SO_2 and SO_3 determines the maximum, with higher temperatures reducing the availability of SO_3 for reaction with CaO. This can probably be rejected as well since it has been shown that the formation of SO_3 was not essential for the sulphation reaction (Dennis & Hayhurst, 1990).

(iii) At a high temperature, the rate of sulphation becomes fast, which causes the surface pores to be filled with $CaSO_4$ solid, thus preventing the entry of SO_2 to the interior of the calcined limestone particle (Dennis & Hayhurst, 1986). At low temperature, the reaction is limited by the diffusion through the solid product layer, so that the rate of reaction becomes very slow. The solid-state diffusion is an activated process and the rate will increase with temperature, hence there must exist an optimum temperature for SO_2 uptake.

Other proposed theories to explain the change of the ultimate conversion to $CaSO_4$ with temperature, suggest the reduction of $CaSO_4$ to CaO. For example:

(iv) The temperature maximum for the ultimate conversion of $CaSO_4$ was regarded as competition between sulphation and reduction, with reduction becoming more important at higher temperatures (Lyngfelt & Leckner, 1989a, 1989b; Hansen *et al.*, 1993; Anthony & Granatstein, 2001).

(v) The depletion of oxygen in the dense phase of a fluidised bed coal combustor, due to increasing volatile combustion at higher temperatures, could inhibit the sulphation above 1173 K, where depleted levels of oxygen might reduce the production of $CaSO_4$ and allowed regeneration of CaO through reduction of $CaSO_4$ by CO formed during incomplete combustion of the coal (Dennis & Hayhurst, 1985).

However, the temperature maxima were found in the current work under oxidising conditions only, with no reducing species present in the fluidised bed. Therefore, it is unlikely that the reduction of $CaSO_4$ could have occurred in the experiments of this study, but it does not invalidate the above theories since significant drops in the maximum conversion were recorded when the reaction was studied in the presence of the combustion of high-volatile coal in the experiments of Dennis & Hayhurst (1985). Figure 6.12 showed that after the peak, the ultimate conversion to $CaSO_4$ of the virgin calcine fell more rapidly with temperature than the cycled calcine did. In fact, the ultimate conversion of $CaSO_4$ of the cycled calcine seemed to be constant at ~ 0.24 between 1123 K and 1223 K. If the chemical nature of the virgin calcine and cycled calcine did not differ much, then the most likely cause for such a difference must come from the difference in the evolution of pore structures. Hence, the theory (iii) above merits further discussion.

If the plugging of the surface pores were the reason for the decrease in the ultimate conversion to $CaSO_4$ at high temperature, then the pore plugging would be more significant for the virgin calcine than for the cycled calcine, because the pores of the virgin calcine are, on average, smaller. Also, the initial Thiele modulus was higher for the virgin calcine. Then at the same temperature, the distribution of the $CaSO_4$ product across the particle would be less uniform for the virgin calcine than cycled material. At a high temperature, *e.g.* 1123 – 1223 K, the virgin calcine would be more likely to experience plugging of the surface pores, preventing SO_2 from accessing unreacted CaO inside the particle, thereby leading to a fall in the ultimate conversion to $CaSO_4$. On the other hand, the cycled calcine at 1123 – 1223 K should manifest a less dramatic decrease in the ultimate conversion, exactly as shown in Figure 6.12. In addition, it might be expected that the peak temperature of the ultimate conversion of $CaSO_4$ of the cycled calcine (1123 K) to be higher than that of the virgin calcine (1073 K).

Turning to lower reaction temperatures, Figure 6.12 shows that the ultimate conversion to $CaSO_4$ is almost constant over the range 973 – 1023 K before starting to increase between 1023 and 1073 K for both the virgin and the cycled calcines. It is unclear why the ultimate conversion of $CaSO_4$ at 1023 K was so close to that at 973 K, but the increase between 1023 K and 1073 K might be explained by the increase in the diffusion coefficient for the product layer with temperature.

One of the key parameters used in the model was the product layer diffusion coefficient given by Eq. (6-12). Using Eq. (6-11), one can estimate the thickness Δh at which diffusion through the product layer becomes limiting for a given local concentration of SO_2. This is demonstrated in Figure 6.17, which plots Eq. (6-11) in the form of the ratio k_{Avg}/k_s as a function of the ratio $r_{pore}/r_{pore,0}$ at different temperatures for (a) the virgin calcine and (b) the cycled calcine. A value of $k_{Avg}/k_s <$ 0.1 was chosen to be the threshold for entering significant control by diffusion through the product layer. Corresponding values of $\left(r_{pore}/r_{pore,0}\right)^{\text{crit}}$ are illustrated by the dashed lines in Figure 6.17. A ratio of $\left(r_{pore}/r_{pore,0}\right)^{\text{crit}}$ close to 0 indicates that the pores will be completely filled when $k_{Avg}/k_s = 0.1$, as shown by the curve for 1223 K in Figure 6.17(a). If $\left(r_{pore}/r_{pore,0}\right)^{\text{crit}}$ exceeds 0, then the pores will only be partially filled when the overall rate becomes limited by the product layer diffusion. The results show that:

(i) An increase in the initial pore radius, $r_{pore,0}$, leads to steeper curves across all temperatures. In the other words, a larger value of $\left(r_{pore}/r_{pore,0}\right)^{\text{crit}}$ indicates a smaller probability of pore plugging;

(ii) A larger value of the pre-exponential factor for product layer diffusion in Eq. (6-12) would raise the curves an equal amount for temperatures, giving a smaller $\left(r_{pore}/r_{pore,0}\right)^{\text{crit}}$ and increased likelihood of pore plugging;

(iii) A higher value of the activation energy for product layer diffusion would lower the low-temperature parts of each curve more than it would the high-temperature part, resulting in larger values of $\left(r_{pore}/r_{pore,0}\right)^{\text{crit}}$ for low temperatures compared with high temperature. Thus, pore-plugging is less likely at low temperatures.

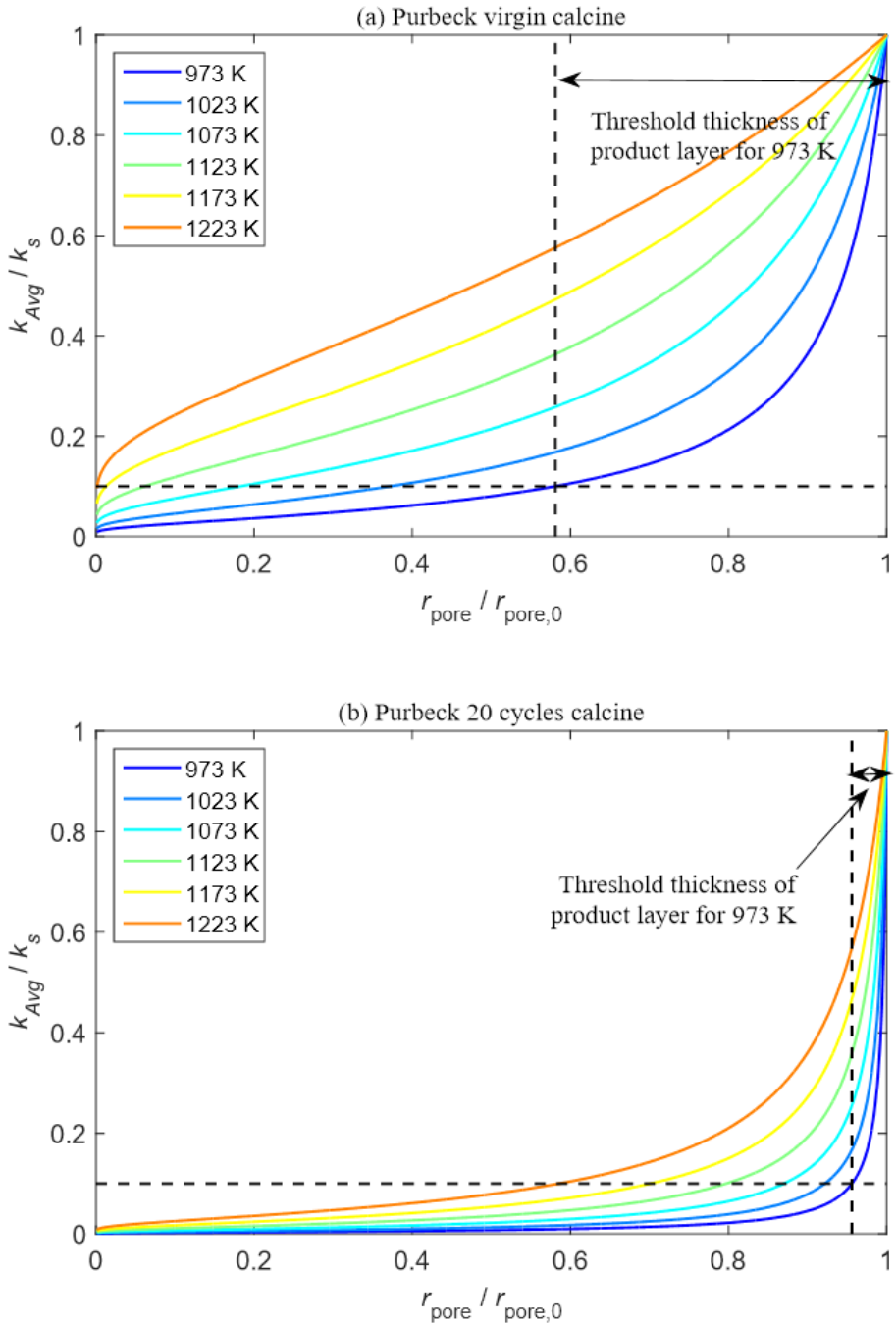

Figure 6.17 Simulation of the ratio k_{Avg}/k_s between the overall and the intrinsic rate constant of sulphation reaction as a function of the ratio $r_{pore}/r_{pore,0}$ at different temperatures for (a) the Purbeck virgin calcine and (b) the Purbeck cycled calcine. The product layer thickness was $\Delta h/r_{pore,0} = 1 - r_{pore}/r_{pore,0}$. A threshold ratio of 0.1 for k_{Avg}/k_s was used here, denoted by the dotted line.

Figure 6.18 shows the variation of the limiting product layer thickness, $1 - \left(r_{pore}/r_{pore,0}\right)^{\text{crit}}$, with temperature for the two types of calcine. The ultimate conversions to $CaSO_4$ at 973 – 1223 K are also plotted on a secondary *y*-axis on the right-hand side of Figure 6.18 to show the correlation with the cut-off product layer thickness. Interestingly for the cycled calcine, the correlation coefficient between the

two series is extremely high ~ 0.98 at 973 – 1123 K because they follow almost the same trend until 1123 K is exceeded. On the other hand, the ultimate conversion to $CaSO_4$ of the virgin calcine does not seem to correlate with the threshold thickness of product layer.

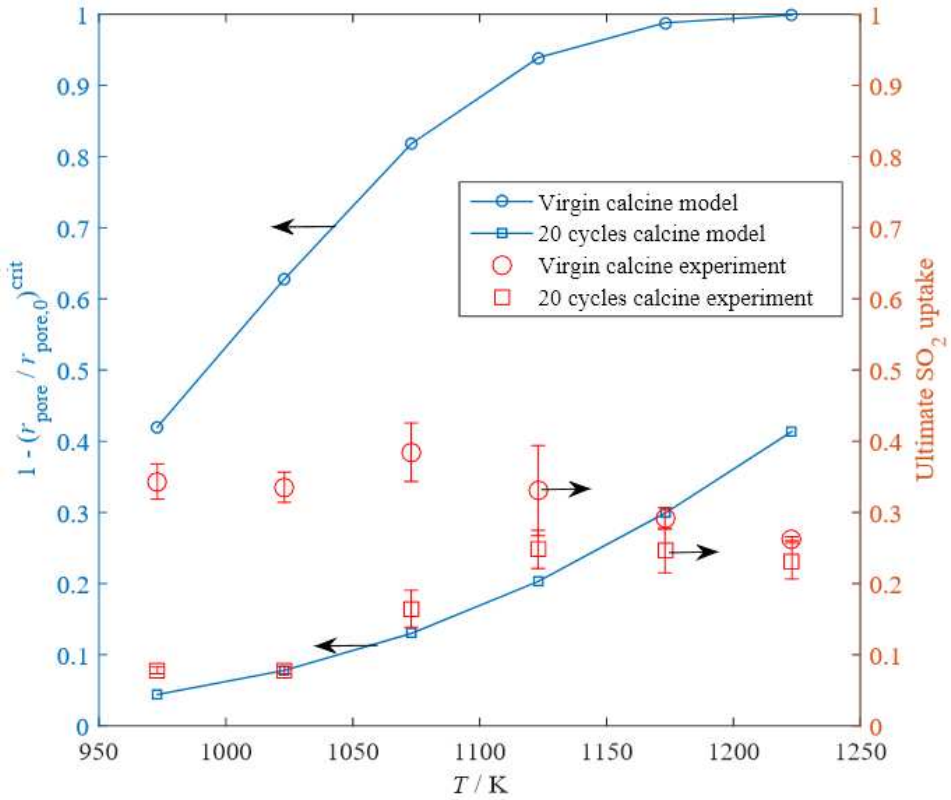

Figure 6.18 The threshold thickness of the product layer $1-\left(r_{pore}/r_{pore,0}\right)^{\text{crit}}$ when the ratio $k_{Avg}/k_s = 0.1$ for Purbeck virgin calcine and the cycled calcine. The experimental measurements of the ultimate conversion to $CaSO_4$ from experiments using 1800 ppm SO_2, 5.2% O_2 balance N_2 are plotted on the secondary *y*-axis on the right to show the correlation with the threshold thickness of product layer.

It should be noted that in Figure 6.17 and Figure 6.18 only the intrinsic rate constant and the product layer diffusion coefficient have been considered and no consideration has been given to intraparticle mass transfer of gas. If the product layer formed inside the particle had a uniform thickness across the particle, then the cut-off thicknesses shown in Figure 6.18 would indeed have a strong correlation with the measurements of the ultimate conversion of $CaSO_4$. However, if the product layer thickness is not uniform, due to significant intraparticle mass transfer resistance at high temperature, then the product layer thickness averaged across the particle would be smaller than that shown in Figure 6.18, and the ultimate conversion to $CaSO_4$ would start to level off. Had the intraparticle mass transfer resistance been considered, the cut-

off thickness of the cycled calcine at 1123 – 1223 K would probably level off and become better correlated with the actual experimental measurements of ultimate conversion. Hence, Figure 6.17 and Figure 6.18 show that the increase in the ultimate conversion to $CaSO_4$ at low temperature might be explained by increases in product layer diffusion coefficient with temperature, at least for the cycled calcine. However, for the virgin calcine, which has a bigger Thiele modulus than the cycled calcine does, it is expected that it will experience more intraparticle mass transfer resistance.

Figure 6.19 shows the simulated evolution of the surface pore diameter with conversion across different temperatures for the virgin and cycled calcines, where the pore diameters at the particle surface are normalised by their initial values and the overall conversions are normalised by the theoretical maximum conversions of the material given by Eq. (6-25). Figure 6.20 shows the simulated profiles of the local porosity across the particle radius when the reaction rates become zero after a long time for the virgin and cycled calcines, where the porosities are normalised by their initial values. As expected from the discussions above, Figure 6.19(a) and Figure 6.20(a) show that the model predicts the complete plugging of the surface pores for the virgin calcine, which becomes more significant as temperature increases. Because of this effect at higher temperatures, the surface pore diameter reduces to zero at a smaller overall conversion and the local porosity profile at the end of the reaction becomes steeper at the particle surface. For the cycled calcine, the fall in the surface pore diameter with overall conversion is slower in Figure 6.19(b) and the porosity profile when the reaction stops in Figure 6.20(b) is less steep. In addition, the 973 – 1073 K profiles in Figure 6.20(b) are almost flat across the particle and are very close to 0, which suggests uniform product layers being formed across the particle at those temperatures. Thus, it seems clear that the pore plugging was in fact more significant in the virgin calcine than in the cycled calcine.

In theory if the experiments were left long enough, 100% of the theoretical maximum conversion can eventually be achieved. Unless there exists a requirement for mechanical work to disrupt the product layer, and this requirement exceeds that can be supplied by the reaction when the layer exceeds a certain thickness (Duo *et al.*, 1994, 2004; Dennis & Pacciani, 2009). However, this theory would be relevant only if the product layer was formed inwards, where the sulphation reaction occurred at the $CaO/CaSO_4$ interface. The literature discussion at the end of section 6.3.1 concluded

that the reaction proceeded by the outward diffusion of Ca^{2+} ions through the $CaSO_4$ product layer and that the reaction occurred, in fact, at the interface between the $CaSO_4$ product and the gas in the pore (Hsia *et al.*, 1993, 1995). Therefore, the most plausible explanation for the experimental maximum conversion being less than the theoretical maximum was that the experiments were incomplete and would take much longer time, *e.g.* > 10 hrs at 973 K, to finish as the rate becomes too small to measure.

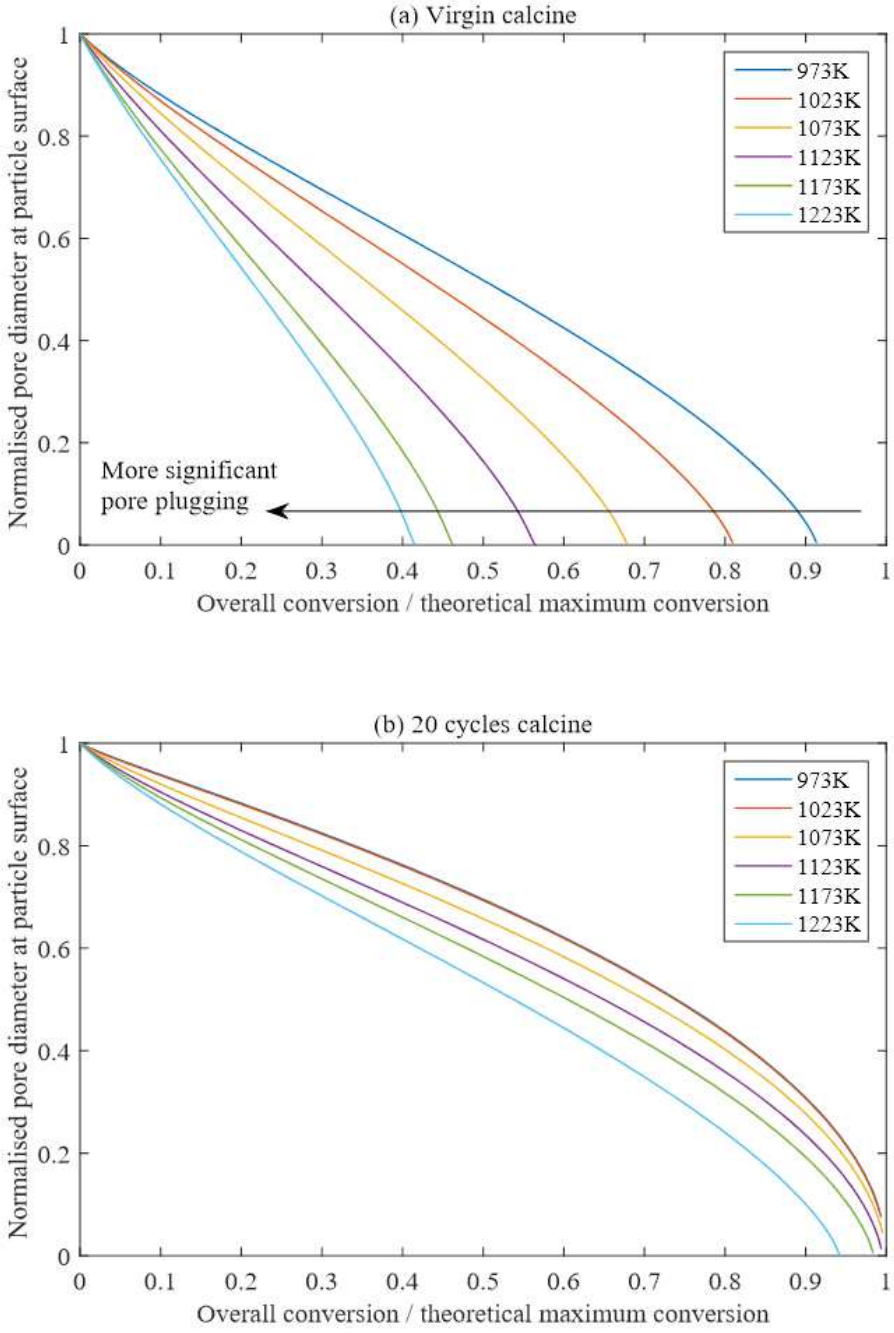

Figure 6.19 Simulated evolution of the normalised pore diameters at the particle surface with overall conversion. The pore diameters are normalised by their initial values and the overall conversion is normalised by the theoretical maximum conversion of $CaSO_4$ of the material.

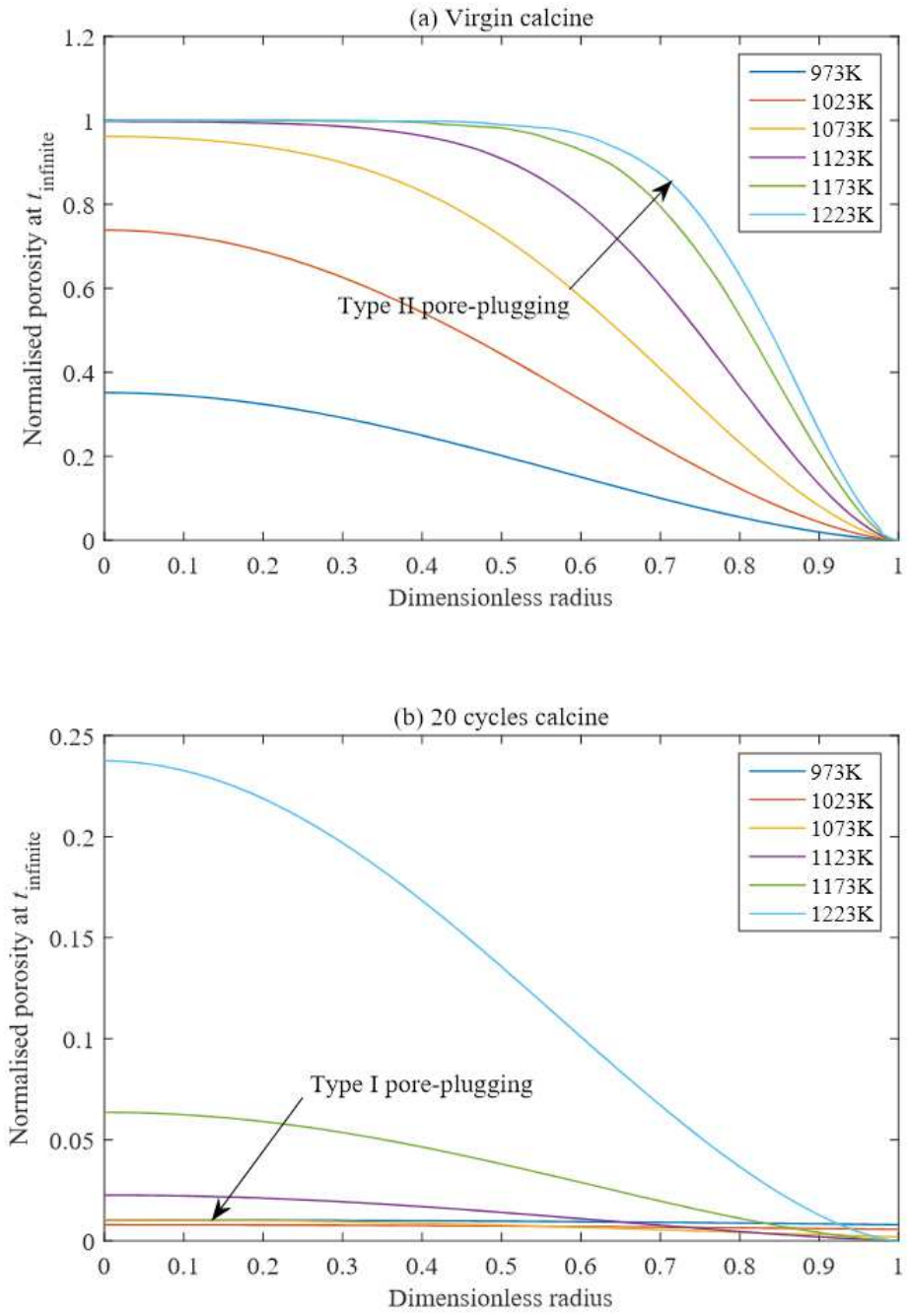

Figure 6.20 Simulated profiles of the local porosity at a long time (t_{infinite}) when sulphation reaction in 1800 ppm SO_2, 5.2% O_2 balance N_2 completely stopped. The porosities are normalised by their initial values.

Therefore, it is proposed that the variation of the ultimate uptake of SO_2 with the temperature consists of two different types:

(i) Type I pore plugging: at low temperature, there is uniform conversion across the particle and the ultimate conversion to $CaSO_4$ was limited by product layer diffusion. As the diffusion coefficient increases with temperature, the thickness of the product layer grows which leads to an increase in the ultimate conversion of $CaSO_4$. Theoretically, if the experiments were left long enough at this temperature, the pores

will be filled with a uniformly thick product layer throughout the entire particle and the theoretical maximum conversion would be achieved. This regime can be seen from the 973 – 1123 K measurements of the cycled calcine. The possible formation of products other than $CaSO_4$ might have an impact on the ultimate conversion, but was not considered here, since experimental evidence in the literature is meagre.

(ii) Type II pore plugging: at high temperature, the product layer near the surface can be so thick that the entrances to the pores become completely sealed thus preventing SO_2 from accessing the particle interior. The higher the temperature, the quicker the blocking of the pores will occur, which leads to the decrease in the ultimate conversion of $CaSO_4$, as observed from the measurements of the virgin calcine at 1073 – 1223 K.

Anything in between type I and II fell into the intermediate stage: as temperature increases, the conversion across the particle is no longer uniform, where the product layer near the surface will be thicker than that at the particle centre. Hence a plateau of the ultimate conversion to $CaSO_4$ appears, as observed from the measurements of the cycled calcine at 1123 – 1223 K, and perhaps the virgin calcine at 973 – 1073 K.

In fact, the above theory might be generalised to any gas-solid reaction involving an increase in the solid volume. For example, there have been few discussions on the pore plugging effect during the carbonation of CaO. Since the ratio of molar volumes for $CaCO_3$/CaO is ~2 and that of $CaSO_4$/CaO is ~ 3, the general view is that the carbonation reaction usually stops due to type I pore plugging, whereas the sulphation reaction stops due to type II pore plugging. It can be shown from simulations that type II pore plugging could occur during the carbonation of the limestone calcines at normal operating conditions in fluidised bed combustors. Figure 6.21 shows the simulated profiles of the local porosity of the 710 – 850 μm dia. Purbeck virgin calcine during carbonation. Here, the carbonation reactions occur in the batch fluidised bed with a stream of 15% CO_2 balance N_2. The same pore structure parameters for the Purbeck virgin calcine were used in the simulation, and the kinetic parameters of carbonation reaction came from the results of the Purbeck limestone calcine after 6 cycles from Chapter 5. The results in Figure 6.21 show a near type I pore plugging at 873 K and a near type II pore plugging at 1023 K. Therefore, the two-type pore-plugging theory proposed above might also be applied to carbonation, or, indeed, to any other reaction

involving an increase in the solid volume when explaining the reasons for incomplete conversion and the temperature maxima of the ultimate conversion to the product solid.

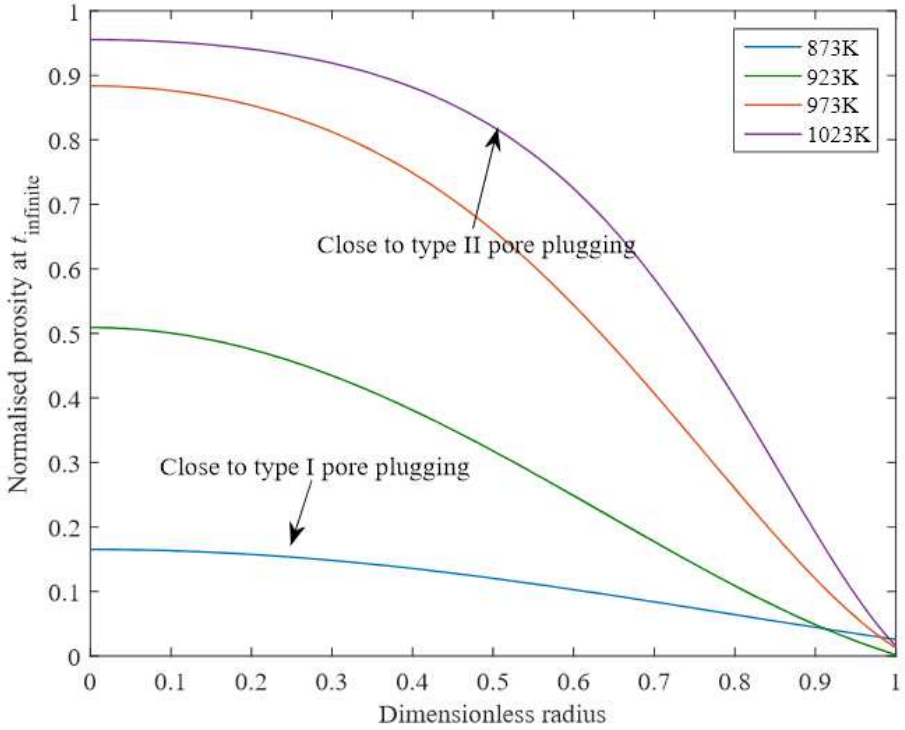

Figure 6.21 Simulated profiles of the local porosity at a long time (t_{infinite}) when the carbonation reaction completely stopped. The porosities are normalised by their initial values. The 710 – 850 μm dia. Purbeck virgin calcine reacts with 15% CO_2 balance N_2 in the batch fluidised bed.

6.6 Conclusions

In this chapter, the general reaction and diffusion model were applied to the sulphation of the limestone calcines under oxidising conditions in a batch fluidised bed. Two calcined Purbeck limestone samples were tested: the virgin calcine and a cycled calcine after 20 calcination-carbonation cycles. Due to incomplete conversion of the particle during sulphation, the $f(X')$ function could not be determined from the experimental measurements. Hence a predefined function $f(X') = 1 - X'$ was used in the model to compare to experimental measurements, where X' was the conversion of $CaSO_4$ normalized by the theoretical maximum conversion allowed by the total pore volume within the particle.

The activation energies of the intrinsic rate constant of sulphation reaction for the virgin calcine and the cycled calcine were both found to be close to ~ 40 kJ mol^{-1}. The activation energies of the product layer diffusivity were determined during the

model fitting, which were 103 and 130 kJ mol^{-1} for the virgin and the cycled calcine respectively. The above values of both types of activation energies were consistent with the values reported previously. At 973 – 1123 K, the predicted rates and conversions matched well with the experimental measurements up to a conversion of 0.25 and 0.05 for the virgin calcine and the cycled calcine respectively. At 1123 – 1223 K, the model showed excellent agreements with the experiments for both the virgin and cycled calcines. For the particles of both calcines, the maximum conversion to $CaSO_4$ seemed to be limited by the pore volume below 300 nm. The virgin calcine had a larger pore volume and surface area but smaller pores, whereas the cycled calcine had a smaller pore volume and surface area with bigger pores. Therefore, the virgin calcine experienced more significant plugging of the surface pores than the cycled calcine did, which were the main reason for the decline in ultimate conversion of $CaSO_4$ with increasing temperature. The most plausible explanation for the maximum conversion achieved in the experiments being smaller than the theoretical value was that the experiments were incomplete and would take much longer time to finish as the rate becomes too small to measure.

It was proposed that the changes in the ultimate conversion to $CaSO_4$ with temperature during sulphation in oxidising conditions followed two typs: (i) type I pore plugging – at low temperature range, the cut-off thickness of product layer was uniform across the particle, thus the ultimate conversion of $CaSO_4$ increased as the product layer diffusivity increases with temperature, and (ii) type II pore plugging – at high temperature the pore entrance at the particle surface becomes completely filled with the product $CaSO_4$ thus preventing gases from accessing unreacted CaO inside the particle. When transitioning from type I to II as temperature increases, the product layer thickness across the particle became non-uniform, so the ultimate conversion reached a plateau because the product layer at the centre is thinner than that at the surface of the particle. These processes were exemplified by the sulphation behaviours of the virgin and the cycled calcines at different temperature. A simulation of the Purbeck virgin calcine during carbonation reaction at different temperatures also shows the two types of pore plugging behaviour, which supports the generalisation of the theory.

Chapter 7 Conclusions

The projected global total consumption of energy is likely to increase by 48% between 2012 and 2040, at which point fossil fuels will still account for ~78% of the global energy use. Coal, the world's most abundant fossil fuel, will play a major role in supporting the development of base-load electricity and will continue to be the largest single fuel used for electricity generation by ~2040. Therefore, the implementation of modern, highly-efficient and clean technologies for the utilisation of coal is the key to the development of economies if the effects of burning coal on society and environment are to be minimised. A rigorously-constructed reaction and diffusion model can help understand the different types of gas-solid reactions involved in the process of the utilisation of fossil fuels, *e.g.* gasification of chars by CO_2 as a part of energy generation process, calcination of $CaCO_3$ during calcium looping for CO_2 capture and sulphation of CaO for SO_2 removal. The overall objective of the work described in this Dissertation was to develop and verify a general reaction and diffusion model for non-catalytic reactions between gases and porous solids, particularly those relevant to the clean use of fossil fuels. Here, the internal pore structure of the solid was characterised by observing the kinetics in a regime limited only by intrinsic chemical reaction. It was hypothesised that a simple arbitrary function, $f(X)$, determined from experimental measurements of rate *vs.* conversion in a kinetically-controlled regime, could be used in place of formal, mathematical pore models, to describe the evolution of pore structure during a reaction influenced by intraparticle mass transfer. The approach was used to study (i) the gasification of chars by CO_2, where the only product was gaseous, (ii) the calcination of $CaCO_3$, where the products were gaseous and solid, and (iii) the sulphation of virgin and sintered CaO by SO_2, where the only product was solid.

The theoretical work developed in Chapter 3 focused on modelling the gas-solid reactions on the scale of a single particle assuming pseudo-steady state, where the Cylindrical Pore Interpolation Model was used to describe the intraparticle mass transfer, the Stefan-Maxwell equations were used for mass transfer external to the particle, the full form of the energy balance equation was employed and the experimentally-measured $f(X)$ function used to describe morphological evolution during

the reaction. The whole system was solved using the method of Orthogonal Collocation on Finite Elements with adaptable numerical meshes for the spatial dimension and marching forward in the time dimension using the method of Finite Differences.

As noted above, it was proposed that a simple arbitrary function, $f(X)$, determined from experimental measurements of rate *vs.* conversion in the kinetically-controlled regime, could be used in place of mathematical pore models, to describe the evolution of pore structure during a reaction influenced by intraparticle mass transfer. Chapter 4 verified the $f(X)$ theory using the gasification of chars by CO_2 as the example, where the gasification kinetics were assumed to follow Ergun's equation. Experiments were conducted in a batch fluidised bed to measure the rates of reaction and the extents of conversion as functions of time, at different temperatures and for various particle sizes, of both lignite char and a less-reactive activated carbon. The results from the model using the experimentally-determined $f(X)$ function were compared with the experimental measurements, with excellent agreement being obtained. The results showed that for the gasification of chars, the $f(X)$ predicted the rate of reaction of particles of various sizes well, all being at the same temperature. However, for the CO_2 gasification of char particles, at least, an $f(X)$ evaluated at one temperature did not predict experimental measurements well at other temperatures. A further investigation using heat-treated chars suggested that the difficulty in applying the $f(X)$ function across different temperatures might be due to the different rate contributions from multiple types of active sites for adsorption within the char particles, thereby suggesting also that the Ergun equation is too simplistic in its treatment of active sites.

To study further the application of the $f(X)$ function across temperature, Chapter 5 examined the calcination of limestone particles, which did not involve gas adsorption hence should not have the complication from multiple types of active sites. The reaction kinetics were modelled as first order in the concentration driving force involving a balance between the calcination (forward) and carbonation (reverse) reactions, where carbonation occurred when $[CO_2]$ was above the equilibrium concentration. Natural limestone particles, which have been subjected to a history of cycling between the calcined and carbonated states, were calcined in a batch fluidised bed, where the reaction rates and the conversions were measured until calcination completed. Excellent agreement between the experiment and the theory was obtained, and the model using the experimentally determined $f(X)$ function predicted the conversion of particles of

various sizes well at temperatures different to that at which the function was derived, thus showing that the $f(X)$ solely dependent on the evolution of the morphology of the particle.

Chapter 5 also investigated the reasons behind the experimentally-observed effects of bulk pressure, temperature and CO_2 mole fraction on the rate of calcination of limestone particles in a fluidised bed. It was found that a rise in either the bulk pressure or the bulk CO_2 mole fraction would increase the local partial pressure of CO_2 inside the particle, which reduced the partial pressure driving force and hence the rate of reaction. The effect of bulk CO_2 mole fraction on the local partial pressure of CO_2 was most significant at high pressure. Hence, to describe the diffusion of CO_2 through the porous particle, the variation of both bulk pressure and CO_2 concentration must be considered. Whilst it was recognised that complex processes occurred at the calcination interface, by using a more rigorous description of reaction and diffusion through the porous particle, the experimentally-observed effects of CO_2 mole fraction and bulk pressure observations can, at least to some extent, be explained.

To investigate whether the reaction and diffusion model could be applied to systems where the product was a solid, Chapter 6 studied the sulphation of the calcined limestone under oxidising conditions. The sulphation reaction involves the formation of a solid product, $CaSO_4$, which took up more volume than the initial reacting solid, hence resulting in a lower surface area, smaller pore volume and more closed pore structure. Experiments were conducted using a virgin calcine and a cycled calcine of a natural limestone in a batch fluidised bed to measure the reaction rates and the conversions up to the point at which the sulphation stopped. However, it was found that, the $f(X)$ function could not be determined from the experimental measurements due to incomplete conversion of the particle during sulphation. Hence, a predefined function $f(X') = 1 - X'$ was used in the model to compare to experimental measurements, where X' was the conversion of $CaSO_4$ normalized by the theoretical maximum conversion allowed by the total pore volume within the particle. At 973 – 1123 K, the predicted rates and conversions matched well to the experimental measurements up to a conversion of 0.25 and 0.05 for the virgin calcine and the cycled calcine, respectively. At 1123 – 1223 K, the model showed excellent agreements with the experiments for both the virgin and cycled calcines. For the particles of both calcines, the maximum conversion to $CaSO_4$ seemed to be limited by the pore volume below 300 nm. The most

plausible explanation for the maximum conversion achieved in the experiments being smaller than the theoretical value was that the experiments were incomplete and would take much longer time to finish as the rate becomes too small to measure. An alternative explanation is that there exists a requirement for mechanical work to disrupt the product layer, and this requirement exceeds what can be supplied by the reaction when the layer exceeds a certain thickness (Duo *et al.*, 1994, 2004; Dennis & Pacciani, 2009). However, this theory would be relevant only if the product layer was formed inwards, *viz.* where the sulphation reaction occurs only at the $CaO/CaSO_4$ interface. This is not, in fact, the case, based on the results of Hsia *et al.* (1993) and Hsia *et al.* (1995), who concluded that the reaction proceeds by the outward diffusion of Ca^{2+} ions through the $CaSO_4$ product layer and that the reaction occurs, in fact, at the interface between the $CaSO_4$ product and the gas in the pore.

Chapter 6 proposed that the changes in the ultimate conversion to $CaSO_4$ with temperature during sulphation in oxidising conditions is of two types, as follows. (1) Type I pore plugging: at low temperatures (*e.g.* experiments with the cycled calcine at 973 – 1123 K), the thickness of the product layer was uniform across the particle, thus the ultimate conversion of $CaSO_4$ increased because the product layer diffusivity increased with temperature. (2) Type II pore plugging – at high temperatures (*e.g.* experiments with the virgin calcine at 1073 – 1223 K), the pore entrance at the particle surface becomes completely filled with the product $CaSO_4$ thus preventing gases from entering while the internal of the particle remained largely unreacted. There is an intermediate stage between type I and II (*e.g.* experiments with the cycled calcine at 1123 – 1223 K and with the virgin calcine at 973 – 1073 K.): as the temperature increases, the product layer thickness across the particle became non-uniform, so the ultimate conversion reached a plateau because the product layer at the centre is thinner than that at the surface of the particle. A simulation of the Purbeck virgin calcine during carbonation reaction at different temperatures also showed the two types of pore plugging behaviour, which supports the generalisation of the theory.

In summary, the work presented in this Dissertation has verified the applicability of the general reaction and diffusion model on all three different non-catalytic gas-solid reactions – gasification, calcination and sulphation. By comparing to the experiments, the theory of using an experimentally determined $f(X)$ function to describe pore evolution during reaction was also verified successfully for at least gasification and

calcination reactions. The models have helped understand some of the experimental observations that lack deterministic explanations by using a rigorous theoretical framework. The approach would aid future work on similar, and other, reactions where simulations are required.

Appendix A: Derivation of the equation of energy

In this section, an energy balance equation at pseudo-steady state will be derived from the standard form of equation of energy for non-catalytic gas-solid reactions. The symbols used here are for this section only.

A.1 Equation of continuity

From Bird *et al.* (2007), the standard equation of continuity of species *n* within a differential volume of $\Delta x \Delta y \Delta z$ with reaction is:

$$\frac{D\rho_n}{Dt} = \frac{\partial \rho_n}{\partial t} + (\boldsymbol{v} \cdot \nabla)\rho_n = -(\nabla \cdot \boldsymbol{J_n}) - \rho_n(\nabla \cdot \boldsymbol{v}) + R_n \tag{A-1}$$

Here ρ_n is the density in kg m^{-3}, $\boldsymbol{J_n}$ is a vector of the advective mass flux in kg m^{-2} s^{-1} (different from the total molar flux, J_n, used in Chaper 3), R_n is the rate of production in kg m^{-3} s^{-1} and $\boldsymbol{v}$ is the velocity vector of the gas mixture. Summed for all *N* species, the equation is hence:

$$\begin{aligned} \frac{D\rho}{Dt} = \frac{\partial \rho}{\partial t} + (\boldsymbol{v} \cdot \nabla)\rho &= -\sum_{n=1}^{N}(\nabla \cdot \boldsymbol{J_n}) - \rho(\nabla \cdot \boldsymbol{v}) + \sum_{i=1}^{N} R_n \\ &= -\rho(\nabla \cdot \boldsymbol{v}) + \sum_{n=1}^{N} R_n \end{aligned} \tag{A-2}$$

because $\sum_{n=1}^{N}(\nabla \cdot \boldsymbol{J_i}) = \nabla \cdot \sum_{n=1}^{N} \boldsymbol{J_n} = 0$.

A.2 Equation of momentum

The standard equation of momentum is:

$$\frac{\partial}{\partial t}(\rho \boldsymbol{v}) = -\left[\nabla \cdot \underline{\boldsymbol{\phi}}\right] + \rho \boldsymbol{g} \tag{A-3}$$

$\boldsymbol{g}$ is the body force *e.g.* gravity. $\underline{\boldsymbol{\phi}}$ is a tensor of combined momentum flux and is equal to

$$\underline{\boldsymbol{\phi}} = P\underline{\boldsymbol{I}} + \underline{\boldsymbol{\tau}} + \rho[\boldsymbol{v} \cdot \boldsymbol{v}^{\boldsymbol{T}}] \tag{A-4}$$

Here P is the total pressure, $\underline{\boldsymbol{I}}$ is an identity tensor, $\underline{\boldsymbol{\tau}}$ is the shear stress tensor and $[\boldsymbol{v} \cdot \boldsymbol{v}^{\boldsymbol{T}}]$ forms a tensor of the product of velocities.

$$\begin{aligned}\frac{D}{Dt}(\rho\boldsymbol{v}) &= \frac{\partial}{\partial t}(\rho\boldsymbol{v}) + (\boldsymbol{v} \cdot \nabla)(\rho\boldsymbol{v}) \\ &= -\left[\nabla \cdot P\underline{\boldsymbol{I}}\right] - \left[\nabla \cdot \underline{\boldsymbol{\tau}}\right] - [\nabla \cdot \rho[\boldsymbol{v} \cdot \boldsymbol{v}^{\boldsymbol{T}}]] + \rho\boldsymbol{g} \\ &\quad + (\boldsymbol{v} \cdot \nabla)(\rho\boldsymbol{v})\end{aligned} \tag{A-5}$$

Using the continuity equation,

$$\begin{aligned}\frac{D}{Dt}(\rho\boldsymbol{v}) &= \boldsymbol{v}\frac{D\rho}{Dt} + \rho\frac{D\boldsymbol{v}}{Dt} = \boldsymbol{v}\left(-\rho(\nabla \cdot \boldsymbol{v}) + \sum_{n=1}^{N} R_n\right) + \rho\frac{D\boldsymbol{v}}{Dt} \\ &= -\rho\boldsymbol{v}(\nabla \cdot \boldsymbol{v}) + \boldsymbol{v}\sum_{n=1}^{N} R_n + \rho\frac{D\boldsymbol{v}}{Dt} \\ &= -\left[\nabla \cdot P\underline{\boldsymbol{I}}\right] - \left[\nabla \cdot \underline{\boldsymbol{\tau}}\right] - [\nabla \cdot \rho[\boldsymbol{v} \cdot \boldsymbol{v}^{\boldsymbol{T}}]] + \rho\boldsymbol{g} \\ &\quad + (\boldsymbol{v} \cdot \nabla)(\rho\boldsymbol{v})\end{aligned} \tag{A-6}$$

It can be shown that $\left[\nabla \cdot \rho[\boldsymbol{v} \cdot \boldsymbol{v}^{\boldsymbol{T}}]\right] = (\boldsymbol{v} \cdot \nabla)(\rho\boldsymbol{v}) + \rho\boldsymbol{v}(\nabla \cdot \boldsymbol{v})$, so the equation becomes:

$$\begin{aligned}\rho\frac{D\boldsymbol{v}}{Dt} &= -\left[\nabla \cdot P\underline{\boldsymbol{I}}\right] - \left[\nabla \cdot \underline{\boldsymbol{\tau}}\right] + \rho\boldsymbol{g} - \boldsymbol{v}\sum_{n=1}^{N} R_n - \left[\nabla \cdot \rho[\boldsymbol{v} \cdot \boldsymbol{v}^{\boldsymbol{T}}]\right] \\ &\quad + (\boldsymbol{v} \cdot \nabla)(\rho\boldsymbol{v}) + \rho\boldsymbol{v}(\nabla \cdot \boldsymbol{v}) \\ &= -\left[\nabla \cdot P\underline{\boldsymbol{I}}\right] - \left[\nabla \cdot \underline{\boldsymbol{\tau}}\right] + \rho\boldsymbol{g} - \boldsymbol{v}\sum_{n=1}^{N} R_n\end{aligned} \tag{A-7}$$

This is effectively the Navier-Stokes equation with non-catalytic equation occurring.

A.3 Equation of energy

The standard equation of energy is also given by Bird *et al.* (2007):

$$\frac{\partial}{\partial t}\left(\rho\widehat{U} + \frac{1}{2}\rho v^2\right) = -\nabla \cdot \boldsymbol{e} + \rho\boldsymbol{v} \cdot \boldsymbol{g} \tag{A-8}$$

where $\widehat{U}$ is the mass specific internal energy and $\boldsymbol{e}$ is a vector of the combined energy flux given by

$$\begin{aligned}\boldsymbol{e} &= \boldsymbol{q} + P\boldsymbol{v} + \left[\underline{\boldsymbol{\tau}} \cdot \boldsymbol{v}\right] + \rho\boldsymbol{v}\left(\widehat{U} + \frac{v^2}{2}\right) \\ &= \boldsymbol{q} + \left[\underline{\boldsymbol{\tau}} \cdot \boldsymbol{v}\right] + \rho\boldsymbol{v}\left(\widehat{U} + \frac{P}{\rho} + \frac{v^2}{2}\right) \\ &= \boldsymbol{q} + \left[\underline{\boldsymbol{\tau}} \cdot \boldsymbol{v}\right] + \rho\boldsymbol{v}\left(\widehat{H} + \frac{v^2}{2}\right)\end{aligned} \tag{A-9}$$

Here $\boldsymbol{q}$ is the heat flux of conduction. And ideal gas law is assumed, so that $\widehat{U} + \frac{P}{\rho} = \widehat{U} + P\widehat{V} = \widehat{H}$. The total differential equation of energy is

$$\begin{aligned}\frac{D}{Dt}\left(\rho\widehat{U} + \frac{1}{2}\rho v^2\right) &= \frac{\partial}{\partial t}\left(\rho\widehat{U} + \frac{1}{2}\rho v^2\right) + (\boldsymbol{v} \cdot \nabla)\left(\rho\widehat{U} + \frac{1}{2}\rho v^2\right) \\ &= -\nabla \cdot \boldsymbol{q} - \nabla \cdot \left[\underline{\boldsymbol{\tau}} \cdot \boldsymbol{v}\right] - \nabla \cdot \rho\boldsymbol{v}\left(\widehat{H} + \frac{v^2}{2}\right) + \rho\boldsymbol{v} \cdot \boldsymbol{g} \\ &\quad + (\boldsymbol{v} \cdot \nabla)\left(\rho\widehat{U} + \frac{1}{2}\rho v^2\right)\end{aligned} \tag{A-10}$$

The left hand side can be splatted by chain rule,

$$\begin{aligned}\frac{D}{Dt}\left(\rho\widehat{U} + \frac{1}{2}\rho v^2\right) &= \left(\widehat{U} + \frac{1}{2}v^2\right)\frac{D\rho}{Dt} + \rho\frac{D\widehat{U}}{Dt} + \rho\frac{D}{Dt}\left(\frac{v^2}{2}\right) \\ &= \left(\widehat{U} + \frac{1}{2}v^2\right)\left(-\rho(\nabla \cdot \boldsymbol{v}) + \sum_{n=1}^{N} R_n\right) + \rho\frac{D\widehat{U}}{Dt} \\ &\quad + \rho\frac{D}{Dt}\left(\frac{v^2}{2}\right) \\ &= -\rho\left(\widehat{U} + \frac{1}{2}v^2\right)(\nabla \cdot \boldsymbol{v}) + \left(\widehat{U} + \frac{1}{2}v^2\right)\sum_{n=1}^{N} R_n + \rho\frac{D\widehat{U}}{Dt} \\ &\quad + \rho\frac{D}{Dt}\left(\frac{v^2}{2}\right)\end{aligned} \tag{A-11}$$

Substitute Eq. (A-11) into (A-10) and rearrange the terms,

$$\rho\frac{D\widehat{U}}{Dt} = -\nabla\cdot\boldsymbol{q} - \nabla\cdot\left[\underline{\boldsymbol{\tau}}\cdot\boldsymbol{v}\right] - \nabla\cdot\rho\boldsymbol{v}\left(\widehat{H}+\frac{v^2}{2}\right) + \rho\boldsymbol{v}\cdot\boldsymbol{g}$$
$$+ (\boldsymbol{v}\cdot\nabla)\left(\rho\widehat{U}+\frac{1}{2}\rho v^2\right) + \rho\left(\widehat{U}+\frac{1}{2}v^2\right)(\nabla\cdot\boldsymbol{v})$$
$$-\left(\widehat{U}+\frac{1}{2}v^2\right)\sum_{n=1}^{N}R_n - \rho\frac{D}{Dt}\left(\frac{v^2}{2}\right)$$
$$= -\nabla\cdot\boldsymbol{q} - \nabla\cdot\left[\underline{\boldsymbol{\tau}}\cdot\boldsymbol{v}\right] - \nabla\cdot\rho\boldsymbol{v}\left(\widehat{H}+\frac{v^2}{2}\right) + \rho\boldsymbol{v}\cdot\boldsymbol{g} + \nabla$$
$$\cdot\rho\boldsymbol{v}\left(\widehat{U}+\frac{v^2}{2}\right) - \left(\widehat{U}+\frac{1}{2}v^2\right)\sum_{n=1}^{N}R_n - \rho\frac{D}{Dt}\left(\frac{v^2}{2}\right) \qquad \text{(A-12)}$$
$$= -\nabla\cdot\boldsymbol{q} - \nabla\cdot\left[\underline{\boldsymbol{\tau}}\cdot\boldsymbol{v}\right] + \rho\boldsymbol{v}\cdot\boldsymbol{g} - \nabla\cdot\rho\boldsymbol{v}\left(\widehat{H}-\widehat{U}\right)$$
$$-\left(\widehat{U}+\frac{1}{2}v^2\right)\sum_{n=1}^{N}R_n - \rho\frac{D}{Dt}\left(\frac{v^2}{2}\right)$$
$$= -\nabla\cdot\boldsymbol{q} - \nabla\cdot\left[\underline{\boldsymbol{\tau}}\cdot\boldsymbol{v}\right] + \rho\boldsymbol{v}\cdot\boldsymbol{g} - \nabla\cdot P\boldsymbol{v}$$
$$-\left(\widehat{U}+\frac{1}{2}v^2\right)\sum_{n=1}^{N}R_n - \rho\frac{D}{Dt}\left(\frac{v^2}{2}\right)$$

From equation (A-7),

$$\rho\frac{D}{Dt}\left(\frac{v^2}{2}\right) = \rho\boldsymbol{v}\frac{D\boldsymbol{v}}{Dt}$$
$$= -\boldsymbol{v}\cdot\left[\nabla\cdot P\underline{\boldsymbol{I}}\right] - \boldsymbol{v}\cdot\left[\nabla\cdot\underline{\boldsymbol{\tau}}\right] + \rho\boldsymbol{v}\cdot\boldsymbol{g} - v^2\sum_{n=1}^{N}R_n \qquad \text{(A-13)}$$

$$\begin{aligned}\rho\frac{D\widehat{U}}{Dt} &= -\nabla\cdot\boldsymbol{q} - \nabla\cdot\left[\underline{\boldsymbol{\tau}}\cdot\boldsymbol{v}\right] + \rho\boldsymbol{v}\cdot\boldsymbol{g} - \nabla\cdot P\boldsymbol{v} - \left(\widehat{U}+\frac{1}{2}v^2\right)\sum_{n=1}^{N}R_n \\ &\quad + \boldsymbol{v}\cdot\left[\nabla\cdot P\underline{\boldsymbol{I}}\right] + \boldsymbol{v}\cdot\left[\nabla\cdot\underline{\boldsymbol{\tau}}\right] - \rho\boldsymbol{v}\cdot\boldsymbol{g} + v^2\sum_{n=1}^{N}R_n \\ &= -\nabla\cdot\boldsymbol{q} - \nabla\cdot\left[\underline{\boldsymbol{\tau}}\cdot\boldsymbol{v}\right] + \boldsymbol{v}\cdot\left[\nabla\cdot\underline{\boldsymbol{\tau}}\right] - \nabla\cdot P\boldsymbol{v} + \boldsymbol{v} \\ &\quad \cdot\left[\nabla\cdot P\underline{\boldsymbol{I}}\right] - \left(\widehat{U}-\frac{1}{2}v^2\right)\sum_{n=1}^{N}R_n \\ &= -\nabla\cdot\boldsymbol{q} - \nabla\cdot\left[\underline{\boldsymbol{\tau}}\cdot\boldsymbol{v}\right] + \boldsymbol{v}\cdot\left[\nabla\cdot\underline{\boldsymbol{\tau}}\right] - P\nabla\cdot\boldsymbol{v} \\ &\quad - \left(\widehat{U}-\frac{1}{2}v^2\right)\sum_{n=1}^{N}R_n\end{aligned} \tag{A-14}$$

$$\rho\frac{D\widehat{H}}{Dt} = \rho\frac{D}{Dt}\left(\widehat{U}+P\widehat{V}\right) = \rho\frac{D\widehat{U}}{Dt} + \frac{DP}{Dt} - \frac{P}{\rho}\frac{D\rho}{Dt} \tag{A-15}$$

$$\begin{aligned}\rho\frac{D\widehat{H}}{Dt} &= -\nabla\cdot\boldsymbol{q} - \nabla\cdot\left[\underline{\boldsymbol{\tau}}\cdot\boldsymbol{v}\right] + \boldsymbol{v}\cdot\left[\nabla\cdot\underline{\boldsymbol{\tau}}\right] - P\nabla\cdot\boldsymbol{v} \\ &\quad - \left(\widehat{U}-\frac{1}{2}v^2\right)\sum_{n=1}^{N}R_n + \frac{DP}{Dt} - \frac{P}{\rho}\frac{D\rho}{Dt}\end{aligned} \tag{A-16}$$

Substitute equation (A-2) into the above equation,

$$\begin{aligned}\rho\frac{D\widehat{H}}{Dt} &= -\nabla\cdot\boldsymbol{q} - \nabla\cdot\left[\underline{\boldsymbol{\tau}}\cdot\boldsymbol{v}\right] + \boldsymbol{v}\cdot\left[\nabla\cdot\underline{\boldsymbol{\tau}}\right] - P\nabla\cdot\boldsymbol{v} \\ &\quad - \left(\widehat{U}-\frac{1}{2}v^2\right)\sum_{n=1}^{N}R_n + \frac{DP}{Dt} - \frac{P}{\rho}\left(-\rho(\nabla\cdot\boldsymbol{v}) + \sum_{n=1}^{N}R_n\right) \\ &= -\nabla\cdot\boldsymbol{q} - \nabla\cdot\left[\underline{\boldsymbol{\tau}}\cdot\boldsymbol{v}\right] + \boldsymbol{v}\cdot\left[\nabla\cdot\underline{\boldsymbol{\tau}}\right] - P\nabla\cdot\boldsymbol{v} \\ &\quad - \left(\widehat{U}-\frac{1}{2}v^2\right)\sum_{n=1}^{N}R_n + \frac{DP}{Dt} + P(\nabla\cdot\boldsymbol{v}) - \frac{P}{\rho}\sum_{n=1}^{N}R_n \\ &= -\nabla\cdot\boldsymbol{q} - \nabla\cdot\left[\underline{\boldsymbol{\tau}}\cdot\boldsymbol{v}\right] + \boldsymbol{v}\cdot\left[\nabla\cdot\underline{\boldsymbol{\tau}}\right] \\ &\quad - \left(\widehat{H}-\frac{1}{2}v^2\right)\sum_{n=1}^{N}R_n + \frac{DP}{Dt}\end{aligned} \tag{A-17}$$

It can be shown that the above equation is equivalent to

$$\rho C_p \frac{DT}{Dt} = -\nabla \cdot \boldsymbol{q} - \nabla \cdot \left[\underline{\boldsymbol{\tau}} \cdot \boldsymbol{v}\right] + \boldsymbol{v} \cdot \left[\nabla \cdot \underline{\boldsymbol{\tau}}\right] - \sum_{n=1}^{N} \widehat{H_n}(-\nabla \cdot \boldsymbol{J_n} + R_n) + \frac{v^2}{2} \sum_{n=1}^{N} R_n + \frac{DP}{Dt} \tag{A-18}$$

C_p is the mass specific heat capacity. Since $\sum_{n=1}^{N}(-\nabla \cdot \boldsymbol{J_n}) = -\nabla \cdot \sum_{n=1}^{N} \boldsymbol{J_n} = 0$,

$$\rho C_p \frac{DT}{Dt} = -\nabla \cdot \boldsymbol{q} - \nabla \cdot \left[\underline{\boldsymbol{\tau}} \cdot \boldsymbol{v}\right] + \boldsymbol{v} \cdot \left[\nabla \cdot \underline{\boldsymbol{\tau}}\right] - \sum_{n=1}^{N} \left(\widehat{H_n} - \frac{v^2}{2}\right) R_n + \frac{DP}{Dt} \tag{A-19}$$

Assuming pseudo-steady state, equation (A-13) will become

$$\rho \boldsymbol{v} \cdot \nabla \left(\frac{v^2}{2}\right) = -(\boldsymbol{v} \cdot \nabla)P - \boldsymbol{v} \cdot \left[\nabla \cdot \underline{\boldsymbol{\tau}}\right] + \rho \boldsymbol{v} \cdot \boldsymbol{g} - v^2 \sum_{n=1}^{N} R_n \tag{A-20}$$

In addition, at pseudo-steady state,

$$\frac{DP}{Dt} \approx (\boldsymbol{v} \cdot \nabla)P = -\rho \boldsymbol{v} \cdot \nabla \left(\frac{v^2}{2}\right) - \boldsymbol{v} \cdot \left[\nabla \cdot \underline{\boldsymbol{\tau}}\right] + \rho \boldsymbol{v} \cdot \boldsymbol{g} - v^2 \sum_{n=1}^{N} R_n \tag{A-21}$$

Therefore, equation (A-19) will become,

$$\begin{aligned} \rho C_p \frac{DT}{Dt} &= -\nabla \cdot \boldsymbol{q} - \nabla \cdot \left[\underline{\boldsymbol{\tau}} \cdot \boldsymbol{v}\right] + \boldsymbol{v} \cdot \left[\nabla \cdot \underline{\boldsymbol{\tau}}\right] - \sum_{n=1}^{N} \left(\widehat{H_n} - \frac{v^2}{2}\right) R_n - \rho \boldsymbol{v} \\ &\quad \cdot \nabla \left(\frac{v^2}{2}\right) - \boldsymbol{v} \cdot \left[\nabla \cdot \underline{\boldsymbol{\tau}}\right] + \rho \boldsymbol{v} \cdot \boldsymbol{g} - v^2 \sum_{n=1}^{N} R_n \\ &= -\nabla \cdot \boldsymbol{q} - \nabla \cdot \left[\underline{\boldsymbol{\tau}} \cdot \boldsymbol{v}\right] - \sum_{n=1}^{N} \left(\widehat{H_n} + \frac{v^2}{2}\right) R_n - \rho \boldsymbol{v} \\ &\quad \cdot \nabla \left(\frac{v^2}{2}\right) + \rho \boldsymbol{v} \cdot \boldsymbol{g} \end{aligned} \tag{A-22}$$

For 1-D spherical coordinate system under pseudo-steady state

$$\begin{aligned} \rho C_p \frac{DT}{Dt} &\approx \rho C_p (\boldsymbol{v} \cdot \nabla)T = \rho C_p \left(v_r \frac{dT}{dr}\right) \\ \rho \boldsymbol{v} \cdot \nabla \left(\frac{v^2}{2}\right) &= \rho v_r \frac{d}{dr}\left(\frac{{v_r}^2}{2}\right) = \rho v_r \cdot v_r \frac{dv_r}{dr} = \sum_{n=1}^{N} G_n v_r \frac{dv_r}{dr} \end{aligned} \tag{A-23}$$

where G_n is the total mass flux of species *n*. Using Fick's law,

$$\nabla \cdot \boldsymbol{q} = \frac{1}{r^2}\frac{d}{dr}\left(r^2\left(-\lambda\frac{dT}{dr}\right)\right) = -\frac{\lambda}{r^2}\frac{d}{dr}\left(r^2\frac{dT}{dr}\right) \tag{A-24}$$

Finally, ignoring the shear stress, the energy equation becomes

$$\frac{\lambda}{r^2}\frac{d}{dr}\left(r^2\frac{dT}{dr}\right) = \rho C_p\left(v_r\frac{dT}{dr}\right) + \sum_{n=1}^{N}\left(\widehat{H_n} + \frac{v^2}{2}\right)R_n + \sum_{n=1}^{N} G_n v_r\frac{dv_r}{dr} \tag{A-25}$$

Appendix B: Coordinate transformation

For any variable *C* of the model in *r* and *t* coordinates to be transformed into $\eta = \frac{r}{r_p}$ and $\theta = t$ coordinates, the following relationships must be true:

$$dC(\eta,\theta) = \frac{\partial C}{\partial \eta}|_\theta d\eta + \frac{\partial C}{\partial \theta}|_\eta d\theta = \frac{\partial C}{\partial r}|_t dr + \frac{\partial C}{\partial t}|_r dt = dC(r,t) \qquad \text{(B-1)}$$

$\theta = t$, so $d\theta = dt$ and θ can be dropped. Since $r_p(t)$ is changing with time, $\eta = \frac{r}{r_p}$ gives:

$$d\eta = \frac{dr}{r_p} - \frac{r}{{r_p}^2} dr_p = \frac{dr}{r_p} - \frac{\eta}{r_p}\frac{dr_p}{dt}dt = \frac{dr}{r_p} - \frac{\eta}{r_p}\dot{r_p}dt \qquad \text{(B-2)}$$

Substitute this into equation (B-1):

$$\begin{aligned} dC(\eta,t) = {} & \frac{\partial C}{\partial \eta}|_t \left(\frac{dr}{r_p} - \frac{\eta}{r_p}\dot{r_p}dt\right) + \frac{\partial C}{\partial t}|_\eta dt = \frac{\partial C}{\partial r}|_t dr + \frac{\partial C}{\partial t}|_r dt \\ & = dC(r,t) \end{aligned} \qquad \text{(B-3)}$$

Collecting terms for *dr* and *dt*:

$$\frac{\partial C}{\partial \eta}|_t \frac{1}{r_p} dr + \left(\frac{\partial C}{\partial t}|_\eta - \frac{\eta}{r_p}\dot{r_p}\right) dt = \frac{\partial C}{\partial r}|_t dr + \frac{\partial C}{\partial t}|_r dt \qquad \text{(B-4)}$$

$$\frac{\partial C}{\partial \eta}|_t = r_p \frac{\partial C}{\partial r}|_t \qquad \frac{\partial C}{\partial t}|_\eta = \frac{\partial C}{\partial t}|_r + \frac{\eta}{r_p}\dot{r_p}\frac{\partial C}{\partial \eta}|_t \qquad \text{(B-5)}$$

Let $F(r,t) = \frac{\partial C}{\partial r}|_t$ and $\psi(\eta,t) = \frac{1}{r_p}\frac{\partial C}{\partial \eta}|_t$, as before

$$dF(r,t) = \frac{\partial F}{\partial r}|_t dr + \frac{\partial F}{\partial t}|_r dt = \frac{\partial \psi}{\partial \eta}|_t d\eta + \frac{\partial \psi}{\partial t}|_\eta dt = d\psi(\eta,t) \qquad \text{(B-6)}$$

Substitute equation (B-2) into equation (B-6), and obtain:

$$\frac{\partial^2 C}{\partial r^2} = \frac{1}{{r_p}^2}\frac{\partial^2 C}{\partial \eta^2} \qquad \text{(B-7)}$$

Since there is no second derivative of time, it is unnecessary to derive the expression.

To sum up, equation (B-5) and (B-7) transform any variable in *r* coordinate to $\eta = \frac{r}{r_p}$ coordinate, taking into account the change of r_p with time. Similarly for external model, where *r* is transformed into $\eta = \frac{r-r_p}{\delta}$ with both r_p and δ changing, the derivatives will be:

$$\frac{\partial C}{\partial \eta}|_t = \delta \frac{\partial C}{\partial r}|_t \qquad \frac{\partial C}{\partial t}|_\eta = \frac{\partial C}{\partial t}|_r + \left(\frac{\eta}{\delta^2}\dot{\delta} + \frac{1}{\delta}\dot{r_p}\right)\frac{\partial C}{\partial \eta}|_t \tag{B-8}$$

The time derivative is not needed as there is no time dependence in the external model.

Appendix C: Numerical solutions to the general reaction and diffusion model

The symbols used here are specific to this appendix, and the definitions can be found within the text. Outside this appendix, please refer to the List of Abbreviations and Acronyms for definitions of symbols.

C.1 The principle of orthogonal collocation

Any dependent variable $y(x)$ can be expanded by using orthogonal polynomials, usually Legendre polynomials (Chang & Finlayson, 1978b), at a number of locations (*i.e.* collocation points) in the independent variable x. Thus y and x can be represented by vectors with the same number of elements as that of the collocation points. At each point $x|_j$, the corresponding value of y is given by the Legendre polynomial expansion:

$$y(x|_j) = \sum_{i=1}^{NP} a_i (x|_j)^{i-1} = a_1 + a_2(x|_j) \cdots a_i(x|_j)^{i-1} \cdots a_{NP}(x|_j)^{NP-1} \quad \text{(C-1)}$$

$$j = 1,2 \ldots NP$$

where *NP* is the total number of collocation points and $a_1 - a_{NP}$ are the unique set of constants that describes the relationship between x and y. Written in a matrix form, the above equation becomes:

$$\begin{bmatrix} y(x|_1) \\ \vdots \\ y(x|_j) \\ \vdots \\ y(x|_{NP}) \end{bmatrix} = \begin{bmatrix} 1 & \cdots & (x|_1)^{i-1} & \cdots & (x|_1)^{NP-1} \\ \vdots & \ddots & \vdots & \ddots & \vdots \\ 1 & \cdots & (x|_j)^{i-1} & \cdots & (x|_j)^{NP-1} \\ \vdots & \ddots & \vdots & \ddots & \vdots \\ 1 & \cdots & (x|_{NP})^{i-1} & \cdots & (x|_{NP})^{NP-1} \end{bmatrix} \begin{bmatrix} a_1 \\ \vdots \\ a_i \\ \vdots \\ a_{NP} \end{bmatrix} \quad \text{(C-2)}$$

$$[y] = [Q] \cdot [a] \qquad [Q]_{ji} = (x|_j)^{i-1} \quad \text{(C-3)}$$

Here $[y]$ is the matrix form of $y(x)$ and $[Q]$ is the matrix containing a set of expressions of *x*. The constant matrix $[a]$ can be calculated from

$$[a] = [Q^{-1}] \cdot [y] \tag{C-4}$$

where $[Q^{-1}]$ is the inverse matrix of $[Q]$ with a dimension of $[NP \times NP]$ and the matrices $[y]$ and $[a]$ have the dimension of $[NP \times 1]$. Differentiating Eq. (C-1) gives:

$$\begin{aligned}\frac{dy(x|_j)}{dx} &= \sum_{i=1}^{NP}(i-1)a_i\left(x|_j\right)^{i-2} \\ &= 0 + a_2 \cdots (i-1)a_i\left(x|_j\right)^{i-2} \cdots (NP \\ &\quad - 1)a_{NP}\left(x|_j\right)^{NP-2}\end{aligned} \tag{C-5}$$

Expressed in matrix form, the first derivative of *y* with respect to *x* becomes:

$$\begin{bmatrix} \frac{dy(x|_1)}{dx} \\ \vdots \\ \frac{dy(x|_j)}{dx} \\ \vdots \\ \frac{dy(x|_{NP})}{dx} \end{bmatrix} \tag{C-6}$$

$$= \begin{bmatrix} 0 & \cdots & (i-1)(x|_1)^{i-2} & \cdots & (NP-1)(x|_1)^{NP-2} \\ \vdots & \ddots & \vdots & \ddots & \vdots \\ 0 & \cdots & (i-1)\left(x|_j\right)^{i-2} & \cdots & (NP-1)\left(x|_j\right)^{NP-2} \\ \vdots & \ddots & \vdots & \ddots & \vdots \\ 0 & \cdots & (i-1)(x|_{NP})^{i-2} & \cdots & (NP-1)(x|_{NP})^{NP-2} \end{bmatrix} \begin{bmatrix} a_1 \\ \vdots \\ a_i \\ \vdots \\ a_{NP} \end{bmatrix}$$

$$[DY] = [C] \cdot [a] = [C] \cdot [Q^{-1}] \cdot [y] = [A] \cdot [y]$$

$$[C]_{ji} = (i-1)\left(x|_j\right)^{i-2} \tag{C-7}$$

$$[A]_{ji} = \left(\sum_{i=1}^{NP}(i-1)\left(x|_j\right)^{i-2}\right)\left(\sum_{j=1}^{NP}[Q^{-1}]_{ji}\right)$$

where $[DY]$ is the matrix form of the first derivative of *y*, $[C]$ is the matrix containing a different set of expressions of *x* and $[A]$ is the product of $[C]$ and $[Q^{-1}]$. Equation (C-7) shows that the first derivative of *y* can be transformed into a simple product of the matrix $[A]$ and the matrix of the dependent variable, $[y]$. The same transformation could be made to the second derivative of *y*:

$$[DDY] = [D] \cdot [a] = [D] \cdot [Q^{-1}] \cdot [y] = [B] \cdot [y] \tag{C-8}$$

$$[D]_{ji} = (i-1)(i-2)\left(x|_j\right)^{i-3}$$

$$[B]_{ji} = \left(\sum_{i=1}^{NP}(i-1)(i-2)\left(x|_j\right)^{i-3}\right)\left(\sum_{j=1}^{NP}[Q^{-1}]_{ji}\right)$$

where $[DDY]$ is the matrix form of the second derivative of y, $[D]$ is the matrix containing another set of expressions of x and $[B]$ is the product of $[D]$ and $[Q^{-1}]$. The matrices $[Q^{-1}]$, $[A]$ and $[B]$, all having a dimension $[NP \times NP]$, can be calculated once the locations of the collocation points $x|_j$ are defined. The system can be made orthogonal if the positions of the collocation points correspond to the roots of an orthogonal polynomial. One of the approaches is to apply orthogonal collocation to the domain ranging from 0 to 1 with equal spacing between two collocation points, hence $x|_j$ can be defined as:

$$x|_j = \frac{1 \times j}{NP-1} = \frac{j}{NP-1} \tag{C-9}$$

This is why the model equations need to be non-dimensionalised in section 3.3. As an example, for $NP = 5$ collocation points, the values of the $[Q^{-1}]$, $[A]$ and $[B]$ matrices are as below:

$$[Q^{-1}] = \begin{bmatrix} 1.0 & 0 & 0 & 0 & 0 \\ -8.3 & 16.0 & -12.0 & 5.3 & -1.0 \\ 23.3 & -69.3 & 76.0 & -37.3 & 7.3 \\ -26.7 & 96.0 & -128.0 & 74.7 & -16.0 \\ 10.7 & -42.7 & 64.0 & -42.7 & 10.7 \end{bmatrix}$$

$$[A] = \begin{bmatrix} -8.3 & 16.0 & -12.0 & 5.3 & -1.0 \\ -1.0 & -3.3 & 6.0 & -2.0 & 0.3 \\ 0.3 & -2.7 & 0 & 2.7 & -0.3 \\ -0.3 & 2.0 & -6.0 & 3.3 & 1.0 \\ 1.0 & -5.3 & 12.0 & -16.0 & 8.3 \end{bmatrix} \tag{C-10}$$

$$[B] = \begin{bmatrix} 46.7 & -138.7 & 152.0 & -74.7 & 14.7 \\ 14.7 & -26.7 & 8.0 & 5.3 & -1.3 \\ -1.3 & 21.3 & -40.0 & 21.3 & -1.3 \\ -1.3 & 5.3 & 8.0 & -26.7 & 14.7 \\ 14.7 & -74.7 & 152.0 & -138.7 & 46.7 \end{bmatrix}$$

By transforming the derivatives of $y(x)$ into the matrix forms in Eq. (C-7) and (C-8), the differential equations become linear equations of matrices, once solved, yielding the values of dependent variable at the location of the collocation point, thus

forming a complete profile of the dependent variable y across the system domain x. In addition, multiple dependent variables (e.g. *N* variables) can be stacked within the same matrix equations as Eq. (C-2) which can be solved simultaneously:

$$\begin{bmatrix} y_1(x|_1) & \cdots & y_k(x|_1) & \cdots & y_N(x|_1) \\ \vdots & \ddots & \vdots & \ddots & \vdots \\ y_1(x|_j) & \cdots & y_k(x|_j) & \cdots & y_N(x|_j) \\ \vdots & \ddots & \vdots & \ddots & \vdots \\ y_1(x|_{NP}) & \cdots & y_k(x|_{NP}) & \cdots & y_N(x|_{NP}) \end{bmatrix} = \begin{bmatrix} 1 & \cdots & (x|_1)^{i-1} & \cdots & (x|_1)^{NP-1} \\ \vdots & \ddots & \vdots & \ddots & \vdots \\ 1 & \cdots & (x|_j)^{i-1} & \cdots & (x|_j)^{NP-1} \\ \vdots & \ddots & \vdots & \ddots & \vdots \\ 1 & \cdots & (x|_{NP})^{i-1} & \cdots & (x|_{NP})^{NP-1} \end{bmatrix} \begin{bmatrix} a_1^1 & \cdots & a_1^k & \cdots & a_1^N \\ \vdots & \ddots & \vdots & \ddots & \vdots \\ a_i^1 & \cdots & a_i^k & \cdots & a_i^N \\ \vdots & \ddots & \vdots & \ddots & \vdots \\ a_{NP}^1 & \cdots & a_{NP}^k & \cdots & a_{NP}^N \end{bmatrix} \quad \text{(C-11)}$$

$$[y_N] = [Q] \cdot [a^N] \qquad [Q]_{ji} = (x|_j)^{i-1} \quad \text{(C-12)}$$

where there are *N* dependent variables of y and *N* sets of constants of a, forming the matrices of $[y_N]$ and $[a^N]$ with a dimension of $[NP \times N]$. The same principle works for transforming the derivatives of *N* dependent variables against x into their corresponding matrix forms:

$$[DY_N] = [A] \cdot [y_N] \qquad [DDY_N] = [B] \cdot [y_N] \quad \text{(C-13)}$$

C.2 The principle of orthogonal collocation on finite elements

For system with a steep gradient in $y(x)$, the method of orthogonal collocation becomes unwieldy because a large number of collocation points is needed to capture the rapid change in values. To circumvent this, the method of Orthogonal Collocation on Finite Element can be used, where the system domain, x, is divided into smaller subdomains, called finite elements, and the method of orthogonal collocation applied to each of them with the constraints of continuous values of the function and its first derivative at the boundaries between the neighbouring elements. For NE finite elements each having NP collocation points (including the boundary points of the element), the total number of collocation points, NT, is given by

$$NT = NE \times (NP - 1) + 1 \quad \text{(C-14)}$$

Thus all of the matrices of the dependent variables *e.g.* y_n, J'_n, P' and T', and the independent spatial variables have a dimension of $[NT \times 1]$. The sharp gradient issue can be resolved by placing more elements in the steep region. This ability to vary the number of finite elements and collocation points, depending on the sharp gradient of the system, is a major advantage of OCFE.

In order to apply orthogonal collocation to each of the finite elements, a further coordinate transformation is needed so that the dimensionless variables of the system domain span from 0 at the first node to 1 at the last node within each finite element. The new spatial coordinate within each of the NE finite elements is defined as

$$w|_i^v = \frac{x|_i^v - x|_1^v}{x|_{NP}^v - x|_1^v} = \frac{x|_i^v - x|_1^v}{\Delta x|^v} \qquad \text{(C-15)}$$

$$dx|_i^v = \Delta x|^v \cdot dw|_i^v \qquad (i = 1,2 \dots NP \quad v = 1,2 \dots NE)$$

where x is equivalent to the independent variable of the system, η, used in section 3.3 and w is the transformed variable to be used by OCFE. The superscript and the subscript of $w|_i^v$ refer to the index of the w within corresponding element, *i.e.* the i^{th} collocation point within the v^{th} finite element, as shown in Figure C.1. The spacing of the v^{th} finite element, Δx^v, is the difference between the dimensionless coordinates of the last collocation point within the element, $x|_{NP}^v$, and that of the first one, $x|_1^v$. The spacing can be reduced if there is a significant sharp gradient within the ODE system, and increased if the sharp gradient is low. In effect for a chosen number of finite elements, this method puts more elements to regions with sharp gradient and less elements to regions with low gradient.

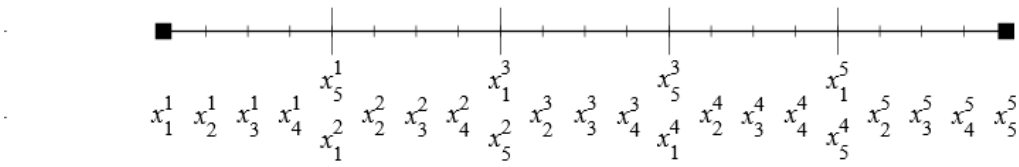

Figure C.1. Showing the system domain divided into 5 finite elements each of which has 5 collocation points. The superscript indicates the finite element and the subscript the collocation point.

The application of OCFE means that the transformation of the dependent variables and their derivatives into matrix forms need to be conducted for every finite element following the pattern shown in Eq. (C-11) to (C-13). After merging the neighboring boundary points between 2 finite elements, the dimension of the stacked

matrix of the dependent variables expands from $[NP \times N]$ for a single element to $[NT \times N]$ for NE elements. As defined earlier, the parameter N is the total number of dependent variables stacked together. The matrices are stacked together as follow:

$$\begin{bmatrix} [y_N]|^{v=1} \\ \vdots \\ [y_N]|^{v} \\ \vdots \\ [y_N]|^{v=NE} \end{bmatrix} = \begin{bmatrix} [Q]|^{v=1} & \cdots & 0 & \cdots & 0 \\ \vdots & \ddots & \vdots & \ddots & \vdots \\ 0 & \cdots & [Q]|^{v} & \cdots & 0 \\ \vdots & \ddots & \vdots & \ddots & \vdots \\ 0 & \cdots & 0 & \cdots & [Q]|^{v=NE} \end{bmatrix} \cdot \begin{bmatrix} [a^N]|^{v=1} \\ \vdots \\ [a^N]|^{v} \\ \vdots \\ [a^N]|^{v=NE} \end{bmatrix}$$

$$\begin{bmatrix} [DY_N]|^{v=1} \\ \vdots \\ [DY_N]|^{v} \\ \vdots \\ [DY_N]|^{v=NE} \end{bmatrix} = \begin{bmatrix} [A]|^{v=1} & \cdots & 0 & \cdots & 0 \\ \vdots & \ddots & \vdots & \ddots & \vdots \\ 0 & \cdots & [A]|^{v} & \cdots & 0 \\ \vdots & \ddots & \vdots & \ddots & \vdots \\ 0 & \cdots & 0 & \cdots & [A]|^{v=NE} \end{bmatrix} \cdot \begin{bmatrix} [y_N]|^{v=1} \\ \vdots \\ [y_N]|^{v} \\ \vdots \\ [y_N]|^{v=NE} \end{bmatrix} \tag{C-16}$$

$$\begin{bmatrix} [DDY_N]|^{v=1} \\ \vdots \\ [DDY_N]|^{v} \\ \vdots \\ [DDY_N]|^{v=NE} \end{bmatrix} = \begin{bmatrix} [B]|^{v=1} & \cdots & 0 & \cdots & 0 \\ \vdots & \ddots & \vdots & \ddots & \vdots \\ 0 & \cdots & [B]|^{v} & \cdots & 0 \\ \vdots & \ddots & \vdots & \ddots & \vdots \\ 0 & \cdots & 0 & \cdots & [B]|^{v=NE} \end{bmatrix} \cdot \begin{bmatrix} [y_N]|^{v=1} \\ \vdots \\ [y_N]|^{v} \\ \vdots \\ [y_N]|^{v=NE} \end{bmatrix}$$

C.3 Boundary conditions and continuity constraints

Before solving the system, some further adjustments of the above equations are needed to include the boundary conditions of the ODEs and the continuity constraints at the boundaries between two neighboring finite elements. In order to add the boundary conditions, the matrix equations need to satisfy the boundary conditions at $w|_1^1$ and $w|_{NP}^{NE}$. This means replacing the first and last rows of matrix elements with the boundary conditions, which usually are Dirichlet (fixed values at the boundary), Neumann (fixed derivatives at the boundary) or Cauchy (fixed value and derivatives at the boundary) type conditions; an example will be given shortly in this section.

Continuity constraints are essential when merging the two boundary nodes between neighbouring elements during stacking of matrix equations, where the value and gradient of the dependent variables at the last node of the v^{th} element must equal to those at the first node of the $(v+1)^{th}$ element. Thus

$$y|_{NP}^{v} = y|_{1}^{v+1} \qquad \left.\frac{dy}{dx}\right|_{NP}^{v} = \left.\frac{dy}{dx}\right|_{1}^{v+1} \tag{C-17}$$

Using Eq. (C-7) and (C-15),

$$y|_{NP}^{v} = y|_{1}^{v+1} \qquad \frac{1}{\Delta x|^{v}} \sum_{i=1}^{NP} [A]_{j=NP,i}\, y|_{i}^{v} = \frac{1}{\Delta x|^{v+1}} \sum_{i=1}^{NP} [A]_{j=1,i}\, y|_{i}^{v+1} \tag{C-18}$$

Once all the derivatives of the dependent variables within the system of ODEs have been substituted by their corresponding matrix equations, the model system can be simplified into a linear matrix equation in the form

$$[M] \cdot [Y] = [F(Y)] \tag{C-19}$$

where $[M]$ is the linear combination of the $[A]$, $[B]$ and other matrices for higher order derivatives of the dependent variables, $[Y]$ is the matrix containing all dependent variables across all collocation points and $[F(Y)]$ is the residual matrix containing non-linear function of Y.

The approximate forms of the matrices $[M]$ and $[F]$ are shown in Figure C.2, which shows how the solution proceeds for 1 dependent variable using 5 finite elements, each having 5 collocation points, thus giving a total number of 21 collocation points. A Neumann boundary condition specified at the first row means a fixed dy/dx at $x = 0$, which represents a commonly used boundary conditions at the centre of a spherical particle (*e.g.* zero gradient of concentration, pressure and temperature). A Dirichlet (fixed values at the boundary) specified at the last row means a fixed value of y at $x = 1$, which is also a common form of boundary conditions at the surface of a spherical particle (*e.g.* concentration, pressure and temperature are the same as the bulk condition). The form of the continuous constraints in Figure C.2 is a result of the Eq. (C-18), where the value continuity means two neighbouring finite elements share the same boundary node marked by the square boxes and the gradient continuity leads to zero cell values in the corresponding $[F]$ matrix.

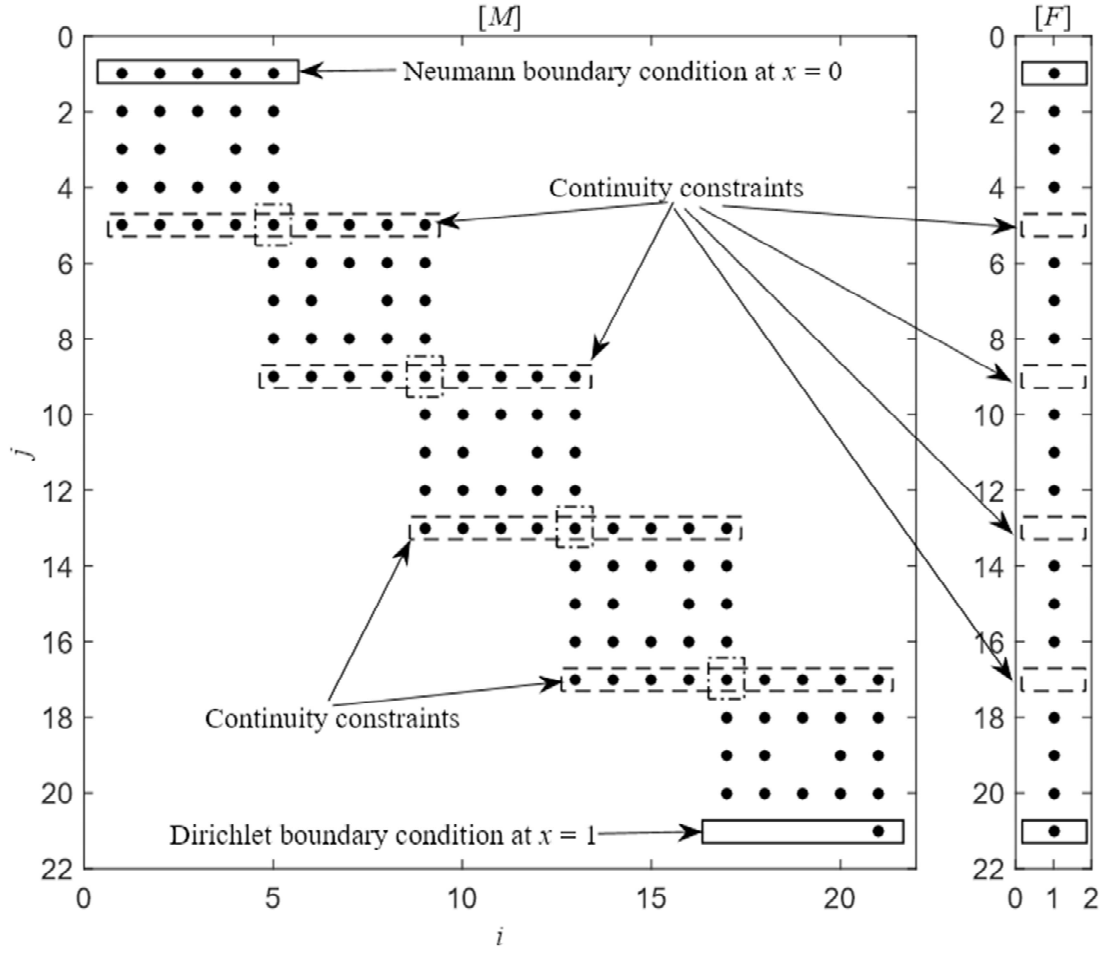

Figure C.2. The schematic form of the matrices $[M]$ and $[F]$ for $NE = 5$, $NP = 5$ and $NT = 21$, where the boundary conditions and the continuity constraints are highlighted. The empty space means a zero value of the matrix cell and the boundary nodes between two finite elements are marked by the square boxes.

A simple example of solving a non-linear, non-homogenous 2nd order ODE is shown here to demonstrate the application of the method:

$$\frac{d^2y}{dx^2} + 3\frac{dy}{dx} + 2y = xy^2 \qquad x = 0\text{: } \frac{dy}{dx} = 0 \qquad x = 1\text{: } y = 1 \tag{C-20}$$

Transforming the derivatives into their matrix forms,

$$[B] \cdot [y] - 3[A] \cdot [y] - 2[y] = [xy^2]$$

$$\underbrace{([B] - 3[A] - [2])}_{[M]} \cdot \underbrace{[y]}_{[Y]} = \underbrace{[xy^2]}_{[F]} \tag{C-21}$$

$$x = 0\text{: } \frac{dy}{dx} = 0 \Rightarrow \sum_{i=1}^{NP} [A]_{j=1,i}\, y|_i^v = 0 \qquad x = 1\text{: } y = 1 \Rightarrow y|_{NP}^{NE} = 1$$

With the help of an established algorithm such as Gaussian elimination or LU decomposition, the solution of the equations can be solved iteratively by inverting the matrices based on the results of the previous iteration:

$$[Y_t] = [M^{-1}] \cdot [F(Y_{t-1})] \tag{C-22}$$

An initial guess of the solution is needed to start the iteration.

C.4 Adaptive meshing algorithm for the finite elements

The adjustment of the spacing of the finite elements can be linked to the appropriate output from the iterative calculation so that it can be updated after each iteration, thus becoming adaptive. Since the distribution of gas concentration is the most direct indication of the gradient of the system, the result of its calculation after each iteration is used to calculate the spacing of all *NE* finite elements. Assume the spacing of the finite element for current iteration, $(\Delta x|^v)_t$, is a fraction of the largest element Δx_0. Here the fraction is an exponentially decay function of the ratio between the gradient of the current element, $|(dy_n/d\Delta x|^v)|_{t-\Delta t}$, and the maximum gradient of the finite element across the whole domain.

$$(\Delta x|^v)_t = \Delta x_0 \exp\left(-\alpha_x \frac{\left|\frac{dy_n}{d\Delta x|^v}\right|_{t-\Delta t}}{\max\left(\left|\frac{dy_n}{d\Delta x|^v}\right|_{t-\Delta t}\right)}\right) \tag{C-23}$$

When the gradient of the current element is zero, *e.g.* a flat concentration profile, the element space is simply Δx_0. However, when the gradient of the current element corresponds to the largest gradient across the entire domain, the element spacing will be $\Delta x_0 \exp(-\alpha_x)$, which is also the smallest element spacing. The parameter α_x is an input value which can take any positive value. The value of Δx_0 can be calculated from summing up all finite elements to 1, hence

$$\sum_{v=1}^{NE} (\Delta x|^v)_t = \Delta x_0 \sum_{v=1}^{NE} \exp\left(-\alpha_x \frac{\left|\frac{dy_n}{d\Delta x|^v}\right|_{t-\Delta t}}{\max\left(\left|\frac{dy_n}{d\Delta x|^v}\right|_{t-\Delta t}\right)}\right) = 1 \tag{C-24}$$

Substitute Δx_0 back into Eq. (C-23),

$$(\Delta x|^{v})_{t} \tag{C-25}$$

$$= \exp\left(-\alpha_x \frac{\left|\frac{dy_n}{d\Delta x|^{v}}\right|_{t-\Delta t}}{\max\left(\left|\frac{dy_n}{d\Delta x|^{v}}\right|_{t-\Delta t}\right)}\right) \Bigg/ \sum_{v=1}^{NE} \exp\left(-\alpha_x \frac{\left|\frac{dy_n}{d\Delta x|^{v}}\right|_{t-\Delta t}}{\max\left(\left|\frac{dy_n}{d\Delta x|^{v}}\right|_{t-\Delta t}\right)}\right)$$

This single factor algorithm is very robust in adjusting the element distribution and easy to implement within the OCFE structure. The initial spacing of the finite elements is uniform, then as calculation proceeds the element spacing changes to adapt to the results of the iterations. The estimated computation cost can be reduced by 50 – 100% when solving for some extremely stiff system. Figure C.3 shows an example of the distributions of the finite element across the particle radius at different iteration stage using the adaptive meshing algorithm and their corresponding concentration profiles.

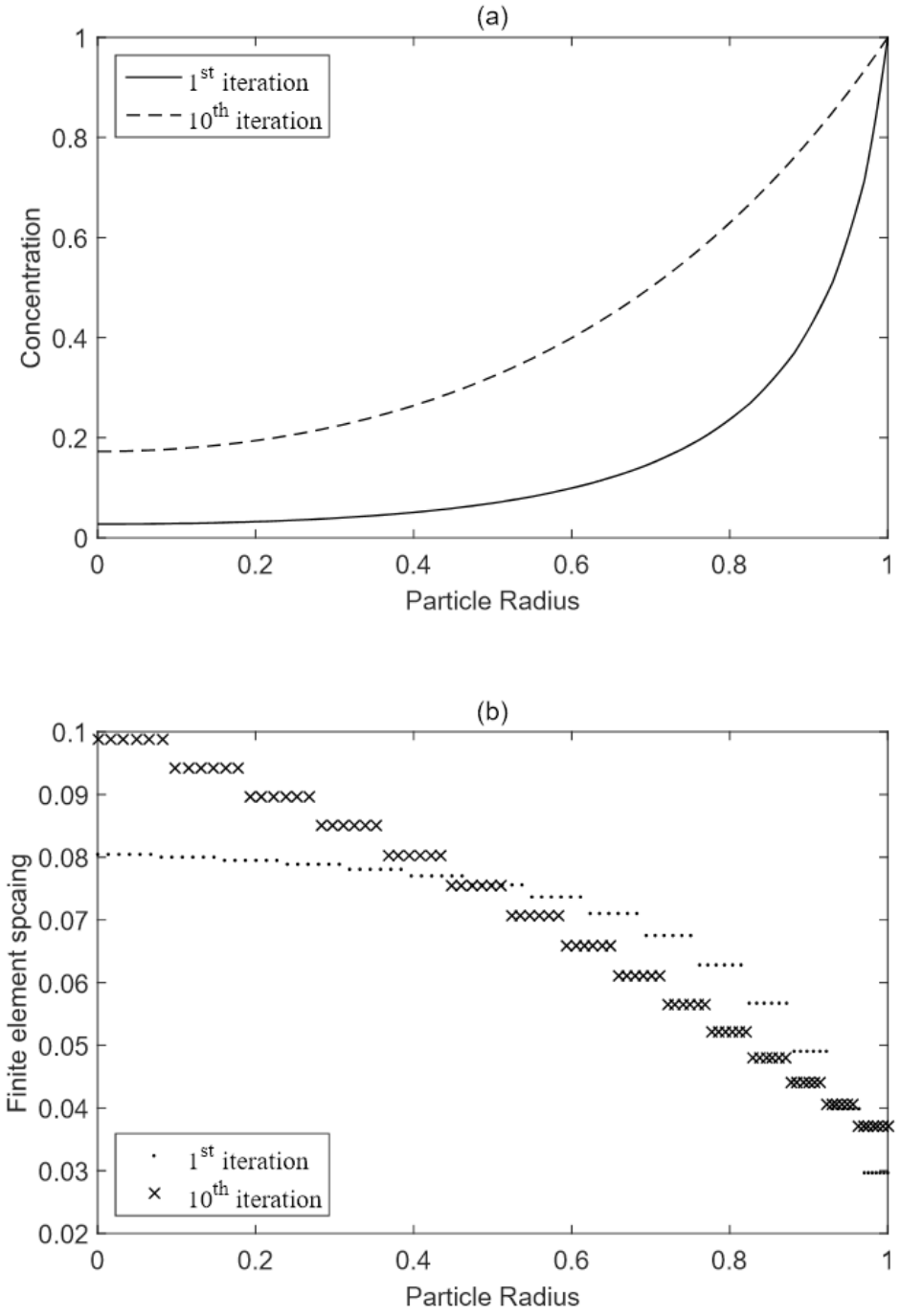

Figure C.3 The spacing of finite elements at different iteration stage using the adaptive meshing algorithm with 15 elements each having 7 collocation points and α_x is 1. Note that only 6 collocation points can be seen in the figure as the boundary points between two neighbouring elements are merged.

Appendix D: Deconvolution of experimental measurements

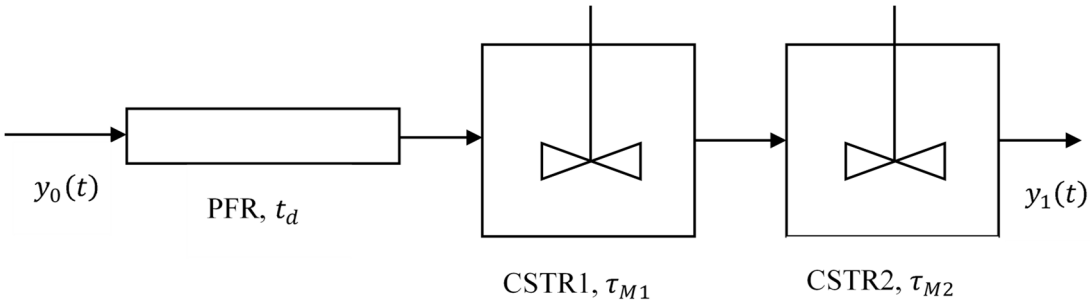

Figure D.1 Model for the deconvolution of the gas concentration in the sampling line and the gas analyser approximated to a PFR with a mean residence time of t_d in series with two CSTRs with a mixing time τ_{M1} and τ_{M2} respectively. The true concentration is y_0 and the measured concentration is y_1.

When gases are sampled from the fluidised bed reactor, they must be transported through a sampling line and into the gas analyser. During an experiment, the mixing within the sampling line and the analyser, could result in a difference between the measured value of concentration and that of the true concentration of gas in the reactor. Here the sampling line and the analyser are modelled as two continuous stirred tank reactors (CSTR) in series with a plug flow reactor (PFR). Figure D.1 shows the model simulating the mixing effect in the sampling line and the analyser, where $y_0(t)$ is the true mole fraction and $y_1(t)$ is the measured mole fraction. The relationship between $y_0(t)$ and $y_1(t)$ is as follow:

$$y_0(t)\mathrm{H}(t-t_d) = (\tau_{M1}\tau_{M2})\frac{d^2y_1(t)}{dt^2} + (\tau_{M1}+\tau_{M2})\frac{dy_1(t)}{dt} + y_1(t) \qquad \text{(D-1)}$$

where $\mathrm{H}(t-t_d)$ is a Heaviside function, t_d is the dead time of the PFR, τ_{M1} is the mean residence time of CSTR1 and τ_{M2} is the mean residence time of CSTR2. When there is a unit impulse change to the $y_0(t)$, the impulse response of $y_1(t)$ is given by

$$y_1(t) = \frac{\exp\left(-\frac{t-t_d}{\tau_{M1}}\right) - \exp(-\frac{t-t_d}{\tau_{M2}})}{\tau_{M1}-\tau_{M2}}\mathrm{H}(t-t_d) \qquad \text{(D-2)}$$

When $\tau_{M2} = 0$, Eqs. (D-1) and (D-2) describe a single CSTR in series with a PFR, which was used in some previous works (Scott, 2004; Saucedo, 2014; Saucedo *et al.*, 2015).

When determining the parameters of the deconvolution model, *i.e.* t_d, τ_{M1} and τ_{M2}, one of the gases will be selected to conduct the measurement of the step response, which could then produce the impulse response by numerical differentiation. After the concentration measured by the analyser stabilised, the recording of the concentration response started at the same time when the flow of the select gas was turned off. The concentration of the gas was measured continuously until it reached the steady state. Figure D.2 shows an example of the step and the inverted impulse response signals measured, where the dead time t_d, can be conveniently estimated from the delay in the response signals. The mean residence time constants τ_{M1} and τ_{M2} were determined by fitting the Eq. (D-2) to the impulse response signal after it started to raise. The values of the τ_{M1} and τ_{M2} shown in Figure D.2(b) are very close to each other, which are in fact the same when kept to only 1 decimal place. However, it does not mean the Eq. (D-2) should be zero. Using Taylor expansion, Eq. (D-2) becomes

$$y_1(t) = \left[\frac{t - t_d}{\tau_{M1}\tau_{M2}} + \frac{(\tau_{M1} + \tau_{M2})}{2}(t - t_d)^2 + \mathrm{O}((t - t_d)^3)\right]\mathrm{H}(t - t_d) \quad \text{(D-3)}$$

Hence, even when there is a very small difference between τ_{M1} and τ_{M2}, Eq. (D-2) is not zero.

The two CSTRs in series with a PFR model fit much better to both the step and the impulse responses compared to the single CSTR in series with a PFR model in Figure D.2. Thus it would give a more realistic results for the deconvolution process. However, the two CSTRs in series with a PFR model is 2nd order system which will yield oscillatory results for the deconvolution process if the measurement is too noisy. Hence in practise, the raw concentration measurements needed to be smoothed before deconvolution. Occasionally, the single CSTR in series with a PFR model was used for the deconvolution process when the two CSTRs in series with a PFR model failed to produce a reliable result.

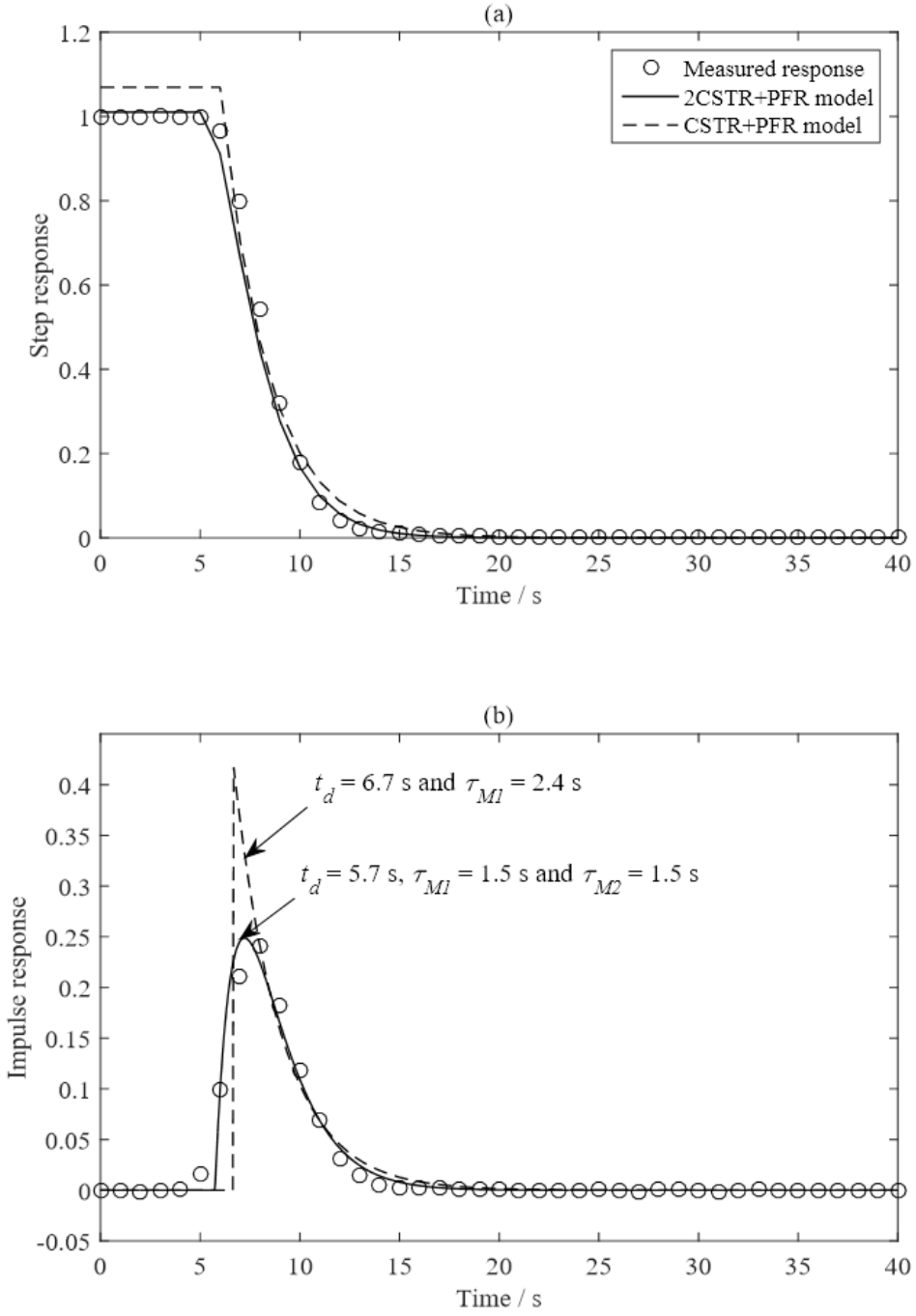

Figure D.2 The fit of the deconvolution model to the step and the impulse response measurements for fluidised bed. For 2 CSTR in series with a PFR, $t_d =$ 5.7 s and $\tau_{M1} = \tau_{M2} =$ 1.5 s; for 1 CSTR in series with a PFR, $t_d =$ 6.7 s and $\tau_{M1} =$ 2.4 s.

Appendix E: Calculation of the effectiveness factor for gasification

Roberts & Satterfield (1965) obtained effectiveness factors for rates of reactions written in the form:

$$Q_{\mathrm{C}} = \frac{k p^{S}_{\mathrm{CO_2}}}{1 + K_{\mathrm{CO_2}} p^{S}_{\mathrm{CO_2}} + K_{\mathrm{CO}} p^{S}_{\mathrm{CO}}} \qquad k = c k_1 \rho_e \times f(X) \tag{E-1}$$

where $K_{\mathrm{CO}} = k_{-1}/k_2$ and $K_{\mathrm{CO_2}} = k_1/k_2$ were the adsorption constants. The effectiveness factor is calculated from

$$\kappa_{eff} = \tanh\left(\frac{\gamma\phi^*}{\phi^*}\right) \qquad \phi^* = \frac{\phi_M}{\phi_C} \tag{E-2}$$

$$\gamma = 1 - 0.4457\alpha^2\phi^* \exp\left(-0.1153\phi^{*2}\right) \qquad \alpha = K p^{S}_{\mathrm{CO_2}}$$

$$\phi_M = L\left(\frac{k'RT}{D^{\mathrm{eff}}_{\mathrm{CO_2}}}\right)^{0.5} \qquad \phi_C = \left(\frac{1+\alpha}{\alpha}\right)\sqrt{2(\alpha - \ln(1+\alpha))} \tag{E-3}$$

Here, $L = r_p/3$ is the characteristic dimension, k' and $D^{\mathrm{eff}}_{\mathrm{CO_2}}$ are given by

$$k' = \frac{k}{w} \qquad w = 1 + \left(\frac{D^{\mathrm{eff}}_{\mathrm{CO_2}}}{D^{\mathrm{eff}}_{\mathrm{CO}}}\right) p^{S}_{\mathrm{CO_2}} K_{\mathrm{CO}} \upsilon_{\mathrm{CO}} + K_{\mathrm{CO}} p^{S}_{\mathrm{CO}} \tag{E-4}$$

$$D^{\mathrm{eff}}_{i} = D_i\left(\frac{\varepsilon_0 + (1-X)\varepsilon_0}{\tau^2_{in}}\right) \tag{E-5}$$

D_i is binary diffusion coefficient of CO or CO_2 in nitrogen. The parameter K is defined as

$$K = \frac{K_{\mathrm{CO_2}} - \left(\frac{D^{\mathrm{eff}}_{\mathrm{CO_2}}}{D^{\mathrm{eff}}_{\mathrm{CO}}}\right) K_{\mathrm{CO}} \upsilon_{\mathrm{CO}}}{w} \tag{E-6}$$

The parameter $\upsilon_{\mathrm{CO}} = 2$ is the stoichiometric value of CO in the gasification reaction.

Reference

Abanades, J. C., Rubin, E. S., & Anthony, E. J. (2004). Sorbent Cost and Performance in CO2 Capture Systems. *Industrial & Engineering Chemistry Research*, **43**(13), 3462–3466. Retrieved from http://pubs.acs.org/doi/abs/10.1021/ie049962v

Allen, D., & Hayhurst, A. N. (1996a). Reaction between gaseous sulfur dioxide and solid calcium oxide mechanism and kinetics. *Journal of the Chemical Society, Faraday Transactions*, **92**(7), 1227. Retrieved from http://xlink.rsc.org/?DOI=ft9969201227

Allen, D., & Hayhurst, A. N. (1996b). Kinetics of the reaction between gaseous sulfur trioxide and solid calcium oxide. *Journal of the Chemical Society, Faraday Transactions*, **92**(7), 1239. Retrieved from http://xlink.rsc.org/?DOI=ft9969201239

Anthony, E. J., & Granatstein, D. L. (2001). Sulfation phenomena in fluidized bed combustion systems. *Progress in Energy and Combustion Science*, **27**(2), 215–236. Retrieved from http://www.sciencedirect.com/science/article/pii/S0360128500000216

Arias, B., Cordero, J. M., Alonso, M., & Abanades, J. C. (2012). Sulfation rates of cycled CaO particles in the carbonator of a Ca-looping cycle for postcombustion CO2 capture. *AIChE Journal*, **58**(7), 2262–2269. Retrieved from http://doi.wiley.com/10.1002/aic.12745

Arias, B., Diego, M. E., Abanades, J. C., Lorenzo, M., Diaz, L., Martínez, D., Alvarez, J., & Sánchez-Biezma, A. (2013). Demonstration of steady state CO2 capture in a 1.7MWth calcium looping pilot. *International Journal of Greenhouse Gas Control*, **18**, 237–245. Retrieved from http://www.sciencedirect.com/science/article/pii/S1750583613002922

Arnošt, D., & Schneider, P. (1995). Dynamic transport of multicomponent mixtures of gases in porous solids. *The Chemical Engineering Journal and the Biochemical Engineering Journal*, **57**(2), 91–99. Retrieved from http://www.sciencedirect.com/science/article/pii/0923046794029008

Avrami, M. (1940). Kinetics of Phase Change. II Transformation-Time Relations for Random Distribution of Nuclei. *The Journal of Chemical Physics*, **8**(2), 212–224. Retrieved from http://aip.scitation.org/doi/10.1063/1.1750631

Barin, I., & Platzki, G. (1995). *Thermochemical data of pure substances*, 3rd ed. Weinheim ; New York: VCH. Retrieved from http://doi.wiley.com/10.1002/9783527619825

Barrett, E. P., Joyner, L. G., & Halenda, P. P. (1951). The Determination of Pore Volume and Area Distributions in Porous Substances. I. Computations from Nitrogen Isotherms. *Journal of the American Chemical Society*, **73**(1), 373–380. Retrieved from http://pubs.acs.org/doi/abs/10.1021/ja01145a126

Basinas, P., Wu, Y., Grammelis, P., Anthony, E. J., Grace, J. R., & Jim Lim, C. (2014). Effect of pressure and gas concentration on CO2 and SO2 capture performance of limestones. *Fuel*, **122**, 236–246. Retrieved from http://linkinghub.elsevier.com/retrieve/pii/S0016236114000489

BGR. (2011). *Energy Study 2012 - Reserves, Resources and Availability of Energy Resources*. The Federal Institute for Geosciences and Natural Resources (BGR) on behalf of the German Mineral Resources Agency (DERA). Hannover, Germany.

Bhatia, S. K., & Perlmutter, D. D. (1980). A random pore model for fluid-solid reactions: I. Isothermal, kinetic control. *AIChE Journal*, **26**(3), 379–386. Retrieved from http://doi.wiley.com/10.1002/aic.690260308

Bhatia, S. K., & Perlmutter, D. D. (1981a). The effect of pore structure on fluid-solid reactions: Application to the SO2-lime reaction. *AIChE Journal*, **27**(2), 226–234. Retrieved from http://doi.wiley.com/10.1002/aic.690270209

Bhatia, S. K., & Perlmutter, D. D. (1983). Effect of the product layer on the kinetics of the CO2-lime reaction. *AIChE Journal*, **29**(1), 79–86. Retrieved from http://doi.wiley.com/10.1002/aic.690290111

Bhatia, S., & Perlmutter, D. (1981b). A random pore model for fluid-solid reactions: II. Diffusion and transport effects. *AIChE Journal*, **27**(2), 247–254.

Bird, R., Stewart, W., & Lightfoot, E. (2007). *Transport phenomena*, 2nd ed. New York: John Wiley & Sons, Inc.

Bischoff, K. B. (1963). Accuracy of the pseudo steady state approximation for moving boundary diffusion problems. *Chemical Engineering Science*, **18**(11), 711–713. Retrieved from http://www.sciencedirect.com/science/article/pii/0009250963850502

Bobbink, R., Hornung, M., & Roelofs, J. G. M. (1998). The effects of air-borne nitrogen pollutants on species diversity in natural and semi-natural European vegetation. *Journal of Ecology*, **86**(5), 717–738. Retrieved from http://doi.wiley.com/10.1046/j.1365-2745.1998.8650717.x

Boot-Handford, M. E., Abanades, J. C., Anthony, E. J., Blunt, M. J., Brandani, S., Mac Dowell, N., Fernández, J. R., Ferrari, M.-C., Gross, R., Hallett, J. P., Haszeldine, R. S., Heptonstall, P., Lyngfelt, A., Makuch, Z., Mangano, E., Porter, R. T. J., Pourkashanian, M., Rochelle, G. T., Shah, N., Yao, J. G., & Fennell, P. S. (2014). Carbon capture and storage update. *Energy Environ. Sci.*, **7**(1), 130–189. Retrieved from http://xlink.rsc.org/?DOI=C3EE42350F

Borgwardt, R. H. (1970). Kinetics of the reaction of sulfur dioxide with calcined limestone. *Environmental Science & Technology*, **4**(1), 59–63. Retrieved from http://dx.doi.org/10.1021/es60036a001

Borgwardt, R. H. (1985). Calcination kinetics and surface area of dispersed limestone particles. *AIChE Journal*, **31**(1), 103–111. Retrieved from http://dx.doi.org/10.1002/aic.690310112

Borgwardt, R. H., & Bruce, K. R. (1986). Effect of specific surface area on the reactivity of CaO with SO2. *AIChE Journal*, **32**(2), 239–246. Retrieved from http://doi.wiley.com/10.1002/aic.690320210

Borgwardt, R. H., Bruce, K. R., & Blake, J. (1987). An investigation of product-layer diffusivity for calcium oxide sulfation. *Industrial & Engineering Chemistry Research*, **26**(10), 1993–1998. Retrieved from http://dx.doi.org/10.1021/ie00070a010

Brown, T. A., Dennis, J. S., Scott, S. A., Davidson, J. F., & Hayhurst, A. N. (2010). Gasification and chemical-looping combustion of a lignite char in a fluidized bed of iron oxide. *Energy & Fuels*, **24**(5), 3034–3048. Retrieved from http://pubs.acs.org/doi/abs/10.1021/ef100068m

Brunauer, S., Emmett, P. H., & Teller, E. (1938). Adsorption of Gases in

Multimolecular Layers. *Journal of the American Chemical Society*, **60**(2), 309–319. Retrieved from http://pubs.acs.org/doi/abs/10.1021/ja01269a023

Burdett, N. A. (1983). The inhibition of the limestone sulphation process during fluidized bed combustion - a theoretical approach. *Journal of the Institute of Energy*, **56**(429), 198–209.

Calo, J. M., & Hall, P. J. (1991). Applications of energetic distributions of oxygen surface complexes to carbon and char reactivity and characterization. In J. Lahaye & P. Ehrburger (Eds.), *Fundamental Issues in Control of Carbon Gasification Reactivity SE - 17*, Vol. 192, 329–368. Springer Netherlands. Retrieved from http://dx.doi.org/10.1007/978-94-011-3310-4_17

Calo, J. M., & Perkins, M. T. (1987). A heterogeneous surface model for the "steady-state" kinetics of the boudouard reaction. *Carbon*, **25**(3), 395–407. Retrieved from http://www.sciencedirect.com/science/article/pii/000862238790011X

Chang, P. W., & Finlayson, B. A. (1978a). Orthogonal collocation on finite elements for elliptic equations. *Mathematics and Computers in Simulation*, **20**(2), 83–92. Retrieved from http://linkinghub.elsevier.com/retrieve/pii/0378475478900319

Chang, P. W., & Finlayson, B. A. (1978b, May). Orthogonal collocation on finite elements. *Mathematics and Computers in Simulation*.

Cordero, J. M., & Alonso, M. (2015). Modelling of the kinetics of sulphation of CaO particles under CaL reactor conditions. *Fuel*, **150**, 501–511. Retrieved from http://www.sciencedirect.com/science/article/pii/S0016236115002288

Cordero, J. M., Alonso, M., Arias, B., & Abanades, J. C. (2014). Sulfation Performance of CaO Purges Derived from Calcium Looping CO 2 Capture Systems. *Energy & Fuels*, **28**(2), 1325–1330. Retrieved from http://pubs.acs.org/doi/abs/10.1021/ef402384z

Córdoba, P. (2015). Status of Flue Gas Desulphurisation (FGD) systems from coal-fired power plants: Overview of the physic-chemical control processes of wet limestone FGDs. *Fuel*, **144**, 274–286. Retrieved from http://linkinghub.elsevier.com/retrieve/pii/S0016236114012745

Cunningham, R. S., & Geankoplis, C. J. (1968). Effects of Different Structures of Porous Solids on Diffusion of Gases in the Transition Region. *Industrial &*

Engineering Chemistry Fundamentals, **7**(4), 535–542. Retrieved from http://pubs.acs.org/doi/abs/10.1021/i160028a002

Dai, P., Dennis, J. S., & Scott, S. A. (2016a). Using an experimentally-determined model of the evolution of pore structure for the gasification of chars by CO2. *Fuel*, **171**, 29–43. Retrieved from http://linkinghub.elsevier.com/retrieve/pii/S0016236115013022

Dai, P., González, B., & Dennis, J. S. (2016b). Using an experimentally-determined model of the evolution of pore structure for the calcination of cycled limestones. *Chemical Engineering Journal*, **304**, 175–185. Retrieved from http://dx.doi.org/10.1016/j.cej.2016.06.068

Dam-Johansen, K., Hansen, P. F. B., & Østergaard, K. (1991). High-temperature reaction between sulphur dioxide and limestone—III. A grain-micrograin model and its verification. *Chemical Engineering Science*, **46**(3), 847–853. Retrieved from http://linkinghub.elsevier.com/retrieve/pii/000925099180191Z

Darton, R. C., LaNauze, R. D., Davidson, J. F., & Harrison, D. (1977). Bubble growth due to coalescence in fluidised beds. *Trans Inst Chem Eng*. Retrieved from http://www.scopus.com/inward/record.url?eid=2-s2.0-0017542588&partnerID=tZOtx3y1

Davidson, J. F., & Harrison, D. (1963). *Fluidised Particles*. Cambridge: Cambridge University Press.

Dennis, J. S. (2017). Chapter 7 Transport in Porous Solids. Chemical Engineering Part IIB Lecture Course - Advanced Transport Processes.: University of Cambridge.

Dennis, J. S., & Hayhurst, A. N. (1985). The effect of temperature on the kinetics and extent of SO2 uptake by calcareous materials during the fluidised bed combustion of coal. *Symposium (International) on Combustion*, **20**(1), 1347–1355. Retrieved from http://linkinghub.elsevier.com/retrieve/pii/S0082078485806263

Dennis, J. S., & Hayhurst, A. N. (1987). The effect of CO2 on the kinetics and extent of calcination of limestone and dolomite particles in fluidised beds. *Chemical Engineering Science*, **42**(10), 2361–2372. Retrieved from http://www.sciencedirect.com/science/article/pii/0009250987801100#

Dennis, J. S., & Hayhurst, A. N. (1990). Mechanism of the sulphation of calcined limestone particles in combustion gases. *Chemical Engineering Science*, **45**(5), 1175–1187. Retrieved from http://www.sciencedirect.com/science/article/pii/0009250990871115

Dennis, J. S., & Hayhurst, a. N. (1986). A simplified analytical model for the rate of reaction of SO2 with limestone particles. *Chemical Engineering Science*, **41**(1), 25–36.

Dennis, J. S., & Pacciani, R. (2009). The rate and extent of uptake of CO2 by a synthetic, CaO-containing sorbent. *Chemical Engineering Science*, **64**(9), 2147–2157. Retrieved from http://www.sciencedirect.com/science/article/pii/S000925090900061X

Dennis, J. S., & Scott, S. A. (2010). In situ gasification of a lignite coal and CO2 separation using chemical looping with a Cu-based oxygen carrier. *Fuel*, **89**(7), 1623–1640. Retrieved from http://linkinghub.elsevier.com/retrieve/pii/S0016236109003809

de Diego, L. F., Rufas, A., García-Labiano, F., de las Obras-Loscertales, M., Abad, A., Gayán, P., & Adánez, J. (2013). Optimum temperature for sulphur retention in fluidised beds working under oxy-fuel combustion conditions. *Fuel*, **114**, 106–113. Retrieved from http://www.sciencedirect.com/science/article/pii/S0016236112002025

Duo, W. L., Laursen, K., Lim, J., & Grace, J. (2004). Crystallization and fracture: Product layer diffusion in sulfation of calcined limestone. *Industrial & Engineering Chemistry Research*, **43**(18), 5653–5662. Retrieved from http://pubs.acs.org/doi/abs/10.1021/ie030837d

Duo, W., Sevill, J. P. K., Kirkby, N. F., & Clift, R. (1994). Formation of product layers in solid-gas reactions for removal of acid gases. *Chemical Engineering Science*, **49**(24), 4429–4442. Retrieved from http://linkinghub.elsevier.com/retrieve/pii/S0009250905800314

EIA. (2016). *International Energy Outlook 2016*. U.S. Energy Information Administration (EIA), Washington, D. C. Retrieved from www.eia.gov/forecasts/ieo/pdf/0484(2016).pdf

Erans, M., Manovic, V., & Anthony, E. J. (2016). Calcium looping sorbents for CO2 capture. *Applied Energy*, **180**, 722–742. Retrieved from http://linkinghub.elsevier.com/retrieve/pii/S0306261916310157

Ergun, S. (1956). Kinetics of the reaction of carbon with carbon dioxide. *The Journal of Physical Chemistry*, **60**(4), 480–485. Retrieved from http://pubs.acs.org/doi/abs/10.1021/j150538a022

Evans, R. B., Watson, G. M., & Mason, E. A. (1961). Gaseous diffusion in porous media at uniform pressure. *The Journal of Chemical Physics*, **35**(6), 2076. Retrieved from http://scitation.aip.org/content/aip/journal/jcp/35/6/10.1063/1.1732211

Fennell, P. S., Pacciani, R., Dennis, J. S., Davidson, J. F., & Hayhurst, A. N. (2007). The Effects of Repeated Cycles of Calcination and Carbonation on a Variety of Different Limestones, as Measured in a Hot Fluidized Bed of Sand. *Energy & Fuels*, **21**(4), 2072–2081. Retrieved from http://dx.doi.org/10.1021/ef060506o

Fuertes, A. B., Marban, G., & Rubiera, F. (1993). Kinetics of thermal decomposition of limestone particles in a fluidized bed reactor. *Chemical Engineering Research and Design*, **71**(A4), 421–428. Retrieved from http://www.scopus.com/inward/record.url?eid=2-s2.0-0027629248&partnerID=tZOtx3y1

Fuertes, A. B., Velasco, G., Fuente, E., & Alvarez, T. (1994). Study of the direct sulfation of limestone particles at high CO2 partial pressures. *Fuel Processing Technology*, **38**(3), 181–192. Retrieved from http://www.sciencedirect.com/science/article/pii/0378382094900477

Fuller, E. N., Schettler, P. D., & Giddings, J. C. (1966). A NEW METHOD FOR PREDICTION OF BINARY GAS - PHASE DIFFUSION COEFFICIENT. *Industrial & Engineering Chemistry*, **58**(5), 19–27.

García-Labiano, F., Abad, A., de Diego, L. F., Gayán, P., & Adánez, J. (2002). Calcination of calcium-based sorbents at pressure in a broad range of CO2 concentrations. *Chemical Engineering Science*, **57**(13), 2381–2393. Retrieved from http://www.sciencedirect.com/science/article/pii/S0009250902001379

Gavalas, G. R. (1980). Analysis of char combustion including the effect of pore

enlargement. *Combustion Science and Technology*, **24**(5–6), 197–210. Retrieved from http://www.tandfonline.com/doi/abs/10.1080/00102208008952438

González, B., Liu, W., Sultan, D. S., & Dennis, J. S. (2016). The effect of steam on a synthetic Ca-based sorbent for carbon capture. *Chemical Engineering Journal*, **285**, 378–383. Retrieved from http://www.sciencedirect.com/science/article/pii/S1385894715013911

Green, D., & Perry, R. (2007). *Perry's chemical engineers' handbook*, 8th ed. New York: McGraw-Hill Professional.

Hajaligol, M. R., Longwell, J. P., & Sarofim, A. F. (1988). Analysis and modeling of the direct sulfation of calcium carbonate. *Industrial & Engineering Chemistry Research*, **27**(12), 2203–2210. Retrieved from http://pubs.acs.org/doi/abs/10.1021/ie00084a002

Hanak, D. P., Anthony, E. J., & Manovic, V. (2015). A review of developments in pilot-plant testing and modelling of calcium looping process for CO 2 capture from power generation systems. *Energy Environ. Sci.*, **8**(8), 2199–2249. Retrieved from http://xlink.rsc.org/?DOI=C5EE01228G

Hansen, P. F. B., Dam-Johansen, K., & Østergaard, K. (1993). High-temperature reaction between sulphur dioxide and limestone—V. The effect of periodically changing oxidizing and reducing conditions. *Chemical Engineering Science*, **48**(7), 1325–1341. Retrieved from http://linkinghub.elsevier.com/retrieve/pii/000925099381013L

Hartman, M., & Coughlin, R. W. (1976). REACTION OF SULFUR DIOXIDE WITH LIMESTONE AND THE GRAIN MODEL. *AIChE Journal*. Retrieved from http://www.scopus.com/inward/record.url?eid=2-s2.0-0016958366&partnerID=tZOtx3y1

Hayhurst, A. N. (2000). The mass transfer coefficient for oxygen reacting with a carbon particle in a fluidized or packed bed. *Combustion and Flame*, **121**(4), 679–688. Retrieved from http://www.sciencedirect.com/science/article/pii/S0010218099001789

Hayhurst, A., & Parmar, M. (2002). Measurement of the mass transfer coefficient and

sherwood number for carbon spheres burning in a bubbling fluidized bed. *Combustion and Flame*, **130**(4), 361–375. Retrieved from http://linkinghub.elsevier.com/retrieve/pii/S0010218002003875

Heesink, A. B. M., Prins, W., & van Swaaij, W. P. M. (1993). A grain size distribution model for non-catalytic gas solid reactions. *The Chemical Engineering Journal and the Biochemical Engineering Journal*, **53**(1), 25–37. Retrieved from http://www.sciencedirect.com/science/article/pii/092304679380004G

Hsia, C., Pierre, G. R. St., & Fan, L.-S. (1995). Isotope study on diffusion in CaSO4 formed during sorbent-flue-gas reaction. *AIChE Journal*, **41**(10), 2337–2340. Retrieved from http://doi.wiley.com/10.1002/aic.690411020

Hsia, C., St. Pierre, G. R., Raghunathan, K., & Fan, L.-S. (1993). Diffusion through CaSO4 formed during the reaction of CaO with SO2 and O2. *AIChE Journal*, **39**(4), 698–700. Retrieved from http://doi.wiley.com/10.1002/aic.690390419

Hu, N., & Scaroni, A. W. (1996). Calcination of pulverized limestone particles under furnace injection conditions. *Fuel*, **75**(2), 177–186. Retrieved from http://www.sciencedirect.com/science/article/pii/0016236195002340#

Hüttinger, K. J., & Fritz, O. W. (1991). The carbon-carbon dioxide reaction: An extended treatment of the active-site concept. *Carbon*, **29**(8), 1113–1118. Retrieved from http://www.sciencedirect.com/science/article/pii/000862239190028H

Hüttinger, K. J., & Nill, J. S. (1990). A method for the determination of active sites and true activation energies in carbon gasification: (II) Experimental results. *Carbon*, **28**(4), 457–465. Retrieved from http://www.sciencedirect.com/science/article/pii/0008622390900392

Iisa, K., Hupa, M., & Yrjas, P. (1992). Product layer diffusion in the sulphation of calcium carbonate. *Symposium (International) on Combustion*, **24**(1), 1349–1356. Retrieved from http://linkinghub.elsevier.com/retrieve/pii/S0082078406801578

IPCC. (2005). *IPCC Special Report on Carbon Capture and Storage*. (B. Metz, O. Davidson, H. de Coninck, M. Meyer, & L. Meryer, Eds.). New York: Cambridge University Press.

Jackson, R. (1977). Transport in porous catalysts. In *Chemical Engineering Monographs*, Vol. 4. New York: Elsevier Scientific Pub. Co.

Kavosh, M., Patchigolla, K., Oakey, J. E., Anthony, E. J., Champagne, S., & Hughes, R. (2015). Pressurised calcination–atmospheric carbonation of limestone for cyclic CO2 capture from flue gases. *Chemical Engineering Research and Design*, **102**, 116–123. Retrieved from http://www.sciencedirect.com/science/article/pii/S0263876215002300

Kawahata, M., & Walker, P. L. (1963). *Mode of porosity development in activated anthracite*. *Proceedings of the Fifth Conference on Carbon*. Elsevier. Retrieved from http://www.sciencedirect.com/science/article/pii/B9780080097084500262

Khinast, J., Krammer, G. F., Brunner, C., & Staudinger, G. (1996). Decomposition of limestone: The influence of CO2 and particle size on the reaction rate. *Chemical Engineering Science*, **51**(4), 623–634. Retrieved from http://dx.doi.org/10.1016/0009-2509(95)00302-9

Kucera, V., Tidblad, J., Kreislova, K., Knotkova, D., Faller, M., Reiss, D., Snethlage, R., Yates, T., Henriksen, J., Schreiner, M., Melcher, M., Ferm, M., Lefèvre, R.-A., & Kobus, J. (2007). UN/ECE ICP Materials Dose-response Functions for the Multi-pollutant Situation. *Water, Air, & Soil Pollution: Focus*, **7**(1–3), 249–258. Retrieved from http://link.springer.com/10.1007/s11267-006-9080-z

Laine, N. R., Vastola, F. J., & Walker, P. L. (1963). The importance of active surface area in the carbon-oxygen reaction. In *Journal of Physical Chemistry*, Vol. 67, 2030–2034. Retrieved from http://www.scopus.com/inward/record.url?eid=2-s2.0-0004614888&partnerID=tZOtx3y1

de las Obras-Loscertales, M., Rufas, A., de Diego, L. F., García-Labiano, F., Gayán, P., Abad, A., & Adánez, J. (2015). Morphological analysis of sulfated Ca-based sorbents under conditions corresponding to oxy-fuel fluidized bed combustion. *Fuel*, **162**, 264–270. Retrieved from http://www.sciencedirect.com/science/article/pii/S0016236115009060

Laurendeau, N. M. (1978). Heterogeneous kinetics of coal char gasification and combustion. *Progress in Energy and Combustion Science*, **4**(4), 221–270.

Retrieved from http://linkinghub.elsevier.com/retrieve/pii/0360128578900084

Levenspiel, O. (1999). *Chemical reaction engineering*, 3rd ed. New York: John Wiley & Sons.

Li, Y., Wang, W., Xie, X., Sun, R., & Wu, S. (2014). SO2 retention by highly cycled modified CaO-based sorbent in calcium looping process. *Journal of Thermal Analysis and Calorimetry*, **116**(2), 955–962. Retrieved from http://link.springer.com/10.1007/s10973-013-3567-4

Lim, J. Y., & Dennis, J. S. (2012). Modeling reaction and diffusion in a spherical catalyst pellet using multicomponent flux models. *Industrial & Engineering Chemistry Research*, **51**(49), 15901–15911. Retrieved from http://pubs.acs.org/doi/abs/10.1021/ie302528u

Lin, L., & Strand, M. (2013). Investigation of the intrinsic CO2 gasification kinetics of biomass char at medium to high temperatures. *Applied Energy*, **109**, 220–228. Retrieved from http://www.sciencedirect.com/science/article/pii/S0306261913003218

Lin, W. (1994). *Interactions between SO2 and NOx Emissions in Fluidised Bed Combustion of Coal*. Ph.D. Thesis, Technical University of Delft. Retrieved from http://repository.tudelft.nl/islandora/object/uuid:80071b72-71f9-4a71-97ee-175cb7eeee5a?collection=research

Liu, W., Dennis, J. S., Sultan, D. S., Redfern, S. A. T., & Scott, S. A. (2012). An investigation of the kinetics of CO2 uptake by a synthetic calcium based sorbent. *Chemical Engineering Science*, **69**(1), 644–658. Retrieved from http://www.sciencedirect.com/science/article/pii/S0009250911008359

Lizzio, A. A., Jiang, H., & Radovic, L. R. (1990). On the kinetics of carbon (char) gasification: Reconciling models with experiments. *Carbon*, **28**(1), 7–19. Retrieved from http://www.sciencedirect.com/science/article/pii/000862239090087F

Lyngfelt, A., & Leckner, B. (1989a). Sulphur capture in fluidised-bed combustors: Temperature dependence and lime conversion. *Journal of the Institute of Energy*, **62**(450), 62–72.

Lyngfelt, A., & Leckner, B. (1989b). SO2 capture fluidised-bed boilers: re-emission of SO2 due to reduction of CaSO4. *Chemical Engineering Science*, **44**(2), 207–213.

Retrieved from http://linkinghub.elsevier.com/retrieve/pii/0009250989850584

Manovic, V., & Anthony, E. J. (2010). Carbonation of CaO-based sorbents enhanced by steam addition. *Industrial and Engineering Chemistry Research*, **49**, 9105–9110. Retrieved from http://pubs.acs.org/doi/abs/10.1021/ie101352s

Manovic, V., Anthony, E. J., & Loncarevic, D. (2009). SO2 Retention by CaO-Based Sorbent Spent in CO2 Looping Cycles. *Industrial & Engineering Chemistry Research*, **48**(14), 6627–6632. Retrieved from http://pubs.acs.org/doi/abs/10.1021/ie9002365

McEnaney, B. (1991). Active Sites in Relation to Gasification of Coal Chars. In *Fundamental Issues in Control of Carbon Gasification Reactivity*, 175–203. Dordrecht: Springer Netherlands. Retrieved from http://www.springerlink.com/index/10.1007/978-94-011-3310-4_10

Meenakshi Sundaram, K. (1982). Catalyst effectiveness factor for Langmuir-Hinshelwood-Hougen-Watson kinetic expressions. *Chemical Engineering Communications*.

Menz, F. C., & Seip, H. M. (2004). Acid rain in Europe and the United States: an update. *Environmental Science & Policy*, **7**(4), 253–265. Retrieved from http://linkinghub.elsevier.com/retrieve/pii/S1462901104000590

Milne, C. R., Silcox, G. D., Pershing, D. W., & Kirchgessner, D. A. (1990). High-temperature, short-time sulfation of calcium-based sorbents. 1. Theoretical sulfation model. *Industrial & Engineering Chemistry Research*, **29**(11), 2192–2201. Retrieved from http://pubs.acs.org/doi/abs/10.1021/ie00107a003

Monchick, L., & Mason, E. A. (1961). Transport Properties of Polar Gases. *The Journal of Chemical Physics*, **35**(5), 1676. Retrieved from http://scitation.aip.org/content/aip/journal/jcp/35/5/10.1063/1.1732130

Montoya, A., Truong, T.-T. T., Mondragón, F., & Truong, T. N. (2001). CO Desorption from Oxygen Species on Carbonaceous Surface: 1. Effects of the Local Structure of the Active Site and the Surface Coverage. *The Journal of Physical Chemistry A*, **105**(27), 6757–6764. Retrieved from http://pubs.acs.org/doi/abs/10.1021/jp010572l

Murthy, M. S., Harish, B. R., Rajanandam, K. S., & Ajoy Pavan Kumar, K. Y. (1994).

Investigation on the kinetics of thermal decomposition of calcium carbonate. *Chemical Engineering Science*, **49**(13), 2198–2204. Retrieved from http://www.sciencedirect.com/science/article/pii/0009250994E0015I

Neufeld, P. D., Janzen, A. R., & Aziz, R. A. (1972). Empirical Equations to Calculate 16 of the Transport Collision Integrals Ω(l, s). *The Journal of Chemical Physics*, **57**(3), 1100. Retrieved from http://scitation.aip.org/content/aip/journal/jcp/57/3/10.1063/1.1678363

Nitsch, W. (1962). UBER DIE DRUCKABHANGIGKEIT DER CACO3-BILDUNG AUS DEM OXYD. *ZEITSCHRIFT FUR ELEKTROCHEMIE*, **66**(8–9), 703–708. Retrieved from http://apps.webofknowledge.com/full_record.do?product=UA&search_mode=GeneralSearch&qid=3&SID=3A2pazJOuXk57tlsyNS&page=3&doc=120

Pacciani, R. (2008). *The Use of Ca-based Solid Sorbents for Capturing CO 2*. Ph.D. Thesis, University of Cambridge.

Pacciani, R., Müller, C. R., Davidson, J. F., Dennis, J. S., & Hayhurst, A. N. (2009). Performance of a Novel Synthetic Ca-Based Solid Sorbent Suitable for Desulfurizing Flue Gases in a Fluidized Bed. *Industrial & Engineering Chemistry Research*, **48**(15), 7016–7024. Retrieved from http://pubs.acs.org/doi/abs/10.1021/ie900181y

Patisson, F., Galant François, M., & Ablitzer, D. (1998). A non-isothermal, non-equimolar transient kinetic model for gas-solid reactions. *Chemical Engineering Science*, **53**(4), 697–708. Retrieved from http://www.sciencedirect.com/science/article/pii/S0009250997003333

Pigford, R. L., & Sliger, G. (1973). Rate of Diffusion-Controlled Reaction Between a Gas and a Porous Solid Sphere - Reaction of SO2 with CaCO3. *Industrial & Engineering Chemistry Process Design and Development*, **12**(1), 85–91. Retrieved from http://pubs.acs.org/doi/abs/10.1021/i260045a017

Radovic, L. R., Steczko, K., Walker, P. L., & Jenkins, R. G. (1985). Combined effects of inorganic constituents and pyrolysis conditions on the gasification reactivity of coal chars. *Fuel Processing Technology*, **10**(3), 311–326. Retrieved from http://www.sciencedirect.com/science/article/pii/0378382085900384

Radović, L. R., Walker, P. L., & Jenkins, R. G. (1983). Importance of carbon active

sites in the gasification of coal chars. *Fuel*, **62**(7), 849–856. Retrieved from https://www.sciencedirect.com/science/article/pii/0016236183900418

Ramachandran, P. A., & Doraiswamy, L. K. (1982). Modeling of noncatalytic gas-solid reactions. *AIChE Journal*, **28**(6), 881–900. Retrieved from http://doi.wiley.com/10.1002/aic.690280602

Rao, R. T., Gunn, D. J., & Bowen, J. H. (1989). Kinetics of calcium carbonate decomposition. *Chemical engineering research & design*, **67**(1), 38–47. Retrieved from http://cat.inist.fr/?aModele=afficheN&cpsidt=7315965

Reif, A. E. (1952). The Mechanism of the Carbon Dioxide–Carbon Reaction. *The Journal of Physical Chemistry*, **56**(6), 785–788. Retrieved from http://pubs.acs.org/doi/abs/10.1021/j150498a033

Roberts, G. W., & Satterfield, C. N. (1965). Effectiveness Factor for Porous Catalysts. Langmuir-Hinshelwood Kinetic Expressions. *Industrial & Engineering Chemistry Fundamentals*, **4**(3), 288–293.

Roberts, M. J., Everson, R. C., Domazetis, G., Neomagus, H. W. J. P., Jones, J. M., Van Sittert, C. G. C. E., Okolo, G. N., Niekerk, D. Van, & Mathews, J. P. (2015). Density functional theory molecular modelling and experimental particle kinetics for CO2 – char gasification. *Carbon*, **93**, 295–314. Retrieved from http://linkinghub.elsevier.com/retrieve/pii/S0008622315004509

Rodhe, H., Langner, J., Gallardo, L., & Kjellstrom, E. (1995). Global scale transport of acidifying pollutants. *Water, Air, & Soil Pollution*, **85**(1), 37–50. Retrieved from http://link.springer.com/10.1007/BF00483687

Rothfeld, L. B. (1963). Gaseous counterdiffusion in catalyst pellets. *AIChE Journal*, **9**(1), 19–24. Retrieved from http://doi.wiley.com/10.1002/aic.690090105

Sahimi, M., Gavalas, G. R., & Tsotsis, T. T. (1990). Statistical and continuum models of fluid-solid reactions in porous media. *Chemical Engineering Science*, **45**(6), 1443–1502. Retrieved from http://linkinghub.elsevier.com/retrieve/pii/000925099080001U

Saucedo, M. A. (2014). *The gasification of solid fuels and its relation to chemical-looping and oxy-fuel combustion*. Ph.D. Thesis, University of Cambridge.

Saucedo, M. A., Dennis, J. S., & Scott, S. A. (2015). Modelling rates of gasification of a char particle in chemical looping combustion. *Proceedings of the Combustion Institute*, **35**(i), 2785–2792. Retrieved from http://linkinghub.elsevier.com/retrieve/pii/S1540748914003150

Saucedo, M. A., Lim, J. Y., Dennis, J. S., & Scott, S. A. (2014). CO2-gasification of a lignite coal in the presence of an iron-based oxygen carrier for chemical-looping combustion. *Fuel*, **127**, 186–201. Retrieved from http://linkinghub.elsevier.com/retrieve/pii/S0016236113006443

Schneider, P. (1978). Multicomponent isothermal diffusion and forced flow of gases in capillaries. *Chemical Engineering Science*, **33**(10), 1311–1319. Retrieved from http://www.sciencedirect.com/science/article/pii/0009250978851124

Scott, S. A. (2004). *The gasification and combustion of sewage sludge in a fluidised bed*. Ph.D. Thesis, University of Cambridge.

Scott, S. A., Davidson, J. F., Dennis, J. S., Fennell, P. S., & Hayhurst, A. N. (2005). The rate of gasification by CO2 of chars from waste. *Proceedings of the Combustion Institute*, **30**(2), 2151–2159. Retrieved from http://linkinghub.elsevier.com/retrieve/pii/S0082078404001146

Sendt, K., & Haynes, B. S. (2005). Density functional study of the chemisorption of O2 on the armchair surface of graphite. *Proceedings of the Combustion Institute*, **30**(2), 2141–2149. Retrieved from http://www.sciencedirect.com/science/article/pii/S0082078404001225?via%3Dihub

Sendt, K., & Haynes, B. S. (2011). Density functional study of the reaction of O2 with a single site on the zigzag edge of graphene. *Proceedings of the Combustion Institute*, **33**(2), 1851–1858. Retrieved from http://linkinghub.elsevier.com/retrieve/pii/S1540748910000313

Senneca, O., Salatino, P., & Masi, S. (1998). Microstructural changes and loss of gasification reactivity of chars upon heat treatment. *Fuel*, **77**(13), 1483–1493. Retrieved from http://www.sciencedirect.com/science/article/pii/S0016236198000568

Senneca, O., Scala, F., Chirone, R., & Salatino, P. (2017). Relevance of structure, fragmentation and reactivity of coal to combustion and oxy-combustion. *Fuel*,

201, 65–80. Retrieved from http://www.sciencedirect.com/science/article/pii/S0016236116311358?via%3Dihub

Silcox, G. D., Kramlich, J. C., & Pershing, D. W. (1989). A mathematical model for the flash calcination of dispersed calcium carbonate and calcium hydroxide particles. *Industrial & Engineering Chemistry Research*, **28**, 155–160. Retrieved from http://cat.inist.fr/?aModele=afficheN&cpsidt=7145609

Simons, G. A., & Finson, M. L. (1979). The Structure of Coal Char: Part I—Pore Branching. *Combustion Science and Technology*, **19**(5–6), 217–225. Retrieved from http://www.tandfonline.com/doi/abs/10.1080/00102207908946882

Singer, S. L., & Ghoniem, A. F. (2013). Comprehensive gasification modeling of char particles with multi-modal pore structures. *Combustion and Flame*, **160**(1), 120–137. Retrieved from http://www.sciencedirect.com/science/article/pii/S0010218012002581

Sotirchos, S. V. (1987). On a class of random pore and grain models for gas-solid reactions. *Chemical Engineering Science*, **42**(5), 1262–1265. Retrieved from http://www.sciencedirect.com/science/article/pii/0009250987800842

Stewart, M. C., Manovic, V., Anthony, E. J., & Macchi, A. (2010). Enhancement of Indirect Sulphation of Limestone by Steam Addition. *Environmental Science & Technology*, **44**(22), 8781–8786. Retrieved from http://pubs.acs.org/doi/abs/10.1021/es1021153

Strange, J. F., & Walker, P. L. (1976). Carbon-carbon dioxide reaction: Langmuir-Hinshelwood kinetics at intermediate pressures. *Carbon*, **14**(6), 345–350. Retrieved from http://www.sciencedirect.com/science/article/pii/0008622376900087

Szekely, J., & Evans, J. W. (1970). A structural model for gas—solid reactions with a moving boundary. *Chemical Engineering Science*, **25**(6), 1091–1107. Retrieved from http://www.sciencedirect.com/science/article/pii/0009250970850539

UNEP. (2012). *Global Environment Outlook: Environment for the future we want*

(GEO-5). United Nations Environment Programme (UNEP). Retrieved from http://web.unep.org/geo/assessments/global-assessments/global-environment-outlook-5

Washburn, E. W. (1921). The Dynamics of Capillary Flow. *Physical Review*, **17**(3), 273–283. Retrieved from http://link.aps.org/doi/10.1103/PhysRev.17.273

WEC. (2013). *World Energy Resources: 2013 survey*. World Energy Council. Retrieved from http://www.worldenergy.org/wp-content/uploads/2013/09/Complete_WER_2013_Survey.pdf

Wen, C. Y. (1968). NONCATALYTIC HETEROGENEOUS SOLID-FLUID REACTION MODELS. *Industrial & Engineering Chemistry*, **60**(9), 34–54. Retrieved from http://pubs.acs.org/doi/abs/10.1021/ie50705a007

Wen, C. Y., & Yu, Y. H. (1966). A generalized method for predicting the minimum fluidization velocity. *AIChE Journal*, **12**(3), 610–612. Retrieved from http://doi.wiley.com/10.1002/aic.690120343

Wu, Y., Blamey, J., Anthony, E. J., & Fennell, P. S. (2010). Morphological changes of limestone sorbent particles during carbonation/calcination looping cycles in a thermogravimetric analyzer (TGA) and reactivation with steam. *Energy and Fuels*, **24**(4), 2768–2776. Retrieved from http://pubs.acs.org/doi/abs/10.1021/ef9012449

Wu, Y., Sun, P., Anthony, E. J., Jia, L., & Grace, J. (2006). Reinvestigation of hydration/reactivation characteristics of two long-term sulphated limestones which previously showed uniformly sulphating behaviour. *Fuel*, **85**(14–15), 2213–2219. Retrieved from http://linkinghub.elsevier.com/retrieve/pii/S0016236106001104

Xu, K., Hu, S., Su, S., Xu, C., Sun, L., Shuai, C., Jiang, L., & Xiang, J. (2013). Study on Char Surface Active Sites and Their Relationship to Gasification Reactivity. *Energy & Fuels*, **27**(1), 118–125. Retrieved from http://pubs.acs.org/doi/10.1021/ef301455x

Young, J. B., & Todd, B. (2005). Modelling of multi-component gas flows in capillaries and porous solids. *International Journal of Heat and Mass Transfer*, **48**(25–26), 5338–5353. Retrieved from http://linkinghub.elsevier.com/retrieve/pii/S0017931005004904

Zawadzki, J. (1932). Zur Kenntnis des Systems Calcium-Schwefel-Sauerstoff. *Zeitschrift für anorganische und allgemeine Chemie*, **205**(1–2), 180–192. Retrieved from http://doi.wiley.com/10.1002/zaac.19322050114

Zawadzki, J., & Bretsznajder, S. (1935). Concerning the temperature increment of the rate of reaction in reactions of the type A(solid)= B-solid+C-gas. *ZEITSCHRIFT FUR ELEKTROCHEMIE UND ANGEWANDTE PHYSIKALISCHE CHEMIE*, **41**, 215–223. Retrieved from http://apps.webofknowledge.com/full_record.do?product=UA&search_mode=GeneralSearch&qid=9&SID=3A2pazJOuXk57tlsyNS&page=1&doc=1

Zhang, Z. (2010). China in the transition to a low-carbon economy. *Energy Policy*, **38**(11), 6638–6653. Retrieved from http://linkinghub.elsevier.com/retrieve/pii/S0301421510004970

Zoia, A., & Latrille, C. (2011). Estimating apparent diffusion coefficient and tortuosity in packed sand columns by tracer experiments. *Journal of Porous Media*, **14**(6), 507–520. Retrieved from http://www.dl.begellhouse.com/journals/49dcde6d4c0809db,77fb6f130f547d4a,5629f3ef00133c34.html